NORTHWESTERN UNIVERSITY

Stratigraphic and Geochemical Investigations of Late Cretaceous Oceanic Anoxic Events and Greenhouse Sea Level Trends

A DISSERTATION

SUBMITTED TO THE GRADUATE SCHOOL
IN PARTIAL FULFILLMENT OF THE REQUIREMENTS

for the degree

DOCTOR OF PHILOSOPHY

Field of Earth and Planetary Sciences

By
Matthew Madden Jones

EVANSTON, ILLINOIS

December 2018

ABSTRACT

Stratigraphic and Geochemical Investigations of Late Cretaceous Oceanic Anoxic Events and Greenhouse Sea Level Trends

Matthew Madden Jones

This dissertation researches the Cenomanian, Turonian, and Coniacian Stages (100.5 - 86.3 Ma) of the Cretaceous Period, a geologic interval of interest due to its extreme global warmth, iconic faunas, and oceanic anoxic events (OAEs). Five globally dispersed geochemical and stratigraphic case studies reconstruct interactions of the mid-Cretaceous carbon cycle with large igneous province (LIP) volcanism, astronomical cycles (i.e., Milankovitch cycles), sea level oscillations, and paleoclimatic and paleoceanographic conditions. Chapters 2 and 3 of the dissertation investigate deep sea and continental drill cores to characterize paleoclimatic conditions and geochemical cycling over multi-million year spans of time in the mid-Cretaceous. From rhythmically bedded cores of Demerara Rise in the tropical North Atlantic, Chapter 2 develops an astronomically-tuned time scale for the Turonian Stage, along with an interpretation for Turonian carbon burial dynamics driving globally-correlative carbon isotope signals. The history of terrestrial environmental conditions in the Cretaceous stratigraphic record is much sparser, including responses to OAEs in the continental environment. Chapter 3 presents a relatively rare and continuous ~5 million-year sedimentary record of Turonian-Coniacian geochemical data and paleoclimate insights from lacustrine shales of the Songliao Basin in northeastern China.

Chapters 4 through 6 have a higher temporal resolution, focusing on a narrower 600-800 kiloyear time interval across the Cenomanian-Turonian Stage boundary (93.9±0.15 Ma), to investigate the causes, timing, and biotic consequences of a major Mesozoic oceanic anoxic event

– OAE2. Chapter 4 presents the most expanded stratigraphic record of OAE2 in the central Western Interior Basin (U.S.) from the SH#1 core recovered during fieldwork in 2014. In addition to generating a finely resolved chemostratigraphic record of OAE2, the proximal SH#1 core preserves distinct geochemical signals of carbonate diagenesis, which trace to flooding surfaces in shoreface deposits nearby. Accordingly, these geochemical signatures record relative sea level through OAE2; they exhibit short eccentricity pacing of parasequences and, therefore, a climatic control on sea level oscillations. Chapter 5 further utilizes stratigraphically expanded and conformable records from the Western Interior to quantify the timing of large igneous province volcanism that triggered OAE2, along with local environmental responses and global phenomenon, such as expanded anoxia. Using this refined chronostratigraphy of OAE2, Chapter 6 assesses the ramifications of rapid rates of LIP volcanism and CO_2 degassing on the marine ecosystem and geochemistry, in particular the effects on marine carbonate chemistry. A global compilation of carbonate contents through OAE2 detects a shoaling of the ocean's carbonate compensation depth (CCD) at pelagic sites while carbonate sedimentation continued at shallower epicontinental sites. Consistent findings of a shoaling CCD, model reconstructions of volcanic fluxes, and morphological alterations in calcifying marine taxa, suggest that ocean acidification, in addition to namesake anoxia, occurred during OAE2, and may have been a fundamental paleoceanographic response to episodes of LIP volcanism through the Mesozoic.

ACKNOWLEDGEMENTS

First and foremost, I would like to thank my doctoral advisor Brad Sageman, who welcomed me into the program at Northwestern University. He gave me a wide-open course of study to foster creativity and independence in my geoscience research, while always keeping the door open when I hit a stumbling point, suggesting new opportunities, and reminding me of what really counts in science and life (and guitar-playing). I will always be grateful for the opportunity I was given to come to Northwestern and study complex and inspiring aspects of the natural world.

I would also like to thank my committee members Andy Jacobson and Matt Hurtgen who provided feedback and encouragement during my time in the program, and were always happy to lend assistance or advice on new ideas without hesitation. Dave Selby of Durham University and Steve Meyers of the University of Wisconsin welcomed me into their labs and graciously shared their research techniques and expertise with me to elevate the quality and perspective of my doctoral research.

In the field and navigating the science of journal article-writing, I was fortunate to have the mentorship and encouragement of co-authors and collaborators Mark Leckie, Tim Bralower, Julio Sepúlveda, Page Chamberlain, Stephen Graham, Yuan Gao, David Uličný, and the IODP Expedition 369 Scientists. Many far flung graduate students, like (now Drs.) Dan Ibarra and Rosie Oakes, along with Amanda Parker, Garrett Boudinot, Chao Ma, and Victoria Fortiz, supported this research over countless time in the field, emails, and conference meetings, and kindly added complementary analyses to the studies when possible. I would not have made my way to graduate education in the first place without the guidance and support of my undergraduate professors at the University of New Hampshire, along with my mentors at H2H Associates in Troy, NY.

This research could not have come to fruition without the assistance and expertise of Northwestern lab managers Grace Schellinger, Koushik Dutta, Andy Masterson, and Meagan Ankney. When I first arrived at Northwestern, I was fortunate to have ever-patient senior graduate students who went above and beyond to teach me the ropes in the Hogan geochemical labs, especially Maya Gomes, Brian Kristall, Greg Lehn, Laurel Childress, and Jeremy Gouldey.

I would also like to thank the Earth and Planetary Science faculty at Northwestern for creating a collegial community for learning and research, especially the Assistant Chair and ultimate student advocate, Trish Beddows. Staff members Lisa, Ben, and Robin were always quick to help with last minute TA'ing requests and the nitty-gritty of how to decipher receipts from China! Thank you for your support.

To each of my fellow grad students, especially you senior grads who were there for the long-haul (Grace Andrews, Eddie, Amir, Jamie, Nooshin, Emiliano, Jiuyuan, Everett), your friendship and drive inspired me to continue this work and unique lifestyle. And I am grateful for the wisdom of postdocs Melissa Chipman, Ben Linzmeier, and Dorothee Husson who helped me navigate the unfamiliar aspects of my research, along with the question "well…what next?" as my PhD drew to a close.

To Merretta, thank you for making my time in Chicago so memorable and reminding me there's more to life than rocks. See you in Ann Arbor soon! To my Parents and Abbey, my wildfire-fighting sister, thanks for supporting me in striking a new path in a new place, encouraging me to get outside growing up, and indulging my obsession with maps when I was young – it may have turned out to be useful in the end!

LIST OF COMMON ABBREVIATIONS

OAE – Oceanic Anoxic Event

CTB – Cenomanian-Turonian Stage Boundary

WIS – Western Interior Seaway

WIB – Western Interior Basin

DSDP – Deep Sea Drilling Project

ODP – Ocean Drilling Program

IODP – International Ocean Discovery Program

GSSP – Global strato-type section and point

GTS – Geologic Time Scale

ATS – Astronomical time scale

CIE – Carbon isotope excursion

$\delta^{13}C$ – Stable isotope ratio of ^{13}C to ^{12}C normalized to geologic standard

kyr – thousands of years in duration

Myr – millions of years in duration

Ma – millions of years in age

TABLE OF CONTENTS

Abstract……………………………………………………………………………………3

Acknowledgements……………………………………………………………………..5

List of Abbreviations…………………………………………………………………...7

Table of Contents……………………………………………………………………….8

List of Figures…………………………………………………………………………10

List of Tables………………………………………………………………………….13

CHAPTER 1: Introduction……………………………………………………………14

CHAPTER 2: Turonian Sea Level and Paleoclimatic Events in Astronomically Tuned Records from the Tropical North Atlantic and Western Interior Seaway…………………………22

CHAPTER 3: Evaluating Late Cretaceous OAEs and the Influence of Marine Incursions on Organic Carbon Burial in an Expansive East Asian Paleo-lake…………………………68

CHAPTER 4: Astronomical Pacing of Relative Sea Level during Oceanic Anoxic Event 2 from the Expanded SH#1 Core, Utah……………………………………………………...…100

CHAPTER 5: Regional Chronostratigraphic Synthesis of the Cenomanian-Turonian OAE2 Interval, Western Interior Basin: Astrochronology, Radioisotope Dating, and New Os and C Chemostratigraphy……………….................……………………………………...149

CHAPTER 6: Volcanic Shoaling of the Marine Calcite Compensation Depth during OAE2…185

References Cited……………………………………………………………………..…205

APPENDICES

Appendix 1: Supplemental material for Demerara Rise study (Chapter 2)…………………….244

Appendix 2: Supplemental material for Songliao Basin study (Chapter 3)…………………... 261

Appendix 3: Supplemental datasets for the SH#1 core, Utah (Chapter 4)………......................274

Appendix 4: Supplemental datasets for the Angus core (Chapter 5)……………..…………………..284

LIST OF FIGURES

Figure 2.1.: Astronomically tuned Late Cretaceous time intervals and map of proto-North Atlantic basin……………………………………………………………………………28

Figure 2.2.: Chemostratigraphy of ODP Sites 1259 and 1261, Demerara Rise…………………...39

Figure 2.3.: Evolutive power spectral analysis (EPSA) and evolutive harmonic analysis (EHA) of Turonian-Coniacian Stage carbonate content at ODP Site 1259 carbonate content...44

Figure 2.4.: Evolutive average spectral misfit results from ODP Site 1259………………………45

Figure 2.5.: Cross-correlation of gaussian smoothed $\delta^{13}C_{org}$ timeseries at ODP Sites 1259 and 1261……………………………………………………………………………………46

Figure 2.6.: Astronomically tuned and spliced geochemical time series from Demerara Rise (Cenomanian-Coniacian Stages)…………………………………………………48

Figure 2.7.: Global correlation of $\delta^{13}C$ chemostratigraphic records spanning Turonian Stage…...58

Figure 2.8.: Spectral analysis of $\delta^{13}C_{org}$ and %TOC time series at Demerara Rise………………61

Figure 3.1.: Palinspastic map, facies map, and cross section of Songliao Basin, N.E. China……75

Figure 3.2.: Carbon and osmium isotope chemostratigraphy of SK1-s core……………………..80

Figure 3.3.: XRF trace element chemostratigraphy of SK1-s core………………………………82

Figure 3.4.: Turonian-Coniacian Songliao Basin – WIB $\delta^{13}C_{org}$ correlation……………………...85

Figure 3.5.: $\Delta^{13}C$ trends in the SK1-s and Angus Aristocrat (WIB) cores………………………88

Figure 3.6.: Turonian-Coniacian initial osmium (Os_i) records in SK1-s core, Angus core, and Demerara Rise ……………………………………………………………………92

Figure 3.7.: Model of biogeochemical cycling in mid-Cretaceous Songliao lake system………...98

Figure 4.1.: Lower Turonian facies map of the Western Interior Basin…………………………105

Figure 4.2.: Lithostratigraphy of the Cenomanian-Turonian Boundary Interval in the Western Interior Basin of Utah-Colorado……………………………………………….107

Figure 4.3.: Map of SH#1 core and KPS outcrop localities in the Grand Staircase Escalante National Monument…………………………………………………………110

Figure 4.4.: Photographs of the SH#1 core and KPS outcrop………………………………..112

Figure 4.5.: KPS outcrop correlation to coulometer and $\delta^{13}C_{org}$ chemostratigraphy of SH#1 core……………………………………………………………………….....119

Figure 4.6.: Isotopic chemostratigraphy of the SH#1 core……………………………………124

Figure 4.7.: $\delta^{13}C_{carb}$ and $\delta^{18}O_{carb}$ covariation cross plot in Tropic Shale, SH#1 core…………….125

Figure 4.8.: Astrochronologic analyses of SH#1 core……………………………………….…...128

Figure 4.9.: Core scanning XRF chemostratigraphy of SH#1 core…………………………...131

Figure 4.10.: Correlation of SH#1 chemostratigraphy to Markagunt Plateau shoreface facies…139

Figure 4.11.: Correlation of astronomically tuned CTB intervals across WIB…………………145

Figure 4.12.: SH#1 – Gongzha, Tibet correlation………………………………………………146

Figure 5.1.: Early Turonian map of central and southern WIB………………………………156

Figure 5.2.: Os and C chemostratigraphy of OAE2, Angus core……………………………161

Figure 5.3.: Os and C chemostratigraphy of OAE2, SH#1 core……………………………….162

Figure 5.4.: Os and C chemostratigraphy of OAE2 in WIB…………………………………166

Figure 5.5.: Osmium and carbon isotope timeseries through OAE2 in central WIB……………174

Figure 5.6.: OAE2 timeseries comparison between central WIB and Eagle Ford……………….175

Figure 5.7.: Astrochronology comparison of OAE2 (Charbonnier et al., 2018)………………. 177

Figure 5.8.: Comparison of radioisotopic ages for OAE2……………………………………180

Figure 5.9.: Schematic timeline of OAE2……………………………………………………182

Figure 6.1.: Global palinspastic map of the Cenomanian-Turonian Boundary (~94 Ma)……… 191

Figure 6.2.: Compilation of carbonate sedimentation trends through OAE2……………………193

Figure 6.3.: Osmium box modeling results for large igneous province volcanism across OAE2..195

LIST OF TABLES

Table 4.1.: Significant temporal periodicities in the astronomically tuned $\delta^{13}C_{carb}$ timeseries from SH#1 core……………………………………………………………………….127

Table 4.2.: Comparison of durations between bentonites at three WIB sites with astrochronologic time scales…………………………………………………………………….141

Table 5.1.: Bulk organic carbon isotope data for OAE2 onset, Angus core…………………….161

Table 5.2.: Rhenium-osmium geochemistry of the Angus and SH#1 cores…………………….162

Table 6.1.: Global compilation of carbonate content trends through OAE2…………………….198

CHAPTER 1

Introduction

1.1. Geologic questions of the early Late Cretaceous

The plate tectonic configuration of Earth during the early Late Cretaceous resembled the modern world in many regards, appearing familiarly on paleomaps with some notable exceptions (Hay et al., 1999). However, the early Late Cretaceous global ocean also inundated continental interiors and hosted now-extinct fauna of ammonites, inoceramids, and mosasaurs, while sea surface temperatures may have approached 30°C at the southern sub-polar latitudes, lush forests flourished at sub-polar to polar latitudes, and ocean crustal production rates were 50-75% greater than today (Hancock and Kauffman, 1979; Larson, 1991; Spicer and Herman, 2011; Friedrich et al., 2012; Huber et al., 2018). This model of the planet, with a similar geography to the Anthropocene yet with an extremely warm climate, has led some geologists to compare the early Late Cretaceous thermal maximum to the potential future climate state of the presently warming planet (Hay, 2011).

To explain these disparate environments despite similar boundary conditions, geologists have pursued deep sea coring, outcrop studies, geochemical analyses, and biostratigraphic investigations. In those endeavors, they have discovered Mesozoic oceanic anoxic events (OAEs), several hundred kiloyear intervals of black shale deposition interpreted to reflect low marine dissolved oxygen levels, as well as high-frequency fluctuations in apparent global sea levels (eustasy) on a planet lacking any known appreciable volume of ice (Schlanger and Jenkyns, 1976; Jenkyns, 2010; Haq, 2014). This dissertation investigates these phenomena through studies of the stratigraphic record. In Chapters 2 and 3, I apply geochemical and stratigraphic approaches to further characterize the broad background paleoclimate conditions of the early Late Cretaceous in tropical marine and mid-latitude terrestrial settings and to test interpretations about eustasy. Later in Chapters 4-6, I employ similar techniques at a higher temporal resolution to refine understanding of the causes, timing, and consequences of the Cenomanian-Turonian Oceanic Anoxic Event 2 (OAE2), one of the most severe Mesozoic OAEs.

Glacial-interglacial eustatic cycles in the “icehouse” climate of the Quaternary are generally attributed to waxing and waning of continental ice sheets (Shackleton, 1987), along with local anomalies from dynamic topography (Moucha et al., 2008). In the greenhouse Cretaceous interval, it is more challenging to confirm the existence of eustatic cycles due to uncertainties in stratigraphic correlation and given the fact that the planet was presumably free of substantial volumes of continental ice (MacLeod et al., 2013). Although Late Cretaceous sea level histories have been proposed from relatively stable cratonic margins (Miller et al., 2005; Haq, 2014), few studies have critically tested the global stratigraphic correlation of the higher-frequency sea level cycles or assessed potential drivers of eustasy (Gale et al., 2008; Haq and Huber, 2017). Confirmation of such global lowstands and highstands would provide a functional correlation framework to link stratigraphic records globally and would motivate studies evaluating potential mechanisms behind Late Cretaceous sea level patterns, such as aquifer eustasy or ephemeral ice sheet growth and decay (e.g., Hay and Leslie, 1990; Stoll and Schrag, 2000).

Chapter 2 investigates whether mid-to-late Turonian Stage regressions of the shallow Western Interior Seaway (WIS) of North America are coeval with previous evidence for cooling at Demerara Rise in the tropical North Atlantic (Bornemann et al., 2008). The records are correlated via astrochronology and carbon isotope chemostratigraphy, developing a new Turonian astronomical time scale and providing insights into paleoclimate upwelling patterns in the tropical Atlantic. Chapter 3 investigates a lacustrine record from the Songliao Basin that is partially time-equivalent to the record at Demerara Rise. Using sedimentary geochemical analyses, I test the hypothesis that marine incursions flooded the terrestrial basin, possibly during eustatic transgression, forming organic carbon-rich shale and a supergiant oil field in northeast China (Wang et al., 2016a). Further, the basin provides a rare, relatively continuous window into continental east Asian paleoclimatic conditions during the Turonian-Coniacian Stages, a largely unknown aspect of the Cretaceous greenhouse interval.

Superimposed on this record of early Late Cretaceous global warmth, is Oceanic Anoxic Event 2 (OAE2, ~94 Ma), a several hundred kiloyear interval of black shale deposition in many basins globally interpreted to reflect vastly expanded marine bottom water anoxia/euxinia (Schlanger and Jenkyns, 1976; Arthur et al., 1987, Schlanger et al., 1987). The record of OAE2, along with other Mesozoic OAEs, may serve as a geologic model for modern biotic stresses and geochemical shifts in the modern global ocean as deoxygenation accelerates (Keeling et al., 2010; Breitburg et al., 2018). A characteristic positive carbon isotope excursion is recorded in carbonate and organic carbon during OAE2, signifying a global-scale perturbation to the carbon cycle and Cretaceous climate system, resulting from the spread of marine anoxia (Scholle and Arthur, 1980). Additional petrologic and geochemical evidence indicates that the event was triggered by prolific large igneous province (LIP) volcanism (Kerr et al., 1997; Kerr, 1998; Snow et al., 2005). This LIP trigger and subsequent biogeochemical feedbacks during OAE2, such as anoxia, led to notable responses in major and trace elemental marine cycles, which are recorded in stratigraphic archives

(Mort et al., 2007; Turgeon and Creaser, 2008; Adams et al., 2010; Pogge von Strandmann et al., 2013; Du Vivier et al., 2014; 2015a; Holmden et al., 2016; Jenkyns et al., 2017; Clarkson et al., 2018). Although isotope geochemical signals are increasingly well resolved across OAE2, the exact response of sea level and paleoclimate thought to sustain the event over hundreds of kiloyear remain areas of active research.

In chapter 4, I present an expanded shallow marine chemostratigraphic record of OAE2 from the SH#1 core, recovered from the Western Interior Basin (WIB) during fieldwork in southern Utah in 2014. This record correlates to nearby shoreface deposits and provides new insights into sea level changes during OAE2. Cyclical patterns in geochemistry within SH#1 record astrochronologic evidence for an outsized role of orbital eccentricity climate forcing in the pacing of relative sea level through the event, which are likely eustatic. Chapter 5 increases the chronostratigraphic resolution of the onset interval of OAE2. The study seeks to determine kiloyear-scale timing of LIP volcanism and carbon cycle responses using osmium isotope (Os_i) chemostratigraphy and an existing astrochronologic time scale in the conformable Angus core of Colorado and the SH#1 core of Utah. The Os_i record also resolves the duration of a minor, yet stratigraphically important hiatus at the base of OAE2 in the Cenomanian-Turonian GSSP in Pueblo, Colorado.

Using this high-resolution, conformable record of volcanism across the onset of OAE2 from Os_i in the Angus core, Chapter 6 assesses the consequences of rapid LIP emplacement and associated CO_2 degassing on the marine realm. Global Cenomanian-Turonian carbonate sedimentation trends compiled in Chapter 6 from pelagic and epicontinental sites indicate a shallowing of the marine calcite compensation depth, in the form of carbonate barren intervals.

This finding of pelagic ocean acidification is consistent with box models of the osmium marine geochemical cycle that indicate orders of magnitude increases in volcanic fluxes ~60 kiloyear prior to OAE2. The results suggest that the rate of volcanism during OAE2 was rapid enough to alter marine carbonate chemistry and shoal the marine calcite compensation depth, impacting marine biotas potentially and mirroring modern trends in the global ocean (Sulpis et al., 2018).

1.2. Primary methodologies

One principal obstacle to reconstructing geologic processes and significant paleoclimate events in Earth history at a global scale, is the challenge of precisely comparing a selected horizon of time from multiple sedimentary records on different continents via stratigraphic correlation (Kauffman, 1988). The temporal uncertainty associated with pre-Cenozoic intercontinental correlations has historically been coarse, on the scale of ± millions of years, due to the uncertainties associated with radioisotopic dating, sparsity of intercalated datable material, uncertainties in biostratigraphy, etc. (e.g., Obradovich et al., 1993), though there have been substantial advances in precision in most recent studies (e.g., Meyers et al., 2012a). Many of the findings in this dissertation hinge on the ability to precisely correlate stratigraphic sections globally at sub-100 kyr resolution, closer to the temporal scale of geologic climate change. To attain such chronostratigraphic resolution, I employ chemostratigraphic techniques using excursions in isotopic ratios and elemental abundances of globally mixed marine geochemical cycles, such as carbon and osmium, to link geographically disparate records.

If unaltered by post-depositional diagenesis, stable carbon isotope ratios ($^{13}C/^{12}C$) of sedimentary carbonates and organic carbon preserve changes in the carbon cycle through geologic time (Kump and Arthur, 1999). Since natural variation in stable carbon isotope ratios is small, it is calculated in delta per-mil notation as $\delta^{13}C$ – a measure of the difference in carbon isotopic ratio of a sample versus a standard reference material, such as the Pee Dee Belemnite (PDB), multiplied by 1,000 (Equation 1.1) (Sharp, 2018 p. 2-2).

Equation 1.1: $$\delta^{13}C = \left(\frac{{}^{13}C/{}^{12}C_{sample}}{{}^{13}C/{}^{12}C_{standard}} - 1 \right) \times 1000$$

The $\delta^{13}C$ of a sample of primary carbonate or aquatic/marine organic carbon is a function of the $\delta^{13}C$ of the dissolved inorganic carbon (DIC) of the water mass from which it formed, as well as any isotopic fractionation imparted during precipitation or photosynthesis, respectively (Anderson and Arthur, 1983). Since the isotopic fractionation is relatively minor in the case of carbonates, and relatively systematic in the case of organic carbon, a significant component of $\delta^{13}C$ in stratigraphic profiles may record changes in $\delta^{13}C_{DIC}$ of water masses. For marine sediments, this means that shifts in the $\delta^{13}C_{DIC}$ of the global ocean can serve as correlative markers among coeval sites, linking stratigraphic records globally (e.g., Jarvis et al., 2006; Joo and Sageman, 2014).

In addition, relative shifts $\delta^{13}C_{DIC}$ are insightful since its value varies through time as a function of changes in the relative fluxes of carbon with characteristic $\delta^{13}C$ to and from the ocean-atmosphere system. Although C fluxes from weathering, volcanism, and carbonate sedimentation all influence marine $\delta^{13}C_{DIC}$, the most significant driver or "lever" of $\delta^{13}C_{DIC}$ is the burial of organic carbon, since it removes isotopically depleted photosynthate, enriching $\delta^{13}C$ in the residual oceanic reservoir (Kump and Arthur, 1999). As a result, positive carbon isotopic excursions in Earth history, such as during OAE2, mark global-scale perturbations to the carbon cycle, resulting from widespread marine anoxia (Scholle and Arthur, 1980). Given the utility of the measurement through geologic time in correlating sites and reconstructing shifts in the carbon cycle, I apply and develop new $\delta^{13}C$ chemostratigraphy correlation techniques in the subsequent chapters of this dissertation.

However, the $\delta^{13}C$ chemostratigraphic signal in carbonates and organic matter can be obfuscated by variations in $\delta^{13}C$ of local water bodies and by post-depositional diagenesis. For time intervals with substantial shifts in volcanic activity or continental weathering rates, such as OAE2, the initial osmium isotope (Os_i) proxy has recently been recognized to generate robust stratigraphic correlations (e.g., Du Vivier et al., 2014). Beneficial criteria of the Os_i proxy include: a geologically brief marine residence time (10s of kyr), on the timescale of geologic climate events; a relatively well mixed marine reservoir, enabling global correlations; and a limited number of diagnostic, isotopically distinct fluxes, namely radiogenic continental weathering and unradiogenic mantle (i.e. volcanism) (Peucker-Ehrenbrink and Ravizza, 2000). Thus, I utilize the Os_i proxy to test for hydrographic connections between the ocean and a paleo-lake system in northeast Asia in Chapter 3 and to assess the timing and magnitude of LIP volcanism through the onset of OAE2 in Chapters 5 and 6.

Another technique utilized to improve time control in the studied stratigraphic successions is astrochronology. Milankovitch Cycles are periodic oscillations in the rotational and orbital parameters of Earth, which influence the amount and distribution of solar radiation on the planet’s surface through time (Hinnov, 2013). They manifest on the timescale of tens to hundreds of thousands of years, durations approaching the rate of rapid geologic climate change, and can be recorded in stratigraphic archives from depositional environments which are sensitive to changes in solar radiation and climate. Since the periodicities of cycles of axial precession, tilt and orbital obliquity (ETP) are constrained by astrophysical models (Laskar et al., 2004; 2011) and calibrated by high-precision uranium-lead geochronology (Machlus et al., 2015), the identification of astronomical cycles in sedimentary successions permits the reconstruction of sedimentation rates, a fundamental measurement in stratigraphy (Meyers et al., 2001). In addition to generating "floating" numerical timescales to determine rates of environmental change during significant paleoclimate events, astrochronologic analyses identify which ETP cycle a given geologic process or paleoenvironment responds most prominently to, providing insights into the manifestation of climate feedbacks and teleconnections in the Earth system (e.g., Meyers et al. 2012a). Given these potentials, I conduct spectral analyses on rhythmic chemostratigraphic records and interbedded strata through the Turonian Stage at Demerara Rise (Chapter 2) and through OAE2 at the SH#1 core in Utah (Chapter 4) to resolve the timing of relative sea level oscillations. In Chapter 3, astrochronology also plays a key role in assigning an age model to $\delta^{13}C$ data from the Songliao Basin to confirm terrestrial-marine correlations. In Chapters 5-6, astrochronologic analysis refines the rate of the Os_i excursion and associated LIP emplacement and CO_2 degassing at the initiation of OAE2 on a kiloyear-scale.

In combination, these three primary techniques are implemented in the subsequent chapters to reconstruct a higher precision chronostratigraphic record of OAE2 and the broader greenhouse Late Cretaceous interval, enabling new inquires to long-standing questions about paleo-sea level and paleoceanographic events.

CHAPTER 2

Turonian Sea Level and Paleoclimatic Events in Astronomically Tuned Records from the Tropical North Atlantic and Western Interior Seaway

Motivation: Demerara Rise − a submarine plateau offshore of Suriname, was a zone of tropical upwelling spanning much of the mid-Cretaceous greenhouse interval. This chapter researches a relatively continuous ~6 million-year succession of fine-grained pelagic sediments at Demerara Rise, a site sensitive to shifts in oceanographic circulation and climate. It details the sedimentary geochemistry at the site to investigate an important sink in mid-Cretaceous carbon cycling dynamics and presents spectral analyses of stratigraphic bedding patterns to test for preservation of Milankovitch cycles – periodic variations in the axial obliquity, axial precession, and orbital eccentricity parameters of the planet that influence Earth's climate over tens of thousands of years. The resulting astronomical time scale and carbon isotope stratigraphy of the Turonian Stage (~89.3-93.9 Ma) at the site is used to correlate and compare deep-marine paleoclimate records to coeval relative sea level trends and biostratigraphic records in the shallow, semi-restricted Western Interior Basin of North America.

Key findings:

- An astronomically tuned carbon isotope ($\delta^{13}C$) chemostratigraphy yields Turonian Stage (Late Cretaceous) duration from Demerara Rise (DR).
- Obliquity modulated tropical Atlantic monsoonal winds intensified upwelling, anoxia, and organic carbon burial at DR through the Turonian Stage.

- TOC increases at DR during many Turonian positive δ^{13}C excursions, suggesting a strong connection between organic carbon burial in equatorial Atlantic and the global carbon cycle.

- A mid-Turonian upper *C. woolgari* hiatus in the Western Interior Basin is coeval with evidence for cooling at DR via δ^{13}C kernel smoothing correlation.

This chapter of research originally appeared in:

Jones, M. M., Sageman, B. B., and Meyers, S. R., 2018, Turonian sea level and paleoclimatic events in astronomically tuned records from the tropical North Atlantic and Western Interior Seaway. *Paleoceanography and Paleoclimatology*, 33. https://doi.org/10.1029/2017PA003158

CHAPTER 2

Turonian Sea Level and Paleoclimatic Events in Astronomically Tuned Records from the Tropical North Atlantic and Western Interior Seaway

Abstract

Multiple hiatuses punctuate the Middle to Upper Turonian Substages of the Western Interior Basin (WIB, USA), interrupting an otherwise highly resolved and relatively conformable Upper Cretaceous stratigraphic record. To determine the duration and possible causes of these hiatuses, while simultaneously reconstructing Turonian carbon cycling, we develop a new astronomically tuned carbon isotope ($\delta^{13}C$) chemostratigraphy from time-equivalent organic carbon-rich shales of the tropical North Atlantic (Demerara Rise—Ocean Drilling Program Leg 207). A Gaussian kernel smoothing and cross-correlation technique is also introduced to quantitatively correlate the astronomically tuned Demerara Rise $\delta^{13}C$ chemostratigraphy to coeval records globally. This analysis reveals a general consistency among ages for Turonian $\delta^{13}C$ excursions from astronomical and radioisotopic timescales. It also indicates that a positive oxygen isotope excursion at Demerara Rise, previously interpreted to signify cooling, is synchronous (~±200 kyr) with the Ogbourne Hardground in the English Chalk, the Bass River—Magothy sequence boundary, and an expansive mid-Turonian hiatus in the WIB. However, the event is not concurrent with maximum regression in the WIB. Trends in $\delta^{13}C$, and additional geochemical data from Demerara Rise (weight percent total organic carbon, weight percent carbonate, and C/N), are consistent with oceanic upwelling conditions modulated by monsoonal winds, which drove significant organic carbon burial in-step with several prominent positive $\delta^{13}C$ excursions (e.g., Hitchwood #2-3). Moreover, $\delta^{13}C$ and weight percent total organic carbon preserve strong

obliquity power (~1 Myr). This suggests that higher cross-equatorial insolation gradients resulting from changes in Earth's axial tilt intensified monsoonal winds, strongly influencing tropical Atlantic organic carbon burial and Turonian carbon cycling dynamics following Ocean Anoxic Event 2.

CHAPTER 2

Turonian Sea Level and Paleoclimatic Events in Astronomically Tuned Records from the Tropical North Atlantic and Western Interior Seaway

2.1. Introduction

The establishment of time-correlative horizons in stratigraphic sections from disparate sedimentary basins is the foundation for reconstruction of Earth history on a global scale. Geochronologic data are critical for anchoring such horizons in a precise temporal context, and high-resolution timescales significantly enhance the interpretive power of physical, chemical, and biologic data collected within such intervals. Improvements in radioisotopic dating (i.e., U/Pb and ^{40}Ar/^{39}Ar geochronology) in recent years have reduced Mesozoic dating uncertainties to plus-minus tens of kiloyears (Schoene et al., 2013), significantly improving temporal resolution, but datable horizons are not present in all locations. Similarly, improvements in astrochronologic techniques have made significant contributions to the refinement of both "anchored" and "floating" timescales, but like datable minerals, these methods are not always applicable, being dependent upon relatively conformable, climate-sensitive facies that record astronomical signals.

Many studies of the Late Cretaceous Epoch are focused on understanding the causes, paleoceanographic setting, and ecological consequences of greenhouse climate dynamics. Floating astrochronologies have been developed for some sections to complement radioisotopic dating and to calculate the timing and duration of biozones, stages, and biogeochemical excursions (Hinnov and Hilgen, 2012). These astronomical timescales (ATS) are constructed by identifying cyclical sedimentation patterns in strata influenced by Milankovitch cycles, periodic variation in Earth's orbital and rotational parameters that influence the distribution of insolation (overview: Hinnov, 2013). Since Milankovitch cycles of short eccentricity, obliquity, and precession manifest over geologically brief periods (in the mid-Cretaceous 95, 39, 22, and 18.5 kyr respectively; Berger et al., 1992), astrochronologies have the potential to greatly reduce Mesozoic timescale uncertainty, including at stage boundaries, because they eliminate the need for ad hoc sedimentation models based on linear or cubic spline interpolation between radioisotopically dated horizons (e.g., Sageman et al., 2014a). The ultimate goal of integrating stratigraphic data and astrochronologies from sections globally is a more robust and temporally resolved Late Cretaceous history. However, two longstanding gaps in the astronomical tuning of Late Cretaceous time exist in the latest iteration of the Geologic Timescale (GTS 2012): (1) within the Turonian Stage (Figure 2.1) and (2) the Lower Campanian Stage (Hinnov and Hilgen, 2012).

Several ATS through portions of the Turonian Stage have been published to date (e.g., Batenburg et al., 2016; Junium et al., 2018; Laurin et al., 2014; Meyers et al., 2001), with two studies approximating the entire stage duration from the Bottaccione Gorge section in the Umbria Marche Basin (Italy; Sprovieri et al., 2013) and the Eagle Ford Formation (Texas, United States; Eldrett et al., 2015a). However, the fact that no global stratotype section and point exists presently for the Turonian-Coniacian Boundary (TCB) complicates chronostratigraphic studies, although the distinct Navigation carbon isotope excursion (CIE) serves as a chemostratigraphic marker of the stage boundary in Europe (Jarvis et al., 2006; Voigt and Hilbrecht, 1997). Our study aims to build on these contributions by determining an age model and independent duration for the Turonian Stage in the tropical North Atlantic. This is achieved through construction of an ATS and a high-resolution stable carbon isotope ($\delta^{13}C$) chemostratigraphy for the relatively

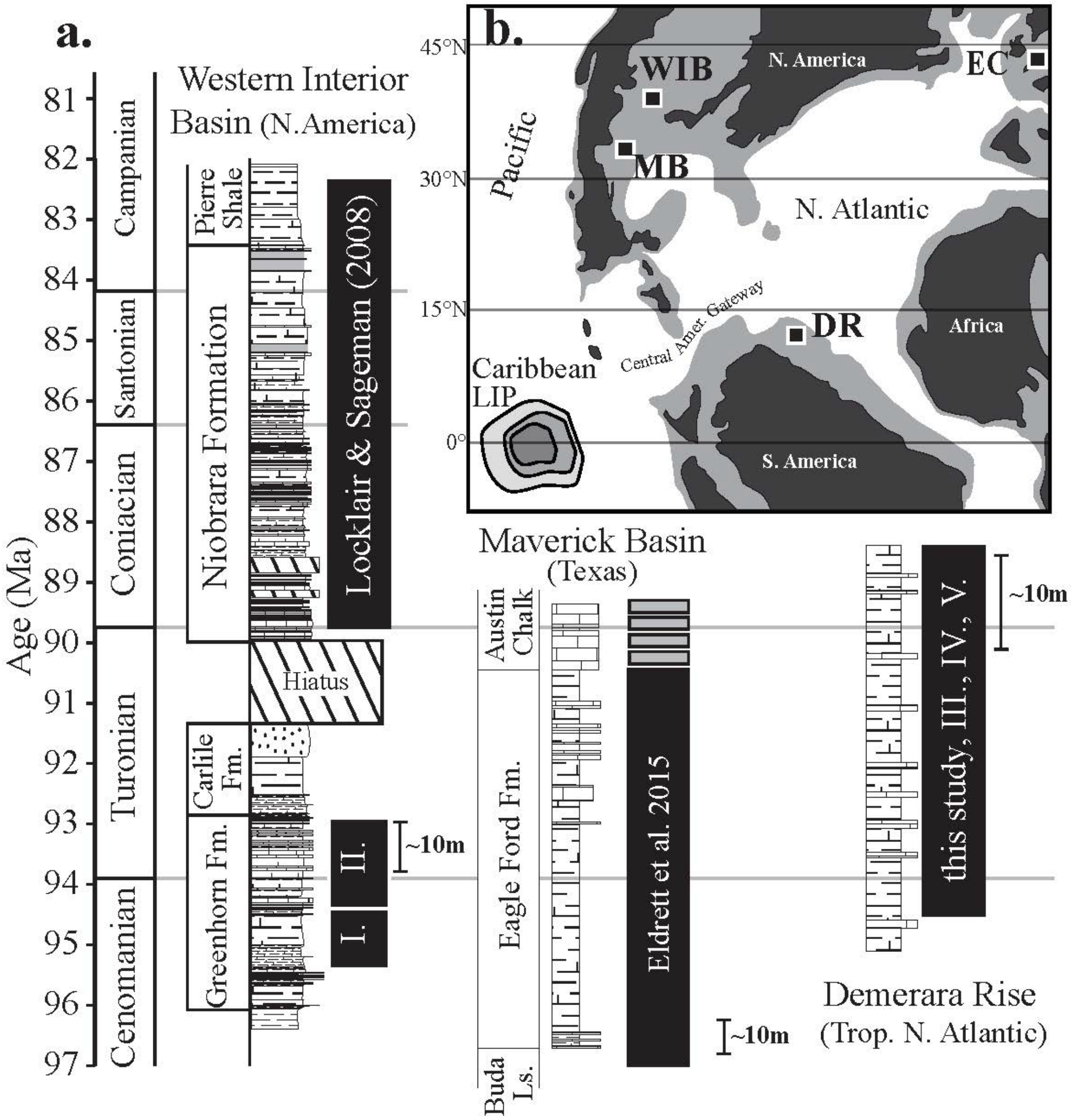

Figure 2.1. (a) Astronomically tuned time intervals (black rectangles) for Late Cretaceous successions from various basins (palinspastic map, b) in the Western Hemisphere (Holmden et al., 2016; Trabucho-Alexandre et al., 2010) (I. = Ma et al., 2014; II. = Meyers et al., 2001; III. = Meyers et al., 2012b; IV. = Friedrich et al., 2008; V. = Junium et al., 2018). Generalized lithologic logs for the Western Interior Basin (WIB; adapted from Joo and Sageman, 2014), Maverick Basin (MB; adapted from Eldrett et al., 2015a), and tropical North Atlantic (DR) are plotted versus time (Meyers, Siewert, et al., 2012; Sageman et al., 2014a) with preliminary astronomical timescales indicated by gray dashed interval (Eldrett et al., 2015a) and hiatuses in WIB indicated by diagonal pattern (e.g., Middle to Late Turonian). The English chalk (EC) composite section of Jarvis et al. (2006) is noted as well. Latest Cenomanian to Early Coniacian astronomical tuning of Demerara Rise interval represents tuning of the entire Turonian Stage from the spliced astronomical timescales of Meyers et al. (2012b) and this study.

conformable, rhythmically bedded strata of Demerara Rise (Ocean Drilling Program (ODP) Leg 207) and the detailed correlation of this record to the Western Interior basin.

Using $\delta^{13}C_{org}$ records and biostratigraphy, we correlate a suite of published deep-marine geochemical, biostratigraphic, and paleoclimatic data sets from ODP Leg 207 cores to recently redated stratigraphic records in the epicontinental shallow-water facies of the Western Interior Basin (North America; Sageman et al., 2014a). This chemostratigraphic correlation is possible due to the global carbon cycle's interconnected sensitivity to fluctuations in the relative fluxes of global organic carbon burial, volcanic CO_2 outgassing, and CO_2 uptake by chemical weathering and carbonate burial (Kump and Arthur, 1999), which are recorded by $\delta^{13}C$ excursions during the Turonian Stage (Hasegawa, 1997; Jarvis et al., 2006; Jenkyns et al., 1994; Joo and Sageman, 2014; Voigt and Hilbrecht, 1997). Most notably, Oceanic Anoxic Event II (OAE2) at the Cenomanian-Turonian Boundary (CTB) has been linked to large igneous province volcanism, enhanced weathering rates, and increased areal extent of marine bottom water anoxia/euxinia, all contributing to the widespread deposition of organic carbon-rich shales and a prominent positive $\delta^{13}C$ excursion (Adams et al., 2010; Arthur and Schlanger, 1979; Du Vivier et al., 2014; Owens et al., 2013; Scholle and Arthur, 1980; Turgeon and Creaser, 2008). Furthermore, Jarvis et al.'s (2006) compilation of Late Cretaceous $\delta^{13}C$ chemostratigraphies from English Chalk records captured a series of other distinct Turonian isotopic excursions representing less pronounced perturbations in the carbon cycle. As a result, high-fidelity Late Cretaceous marine $\delta^{13}C$ chemostratigraphies provide critical insights into the triggers of geochemical perturbations, as well as Earth System responses and feedbacks in the greenhouse climate (Kump and Arthur, 1999). In addition to providing information about principal geologic processes, Late Cretaceous CIEs have the potential to serve as correlative horizons between disparate sedimentary basins, anchoring local stratigraphic and paleobiological investigations in a global chronostratigraphic framework. Attaining the highest temporal resolution for $\delta^{13}C$ excursions via astrochronology is of paramount importance for studies assessing global paleoclimatological change using deep-time stratigraphic archives.

Lastly, this study tests the agreement between independent Turonian astronomical and radioisotopic timescales from the Western Interior Basin, the tropical proto North Atlantic, and European Tethyan localities, by evaluating the global synchroneity and fidelity of CIEs in the Late Cretaceous greenhouse, through comparison of timing and durations. To achieve this objective, a comprehensive statistical methodology is applied, including (1) astrochronologic testing via the Average Spectral misfit method (Meyers and Sageman, 2007; Meyers et al., 2012b), (2) timescale development with frequency domain minimal tuning (Meyers et al., 2001; Park and Herbert, 1987), and (3) evaluation of the floating astronomically tuned $\delta^{13}C$ records using kernel smoothing and cross-correlation techniques to provide a rigorous means for quantitative stratigraphic correlation across multiple sites. Coupling astrochronology and $\delta^{13}C$ chemostratigraphic records offers the opportunity to strengthen the Late Cretaceous chronostratigraphic framework to ultimately address questions about global biogeochemical, paleoclimatic, sea level (eustasy), and paleobiologic change during the dynamic Turonian Stage, including the recovery from OAE2 through subsequent carbon system perturbations represented by substantial CIEs (i.e., Jarvis et al., 2006).

2.2. Geologic Background

2.2.1. Turonian Gap in Late Cretaceous Western Interior Basin Chronostratigraphy

Development of Late Cretaceous astrochronologies in the Western Hemisphere has focused on strata within the North American Western Interior foreland basin (WIB) (Eldrett et al., 2015a; Locklair and Sageman, 2008; Ma et al., 2014; Meyers et al., 2001). The WIB is an ideal setting to develop and test astrochronologies due to the readily traceable lithostratigraphic units, abundant bentonites from active arc volcanism, well-resolved ammonite and inoceramid biostratigraphy, and rhythmically bedded hemipelagic facies (Kauffman and Caldwell, 1993; Meyers et al., 2012a; Obradovich, 1993). As a result, a high-precision astronomically tuned Late Cretaceous WIB chronostratigraphy is emerging (Figure 2.1). However, this astronomical tuning is punctuated by a gap in the Middle to Upper Turonian substages in the central WIB. The gap is primarily due to a lowstand which has been inferred to reflect a global eustatic signal (Haq, 2014) and is expressed by widespread hiatuses in the Western Interior (Merewether and Cobban, 1986). These multiple hiatuses, coupled with low-carbonate content in the strata (Glenister and Kauffman, 1985), make the units of the Turonian regressive Greenhorn hemicycle (Carlile Shale Fm.) ill-suited for astrochronologic analysis.

The eustatic interpretation for this gap is founded on the observation that other basins, on both passive and active margins, also record shoaling facies and/or hiatuses in the Middle to Upper Turonian. These include the Gulf of Mexico (Donovan et al., 2012; Mancini et al., 2008), the Western Tethys (Italy) (Galeotti et al., 2009), northern Europe (Hancock, 1993), the Russian Platform (Siberia) (Sahagian et al., 1996), New Jersey, United States (Miller et al., 2004), Cauvery Basin of S.E. India (Sundaram et al., 2001), Kazakhstan (Walaszczyk et al., 2013), and northern Australia (Henderson, 1998). Most recently, a comprehensive discussion of Turonian eustasy (Haq and Huber, 2017) has noted the interval as a significant global sea level lowstand labeled by Haq (2014) as KTu4 (>75 m) and Miller et al. (2005) as the Bass River and Magothy sequence boundary (~25 m). Despite timescale uncertainties and challenges in reconstructing absolute magnitudes of eustatic sea level variation (Flament et al., 2013; Moucha et al., 2008; Petersen et al., 2010; Raymo et al., 2011; Rovere et al., 2014), these regressions broadly align in timing and magnitude with shoaling facies and forced regressions in the WIB, such as the Ferron and Codell Sandstones (Gardner, 1995; Zhu et al., 2012). Regardless of its cause, this gap has hindered extensive astrochronologic tuning of the Turonian Stage in the WIB and elsewhere, with just two studies to date proposing to capture the entire stage with only minor hiatuses (Eldrett et al., 2015a; Sprovieri et al., 2013). Therefore, it is challenging to confidently determine with sufficient resolution whether Turonian lowstands and hiatuses are coeval among all basins or even correspond to a common δ^{13}C excursion. Analysis of a near-continuous Turonian record Demerara Rise that integrates astronomical tuning with a δ^{13}C data set and correlation of this record to epeiric settings in the WIB offers the potential to improve global Turonian chronostratigraphy and assist in evaluating possible drivers for a eustatic lowstand.

2.2.2. Turonian Stage at Demerara Rise

Demerara Rise in the tropical North Atlantic (Figure 2.1) is an ideal location to develop a Turonian astrochronology and high-resolution δ^{13}C chemostratigraphy, given rhythmically bedded lithologies, existing microfossil biostratigraphy, and organic carbon-rich facies (Erbacher et al., 2005; Hardas and Mutterlose, 2007). The Ocean Drilling Program cored the Demerara submarine plateau at five sites in 2003 (Leg 207, Sites 1257–1261) recovering a near-continuous Cenomanian-Santonian interval of organic carbon-rich calcareous claystones interbedded with thin foraminiferal packstones and occasional glauconite deposition (Shipboard Scientific Party, 2004). This interval was deposited continuously below storm wave base (> ~100-m water depth). In addition to coring, the site was surveyed using downhole geophysical well logging, including a high-resolution Formation MicroScanner (FMS) log from Sites 1260 and 1261, measuring changes in bulk sediment conductivity. Meyers et al. (2012b) published an ATS derived from the FMS log through the OAE2 interval at Site 1261 indicating a strong obliquity signal, amplified through the event relative to eccentricity and precession signals and demonstrating the locality's suitability for astronomical tuning. Although Site 1259 was not logged using FMS, variation in high-resolution carbonate content data, dominated by cyclicity in the 400-kyr eccentricity band (Friedrich et al., 2008), provides a basis for the new astrochronologic analysis of this interval. Nannofossil biostratigraphy through the OAE2 interval at all sites (Hardas and Mutterlose, 2007) and the Middle to Upper Turonian at Site 1259 (Bornemann et al., 2008) provide datums and time control. Additionally, Erbacher et al.'s (2005) $\delta^{13}C_{org}$ data, centering on the positive OAE2 CIE at all Demerara Rise sites, serve as a robust stratigraphic marker for the CTB and provide a foundation and guide for this study's new high-resolution $\delta^{13}C_{org}$ record.

In addition to the potential for timescale refinement, cores from Demerara Rise have provided a valuable window into paleoceanographic conditions in the tropical Atlantic Ocean through the mid-Cretaceous greenhouse via a suite of geochemical investigations. Geochemical characterization of organic matter (Forster et al., 2004) indicates that the anomalously organic carbon-rich shales (total organic carbon [TOC] > 20% in instances) originated from marine organic matter (Meyers et al., 2006), despite elevated C/N ratios, since nitrogen isotopes and hydrogen indices reflect preferential microbial degradation of nitrogen-bearing organic compounds in the persistent anoxic bottom waters at Demerara Rise (Junium and Arthur, 2007). Paleoclimatic investigations derived from the paleotemperature proxy TEX_{86} (Bornemann et al., 2008; Forster et al., 2007) and well-preserved foraminiferal test $\delta^{18}O$ records (Bornemann et al., 2008) have suggested cooling in the Middle to Late Turonian punctuating the otherwise warm greenhouse of the mid-Cretaceous. However, similar cooling signals are not detected in $\delta^{18}O$ data sets of well-preserved foraminifera from other mid-Cretaceous records, such as the Cenomanian Stage at Blake Nose (Ando et al., 2009) and the Turonian Stage in Tanzania (MacLeod et al., 2013).

Given the deep-shelf paleowater depth estimates of Demerara Rise (Shipboard Scientific Party, 2004), the site's lithologies and geochemistry may have been sensitive to major reorganizations of intermediate-water circulation. Neodymium isotope analyses of fossilized fish teeth provide insight into tropical North Atlantic paleocirculation and indicate major reorganization of water sources during OAE2, with basinal and global implications for oceanic circulation patterns (MacLeod et al., 2008; Martin et al., 2012). Thus, extension of the Meyers et al. (2012b) and Junium et al. (2018) floating ATS through the entire Turonian should significantly expand the utility of published records by allowing rates and durations of biogeochemical, oceanographic, and climatic changes to be calculated. In particular, our new timescale provides a means to test the synchroneity of environmental, sea level, and biotic events at multiple localities, comparing tropical pelagic data with recently redated (Sageman et al., 2014a) records of midlatitude shallow water sites in the WIB via $\delta^{13}C_{org}$ chemostratigraphy.

2.3. Methods

2.3.1. Geochemical Analyses

Sedimentary samples (n = 236) were analyzed for weight percent total organic carbon (%TOC), weight percent carbonate (%Carb), C/N atomic ratios, and bulk organic carbon isotope ratios ($\delta^{13}C_{org}$). Sampling at 20-cm resolution was guided by existing biostratigraphic records to target the Turonian Stage at Demerara Rise from ODP Leg 207 Sites 1259 and 1261 (Bornemann et al., 2008; Shipboard Scientific Party, 2004). Site 1259 was sampled from 508.4- to 530.0-m composite depth (MCD), and Site 1261 was sampled from 594.11 to 639.60 MCD. Bulk samples were crushed in tungsten carbide containers and analyzed for %TOC and %Carb using a UIC Coulometer following standard CO_2 coulometric procedures (Huffman, 1977). We also calculate %TOC free of carbonate (%TOC-cf) to analyze changes in organic carbon burial independent of carbonate dilution. For measurement of C/N and $\delta^{13}C_{org}$, samples were acidified with 2N HCl for 12 hr, after which insoluble residue was filtered with 750-ml DI water. $\delta^{13}C_{org}$ and C/N values were measured on a Thermo Delta-V-Plus isotope ratio mass spectrometer with a Costech ECS4010 Elemental Analyzer peripheral in continuous He flow. The average standard deviation (1σ) of duplicate calibrated standards and unknown ($n = 19$) $\delta^{13}C$ values was <0.15‰.

2.3.2 Astrochronologic Testing and Timescale Construction

Prior work at Demerara Rise Site 1261 developed an astrochronology through the CTB interval using FMS data, which reflects carbonate content (Meyers et al., 2012b). The present study utilizes the same quantitative approach to extend the CTB astrochronology through the entire Turonian. The %Carb data of Friedrich et al. (2008) from Site 1259 are analyzed to build on their wavelet analysis findings (see Sect. 2.2.2) and extend the recent study of Junium et al. (2018), which developed an astrochronology for a portion of the Turonian at Site 1259. The ATS is constructed using the multitaper method (Thomson, 1982), evolutive power spectral analysis (EPSA; Meyers and Hinnov, 2010; Park and Herbert, 1987), evolutive harmonic analysis (EHA; Meyers et al., 2001), average spectral misfit analysis (ASM; Meyers and Sageman, 2007; Meyers et al., 2012b), and frequency domain minimal tuning (Meyers et al., 2001; Park and Herbert, 1987). This approach provides the ability to quantitatively test for astronomical influence in the record (evaluate the null hypothesis of "no astronomical signal") while simultaneously evaluating the optimal sedimentation rate given a range of plausible models. The Site 1259 astrochronology is subsequently anchored and linked to the prior results from Site 1261 (Meyers et al., 2012b) using biostratigraphic and chemostratigraphic constraints (see below). All astrochronologic analyses are conducted using the Astrochron package in R (Meyers, 2014). See Meyers et al. (2012b), Junium et al. (2018), and Meyers (2014) for further details on the analytical approaches implemented.

Correlation of geophysical logs to MCD scale at Site 1261: At Site 1261 there were discrepancies between the depth below sea level of distinct marker beds as reported in the logging and core depth scales. A correction was applied to align the core depth scale (MCD) to the logging depth scale (meters below sea floor-logging: MBSF-log) for accurate comparison and evaluation of sedimentation rates (Table A1.1).

2.3.3. $\delta^{13}C_{org}$ Stratigraphic Correlation Techniques

Raw $\delta^{13}C_{org}$, C/N, %TOC, and %Carb results were converted from depth scales to floating timescales using the existing and newly developed ATS at Sites 1261 and 1259, respectively. Floating ages for geochemical sample depths were assigned by linearly interpolating time values from each ATS. Resulting tuned $\delta^{13}C_{org}$ time series were smoothed to diminish noise in the $\delta^{13}C$ signal, possibly arising from changes in organic matter type and/or analytical noise. While samples were collected at evenly spaced depth horizons, time series are unevenly sampled due to variations in sedimentation rate. Because of this, a Gaussian kernel smoothing and interpolation approach was implemented to estimate a continuous, evenly sampled $\delta^{13}C_{org}$ signal for correlation. When assigning values to any arbitrary point (t) along the smoothed and continuous $\delta^{13}C$ time series, a weighted average of all $\delta^{13}C$ data points was applied. Weighing of individual $\delta^{13}C$ values was determined by distance from t and scaled by a Gaussian kernel (Equation 2.1). This approach is similar to a moving average that weighs nearby $\delta^{13}C$ values more heavily than more distant points in space or time. Rehfeld et al. (2011) demonstrated that Gaussian kernel smoothing was the most robust correlation approach of several methods testing irregularly sampled synthetic stratigraphic data sets. Compared to simple (unsmoothed) linear interpolation, Gaussian kernel smoothing recorded an ~40% lower root mean square error in the correlation of irregularly sampled synthetic time series (versus original) for data sets with increasing skewness values (i.e., lower symmetry). Due to its excellent performance, kernel smoothing has been applied to paleoclimate data sets to remove long-term trends in the time domain (e.g., Dakos et al., 2008) and more recently to smooth Holocene speleothem $\delta^{18}O$ data sets (Gaussian kernel; Oster and Kelley, 2016) and Late Cretaceous paleosol records (Epanechnikov kernel; Gao et al., 2015). For this study, the standard deviation (σ) of the Gaussian kernel smoother was assigned to 75 kyr ($2\sigma = \pm150$ kyr) for $\delta^{13}C_{org}$ records, to account for sampling resolution, and with consideration for the residence time of carbon and the geologically short timescales (i.e., <100 kyr) over which $\delta^{13}C_{org}$ records can fluctuate.

$$\textbf{Equation 2.1: } \boldsymbol{\delta^{13}C_{smooth}(t)} = \frac{\sum_{i=1}^{N}\left(e^{-\frac{(t_i-t)^2}{2\sigma^2}} \times \delta^{13}C_{raw}(i)\right)}{\sum_{i=1}^{N}\left(e^{-\frac{(t_i-t)^2}{2\sigma^2}}\right)}$$

Once $\delta^{13}C$ chemostratigraphies were smoothed and interpolated to continuous time series, records were cross-correlated to determine potential stratigraphic correlation horizons. The method developed for correlating $\delta^{13}C$ records is similar to the approach of Mitchell et al. (2008) who anchored floating geologic records to La2004 astronomical insolation age solutions (Laskar et al., 2004) using Pearson product correlation. Our signal processing technique identifies possible correlation horizons between two floating time series by calculating the Pearson correlation coefficient (ρ) for overlapping segments of smoothed $\delta^{13}C$ values (e.g., $\delta^{13}C_{1261}$, and $\delta^{13}C_{1259}$) while iteratively shifting (lagging) one function in time ($i + \tau$; Equation 2.2, Zelterman, 2015). The ρ value becomes a function of time lag (τ), and local maxima indicate optimal alignment between the two-time series for a given τ. These maxima are potential time equivalent horizons for correlation. Problematically, carbon isotope excursions may be nonunique in their expression with similar amplitudes and/or durations for distinct geochemical events through geologic time. Therefore, it is important to critically evaluate all cross-correlation maxima by considering biostratigraphic constraints and discarding implausible stratigraphic correlations.

$$\textbf{Equation 2.2: } \boldsymbol{\rho_{1259,1261}(\tau) = \frac{\sum_{i=1}^{n}\left(\left(\delta^{13}C_{1261}(i+\tau)-\mu_{1261}\right)\times\left(\delta^{13}C_{1259}(i)-\mu_{1259}\right)\right)}{\sqrt{\sum_{i=1}^{N}\left(\delta^{13}C_{1261}(i+\tau)-\mu_{1261}\right)^2\times\sum_{i=1}^{N}\left(\delta^{13}C_{1259}(i)-\mu_{1259}\right)^2}}}$$

2.4 Results

2.4.1 $\delta^{13}C$, %TOC, %Carb, and C/N Chemostratigraphies

2.4.1.1 Site 1261

The most prominent result from the Site 1261 $\delta^{13}C_{org}$ chemostratigraphy is a major positive CIE (+7‰) between 629.0 and 636.81 MCD, previously identified as OAE2 (Figure 2.2b and Table A1.3; Erbacher et al., 2005). Above a core gap, a recovery to baseline $\delta^{13}C_{org}$ values from an enriched value (-24.95‰) is preserved. Further upcore, a zone of highly variable ($2\sigma = 1.8$‰) $\delta^{13}C_{org}$ values was recorded from 605.49 to 608.89 MCD. Aside from these intervals, the Site 1261 $\delta^{13}C_{org}$ values tend to cluster near a baseline value that shifts from roughly -27.5‰ to -28.5‰ above a 45-cm thick bioturbated glauconite-rich claystone bed from 603.48 to 603.92 MCD (Shipboard Scientific Party, 2004).

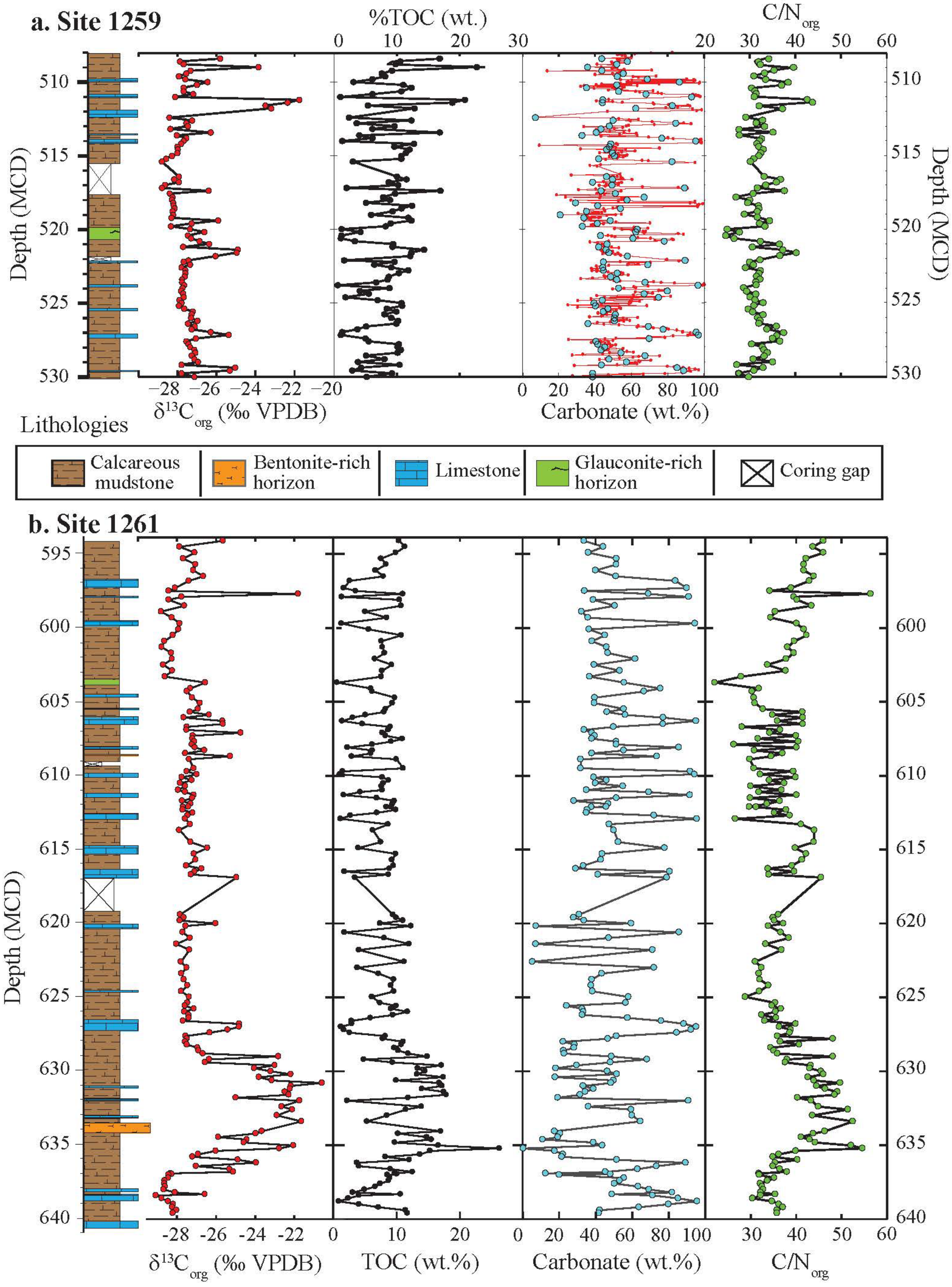
a. Site 1259
%TOC (wt.)
0
10
20
30
C/N$_{org}$
20
30
40
50
60
Depth (MCD)
510
515
520
525
530
−28 −26 −24 −22 −20
δ^{13}C$_{org}$ (‰ VPDB)
0 20 40 60 80 100
Carbonate (wt.%)
Lithologies
Calcareous mudstone
Bentonite-rich horizon
Limestone
Glauconite-rich horizon
Coring gap
b. Site 1261
Depth (MCD)
595
600
605
610
615
620
625
630
635
640
-28 -26 -24 -22
δ^{13}C$_{org}$ (‰ VPDB)
0 10 20
TOC (wt.%)
0 20 40 60 80 100
Carbonate (wt.%)
30 40 50 60
C/N$_{org}$

Figure 2.2. (previous page) Chemostratigraphic data from (a) Site 1259 and (b) Site 1261 at Demerara Rise depicting (from L-R) $\delta^{13}C_{org}$, %TOC, %Carb, C/N. Red %Carb values at Site 1259 from Friedrich et al. (2008). %TOC = weight percent total organic carbon; %Carb = weight percent carbonate; MCD = meter composite depth.

Major oscillations in carbonate content (mean = 52.2%, min = 5.5%, and max = 96.7%), even between consecutive samples, underscore decimeter-scale stratigraphic intervals of high variability (Figure 2.2b and Table A1.3). Despite short-term variability, %Carb values follow general trends through the interval in terms of changing minimum and maximum values for a given depth range. In the OAE2 interval, only one value exceeds 70% carbonate, and minimum values cluster near 20% with a relatively carbonate depleted interval (<50%) between 634.06 and 635.62 MCD. Overlying the OAE2 interval is a thick limestone bed that is superposed by an interval (620.00–622.99 MCD) with highly variable carbonate content (5.5–85.8%). At depths less than 620.00 MCD, %Carb continues to oscillate, but minimum values are rarely <35%, while maximum values are generally >80%, indicating higher purity foraminiferal packstones. %TOC data produced prior to isotopic analysis are consistent with data from Erbacher et al. (2005). %TOC values are highest in the OAE2 interval, generally exceeding 8% with many measurements approaching 20%. Above the OAE2 interval, %TOC values oscillate rhythmically between 1% and 11%, with highest values corresponding to comparatively carbonate-lean beds. C/N data generally lie between 30 and 40 (atomic ratio) in strong agreement with the data set of Junium and Arthur (2007). C/N values are elevated in the OAE2 interval (31.8–54.6) and also increase linearly above a prominent glauconite-rich bed (603.30 MCD) to elevated levels (>40). C/N reaches a conspicuous minimum of 22.1 at 603.70 MCD in the comparatively organic-lean (TOC = 0.53%) glauconite-rich bed. Overall, C/N ratios show positive correlation with $\delta^{13}C_{org}$ values, suggesting potential influence from similar biogeochemical processes.

2.4.1.2. Site 1259

The $\delta^{13}C_{org}$ chemostratigraphy at Site 1259 displays several prominent excursions from baseline values that reach a long-term minimum for the interval between 515.4 and 517.2 MCD (~-28.8‰; Figure 2.2a and Table A1.3). Near the base of the sampled interval, a ~+2‰ excursion in $\delta^{13}C_{org}$ is recorded between 526.4 and 527.2 MCD. A zone of high $\delta^{13}C_{org}$ variability with values showing up to +2‰ enrichment from baseline values (~-27.5‰), identified by Erbacher et al. (2005) as interval "G," is present between 519.2 and 522.1 MCD. Overlying this high variability interval, baseline $\delta^{13}C_{org}$ values become more depleted (~-28.2‰) and eventually shift to a minimum for all samples analyzed from Leg 207. Above this, values become steadily more enriched in what may qualify as a +1‰ excursion, until a narrow interval of extremely enriched values (~-22‰). This ~+6‰ excursion is similar in magnitude to OAE2 at Site 1261 and is the most prominent perturbation in $\delta^{13}C_{org}$ values at Site 1259.

Values of %Carb oscillate at Site 1259 (~40–95%) similar to those at Site 1261. However, minimum values tend to have higher carbonate contents comparatively (greater than 40%; Figure 2.2a and Table A1.3). One interval overlying a glauconite-rich bed (~518–520 MCD) preserves lower %Carb values not exceeding ~50% and dipping as low as ~20%. Site 1259's %TOC values mimic those at Site 1261. TOC values generally oscillate from 1% to 12%. However, zones in the uppermost interval (<514 MCD) exceed this envelope in some instances and approach 20% TOC in the $\delta^{13}C_{org}$ excursion near ~511.5 MCD. C/N ratios at Site 1259 are less enriched than ratios at Site 1261 overall. C/N throughout the interval oscillates mostly between 30 and 40, and maxima-minima in the data track $\delta^{13}C_{org}$ trends (e.g., ~511.5, 521.5, and 527 MCD). C/N ratios are reduced through the ~80-cm thick glauconite-rich interval, to values of 24.8–27.7, and enriched (>40) through several data points in the prominent +6‰ $\delta^{13}C_{org}$ excursion in the upper interval (~511.3 MCD).

Overall, the conspicuous rhythmically bedded nature of lithofacies at Sites 1261 and 1259 was recorded by significant variations in sediment geochemistry (Figure 2.2), with average 2-sigma standard deviations for $\delta^{13}C_{org}$, %TOC, %Carb, and C/N over 5-m intervals of 2.42‰, 6.8%, 42.0%, and 7.7%, respectively.

2.4.2 Astrochronology of Site 1259 and Sedimentation Rates

The EPSA and EHA results from the Site 1259% Carb data reveal a strong and significant (≥ 90% harmonic F-test confidence level) cycle that gradually shifts from ~0.3 cycles/m at the base of the study interval to ~1 cycle/m at 510 MCD (Figure 2.3), suggesting a sedimentation rate decrease throughout most of the Turonian. To quantitatively test for astronomical influence on the %Carb record, and further evaluate hypothesized sedimentation rate changes through the stratigraphic interval, the EHA results in Figure 2.3 are employed for Evolutive Average Spectral Misfit analysis (Figure 2.4). Following Junium et al. (2018), the ASM analysis investigates 200 sedimentation rates spanning 0.1 to 3 cm/kyr, using a logarithmic scaling grid (Meyers et al., 2012b); this range of sedimentation rates is based on the biostratigraphically constrained estimates of Bornemann et al. (2008). The theoretical target periods of Meyers et al. (2012b) (their Table S1) are employed in the analysis. Evolutive ASM analysis reveals five regions of the stratigraphic record with high signal/noise and very low null hypothesis significance levels (Figure 2.4). The results confirm the presence of an astronomical signal as proposed by Friedrich et al. (2008) and yield a consistent interpretation of the cycle between 0.3 and 1 cycles/m as the 405-kyr long eccentricity cycle (see Figures 2.3 and A1.1).

A floating ATS is constructed from the Site 1259 %Carb data using frequency domain minimal tuning. As in Junium et al. (2018), the spatial frequency drift of the long eccentricity cycle (405 kyr; Figure 2.3) is tracked for all results that achieve an 80% F test confidence level (Figure A1.2a). A sedimentation rate history is then derived by assigning this variable spatial cycle a constant temporal period of 405 kyr (Figure A1.2b). Finally, the floating ATS is constructed by numerically integrating the sedimentation rate curve (Figure A1.2c). The result is a floating ATS that extends from the Turonian into the Coniacian at Site 1259.

2.4.3. $\delta^{13}C$ Spliced and Anchored Turonian Stage at Demerara Rise

2.4.3.1. Correlation of Site 1261 (Lower Turonian) and Site 1259 (Lower-Upper Turonian)

Previously published biostratigraphic investigations identified the interval in Site 1261 as Cenomanian-Lower Turonian (Hardas and Mutterlose, 2007) and Site 1259 as Lower (part)-Upper Turonian (Bornemann et al., 2008), with a glauconite-rich bed and coeval $\delta^{13}C_{org}$ variable horizon G serving as a regionally detectable and potentially isochronous lithostratigraphic bed (Erbacher et al., 2005; Nederbragt et al., 2007). Since the ATS developed by Meyers et al. (2012b) for Site 1261 did not extend through the glauconite-rich interval (~604 MCD), it was necessary to link the records via stratigraphic correlation of $\delta^{13}C_{org}$ data. Once $\delta^{13}C_{org}$ data from Sites 1259 and 1261 were converted to Gaussian-smoothed ($2\sigma = \pm 150$ kyr) and interpolated floating time series, a cross correlation was conducted to determine potential stratigraphic correlation horizons (Figure 2.5). Cross-correlation maxima greater than $\rho = +0.8$, or potential tie points between the sites, were detected at lag times (τ) of 1581, 1106, +728, +3480, and +4703 kyr, for floating ATS beginning ($t = 0$) at 528.75 MCD (Site 1259) and 638.28 MCD (Site 1261). Since $\tau > 0$ results in biostratigraphic discrepancies (i.e., differing biozones overlapping in time) as well as violations of stratigraphic superposition (based on the prominent glauconite bed), these potential stratigraphic

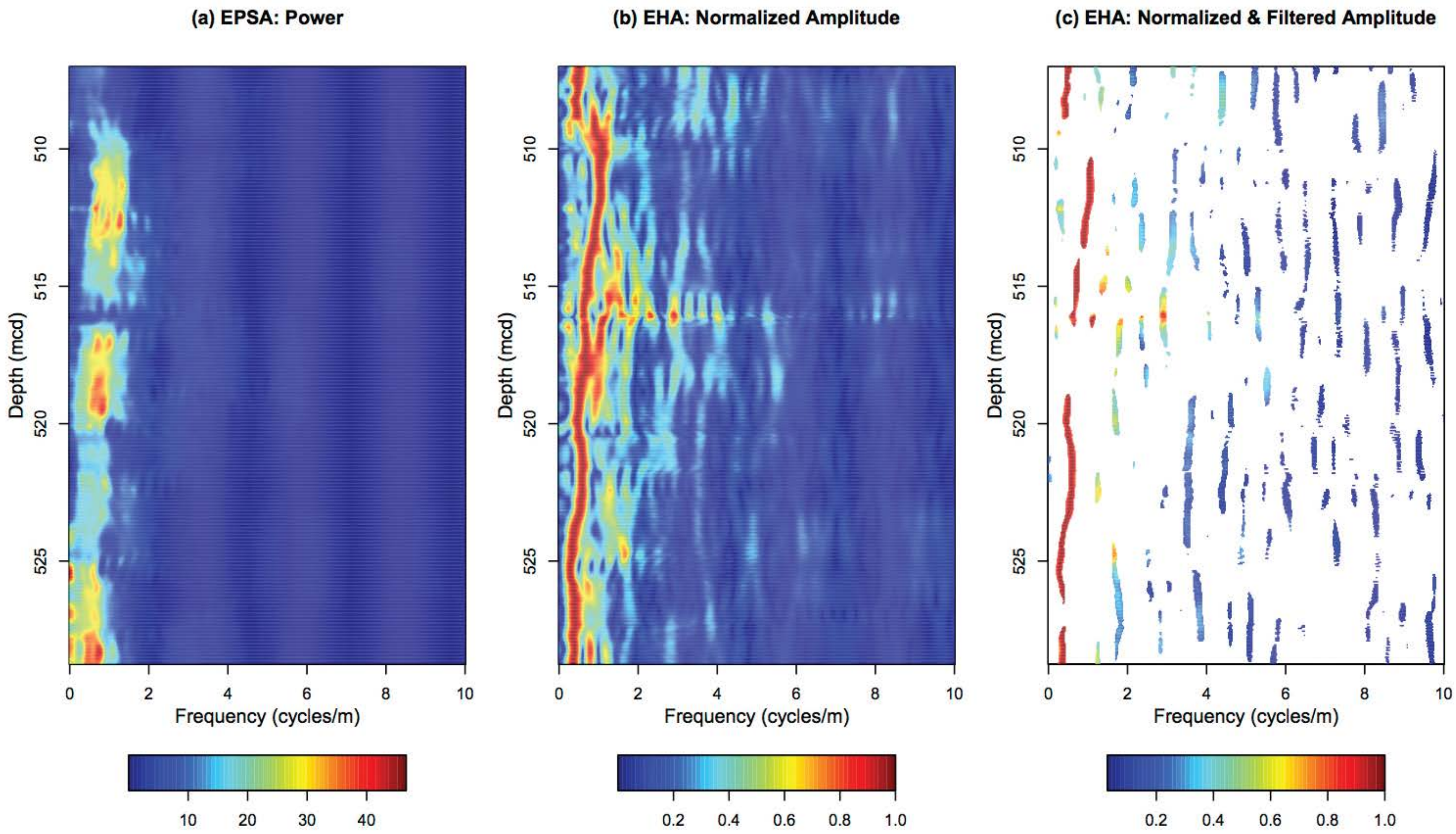

Figure 2.3. Multitaper method evolutive power spectral analysis (EPSA) and evolutive harmonic analysis (EHA) results for %Carb data from 1259A. The analysis was conducted utilizing a 4-m window with a 5-cm step and three 2π discrete prolate spheroidal sequences (DPSS) tapers. A linear trend was removed from each 4-m window prior to analysis. (a) EPSA results. (b) Normalized amplitude EHA results (the maximum amplitude in each 4-m window is normalized to unity). (c) Normalized amplitude results, filtered at the 90% F test confidence level (white area is <90%; colors indicate normalized amplitude as in panel b). Based on astrochronologic testing with average spectral misfit, the dominant low-frequency signal observed (0.25–1.075 cycle/m) is attributable to the 405-kyr long eccentricity cycle (see Figure 2.4 and Figure A1.1).

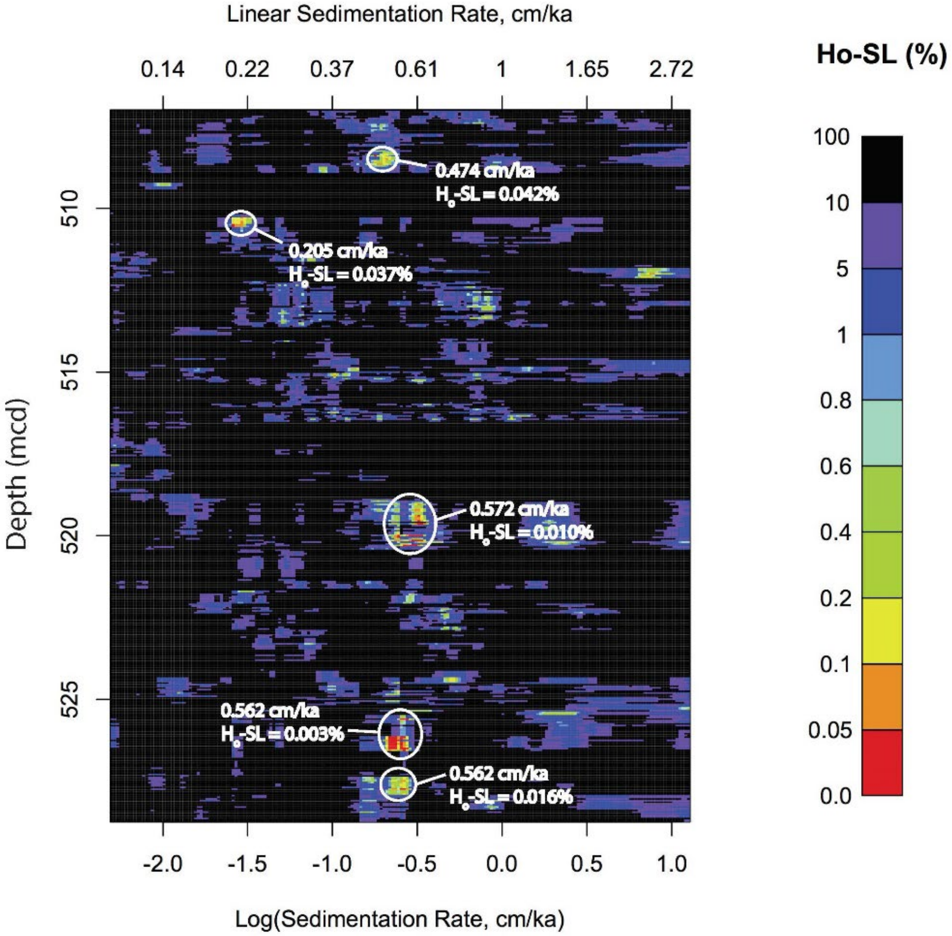

Figure 2.4. Hole 1259A Evolutive Average Spectral Misfit analysis, conducted on the evolutive harmonic analysis results presented in Figure 2.3. Null hypothesis significance levels are plotted. The ASM analyses utilize the seven predicted precession, obliquity, and eccentricity periods of Laskar et al. (2004, 2011) and their uncertainties (see Table A1.4). Two hundred sedimentation rates are investigated on a logarithmic grid, spanning 0.1 to 3 cm/kyr, with a critical significance level of 0.5%. Null hypothesis significance levels are determined using 100,000 Monte Carlo simulations at each sedimentation rate, and the simulated spectra have the same number of significant frequencies (≥ 90% F-test confidence level) as identified in each data spectrum. The average spectral misfit analyses follow the updated procedures outline in Meyers et al. (2012b). Representative sedimentation rates with null hypothesis significance levels ≤0.05% are indicated.

Figure 2.5. (next page) (a) Cross-correlation (Equation 2.2) of Gaussian kernel smoothed ($2\sigma = \pm150$ kyr) $\delta^{13}C_{org}$ time series on floating astronomical timescale from Sites 1261 and 1259. Five maxima of cross-correlation as a function of lag time (τ; with $\rho > +0.8$) are indicated by dashed lines. (b) Shaded intervals of overlap for a given lag (τ = -1106 kyr) indicate time equivalent horizons compared. A high correlation value is noted for this τ given overlap of a carbon isotope excursion, despite its relatively minor amplitude.

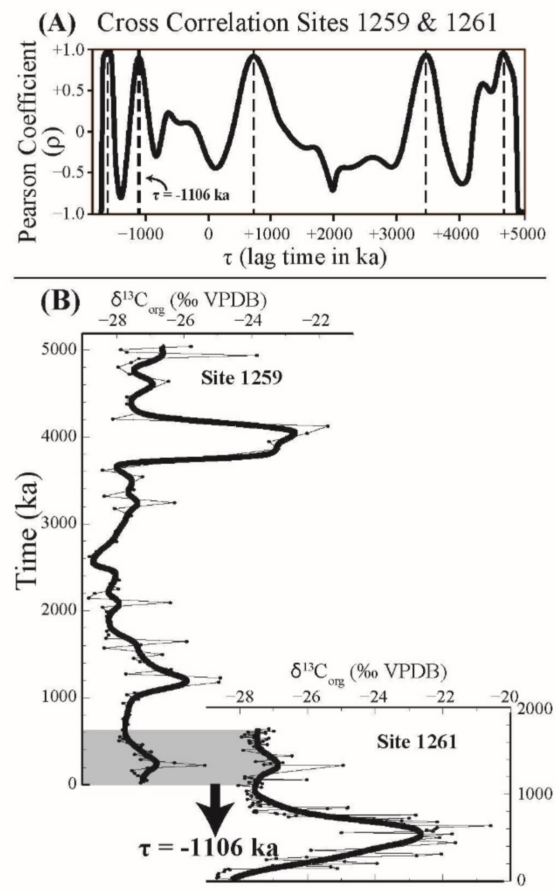

correlations were rejected. For τ = 1581 kyr, only six $\delta^{13}C_{org}$ raw data points with low $\delta^{13}C$ variability (<0.2‰) overlap between the two records, suggesting that this possible stratigraphic correlation is likely an artifact of low sample set overlap, and this interval also lacks CIEs for the cross-correlation test. Given these logical considerations and agreement in CIE morphologies and durations, it is possible to eliminate all stratigraphic correlation options except one (τ = 1106 kyr), permitting unambiguous splicing of records from Sites 1261 and 1259. After testing uncertainty in this correlation with various kernel smoother standard deviations, 1094 ± 30 kyr was added to the floating timescale from Site 1259, to bring the two $\delta^{13}C$ time series into alignment.

Splicing the timescales of Sites 1259 and 1261 via $\delta^{13}C_{org}$, lithostratigraphic, and biostratigraphic correlation produced an astronomically tuned, composite chemostratigraphic record for the Turonian Stage at Demerara Rise (Figure 2.6). This spliced timescale was subsequently anchored to an absolute age for the base of OAE2 of 94.45 ± 0.16 Ma. This initiation age for OAE2 was imported from the robust WIB chronostratigraphic framework which includes $\delta^{13}C_{org}$ records and floating astrochronologic timescales from the Portland and Angus cores anchored to a CTB age of 93.9 ± 0.15 Ma (Ma et al., 2014; Meyers et al., 2012). The anchor age for the onset of OAE2 is consistent with recent estimates from Morocco (~94.3–94.4 Ma; Kuhnt et al., 2017) and is within temporal uncertainty of the base of the main body of the OAE2 CIE in Texas (94.7 ± 0.16; Eldrett et al., 2015a). Eldrett et al. (2017) proposed that a hiatus may exist at the base of OAE2 at Demerara Rise from palynological assemblage data, which could add additional temporal uncertainty in anchoring the ATS. However, records at Demerara Rise preserve a characteristic, geologically short (tens of kiloyears) lag between osmium and carbon isotope excursions at the OAE2 onset (Du Vivier et al., 2014; Turgeon and Creaser, 2008). Moreover, the ATS duration of OAE2 at Demerara Rise is consistent with typical estimates globally (Meyers et al., 2012b). These chronostratigraphic observations suggest that the duration of any potential hiatus at the base of OAE2 in Site 1261 is much shorter than the stated uncertainty of the anchoring age.

2.4.3.2. Lithostratigraphic, Biostratigraphic, and Chemostratigraphic Event Ages at Demerara Rise

The spliced and anchored ATS for Sites 1259 and 1261 provide an estimate of absolute ages of noteworthy lithostratigraphic, biostratigraphic, and chemostratigraphic events at Demerara Rise (Figure 2.6). The most prominent CIEs, defined by their smoothed ($2\sigma = \pm150$ kyr) $\delta^{13}C_{org}$ record of maxima/minima, occur as two major positive excursions at 94.047 ± 0.16 and 89.450 ± 0.191 Ma and a long-term $\delta^{13}C_{org}$ minimum at 90.926 ± 0.191 Ma (see Text A1.2 for temporal

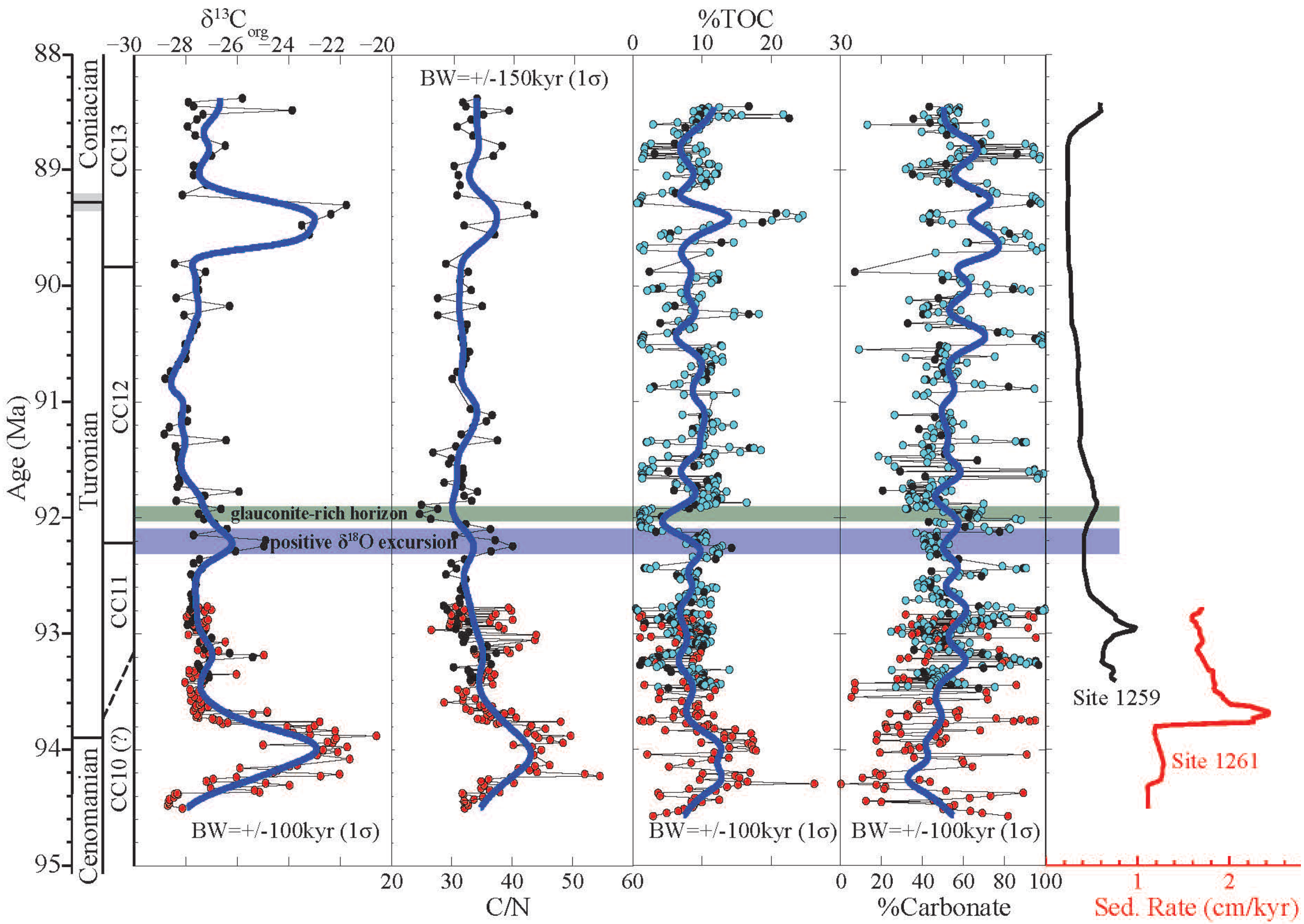

$\delta^{13}C_{org}$
−30
−28
−26
−24
−22
−20
%TOC
0
10
20
30
BW=+/-150kyr (1σ)
Age (Ma)
88
89
90
91
92
93
94
95
Coniacian
Turonian
Cenomanian
CC13
CC12
CC11
CC10 (?)
glauconite-rich horizon
positive $\delta^{18}O$ excursion
BW=+/-100kyr (1σ)
BW=+/-100kyr (1σ)
BW=+/-100kyr (1σ)
20
30
40
50
60
C/N
0
20
40
60
80
100
%Carbonate
Site 1259
Site 1261
1
2
Sed. Rate (cm/kyr)

Figure 2.6. (previous page) Astronomically tuned and spliced geochemical data sets from the late Cenomanian-early Coniacian stages at Demerara Rise (raw data: Table A1.3). Data are anchored to the age of onset of the OAE2 $\delta^{13}C_{org}$ excursion, 94.45 ± 0.16 Ma. $\delta^{13}C_{org}$, C/N, %TOC, %Carbonate, data from Site 1261 (red circles) and 1259 (black circles—this study; teal circles—Friedrich et al., 2008) are displayed, with thick dark blue lines representing Gaussian kernel smoothed data ($1\sigma = \pm 100$ kyr for $\delta^{13}C_{org}$, %TOC, %Carb and $1\sigma = \pm 150$ kyr for C/N) to highlight trends. The light green shading at 92.0 Ma represents a particularly glauconite-rich interval, and light-blue shading indicates the location of the positive $\delta^{18}O_{foram}$ excursion at Site 1259 (Bornemann et al., 2008). Nannofossil biostratigraphy from Bornemann et al. (2008). Sedimentation rates from Site 1261 Meyers et al. (2012b) and Site 1259 (this study) are plotted on far right.

uncertainty calculation). Lower-amplitude excursions are recorded at 93.253 ± 0.191 Ma (a cross-site correlative excursion), 92.299 ± 0.191 Ma (interval of high-variability spanning 91.804–92.458 Ma), and 90.254 ± 0.191 Ma.

The distinct regionally detected mid-Turonian glauconite bed is placed at 91.956 to 92.078 (±0.191) Ma at Site 1259. First occurrences and last occurrences of marker nannofossil, as well as nannobiozone boundary ages are calculated (Table A1.7). Additionally, a revised age for a positive oxygen isotope ($\delta^{18}O$) excursion in planktic foraminifera near the CC11/CC12 biozone boundary (Bornemann et al., 2008) is calculated as spanning 92.146 to 92.352 (±0.191) Ma (most enriched value = 92.230 ± 0.191 Ma). This age for the $\delta^{18}O$ excursion, cited previously as evidence for polar ice-growth on Antarctica, is roughly 1.0 Myr older than the original estimate based on GTS 2004 nannofossil biozone boundary ages.

2.4.4. Stratigraphic Correlation to Western Interior Seaway Records

The development of a Turonian ATS coupled with high-resolution $\delta^{13}C_{org}$ records at Demerara Rise permits comparison of the timing and duration of CIEs from other astronomically tuned localities, such as Texas and Italy, in an effort to test the agreement of each ATS. $\delta^{13}C_{org}$ profiles are consistent among the Eagle Ford (EF) in Texas, WIB composite, and Demerara Rise records including significant CIEs such as OAE2, a Middle Turonian event, and a $\delta^{13}C_{org}$ minimum with subsequent enrichment in the Upper Turonian (Figure 2.7). To avoid false pattern recognition of CIEs, consistency between the records was quantitatively evaluated by kernel smoothing the raw $\delta^{13}C_{org}$ time series ($2\sigma = \pm 150$ kyr) and then identifying maxima/minima in smoothed $\delta^{13}C_{org}$ time series as testable correlative stratigraphic horizons. Although offsets in the numerical ages of radioisotopically constrained $\delta^{13}C$ records in the WIB and EF are within temporal uncertainty (see Sect. 2.4.3.1), median ages for the CTB in the records are offset by 170 kyr. Therefore, we compare the relative durations between the CIEs and the CTB at the analyzed localities and do not compare anchored numerical ages of the events to avoid biasing comparisons (Table A1.8). When compared to Demerara Rise, CIE durations from the CTB displayed median absolute offsets of 185 (EF) and 74 (WIB) kyr, respectively. The largest discrepancies among durations between CIEs in the EF and Demerara Rise records were for the Round Down (+336 kyr) and Bridgewick (314 kyr) CIEs. However, the offset was minimal (+119 kyr) for the Hitchwood #1 CIE, which has the longest duration after the CTB, and is very close to the estimated floating ATS uncertainty (±111 kyr; see Table A1.2) for the Demerara Rise record. For the time interval younger than the Hitch-wood #1 Event, there is poor agreement between the Demerara Rise and EF record, with the high-amplitude Hitchwood #2-3 Event absent in the EF and WIB records. However, the EF ATS thro-ugh this interval of the Austin Chalk is preliminary at this point (Eldrett et al., 2015a; Figure 2.1).

2.4.5. Band-Passed Geochemical Time Series

Following astronomical tuning, the strength of astronomical signals was evaluated from EHA spectrograms and band-pass filtering of geochemical time series ($\delta^{13}C_{org}$, %TOC, %Carb, and C/N; Figure 2.8). Since the temporal resolution of sampling decreases upcore at Site 1259 due to a general reduction in sedimentation rates, the most suitable periods for detection are the longer period stable long eccentricity (405 kyr) and long obliquity (~1.2 Myr). The spliced $\delta^{13}C_{org}$ EHA spectrogram (3.0 Myr window) is mostly dominated by amplitude and significant F tests (confidence level = 90%) in the long obliquity band (~0.8–0.9 cycles/Myr), with a node of lower amplitude occurring near 90.8–91.2 ± 0.19 Ma, coeval with the most depleted $\delta^{13}C_{org}$ values (negative Bridgewick CIE) of the Cenomanian-Coniacian (Figure 2.8). The %Carb EHA spectrogram on the other hand is dominated by power in the stable long eccentricity band (Figure A1.3), similar to previous results (Friedrich et al., 2008; Junium et al., 2018). However, a smaller-amplitude, yet significant long obliquity band appears throughout the %Carb record as well. Interestingly, the %TOC-cf EHA spectrogram also records high-amplitude in the obliquity band for the majority of the interval (Figure 2.8; see Table A1.3 for %TOC-cf values).

2.5. Discussion

2.5.1. Linkage Between Tropical North Atlantic Upwelling Zones, Mid-Cretaceous Carbon Cycling, and Astronomical Pacing

Comparison of the bulk geochemical data from Sites 1261 and 1259 indicates common trends among the various proxies that we interpret as driven by changes in paleoceanographic circulation and concurrent responses of biogeochemical cycling in the water column. Interpretations of Demerara Rise as an upwelling zone throughout the mid-Cretaceous, based on exceptionally high %TOC (Shipboard Scientific Party, 2004; Erbacher et al., 2005), redox sensitive trace metals suggesting depleted O_2 conditions (Hetzel et al., 2009), P/C_{org} ratios (Kraal et al., 2010), and physical oceanographic modeling (Trabucho-Alexandre et al., 2010), are consistent with our new data. Weight %TOC values in the studied interval regularly exceed 10%, consistent with low O_2 conditions in the distal shelf environment. Likewise, enriched C/N values of organic matter, previously identified as marine in origin, have been interpreted as indicators of anoxic intervals where microbes preferentially degrade N-bearing compounds in organic-rich sediment (Junium and Arthur, 2007). Additionally, two sustained high-magnitude CIEs are identified at Demerara Rise for OAE2 (~+7‰; Erbacher et al., 2005; this study) and the Hitchwood #2-3 CIE (~+6.5‰), along with sporadic enrichment elsewhere in the Turonian record (Figure 2.6). These comparatively elevated $\delta^{13}C_{org}$ values most likely stem from localized enrichment of $\delta^{13}C_{DIC}$ due to regional organic carbon burial. A decrease in the magnitude of photosynthetic C-isotope fractionation (ε_p) potentially also contributed to high $\delta^{13}C_{org}$ in CIEs. As is observed in the modern Peru Upwelling Zone, ε_p is diminished by rapid growth rates associated with enhanced net primary productivity (NPP), driven by nutrient-rich upwelled bottom waters (Bidigare et al., 1997; Kump and Arthur, 1999; Laws et al., 1995). As a result, the significant positive correlations ($p < 0.01$) of enriched $\delta^{13}C_{org}$ versus C/N ($r = +0.76$; calculated via Astrochron's "surrogateCor" function as implemented by Baddouh et al., 2016) and $\delta^{13}C_{org}$ versus %TOC-cf (Site 1259 $r = +0.61$; Site 1261 $r = +0.74$) at Demerara Rise stem from periods of enhanced upwelling driving lower ε_p, higher NPP from nutrient delivery, a shoaling OMZ, and subsequent organic carbon preservation in anoxic bottom/pore waters (Tables A1.5-A1.6). The high variability not only in %TOC and C/N but also in $\delta^{13}C_{org}$ indicates that NPP rates were dynamic and modulated by fluctuating bottom water upwelling intensity and ocean circulation.

The Demerara Rise $\delta^{13}C_{org}$ chemostratigraphy cannot, however, be interpreted as a result of local upwelling intensity and NPP alone, since it shows remarkable similarity with other Turonian $\delta^{13}C$ records from the WIB and elsewhere (Figure 2.7). There is strong agreement among Turonian $\delta^{13}C_{org}$ records globally (see Sect. 2.5.3) from a variety of localities and depositional environments (terrestrial to deep marine) (Jarvis et al., 2015; Joo and Sageman, 2014). The correlation through specific positive CIEs, of increased $\delta^{13}C_{org}$ and C/N values (OAE2, Holywell, Round Down, Hitchwood #2-3), as well as enriched $\delta^{13}C_{org}$ and %TOC (OAE2, Round Down, Hitchwood #2-3), supports the hypothesis that tropical North Atlantic upwelling zones were critical depocenters for organic carbon burial and therefore major influences on the $\delta^{13}C$ of global marine DIC (Jiménez Berrocoso et al., 2010; Trabucho-Alexandre et al., 2010). Conversely, CIEs (e.g., Hitchwood #1) that do not record sympathetic changes in C/N or %TOC at Demerara Rise were likely driven by changes elsewhere in the global carbon cycle. These data suggest that upwelling was accelerated, and global oceanic circulation became more vigorous during positive CIEs, and likewise, circulation slowed during negative CIEs (e.g., Bridgewick) throughout the Turonian.

Elsewhere along the margins of the proto-North Atlantic (e.g., N.W. African shelf and offshore Senegal), expansive deposits of OC-rich mudstones have been identified as important sinks in driving the positive CIE for OAE2, signifying the basin's large areal expanse of OC depocenters (Kolonic et al., 2005; Kuypers et al., 2002). The persistence of this correlation ($\delta^{13}C_{org}$ versus %TOC and C/N) through the Turonian at Demerara Rise suggests that the tropical North Atlantic continued to play a critical role for net global organic carbon burial throughout the mid-Cretaceous greenhouse. The positive correlation of $\delta^{13}C_{org}$ with C/N and %TOC at Demerara Rise also suggests that organic carbon burial in the tropical North Atlantic was influential enough on global carbon cycling to shift marine $\delta^{13}C_{DIC}$, such that positive CIEs (most visibly OAE2, Round Down, and Hitchwood #2-3) paced at ~1 Myr periodicity (see Sect. 2.5.2) could be detected worldwide throughout the Turonian Stage.

2.5.2. Obliquity Dominance in Low-Latitude Late Cretaceous Records

The EHA spectrogram of the Turonian Demerara Rise $\delta^{13}C_{org}$ time series displays high power in the long obliquity frequency band (~1 Myr), similar to results from the mid-latitudinal $\delta^{13}C$ records of the Bohemian Basin, Czech Republic (Laurin et al., 2015). Previously, the imprint of obliquity cycles on stratigraphic records has been attributed to influence from mid- to high-latitude climate system components (e.g., ice sheets, organic carbon reservoirs, and feedbacks), due to the significant impact changing obliquity has on altering high-latitude insolation curves (Laurin et al., 2015; Wendler et al., 2014). Recently, however, Bosmans et al. (2015) modeled obliquity-driven climate processes at low latitudes originating from strengthening of the summer intertropical insolation gradient (SITIG) with increased tilt. These global climate models predict a doubling of monsoonal wind speed and precipitation between minimum (22.04°) and maximum (24.45°) tilt. One explanation for the strong signal of long obliquity in the Turonian $\delta^{13}C_{org}$ and %TOC-cf EHA spectrograms is that increased monsoonal winds accelerated upwelling at Demerara Rise (Figure 2.8). The resulting increase in NPP coupled organic carbon burial (reflected by %TOC-cf) to the obliquity cycle. Furthermore, the strong correlation between $\delta^{13}C_{org}$ and %TOC-cf and agreement in their spectral amplitude signatures indicate that the carbon cycle was strongly influenced by organic carbon deposition along the southern and eastern margins of the tropical proto-North Atlantic throughout the Turonian (see Sect. 2.5.1).

The stable long eccentricity cycle's overt presence in the %Carb and foraminiferal assemblages and more subtle signal in %TOC-cf and $\delta^{13}C_{org}$ (Figure 2.8) suggests that eccentricity-related changes (via precession modulation) in the position of the Intertropical Convergence Zone also influenced upwelling rates, NPP, and carbon cycling (Friedrich et al., 2008). A node in the long obliquity amplitude of $\delta^{13}C_{org}$ coeval with the long-term $\delta^{13}C_{org}$ minimum may arise from modulation of the ~1-Myr obliquity cycle or may record a change in the sensitivity of the carbon cycle to obliquity, either option leading to a decreased global organic carbon burial flux. One caveat to the SITIG model is the OAE2 interval, during which organic carbon burial rates paced by obliquity increased outside of the tropical North Atlantic including at DSDP Site 603B along the basin's NW margin (Herbin et al., 1987; Kuypers et al., 2004; Meyers et al., 2012b). It is necessary to invoke paleoclimatic and paleoceanographic processes independent or complementary to SITIG, such as some discussed in detail by Meyers et al. (2012b) (e.g., ocean circulation reorganization, altering intermediate/deep water formation), to explain the ubiquitous obliquity signal detected in extratropical records through OAE2. The strong ~1-Myr signal in the %TOC-cf record suggests that organic carbon burial in the tropical North Atlantic was modulated by obliquity and that high-latitude carbon reservoirs were not necessarily required for generating the obliquity-band dominated Turonian $\delta^{13}C_{org}$ record.

2.5.3. GTS Implications and Correlation to Other Turonian $\delta^{13}C$ Records

The astrochronology from Demerara Rise provides a near-continuous record of the timing of late Cenomanian to early Coniacian CIEs for refinement of the GTS and comparison to records globally. Stage boundaries were assigned using CIE onsets and terminations as time horizons, along with biostratigraphic constraints. The CTB (93.9 ± 0.15 Ma; Meyers et al., 2012a) was placed at Site 1261 by first identifying the onset of the OAE2 CIE (94.45 ± 0.16 Ma) and then calculating the rock-thickness equivalent to 525–565 kyr (Ma et al., 2014; Sageman et al., 2006) preserved above this horizon, up to the CTB, using the new astrochronology (see Sect. 2.4.3 and Text A1.2). Previously, the TCB was identified in Site 1259 at two possible horizons, the CC12/13 nannofossil boundary and a negative $\delta^{13}C_{carb}$ excursion in foraminifera samples at ~507 MCD (Bornemann et al., 2008). The CC12/CC13 approximation of the TCB is frequently utilized (e.g., Perch-Nielsen, 1985). The age of the CC12/13 boundary at Demerara Rise is 89.90 ± 0.19 Ma and is within temporal uncertainty of estimates from the Eagle Ford (89.72 Ma), representing one possible approximation of the TCB (Eldrett et al., 2015a). However, more recent biostratigraphic investigations indicate that the TCB falls higher within the CC13 biozone (Burnett, 1998; Corbett et al., 2014) and that a common basal CC13 marker, the F.O. of *Marthasterites furcatus*, is diachronous (Lees, 2008). The new ATS from Site 1259 also indicates that the alternative TCB placement from Bornemann et al. (2008) at ~507 MCD is too young, since the duration of the Turonian Stage in that scenario (>6 Myr) would be inconsistent with radioisotopic estimates. Therefore, we propose a third candidate horizon for the TCB at Site 1259 utilizing the chemostratigraphic marker of the negative Navigation CIE to identify the boundary (Jarvis et al., 2006; Voigt and Hilbrecht, 1997; Walaszczyk et al., 2010). We place this horizon at Site 1259 at 511.00 MCD from $\delta^{13}C_{org}$ chemostratigraphy, overlying the Hitchwood Events (Figures 2.2, 2.6, and 2.7).

It is possible that the high-amplitude excursion marking the uppermost Turonian in Site 1259 represents an artifact of local environmental conditions that do not correspond to changes in the global carbon cycle, since other localities preserving the Hitchwood Events record a more diminutive excursion (Figure 2.7). However, we consider this scenario less likely, because the succession does not preserve other sustained high amplitude CIEs that cannot be correlated. Additionally, the ATS durations between the Bridgewick and Navigation CIEs (~1.6 Myr) are consistent between Demerara Rise and the well-resolved Late Turonian substage and TCB interval of the Bohemian Basin (Laurin et al., 2015) (Figures 2.6, 2.7). Therefore, we favor the interpretation of the Demerara Rise chemostratigraphy and spliced ATS that yields a floating duration of 4.62 ± 0.15 Myr for the Turonian Stage and TCB age of 89.28 ± 0.21 Ma (Table A1.2).

The presented estimates for the duration of the Turonian Stage and age of the TCB are equivalent within uncertainty from recent calculations in the GTS 2012 and radioisotopic dating of bentonites in the WIB (U/Pb zircon and Ar/Ar ages: Sageman et al., 2014a). However, they suggest a younger TCB age and longer Turonian duration. The astronomical duration for the Turonian Stage from Demerara Rise is consistent with, but slightly longer than, the ATS calculations from the pelagic carbonate-rich Bottaccione Gorge section (Italy; 4.44 Myr; Sprovieri et al., 2013) and the Eagle Ford in Texas (4.38 Myr; Eldrett et al., 2015a). Our results suggest that earlier placement of the Navigation CIE in the Eagle Ford is likely below the TCB (Eldrett et al., 2017). That CIE instead may represent the termination of Hitchwood #1, with Hitchwood #2-3 and more late Turonian strata overlying. However, it is also possible that the Hitchwood Events are more poorly preserved in the WIB than at North Atlantic and Tethys sites (see Sect. 2.5.4 for further discussion of Hitchwood Events).

Overall, the median difference in the relative timing of named Turonian CIEs among $\delta^{13}C$ records in Texas, the WIB, and the Bohemian Basin versus Demerara Rise is 79 kyr—less than one short eccentricity cycle, indicating an overall consistency in astronomical and radioisotopic timescales among disparate basins (Table A1.8). Eight discrepancies (of 24 comparisons) in CIE timing exceeding 200 kyr are attributed to undetected hiatuses, sampling resolution limitations, core depth uncertainty, bandwidth choice of the Gaussian kernel smoother, local variation in CIE expression, and uncertainties inherent in ATS development (e.g., window size and bandwidth). For example, age offsets for the Glynde CIE (~400 kyr) and less definitively the Pewsey CIE between Demerara Rise and the WIB likely partially arise due to a previously unaccounted hiatus in the WIB's mid-Turonian Carlile Formation (see Sect. 2.5.4).

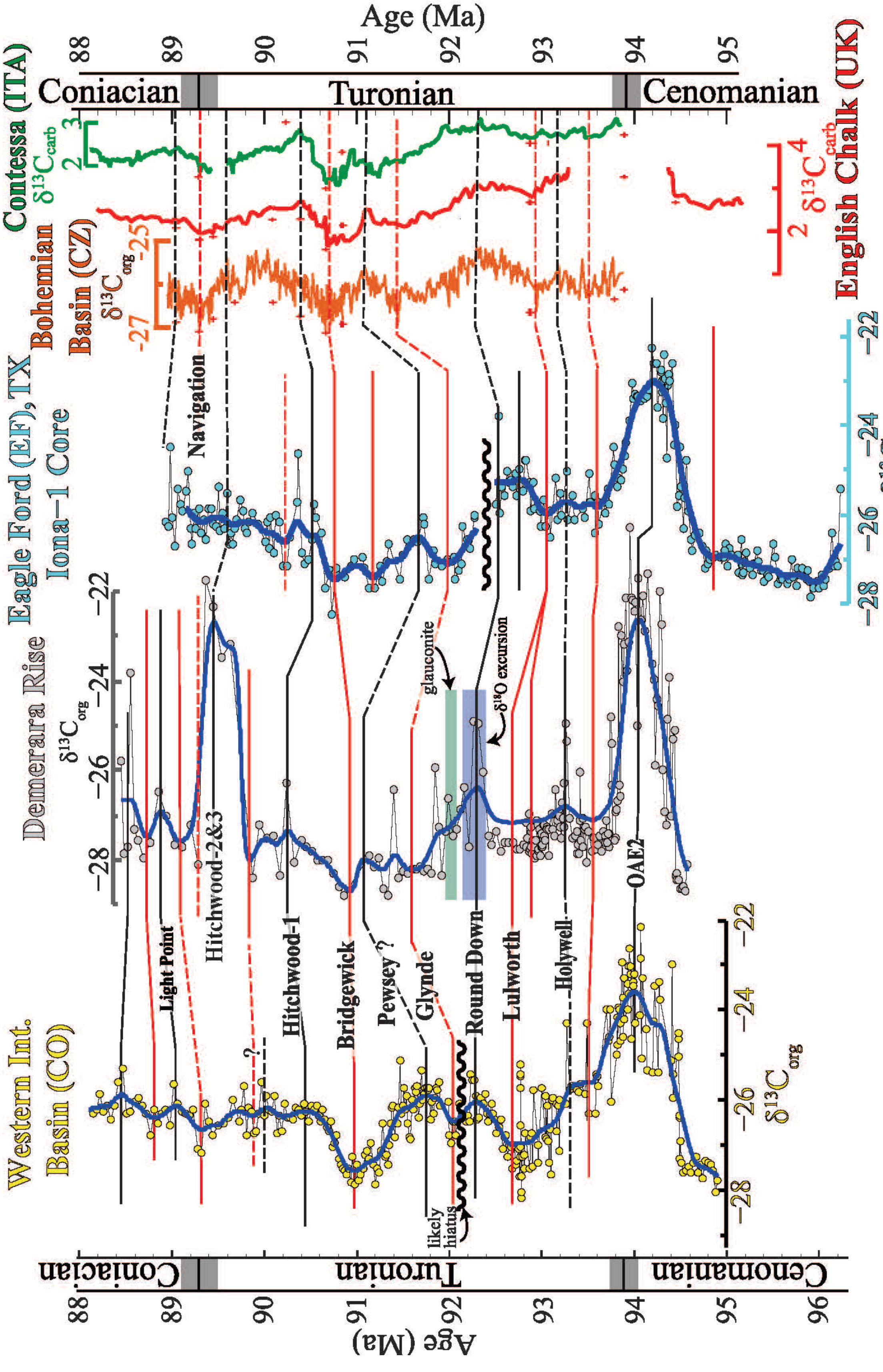
Western Int. Basin (CO)
δ13Corg
Demerara Rise
δ13Corg
Eagle Ford (EF), TX
Iona–1 Core
δ13Corg
Bohemian Basin (CZ)
δ13Corg
Contessa (ITA)
δ13Ccarb
English Chalk (UK)
δ13Ccarb
Age (Ma)
Coniacian
Turonian
Cenomanian
88
89
90
91
92
93
94
95
96
−28
−26
−24
−22
-27
-25
2
3
4
Navigation
Light Point
Hitchwood-2&3
Hitchwood-1
Bridgewick
Pewsey ?
Glynde
Round Down
Lulworth
Holywell
OAE2
likely hiatus
glauconite
δ18O excursion
?

Figure 2.7. (previous page) Proposed Turonian $\delta^{13}C$ age model and correlation of raw and Gaussian kernel smoothed ($1\sigma = \pm 75$ kyr; blue) $\delta^{13}C_{org}$ time series from Demerara Rise astronomical timescales (data from Erbacher et al., 2005; Meyers et al., 2012b; this study). Fully astronomically tuned and radioisotopically dated sections include the Eagle Ford (light blue; Eldrett et al., 2015a). Radioisotopically dated and partially astronomically tuned records from the Western Interior Basin (yellow; Joo and Sageman, 2014). The partially astronomically tuned Turonian record from the Bohemian Basin, Czech Republic, plots in orange (Laurin et al., 2015) and biostratigraphically constrained records from the English Chalk (UK) plots in red (Jarvis et al., 2006), and Contessa (Italy) plots in green (Stoll and Schrag, 2000). Potential correlative horizons, including $\delta^{13}C$ maxima and minima (absolute carbon isotope excursion [CIE] magnitude >0.5‰) of the smoothed time series, are indicated by black (positive CIEs) and red (negative CIEs) horizontal lines (Table A1.8). Qualitative visually assigned correlations are marked by black/red dashed horizons on occasion. We shift absolute ages in Iona-1 core chemostratigraphy 250-kyr younger to align the onset of the main body of OAE2 for comparison. The age model for European sections is adapted from Laurin et al. (2015). Red crosses represent horizons with time control from an astronomical age model of the Upper Turonian (Laurin et al., 2014) and spline-fitted ammonite biozones ages from the WIB. For stratigraphic correlation and comparison, the mid-Turonian interval (between Upper and Lower Turonian tie points) for European sections was linearly scaled such that the duration of the Turonian Stage in Europe was equivalent to the presented Turonian Stage duration at Demerara Rise (i.e., Cenomanian-Turonian Boundary and Turonian-Coniacian Boundary ages are the same in both basins).

Caution is warranted when correlating the Upper Turonian interval of Site 1259 at Demerara Rise, due to low sedimentation rates (<0.3 cm/kyr) and relative stratigraphic condensation compared to the many Tethys $\delta^{13}C$ chemostratigraphic records (Uličný et al., 2014; Voigt and Hilbrecht, 1997; Wiese, 1999). There is little evidence for hiatuses of significant duration in the Turonian Stage at Demerara Rise, given no drastic changes in sedimentation rate and consistency between ATS and radioisotopic durations for the Turonian Stage. However, limited time resolution of Upper Turonian samples (e.g., 70–90 kyr/sample at Site 1259 above 513 MCD) compared to the OAE2 interval in Site 1261 (<20 kyr/sample) undermines full resolution of the Hitchwood CIE sequence as preserved in European chemostratigraphic records (i.e., HW-1, HW-2, and HW-3 of Jarvis et al., 2015). The upper Hitchwood CIE at Demerara Rise (Figure

2.7) may actually preserve an amalgamated record of Hitchwood #2 and #3 from the Bohemian Basin, due to lower temporal resolution of samples.

2.5.4. Integrated Tropical North Atlantic and Western Interior Histories for the Turonian Stage: A Chronology

The astronomically tuned $\delta^{13}C_{org}$ chronostratigraphic record from Demerara Rise permits the correlation of paleoceanographic changes at an open ocean locality to paleobiologic and sequence stratigraphic events in the epeiric WIB, to assess synchroneity in global sea level and climate events.

2.5.4.1. Round Down Event

A positive $\delta^{18}O$ excursion in foraminifera at Demerara Rise has led to speculation that this event represents a period of global cooling in the otherwise warm greenhouse of the Late Cretaceous (Figures 2.6 and 2.7; Bornemann et al., 2008). Previously, the CIE accompanying the $\delta^{18}O$ excursion was interpreted as the Pewsey Event; however, the astronomically tuned and intercontinentally correlated $\delta^{13}C_{org}$ record demonstrates that this CIE represents the Round Down event instead, as suggested by Uličný et al. (2014). Additionally, a regionally pervasive glauconite-rich bed punctuates the thick package of rhythmically bedded claystones and foraminiferal packstones (Nederbragt et al., 2007). The presence of glauconite in marine strata has commonly been interpreted to reflect deposition at mid-shelf or deeper water depths (> 50 m) and/or sediment starvation related to relative sea level change (Amorosi, 1995; Loutit et al., 1988), but some authors have challenged these interpretations (Chafetz and Reid, 2000). Fundamentally, glauconite forms within microenvironments that are reducing compared to surrounding better oxygenated environments (Hower, 1961). Given various independent constraints on the Demerara Rise deposi-

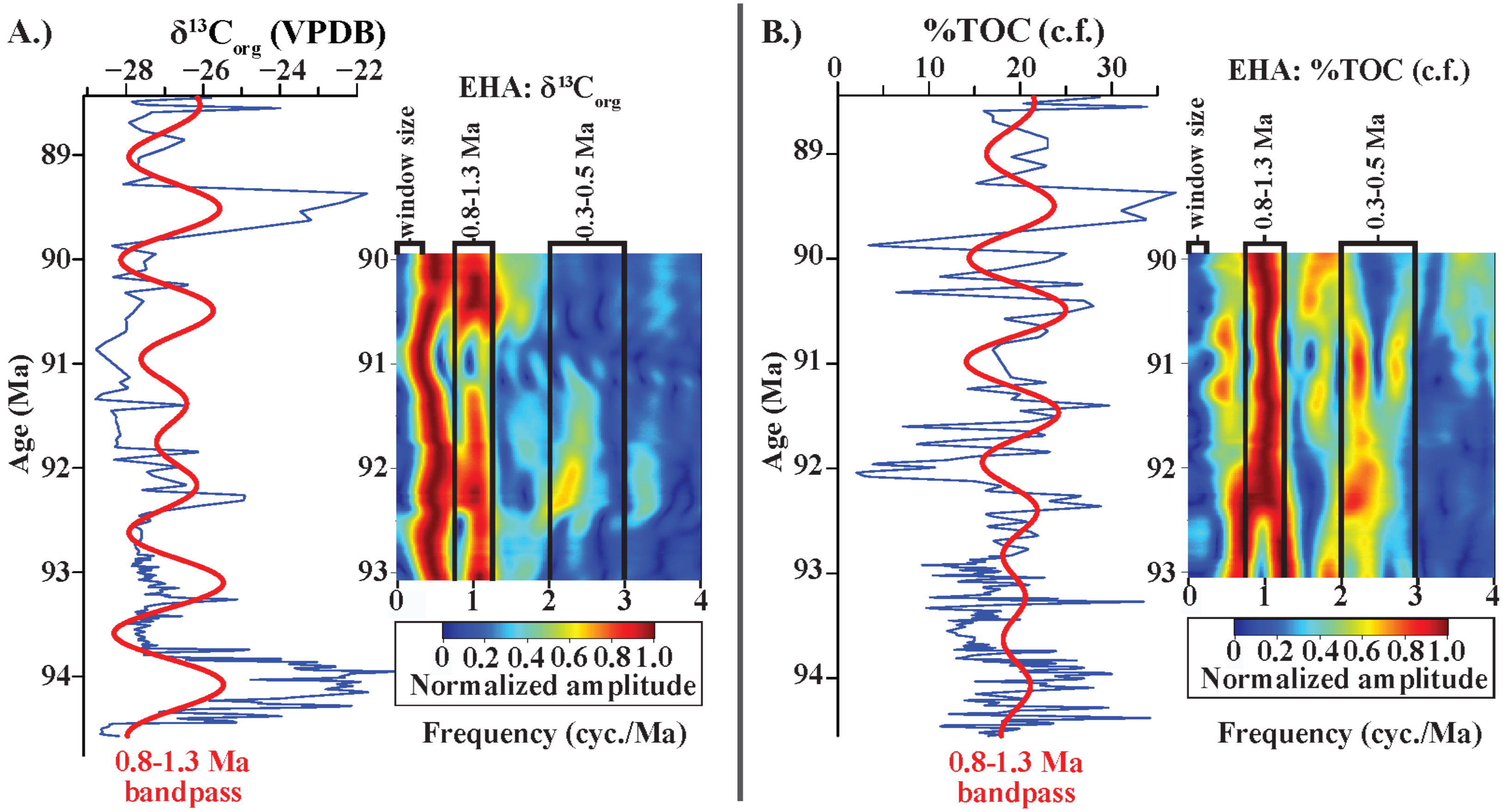

Figure 2.8. Evolutive harmonic analysis (EHA) spectrograms and band-pass filtered records of (a) $\delta^{13}C_{org}$ and (b) %TOC-cf (carbonate free) from the astronomically tuned and spliced Demerara Rise succession. Spectrograms calculated with EHA routine of Astrochron using window size of 3 Myr. Strong amplitude (normalized) in ~1-Myr frequency band for both $\delta^{13}C_{org}$ and %TOC-cf suggests an influence of long obliquity on both the global carbon cycle and organic carbon burial at Demerara Rise, respectively. Lower amplitude but distinct peaks in the stable 405-kyr eccentricity band are recorded in both records, especially %TOC-cf. Although it is more difficult to resolve, amplitude in the ~0.5 cyc./Myr band (long eccentricity ~2.4 Myr) is detected in both records (more so for $\delta^{13}C_{org}$).

tional environment, the glauconitic horizon most likely reflects: (1) a relative fall in sea level such that the sediment-water interface was exposed to better oxygenated surface waters, (2) oxygenation of intermediate North Atlantic bottom waters through global cooling or circulation reorganization, (3) diminished upwelling rates that limited NPP, or (4) sediment starvation associated with rapid rise in sea level, or some combination of these processes. The presence of quartz sand and bioturbation in the prominent glauconitic layer (Shipboard Scientific Party, 2004), as well as decreased C/N values with lower %TOC, suggests higher dissolved O_2 in the water column and pore water. Oxygenation is consistent with a cooling of bottom water, potentially a fall in sea level on the distal shelf, and/or changing circulation configurations.

Stratigraphic correlation of the Demerara Rise geochemical and relative sea level records to Colorado (Joo and Sageman, 2014) via $\delta^{13}C$ kernel smoothing techniques permits comparison of relative sea level fluctuations during the Round Down CIE (Figure 2.7). The deposition of glauconite sands at Demerara Rise in the uppermost Round Down CIE correlates to the upper *Collingnoniceras woollgari* ammonite biozone in the upper interval of the Fairport Shale Member (Joo and Sageman, 2014). In the central to axial basin of the WIB, the termination of the Round Down CIE is coincident with a disconformable contact of the Fairport Chalky Shale Member with the overlying Blue Hill Shale, documented at Mesa Verde, Colorado (Leckie et al., 1997, unpublished data), Pueblo, Colorado (Glenister and Kauffman, 1985), and in the Denver Basin's Angus core (Joo and Sageman, 2014; Figure 2.7). In the western foredeep of the WIB, the progradational, laterally continuous Coon Spring Sandstone Bed of central Utah is of *C. woollgari* age (Gardner, 1995; Molenaar and Cobban, 1991); collectively these observations are consistent with shallowing in the WIB. Additionally, in the Iona-1 core from the Maverick Basin of Texas, the Round Down CIE is overlain by an influx of boreal palynological assemblages and a disconformity at the contact of the Rock Pens and Langtry Members of the Boquillas Fm., hypothesized to relate to changing salinity and circulation patterns in the seaway (Eldrett et al., 2015a, 2017).

From the various anchored ATS, the average age of the Gaussian smoothed Round Down CIE is 92.30 ± 0.19 Ma, placing the event in the mid-Middle Turonian, consistent with Haq's (2014) KTu4, the Ogbourne Hardground in the English Chalk (Gale, 1996), and Miller et al.'s (2004) Bass River-Magothy sequence boundaries—arguably the largest amplitude eustatic event of the Turonian Stage (Haq and Huber, 2017). This correlation suggests that the positive $\delta^{18}O$ excursion and glauconitic horizon at Demerara Rise is coincident with a relative sea level fall at multiple locations in the central and southern WIB as indicated by areally extensive hiatuses. Interestingly, however, our results indicate that the largest amplitude Turonian sea level fall is not coeval with maximum regression in the WIB between the Greenhorn and Niobrara cyclothems recorded by deposition of the Ferron Sandstone and Codell Sandstone (see below). Instead, the event is associated with the thinner Coon Springs Bed and more subtle disconformable contacts of stratigraphic members within the Carlile Shale. This suggests that basin-scale controls on accommodation space, such as changes in rates and patterns of foreland subsidence (i.e., Catuneanu et al., 1997; Liu and Nummedal, 2004; White et al., 2002), were more critical in driving long-term relative sea level patterns in the WIB than eustasy during the Middle to Late Turonian.

2.5.4.2. Bridgewick Event

Following the Round Down CIE through the negative Bridgewick CIE (90.8–91.6 Ma), $\delta^{13}C$ values at Demerara Rise remain depleted compared to the more enriched background $\delta^{13}C$ values following OAE2 and observed later in the Coniacian Stage. Although there is no distinct geochemical evidence for a paleoclimate event at Demerara Rise in this late-Middle Turonian interval, globally it is characterized by hiatuses and shallowing of facies, possibly contributing to the mid-Cretaceous minimum in $\delta^{13}C_{org}$. Across North American basins, the late-Middle Turonian is marked by evidence of protracted regression: (1) the nonmarine Magothy Sequence on the passive margin of New Jersey (Miller et al., 2004), (2) the Codell Sandstone, which is associated with multiple unconformities throughout the central WIB (Fisher et al., 1985; Merewether and Cobban, 1986), and (3) multiple forced regressions in the prograding Ferron clastic wedge (Gardner, 1995) through the *Prionocyclus hyatti* to *Prionocyclus macombi* (~91.24 ± 0.09 Ma; Sageman et al., 2014a) ammonite biozones.

In addition, the forced regressions of the Ferron are interpreted by Zhu et al. (2012) to occur in the Milankovitch short eccentricity frequency band. Although $^{40}Ar/^{39}Ar$ age uncertainty for the Ferron ashes precludes a rigorous radioisotopic test of forced regression recurrence, this corresponds to a node in long obliquity amplitude in $\delta^{13}C_{org}$ from Demerara Rise and a shift to higher amplitude in the ~405-kyr long eccentricity band of %TOC-cf, prior to reverting to long obliquity dominance at ~91 Ma (Figure 2.8). The cooccurrence of forced regressions, low global sea level, and a minimum in long obliquity are consistent with Antarctic continental ice accumulation. The occurrence of the first two positive $\delta^{18}O$ excursions in European sections in the late-Middle to Late Turonian correlates to this interval (Jarvis et al., 2015; Stoll and Schrag, 2000; Voigt and Wiese, 2000). However, $\delta^{18}O$ evidence for ice sheet growth is equivocal through this interval at Demerara Rise with no significant positive excursion (Bornemann et al., 2008). It may be the case that alternative drivers of eustasy, such as aquifer storage (Wendler et al., 2016) or otherwise, were responsible for these sedimentation patterns (see Haq and Huber, 2017, for detailed discussion). Given the widespread occurrence of lower sea levels during this period of relatively depleted $\delta^{13}C$ values, it is plausible that a late-Middle Turonian decrease in global flooded continental shelf area led to diminished marine organic carbon burial rates (such that $\delta^{13}C$ became more depleted). Despite the tropical North Atlantic's importance in Turonian carbon burial, it appears that continued elevated %TOC values at Demerara Rise did not sequester enough OC to offset the decrease in OC burial on previously flooded continental shelves.

2.5.4.3. Hitchwood Events

The latest Turonian to early Coniacian record at Demerara Rise is marked by the ~ +2‰ Hitchwood #1 CIE, followed by Hitchwood #2-3, a high-magnitude positive $\delta^{13}C$ excursion (+6‰–7‰), which has no correlative high-magnitude expression in the $\delta^{13}C$ record of the WIB and Texas (Figure 2.7). One possible explanation for this discrepancy is that the amplified CIE at Demerara Rise was driven locally by accelerated phytoplankton growth rates, stimulated by rapid upwelling during Hitchwood #2-3 (see Sect. 2.5.1 and 2.5.3). The event may simply be a lower amplitude ~ +1‰ CIE (CL-1 core's T6 horizon; Joo and Sageman, 2014) in the WIB due to lower NPP in surface waters. This explanation is complicated by the fact that Hitchwood #2 and #3 are preserved by significant $\delta^{13}C$ enrichment in the Bohemian Basin (Jarvis et al., 2015; Uličný et al., 2014) and elsewhere (Wendler, 2013), indicating similar enrichment trends outside of the proto-North Atlantic basin. Interestingly, the highly enriched $\delta^{13}C_{org}$ values, %TOC, and C/N of Hitchwood #2-3 at Site 1259 mimic values during OAE2, suggesting that an increasing obliquity signal strengthened monsoonal winds and upwelling during this CIE as well (see Sect. 2.5.2).

Another possible explanation for the discrepancy is that the Hitchwood #2-3 CIEs occurred during an interval recorded as hiatus in the WIB and Texas, as postulated by Jarvis et al. (2015)

for the negative Navigation CIE. The latter event is largely absent in the WIB (Figure 2.7) due to a regional hiatus (Sageman et al., 2014a; Walaszczyk et al., 2014) but was not represented in the age model of Joo and Sageman (2014) due to its relatively minor and uncertain duration. If this hiatus in the lowermost Ft. Hayes Limestone (hardground Bed 29 Pueblo, CO) represents a duration approaching 400 kyr, it is feasible that the most enriched $\delta^{13}C_{org}$ values of the Hitchwood Events are simply not recorded in the central WIB (Angus core) due to nondeposition or subsequent erosion.

2.6. Conclusions

Findings presented here emphasize that Demerara Rise and the greater tropical proto-North Atlantic were a locus of elevated organic carbon burial not only during OAE2 but also additionally during other CIEs of the Middle to Late Turonian. Despite relatively low sedimentation rates on the distal shelf, organic carbon burial was enhanced by upwelling-driven oxygen deficiency in bottom and pore waters. Correlations in both smoothed and raw $\delta^{13}C_{org}$ versus %TOC and $\delta^{13}C_{org}$ versus C/N support the idea that tropical upwelling sites and organic carbon depocenters in the proto-North Atlantic basin played an important role through the mid-Cretaceous carbon cycle. The combination of the presented anchored ATS, developed through e-ASM techniques, with high-resolution $\delta^{13}C_{org}$ chemostratigraphy produces an astronomical duration for the Turonian Stage at Demerara Rise. In addition, a Gaussian kernel smoothing and cross-correlation method for quantitative stratigraphic correlation of astronomically tuned $\delta^{13}C$ records is introduced. Although best practices for assigning appropriate smoothing bandwidths, sampling resolution, and correlation thresholds must be tested in future studies, the method has generated a stratigraphic correlation of $\delta^{13}C$ chemostratigraphies from disparate locales (separated by thousands of kilometers), demonstrating consistency among several Turonian astrochronologies.

Notably, the mid-Turonian positive oxygen isotope excursion at Demerara Rise does not correlate to the major lowstand associated with the boundary between the Greenhorn and Niobrara Cyclothems in the WIB. However, the quantitative correlation approach employed here does link this potential geochemical and lithologic evidence for cooling to a more minor hiatus in shallow marine sites, such as the WIB, Texas, and elsewhere (Haq and Huber, 2017) during the Round Down CIE. Further investigation is required to decipher whether small-scale, ephemeral Antarctic ice buildup (Miller et al., 2005), groundwater storage (Wendler et al., 2016), or some yet to be considered process was driving an apparently synchronous eustatic fall in mid-Turonian sea level.

Lastly, band-pass filtering of astronomical frequencies of the geochemical data set constrains interpretations for climate forcings driving organic carbon burial, upwelling, and a shoaling chemocline at Demerara Rise. Multiple interpretations (i.e., cross-equatorial gradient or high-latitude processes) remain plausible for the prominent ~1-Myr obliquity signal in Turonian $\delta^{13}C_{org}$ records.

CHAPTER 3

Evaluating Late Cretaceous OAEs and the Influence of Marine Incursions on Organic Carbon Burial in an Expansive East Asian Paleo-lake

Motivation: The recently drilled SK1-S core from the Songliao Basin in northeast China recovered ~1000 m of terrestrial Upper Cretaceous strata deposited by a long-lived lake system. Although many marine sections preserve oceanic anoxic events (OAEs) for study, coeval terrestrial records are rare, obscuring a fully global reconstruction of the events. This chapter investigates the paleoclimate and carbon cycling of the Songliao Basin to test whether paleoenvironmental conditions in terrestrial depositional settings responded to climate feedbacks of OAEs.

Key findings:

- Late Cretaceous Songliao lake system in northeast China preserves evidence for terrestrial climate change during Oceanic Anoxic Event 3 (OAE3).
- Coeval marine Os_i data show no evidence for prolific volcanism at onset of OAE3.
- Carbon isotope chemostratigraphy indicates pCO_2 drawdown during OAE3 (~88 Ma).
- No osmium isotope (Os_i) evidence of marine incursions in organic carbon-rich Qingshankou Formation.
- Non-marine depositional model presented for Qingshankou Formation's source rocks.

This chapter of research originally appeared in:

Jones, M. M., Ibarra, D. E., Gao, Y., Sageman, B. B., Selby, D., Chamberlain, C. P., and Graham, S. A., 2018, Evaluating Late Cretaceous OAEs and the influence of marine incursions on organic carbon burial in an expansive East Asian paleo-lake: *Earth and Planetary Science Letters*, v. 484, p. 41-52. https://doi.org/10.1016/j.epsl.2017.11.046

CHAPTER 3

Evaluating Late Cretaceous OAEs and the Influence of Marine Incursions on Organic Carbon Burial in an Expansive East Asian Paleo-lake

Abstract

Expansive Late Cretaceous lacustrine deposits of East Asia offer unique stratigraphic records to better understand regional responses to global climate events, such as oceanic anoxic events (OAEs), and terrestrial organic carbon burial dynamics. This study presents bulk organic carbon isotopes ($\delta^{13}C_{org}$), elemental concentrations (XRF), and initial osmium ratios ($^{187}Os/^{188}Os$, Os_i) from the Turonian–Coniacian Qingshankou Formation, a ~5 Myr lacustrine mudstone succession in the Songliao Basin of northeast China. A notable $\delta^{13}C_{org}$ excursion (~+2.5‰) in organic carbon-lean Qingshankou Members 2–3 correlates to OAE3 in the Western Interior Basin (WIB) of North America within temporal uncertainty of high-precision age models. Decreases in carbon isotopic fractionation ($\Delta^{13}C$) through OAE3 in the WIB and Songliao Basin, suggest that significantly elevated global rates of organic carbon burial drew down pCO_2, likely cooling climate. Despite this, Os_i chemostratigraphy demonstrates no major changes in global volcanism or weathering trends through OAE3. Identification of OAE3 in a lake system is consistent with lacustrine records of other OAEs (e.g., Toarcian OAE), and underscores that terrestrial environments were sensitive to climate perturbations associated with OAEs. Additionally, the relatively radiogenic Os_i chemostratigraphy and XRF data confirm that the Qingshankou Formation was deposited in a non-marine setting. Organic carbon-rich intervals preserve no compelling Os_i evidence for marine incursions, an existing hypothesis for generating Member 1's prolific petroleum source rocks. Based on our results, we present a model for water column

stratification and source rock deposition independent of marine incursions, detailing dominant biogeochemical cycles and lacustrine organic carbon burial mechanisms.

CHAPTER 3

Evaluating Late Cretaceous OAEs and the Influence of Marine Incursions on Organic Carbon Burial in an Expansive East Asian Paleo-lake

3.1. Introduction

Upper Cretaceous marine strata preserve evidence for greenhouse warmth on a planet with high pCO_2 (e.g., Pagani et al., 2014) and lacking sustained ice sheets (MacLeod et al., 2013). Oceanic anoxic events (OAEs) are superimposed on this stratigraphic record of excessive warmth, as relatively brief intervals (<1 Myr) of enhanced organic carbon burial in many basins globally (Jenkyns, 2010 and references therein) accompanied by positive stable carbon isotope excursions (CIEs) (Scholle and Arthur, 1980). Precise correlations of terrestrial and marine records are critical for developing a unified Late Cretaceous paleoclimate reconstruction and understanding the terrestrial response to OAEs, as well as for testing hypotheses for the causal mechanisms of OAEs. However, such correlations are complicated in terrestrial basins due to the common occurrence of hiatuses, lateral heterogeneity in lithofacies, and limited biostratigraphic age control. Despite challenges, some workers have employed carbon isotope ($\delta^{13}C$) chemostratigraphy to identify Mesozoic OAEs in terrestrial strata and assess local paleoclimate responses (e.g., OAE2, Barclay et al., 2010; OAE1a, Ludvigson et al., 2010). Although comparatively rare in the geologic record, lacustrine facies offer promise in reconstructing robust terrestrial paleoclimate records given relatively continuous, expanded mudstone successions. Paleo-lakes are also suitable for testing hypotheses about OAEs' triggering mechanisms, such as accelerated weathering, and for better resolving regional environmental responses (e.g., Toarcian OAE: Xu et al., 2017).

In the non-marine Songliao Basin of northeast China, the SK1-S core provides a relatively continuous Late Cretaceous stratigraphic record from lacustrine and fluvial units influenced by local tectonic and climatic conditions (Figure 3.1) (Wang et al., 2013). In addition, the organic carbon-rich mudstones of the Turonian–Coniacian Qingshankou Member 1 are primary petroleum source rocks in China's largest and longest producing non-marine oil and gas basin (Feng et al., 2010). As a result, the depositional history of the Qingshankou Formation has been heavily studied and debated, with some authors arguing that episodic incursions of marine waters during Member 1 drove water column stratification in the basin creating conditions favorable to preservation of organic carbon (e.g., Hou et al., 2000). More recently, the sporadic presence of biomarkers typical of marine algae and sponges in Member 1 and lowermost Members 2 and 3 (Hu et al., 2015), and pyrite sulfur isotopic records in Member 1 of SK1-S (Huang et al., 2013) have been interpreted as evidence for transient or even prolonged marine connections. However, the marine incursion hypothesis for source rock deposition in Qingshankou Member 1 remains controversial, as paleogeographic reconstructions note considerable distances to the nearest marine waters (>500 km; Yang, 2013) (Figure 3.1) and because no well-preserved uniquely marine micro- or macro-fossils have been reported from the Qingshankou Formation in SK1-S (Xi et al., 2016). Others have interpreted a consistently non-marine water body during the deposition of the Qingshankou Formation (Chamberlain et al., 2013).

To assess the influence of OAEs and marine incursions on lacustrine organic carbon burial rates in the dominantly terrestrial Songliao Basin (Wang et al., 2016a), we present sedimentary geochemical measurements of the expanded mudstones of the Qingshankou Formation. The new mid-Turonian to late-Coniacian $\delta^{13}C_{org}$ records (this study; Hu et al., 2015) serve as a test of $\delta^{13}C_{org}$

correlation robustness from an East Asian lacustrine basin to the epicontinental marine $\delta^{13}C_{org}$ in the North American Western Interior Basin (WIB) (Joo and Sageman, 2014). Utilizing recently updated radioisotopic and astrochronologic age models (Locklair and Sageman, 2008; Wu et al., 2013; Sageman et al., 2014a; Wang et al., 2016b), we identify the Coniacian Oceanic Anoxic Event 3 (OAE3) in Qingshankou Members 2 and 3 and investigate the event in a lake system using geochemical proxies.

Coupled with $\delta^{13}C$ chemostratigraphy, we present an initial osmium isotope ($^{187}Os/^{188}Os$ denoted as Os_i) chemostratigraphy from the Songliao Basin to test the marine incursion hypothesis. The Os_i data serve as a proxy for marine connectivity and basin restriction (e.g., Du Vivier et al., 2014), since values reflect a mixture of osmium derived from relatively homogenized open marine waters (Gannoun and Burton, 2014), mixing over geologically brief intervals ($\tau < 10$ kyr, Oxburgh, 2001; Rooney et al., 2016), and local continental weathered osmium which tends to be more radiogenic (higher Os_i) (Peucker-Ehrenbrink and Ravizza, 2000). As a result, lacustrine formations, isolated from the marine osmium reservoir, generally preserve higher Os_i values due to the flux of proximal radiogenic osmium and limited unradiogenic osmium fluxes (e.g., cosmogenic dust and hydrothermal sources) (Poirier and Hillaire-Marcel, 2011; Cumming et al., 2012; Xu et al., 2017), with the caveat that lacustrine basins weathering ophiolitic lithologies preserve more unradiogenic Os_i (Kuroda et al., 2016). Thus, typical basins with a history of marine connections should record more non-radiogenic Os_i when compared to contemporaneous lacustrine basins. To constrain open marine Os_i values during deposition of Qingshankou Member 1, we present time correlative records from Turonian mudstones from the tropical North Atlantic. Furthermore, we interpret Os_i records as one proxy for continental weathering intensity through

Qingshankou Members 2 and 3 (OAE3 interval as demonstrated by this study) and other intervals of SK1-S lacking additional evidence for marine incursions. Finally, to characterize marine osmium cycling and potential perturbations across OAE3 (e.g., LIP volcanism, continental weathering), we present a third small Os_i sample set from the Angus core in the WIB (Denver Basin, Colorado).

Additionally, we present trace element (XRF) analyses spanning the Qingshankou Formation to reconstruct bottom-water redox conditions through major events in the lake's evolution, such as source rock deposition in Member 1 and OAE3 in Members 2 and 3, using established interpretive frameworks (Tribovillard et al., 2006; Sageman et al., 2014b). To conclude, we propose a depositional model, independent of marine connections, to characterize lacustrine biogeochemical cycling during accumulation of the Qingshankou Formation. This model provides a footing for future research to further evaluate scenarios for water column stratification and organic carbon deposition in mid-latitude paleo-lakes discussed herein.

3.2. Geologic materials SK1-S core

The terrestrial Songliao Basin in northeast China preserves a long-lived Jurassic–Cretaceous stratigraphic record in a deep (>5 km) backarc rifted sag basin (Figure 3.1) (Graham et al., 2001; Wang et al., 2013, 2016a). An International Continental Drilling Project coring campaign recovered a sedimentary succession spanning the mid-Turonian to Campanian in two overlapping cores (SK1-S and SK1-N) in 2009. Three fluvio-deltaic formations (oldest to youngest: Quantou, Yaojia, Sifangtai) separated by two thick lacustrine formations (Qingshankou, Nenjiang) comprise the succession. A chronostratigraphic framework has been developed for SK1-S based on lithostratigraphy (Gao et al., 2009; Wang et al., 2009), and biostratigraphy of ostracod, charophyte, and, in the lower Nenjiang Formation, foraminifera (Wan et al., 2013; Xi et al., 2016). Recently published high-precision zircon U–Pb dates (Wang et al., 2016b) and astrochronology

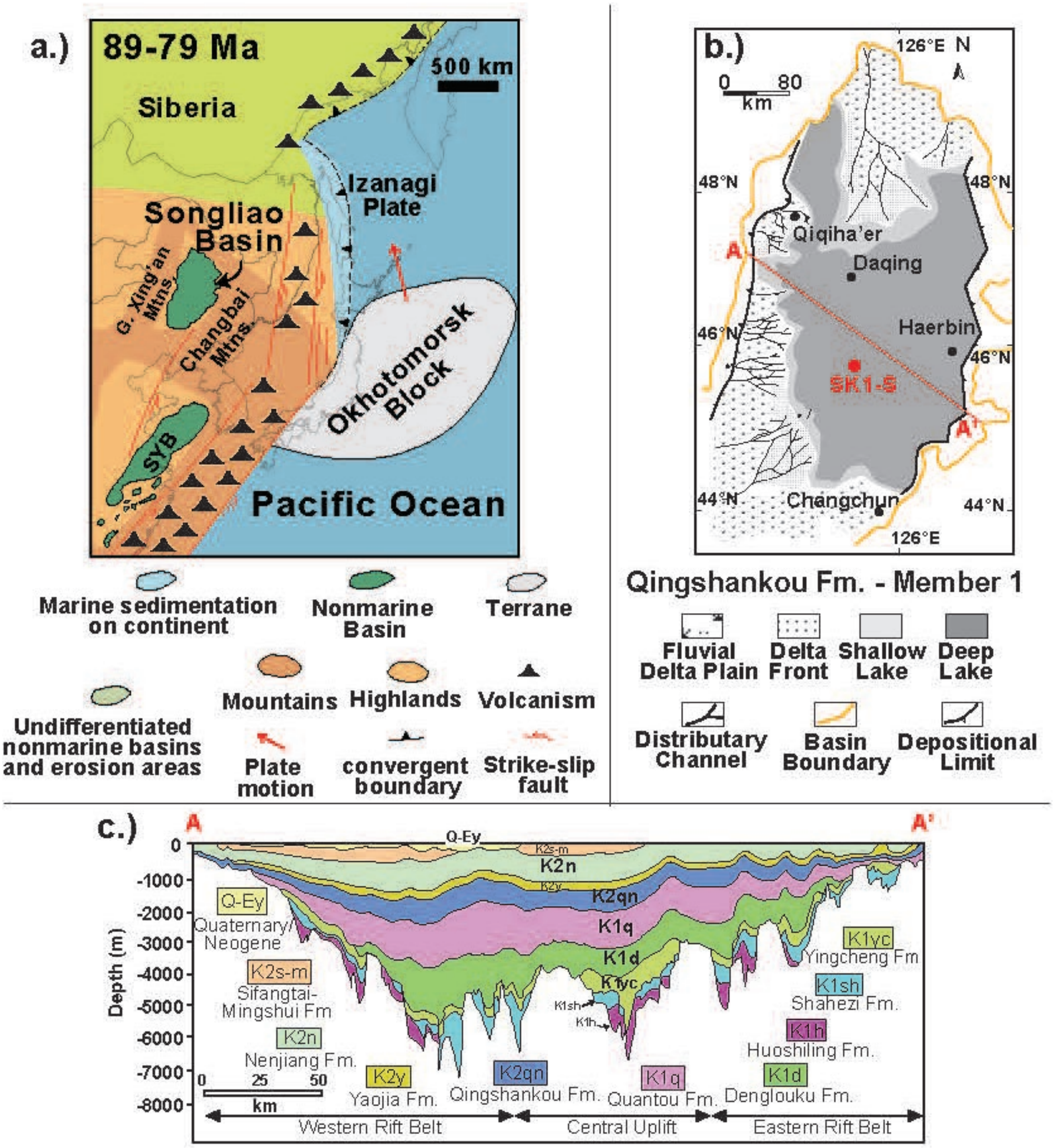

Figure 3.1 a.) Palinspastic map of East Asia during the Coniacian-E. Campanian, including the studied Songliao Basin and surrounding physical geographic and plate tectonic features (SYB = Subei–Yellow Sea Basin; modified from Yang, 2013). b.) Map of SK1-S core and facies during deposition of Qingshankou Member 1 (modified from Feng et al., 2010). c.) Cross section A–A' from Wang et al. (2013) depicting Cretaceous lithostratigraphic units of the Songliao Basin including the Qingshankou Formation (K2qn - purple).

(Wu et al., 2013) in the Turonian–Coniacian Qingshankou Formation, the stratigraphic focus of this study, provide precise temporal constraints (±181 kyr) necessary for global correlation and the interpretation of proxy data in the context of global climate events such as OAEs. The Qingshankou Formation is subdivided into the lower 93 m-thick organic-rich laminated mudstone in Member 1 (Gao et al., 2009) and the upper 395 m-thick undifferentiated grey shales of Members 2 and 3 (Wang et al., 2009).

3.3. Methods

3.3.1. Sampling and SK1-S timescale

We collected samples from SK1-S for this study at roughly 5–10 m spacing through the upper Quantou, Qingshankou, and lower Yaojia formations from the China University of Geosciences Beijing core repository. For all Qingshankou Formation samples analyzed, we assign numerical ages by anchoring the floating astronomical time scale from SK1-S (Wu et al., 2013) to a CA-ID-TIMS U/Pb zircon dated bentonite horizon (Ash S1705 m = 90.97 ± 0.12 Ma; Wang et al., 2016b) (Table A2.4). Considering radioisotopic and astrochronologic sources of uncertainty, we calculate ±181 kyr (2σ) precision for the anchored SK1-S time scale (see Text A2.4).

3.3.2. Carbon geochemistry

We measured samples collected from the SK1-S core for bulk organic carbon isotope ratios ($\delta^{13}C_{org}$), atomic carbon to nitrogen ratios (C/N), weight percent total organic carbon (TOC), and weight percent carbonate at Northwestern University (see Text A2.1). Additionally, we measured a sample set from the Angus core in the WIB for bulk carbonate carbon isotopes ($\delta^{13}C_{carb}$) to calculate $\Delta^{13}C$ ($\delta^{13}C_{carb}$–$\delta^{13}C_{org}$) to approximate changes in carbon isotope fractionation across OAE3 and compare to $\Delta^{13}C$ in the Songliao Basin (see Text A2.7).

3.3.3. X-ray fluorescence (XRF)

Methods outlined in the appendix (Text A2.2) are used to measure major and minor trace element concentrations of sample powders.

3.3.4. Initial osmium isotope analysis

To measure hydrogenous Os_i values, we analyzed ten samples from the Qingshankou Formation on a Thermo Scientific Triton thermal ionization mass spectrometer at Durham University via the established procedures of Selby and Creaser (2003) (see Text A2.3). We selected samples in Member 1 and lowermost Members 2 and 3 from horizons proposed to record biomarker evidence for marine incursions (Hu et al., 2015). Additionally, we analyzed samples from the Turonian-aged black shales of Site 1259 at Demerara Rise (Tropical North Atlantic ODP Leg 207) and Coniacian OAE3 interval in the Angus core from the WIB. We present these sample sets to characterize open and epicontinental marine Os_i values, respectively, for comparison with the coeval Qingshankou Formation record and to test the hypothesis of marine incursions into the Songliao Basin. To correct for post-depositional ^{187}Re decay to ^{187}Os (see Text A2.3), we assign numerical ages to samples using an age model at Demerara Rise (updated from Bornemann et al., 2008) and the existing Angus core (Joo and Sageman, 2014) and SK1-S age models (Sect. 3.3.1).

3.4. Results

3.4.1. Bulk carbon chemistry TOC, C/N trends

Weight percent TOC decreases upcore within the Qingshankou Formation from maximum values in the laminated Member 1, consistently above 2% and up to ~8% TOC, to values in Members 2 and 3 that rarely exceed 1% TOC. In TOC-rich Member 1, C/N ratios are elevated

(C/N = 8.5–25.6) above typical lacustrine algal values (C/N < 8; Meyers, 1994) (Figure 3.2; see Table A2.2). Occasionally, discrete horizons in Members 2 and 3 record elevated TOC spikes punctuating the background pattern of decaying TOC levels. These horizons are accompanied by increased C/N and enriched $\delta^{13}C_{org}$, with C/N (C/N = 15–25) approaching land-based vascular plant organic matter values (C/N > 25; Meyers, 1994) above the background lacustrine algal organic matter values. Additionally, new percent carbonate values are low, yet detectable throughout the studied interval (median = 6.9%, max = 22.5%) from scattered ostracods (Chamberlain et al., 2013; Wan et al., 2013).

3.4.2. Carbon isotopes

Bulk organic carbon isotope values in the studied interval are highly variable (−24 to −32.5‰) (Figure 3.2; Table A2.2). Some of this variability corresponds to changing facies, such as comparatively enriched $\delta^{13}C_{org}$ in fluvial facies of the Quantou and Yaojia Formations (generally $\delta^{13}C_{org} > -27$‰). However, lacustrine $\delta^{13}C_{org}$ values are also highly variable. Samples from Qingshankou Member 1 are strongly depleted in bulk $\delta^{13}C_{org}$, with an average value of −30.61‰ (1σ SD = ±1.33‰) and minimum of −32.4‰. Interestingly, the bulk $\delta^{13}C_{org}$ of Member 1 is more depleted than both average Cretaceous marine (−27 to −29‰) and terrestrial (−24 to −25‰) end members (Arthur et al., 1985). The $\delta^{13}C_{org}$ values of Members 2 and 3 are more enriched (median = −28.7‰). However, this interval preserves high $\delta^{13}C_{org}$ variability (1σ SD ± 1.5‰). A sustained positive carbon isotope excursion (+3.0 to +4.5‰) is noted in Members 2 and 3 (1380–1440 m) corresponding closely to the timing of OAE3 as recorded by a +1‰ CIE in the WIB (Joo and Sageman, 2014). Smoothed $\Delta^{13}C$ in SK1-S decreases up-core from the base of Member 1 from ~36‰ to ~31‰, and further decreases by ~−3‰ through OAE3. In the Angus core (WIB), smoothed $\Delta^{13}C$ records a similar but lower magnitude decrease (~−0.5‰) through OAE3 (Table A2.3). In that interval, $\delta^{13}C_{carb}$ is relatively stable (1σ SD ± 0.19‰) with average $\delta^{13}C_{carb}$ values (+1.84‰) comparable to coeval values in the English Chalk reference curve (Jarvis et al., 2006).

3.4.3. XRF data

Given that facies changes can significantly alter elemental chemistry of sediments, we limit discussion and interpretation of XRF data to the lacustrine facies of the Qingshankou Formation. Redox sensitive trace elements that accumulate in low oxygen conditions, such as Co, Cr, Ni, Pb, V, and Cu, show subtle to significant enrichment in the TOC-rich Qingshankou Member 1, whereas Mn, which remobilizes in anoxic environments, shows decreased concentrations (Figure 3.3). The V+ Cr concentrations, a trace element proxy for nitrate reduction and low O_2 (Sageman et al., 2014b), are significantly enriched in Member 1 (>200 ppm) above background values for the Qingshankou Formation (~150 ppm) (Figure 3.3). Copper concentrations spike at 1770 m and are strongly positively correlated with TOC ($r^2 = 0.87$) and C/N ($r^2 = 0.73$) in Member 1 ($n = 7$).

Several trace elements and elemental ratios serve as proxies for water column euxinia where free hydrogen sulfide, a product of sulfate reduction, is present (Figure 3.3) (Tribovillard et al., 2006). The V/(V+ Ni) values, a proxy for anoxia and euxinia (Hatch and Leventhal, 1992), average 0.68–0.74 in the Qingshankou Formation with enrichments in Member 1 (0.74–0.77). Throughout the Qingshankou Formation the V/(V+ Ni) ratios fall consistently into the non-sulfidic anoxic range. The concentrations of Mo, one of the most robust elemental indicators of euxinia, average 8 ppm (1σ SD ± 5 ppm, max [Mo] = 21.7 ppm) and show no notable increase in Qingshankou Member 1. Ratios of Mo/Al average 0.78×10^{-4} (1σ SD ± 0.48×10^{-4}) exceed average

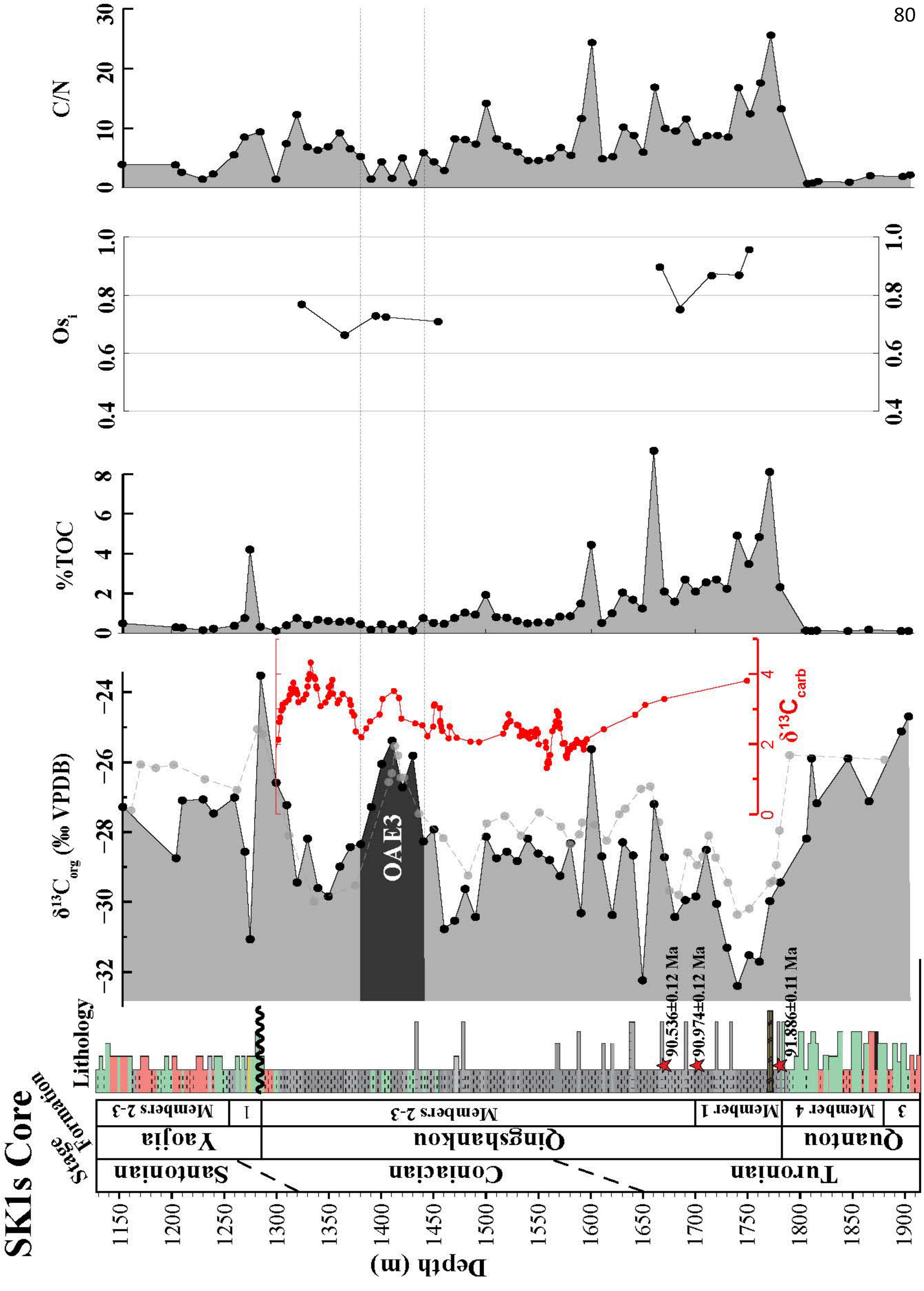
SK1s Core
Depth (m)
1150
1200
1250
1300
1350
1400
1450
1500
1550
1600
1650
1700
1750
1800
1850
1900
Stage
Formation
Lithology
Santonian
Coniacian
Turonian
Yaojia
Qingshankou
Quantou
Members 2-3
1
Members 2-3
Member 1
Member 4
3
90.536±0.12 Ma
90.974±0.12 Ma
91.886±0.11 Ma
δ13Corg (‰ VPDB)
−24
−26
−28
−30
−32
OAE3
δ13Ccarb
0
2
4
%TOC
0
2
4
6
8
Osi
0.4
0.6
0.8
1.0
C/N
0
10
20
30

Figure 3.2. (previous page) Chemostratigraphic record from SK1-S core spanning the upper Quantou through the Yaojia formations. Stratigraphic column modified from Wu et al. (2013). Red stars represent bentonite horizons with CA-ID-TIMS U/Pb zircon ages (Wang et al., 2016a, 2016b). Hiatus at the Qingshankou/Yaojia contact identified by Feng et al. (2010). The $\delta^{13}C_{carb}$ (red) data are from Chamberlain et al. (2013) and faded gray $\delta^{13}C_{org}$ values from Hu et al. (2015).

shale values (0.32×10^{-4}, Wedepohl, 1971) throughout most of the Qingshankou, suggesting authigenic enrichment. However, Mo/TOC is poorly correlated ($r^2 = 0.19$) and reaches a minimum in the TOC-rich Member 1. Despite high TOC, the S/Fe and Fe/Al ratios, which are known to increase with authigenic pyrite formation, do not increase in Member 1 (Figure 3.3). Also, we calculate the chemical index of alteration (CIA), which is a proxy for weathering intensity (Figure 3.3) (Nesbitt and Young, 1982). The carbonate corrected CIA is relatively stable throughout the Qingshankou Formation, although it does preserve a ~10% decrease during the OAE3 CIE, typically indicative of decreased weathering intensity.

3.4.4. Initial osmium isotope ratios

The Os_i from the Qingshankou Formation range between 0.66 and 0.96 (Figures 3.2 and 3.6). Osmium concentrations are similar through the interval (^{192}Os conc. = 7–17 ppt; Table A2.1). Rhenium concentrations are generally higher in Qingshankou Member 1 (avg. Re conc. = 3.80 ppb, 1σ SD ± 0.18 ppb) than in Members 2 and 3 (avg. Re conc. = 1.99 ppb, 1σ SD ± 1.66 ppb), except for one point at 1325 m (Table A2.1). The Os_i values are the most radiogenic through the TOC-rich mudstones in the Member 1 (avg. Os_i = 0.90, 1σ SD ± 0.05) (Figure 3.6). In the lowermost Members 2 and 3, one sample at ~1685m yields a slightly less radiogenic value (Os_i =0.76) compared to the samples below (Os_i = 0.87) and above (Os_i = 0.91). Relatively stable (Os_i range = 0.11) Os_i values from the upper sample set in Qingshankou Members 2 and 3 characterize

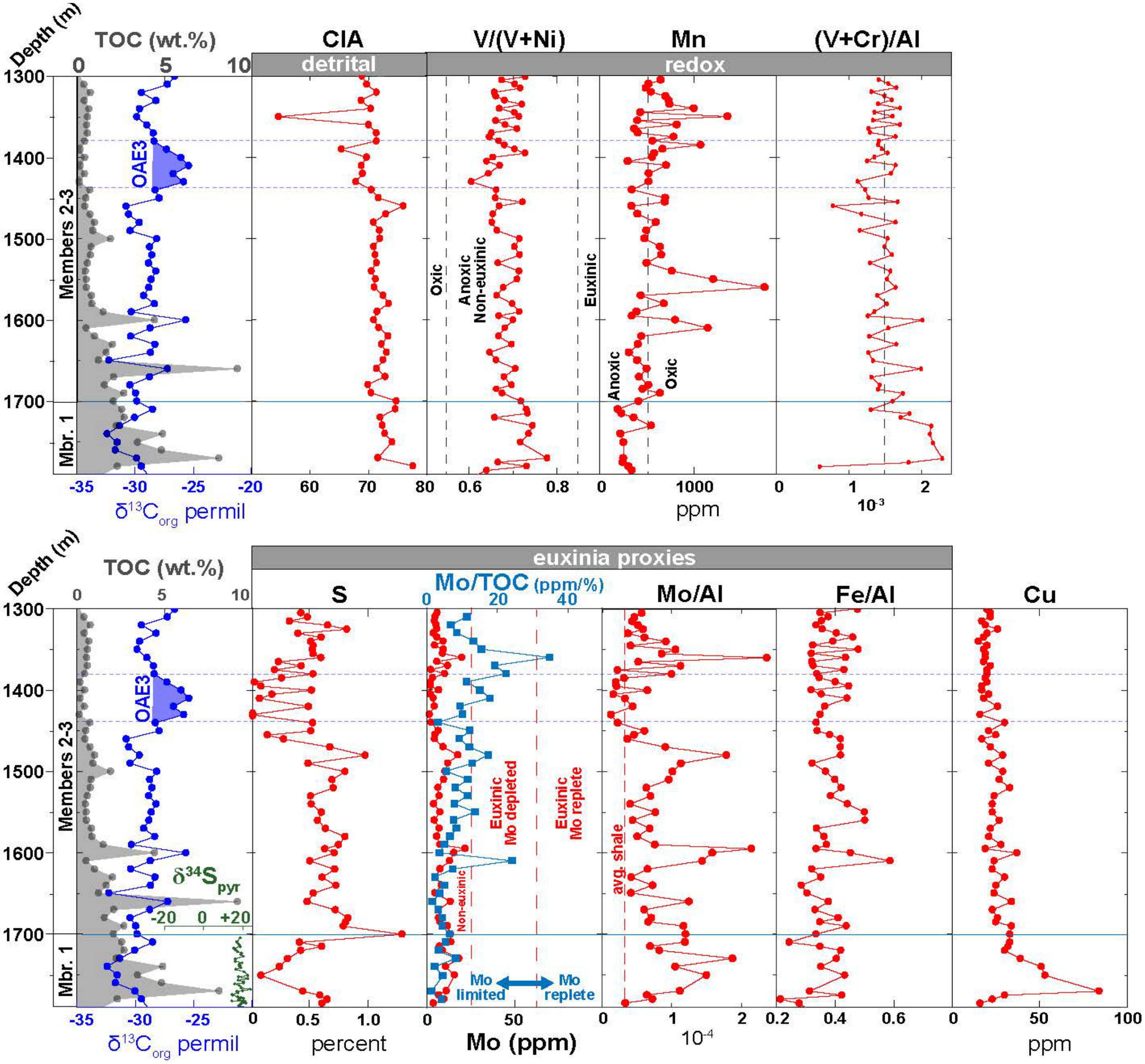
Depth (m)
TOC (wt.%)
0
5
10
1300
1400
1500
1600
1700
Members 2-3
Mbr. 1
OAE3
-35
-30
-25
-20
δ13Corg permil
CIA
detrital
60
70
80
V/(V+Ni)
redox
Oxic
Anoxic
Non-euxinic
Euxinic
0.6
0.8
Mn
Anoxic
Oxic
0
1000
ppm
(V+Cr)/Al
0
1
2
10-3
euxinia proxies
δ34Spyr
-20
0
+20
S
0
0.5
1.0
percent
Mo/TOC (ppm/%)
0
20
40
Non-euxinic
Euxinic
Mo depleted
Euxinic
Mo replete
Mo
limited
Mo
replete
0
50
Mo (ppm)
Mo/Al
avg. shale
0
1
2
10-4
Fe/Al
0.2
0.4
0.6
Cu
0
50
100
ppm

Figure 3.3. (previous page) Trace element concentration data from Qingshankou Member 1 and Qingshankou Members 2 and 3 in the SK1-S core. Detrital proxies include the chemical index of alteration (CIA). Redox thresholds for V/V+ Ni are from Hatch and Leventhal (1992). Dashed lines in Mn and V+ Cr plots represent median concentrations. $\delta^{34}S_{pyr}$ data are from Huang et al. (2013). Redox thresholds for Mo concentrations from Scott and Lyons (2012).

the SK1-S interval spanning OAE3. The Os_i values in this interval are slightly less radiogenic (avg. $Os_i = 0.72$) than in Qingshankou Member 1.

A time correlative open marine section from ODP Site 1259 at Demerara Rise, yields samples highly enriched in osmium (^{192}Os conc. = 31–366 ppt) and highly variable in rhenium concentrations (Re conc. range = 12–142 ppb) (Table A2.1). The Os_i values are more unradiogenic than values recorded in the Songliao Basin and are relatively stable over approximately 3 Myr, ranging between 0.55 and 0.71 (avg. $Os_i = 0.61$, 1σ SD ± 0.06) (Figures 3.2 and 3.6; Table A2.1). The Os_i samples from the marine WIB spanning OAE3 preserve no prominent excursion through the event ($Os_i = 0.54–0.58$) and are highly enriched in osmium (^{192}Os conc. = 136–260 ppt) and rhenium (Re conc. = 191–361 ppb).

3.5. Interpretation

3.5.1. Qingshankou Formation $\delta^{13}C_{org}$ chemostratigraphy and OAE3

Carbon isotope excursions have proven utility as isochronous horizons to correlate stratigraphic records globally (Jarvis et al., 2006; Wendler, 2013). However, a host of factors in a given sedimentary basin can alter bulk organic carbon isotopic ratios ($\delta^{13}C_{org}$) in addition to changes in the global carbon cycle, such as changing organic matter type and metabolic pathways. Our comparison of Gaussian kernel smoothed $\delta^{13}C_{org}$ records from the Songliao Basin and WIB (Joo and Sageman, 2014) demonstrates one negative CIE, possibly the Bridgewick Event (Jarvis et al., 2006), and one positive CIE, OAE3 (also referred to as the Whitefall/Kingsdown CIEs), which broadly correspond in age and duration (Figure 3.4). Despite similar CIE durations, we detect an offset of 330 kyr after cross-correlation of the two basins' anchored $\delta^{13}C_{org}$ time series, with ages of the Songliao Basin CIEs being older than ages of the WIB CIEs (Figure A2.5). This offset could arise from the presence of "reworked and/or detrital zircon" in radioisotopically dated samples of SK1-S (Wang et al., 2016b), or undetected Upper Turonian/Lower Coniacian hiatuses in SK1-S or the WIB (Sageman et al., 2014a). Although partially offset in age, we note that these CIEs overlap within temporal uncertainty of time scales in the Songliao Basin (±181 kyr, Sect. 3.3.1) and in the WIB (e.g., Turonian/Coniacian Boundary = ±380 kyr; Sageman et al., 2014a). Moreover, the similarity in the timing and duration of CIEs signifies agreement between East Asian and North American time scales, validating intercontinental comparison of geologic datasets (e.g., paleoclimatic, paleobiologic). We note that the CIEs are amplified in the lacustrine Songliao Basin (+3.0 to +4.5‰) compared to the marine WIB (~+1‰) (Joo and Sageman, 2014) and other marine $\delta^{13}C_{carb}$ records in the WIB (Tessin et al., 2015; this study) and elsewhere (Wagreich, 2012; Wendler, 2013, and references therein).

The identification of OAE3 within a lake system in the terrestrial Qingshankou Members 2 and 3 permits comparisons to marine records of the event aided by a highly resolved temporal framework. The lowest TOC levels in the Qingshankou Formation in SK1-S occur during OAE3 (Figure 3.2). This is also the case for OAE2, since the event is preserved in the TOC-lean Quantou Formation in SK1-S (Chamberlain et al., 2013). Accordingly, we confirm that OAEs do not necessarily correspond to lake anoxic events in East Asian lake systems (Wu et al., 2013), and that these lakes were not significant organic carbon depocenters during OAEs. We infer that during

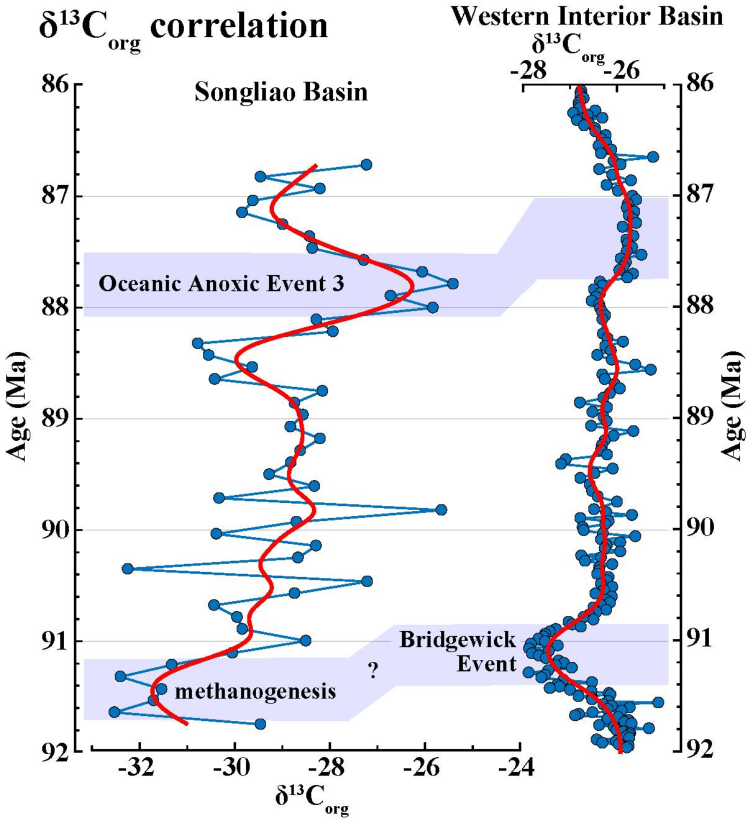

Figure 3.4. Correlation of $\delta^{13}C_{org}$ time series from the Songliao Basin (this study) and Western Interior Basin (N. America) (Joo and Sageman, 2014). Red lines represent Gaussian kernel smoothed $\delta^{13}C_{org}$ values ($\sigma = \pm150$ kyr). The Songliao time scale derived from astronomical time scale (Wu et al., 2013) anchored to a U/Pb zircon age date (Wang et al., 2016a; 2016b) (Sect. 3.3.1 and Text A2.4).

OAE3, reduced primary productivity and/or enhanced bottom-water oxygenation through regular lake overturning, in response to climatic forcing, played a role in decreasing organic carbon preservation.

In both SK1-S and the WIB, $\delta^{13}C_{org}$ enrichment and a diminutive excursion in $\delta^{13}C_{carb}$ (Figure 3.2) (ostracod – Chamberlain et al., 2013) across OAE3 controls a decrease in $\Delta^{13}C$ (Figure 3.5). In SK1-S, this $\delta^{13}C_{org}$ excursion is not likely due to changing organic matter source given consistently low C/N. Another coeval $\Delta^{13}C$ record from the Portland core (Colorado) in the WIB with variable organic matter type has been interpreted as diagenetically altered (Tessin et al., 2015). However, there is little evidence for $\delta^{13}C_{org}$ or $\delta^{13}C_{carb}$ diagenesis in the Angus core in the OAE3 interval (Figures A2.2-A2.3). Therefore, we attribute the OAE3 $\delta^{13}C_{org}$ excursion and decreased $\Delta^{13}C$ to diminished fractionation between dissolved inorganic carbon and photosynthate, driven by decreased dissolved CO_2 levels (Kump and Arthur, 1999). In the marine record, this is consistent with atmospheric pCO_2 drawdown commensurate with organic carbon sequestration in marine shales globally, as has been inferred for OAE2 (e.g., Jarvis et al., 2011).

However, lacustrine pCO_2 proxies (i.e., $\Delta^{13}C$) cannot be interpreted as direct records of atmospheric pCO_2 since modern large lakes analogous to the depositional environment of the Qingshankou Formation are net sources of CO_2 to the atmosphere, such as the East African rift lakes (Alin and Johnson, 2007). Over longer time periods, riverine inputs of dissolved CO_2 are the primary control on modern lacustrine CO_2 levels in mid-latitude lakes, and vary as a function of soil pCO_2 and catchment productivity (Maberly et al., 2013). The sedimentary geochemistry of modern and Lower Cretaceous rift lakes in Africa record these landscape processes as well (Harris et al., 2004; Talbot et al., 2006), since dissolved CO_2 levels exert a significant control on carbon isotope fractionation in lakes (Hollander and Smith, 2001). During OAE3, the Songliao lake system preserves a comparatively larger shift in $\delta^{13}C_{org}$ and $\Delta^{13}C$ than the WIB (Figure 3.5). We attribute this to a greater decrease in dissolved CO_2 in the Songliao lake system, driven by reduced soil productivity in the basin's catchment through OAE3. This is consistent with a scenario of atmospheric pCO_2 drawdown and cooling reflected in decreased marine $\Delta^{13}C$ in the WIB.

Compared to OAE2, pCO_2 drawdown through OAE3 is interesting since the event is not represented by a discrete archetypal black shale or anoxic/euxinic interval (Wagreich, 2012;

Lowery et al., 2017a) and preserves a relatively diminished marine CIE (Jarvis et al., 2006; Locklair et al., 2011; Joo and Sageman, 2014). One mechanism for sustaining an OAE invokes enhanced weathering of continentally derived nutrients (e.g., P), following volcanic CO_2 pulses from large igneous province (LIPs) emplacement (Jenkyns, 2010). However, marine Os_i values spanning OAE3 in the WIB do not record evidence for submarine LIP volcanism (i.e., unradiogenic Os_i shift) (Figure 3.6; Sect. 3.5.3), as is the case for OAE2 (Turgeon and Creaser, 2008; Du Vivier et al., 2014); nor do they record evidence for accelerated global continental weathering rates (i.e., a shift to more radiogenic Os_i). Likewise, weathering proxies from the Songliao Basin's OAE3 interval are either stable, such as Os_i (Figures 3.2 and 3.6), or suggest a decrease in weathering intensity, such as $\Delta^{13}C$ (Figure 3.4) and CIA (Figure 3.3). Although we caution that these local observations are of a relatively minor OAE and cannot be assumed globally representative, these results suggest that the perturbations to the Earth system that triggered and sustained OAE3 are unique from those that triggered more severe OAEs (e.g., OAE2, Toarcian OAE).

Overall, the Qingshankou Formation $\delta^{13}C_{org}$ chemostratigraphy is highly variable through Member 1 and the lowermost Members 2 and 3. This suggests that dynamic local biogeochemical cycling and environmental conditions, in addition to the global carbon cycle, affected the $\delta^{13}C_{org}$ values in this interval (Figure 3.2). Furthermore, we interpret the combination of highly depleted $\delta^{13}C_{org}$ values (−32.4‰ minimum), high C/N typical of nitrogen-poor anoxic bottom-waters (Meyers, 1994), and redox-sensitive XRF data (Sect. 3.5.2), as evidence that methanogenesis and methanotrophy (Hollander and Smith, 2001) influenced bulk $\delta^{13}C_{org}$ values in the TOC-rich Qingshankou Member 1. Extremely $\delta^{13}C$ depleted methyl hopane compounds (−42 to −50‰) in Member 1 equivalent oil shales from the Ngn-02 core (Bechtel et al., 2012) confirm the role of

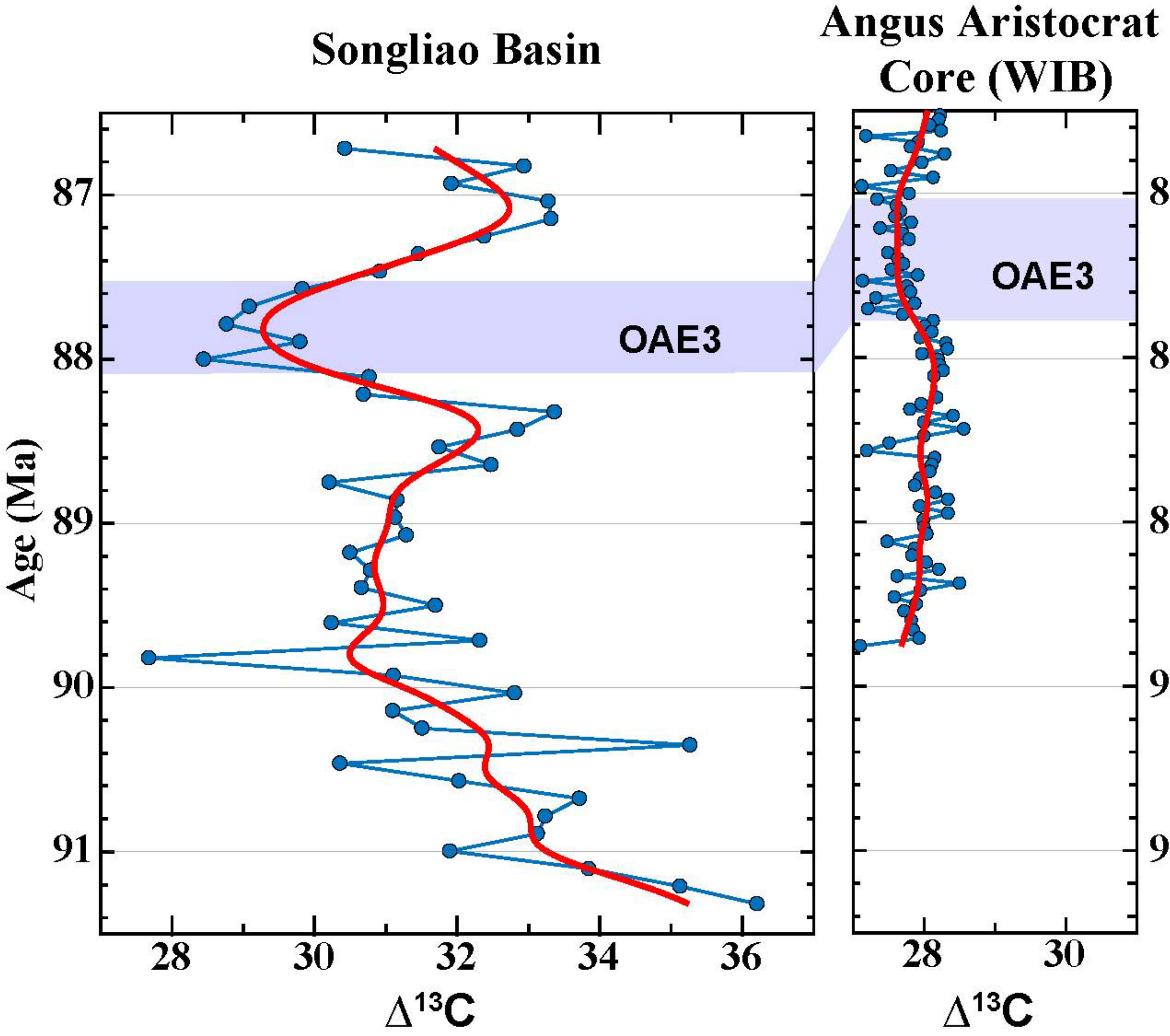

Figure 3.5. Record of $\Delta^{13}C$ ($\delta^{13}C_{carb}$–$\delta^{13}C_{org}$) changes, approximating carbon isotope fractionation across OAE3 in the Songliao Basin and Western Interior Basin (WIB) of North America. Red lines represent Gaussian kernel smoothed $\Delta^{13}C$ values (σ = ±150 kyr).

methanotrophy in the unit. As a result, we cannot solely attribute the depleted $\delta^{13}C_{org}$ in Member 1 to the global Bridgewick CIE, and instead we interpret this interval as at least partially recording burial of lacustrine methanotrophic biomass. Increased dissolved CO_2 in the lake from increased catchment productivity may have also contributed to the amplified negative CIE in Member 1 (Hu et al., 2015).

3.5.2. Low sulfate and redox conditions in lacustrine Qingshankou Formation

The redox sensitive trace element dataset from Qingshankou Member 1 (Sect. 3.4.3) provides a record of non-euxinic anoxic bottom-waters during deposition. Consistent trends among a variety of the evaluated trace element proxies lend confidence to the paleo-redox reconstructions. Combined, low Mn (<400 ppm), elevated V+Cr (>200 ppm) and (V+Cr)/Al, and elevated V/(V+Ni) (>0.7, Hatch and Leventhal, 1992) in Member 1 indicate anoxia (Figure 3.3).

Compared to the marine realm, biogeochemical cycling in anoxic lakes typically operates with fundamentally different dominant microbial pathways (e.g., methanogenesis and methanotrophy), since lakes generally have much lower concentrations of dissolved sulfate and redox-sensitive trace elements such as molybdenum. Microbial sulfate reduction (MSR) in anoxic low sulfate lakes tends to draw down the sulfate reservoir and limit sulfur isotope fractionation leaving pyrite isotopic values enriched (Gomes and Hurtgen, 2013). In Qingshankou Member 1, $\delta^{34}S_{pyrite}$ is highly enriched (+15 to +20‰) (Figure 3.3) (Huang et al., 2013). Huang et al. (2013) attributed this to a complex disproportionation and transport model dependent on isotopic heterogeneity within the basin. However, considering our new trace element data, we propose an alternative interpretation, namely that the enriched $\delta^{34}S_{pyr}$ values were consequences of inhibited MSR fractionation related to low sulfate concentrations under non-marine depositional conditions. This phenomenon is noted in Holocene non-marine Black Sea mudstones (≤8 kyr) deposited during basin isolation from the global ocean (Calvert et al., 1996). In another test of sulfate levels and seawater connectivity, TOC/S ratios are generally <2.8 in marine sediments (Berner, 1982), although some lacustrine mudstone values fall below this threshold (e.g., Calvert et al., 1996). In Qingshankou Member 1, TOC/S ratios all exceed this threshold (average TOC/S = 14; this study) and are consistent with pyrite burial limited by low sulfate levels (Bechtel et al., 2012).

Concentrations of molybdenum (avg. = 8 ppm), another robust proxy for the presence of free sulfide, remain below minimum thresholds established for euxinic mudstones (25 ppm Mo-depleted waters, 65 ppm Mo-replete waters, Scott and Lyons, 2012), but molybdenum concentrations and Mo/Al values do exceed average shale values (2.6 ppm and 0.32×10^{-4} respectively, Wedepohl, 1971), suggesting MSR was active, but limited by low sulfate and molybdate concentrations in the lake (Figure 3.3). In Mo-replete marine waters, sedimentary Mo concentrations positively correlate with TOC (Algeo and Lyons, 2006). However, this relationship is not observed in the Qingshankou Formation ($r^2 = 0.19$) and Mo/TOC ratios are lowest in the TOC-rich Member 1 (Figure 3.3) (Sect. 3.4.3). Influxes of sulfate and molybdenum-replete marine water would have elevated MSR and corresponding pyrite burial, leading to increases in Fe/Al, Mo/TOC, and S concentrations. Our proxy results from SK1-S do not record such shifts, and we therefore infer that low sulfate non-marine conditions prevailed throughout deposition of the Qingshankou Formation.

Depleted bulk $\delta^{13}C_{org}$ (this study; Hu et al., 2015) and methyl hopane $\delta^{13}C$ values (Bechtel et al., 2012) reinforce the hypothesis that sulfate reduction was limited and that methanogenic and methanotrophic microbial metabolisms were prevalent during deposition of Qingshankou Member 1 (Sect. 3.5.1). Additionally, concentrations of certain trace elements, such as Cu, Ni, Co, that play central roles in enzymes facilitating methanogenesis and methanotrophy (Glass and Orphan, 2012), spike in Member 1. This may indicate enhanced methanogenesis and methanotrophy in the anoxic lacustrine mudstones (Figure 3.3). Alternatively, it could reflect that metals are complexed with organic matter independent of methantrophic activity in Member 1 (TOC and Cu covariance: $r^2 = 0.88$). Regardless, proxies such as elemental concentrations, methanotrophic biomarkers, sulfur isotopes, laminated mudstones, and bulk $\delta^{13}C_{org}$, consistently indicate persistent anoxia and methanogenesis in low sulfate waters (i.e., MSR inhibited) during deposition of the TOC-rich Qingshankou Member 1.

3.5.3. Seawater incursion hypothesis and Os_i chemostratigraphy

Incursions of dense marine water into the Songliao Basin during sea level highstands have been invoked as a mechanism to stratify the basin's water column, intensifying bottom-water anoxia, and ultimately driving deposition of Member 1's TOC-rich source rocks (Hou et al., 2000; Huang et al., 2013; Hu et al., 2015). Mixing of marine and lacustrine water bodies, each with distinct chemical properties, would perturb the chemostratigraphic record, including Os_i values. However, our Os_i chemostratigraphy from SK1-S preserves no compelling evidence for marine incursions in TOC-rich intervals. Instead, the Os_i data in Member 1 are consistently the most radiogenic values of SK1-S (Figure 3.6). We conclude that this observation is inconsistent with incursions of less radiogenic open marine osmium as measured at Demerara Rise, and resembles the more radiogenic Os_i records existing from lacustrine mudstones elsewhere (Poirier and Hillaire-Marcel, 2011; Cumming et al., 2012; Xu et al., 2017). At Demerara Rise, an average open marine Os_i of ~0.6 for mid-Turonian to Coniacian samples is considered to be the best estimate of the steady-state open marine value for the Late Cretaceous governed by plate tectonic configurations (i.e., long-term average continental weathering and hydrothermal fluxes) given similar results from comparably aged marine records, such as post-OAE2 (Du Vivier et al., 2014) and our new WIB OAE3 data (Figure 3.6). However, we note that the WIB Os_i data is likely more radiogenic than open marine Os_i, due to the marine basin's epicontinental setting and mixing with continentally derived osmium.

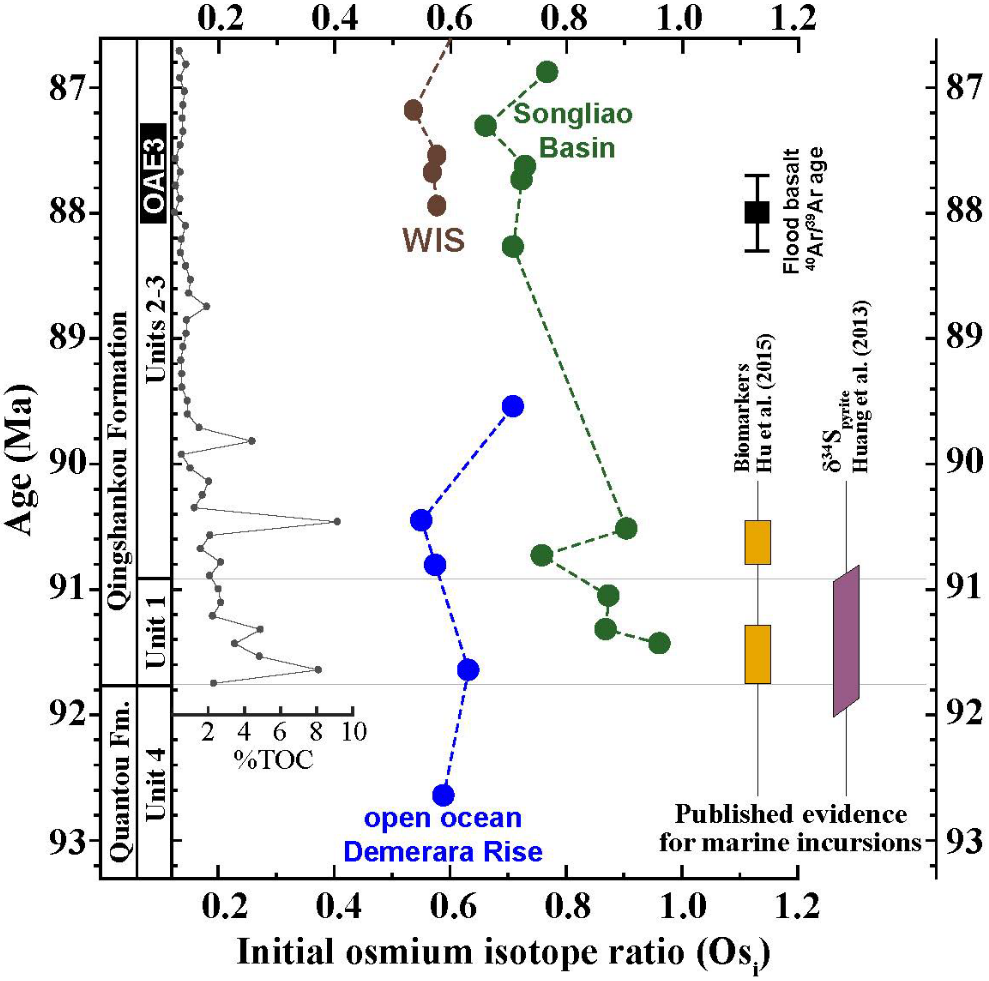

Figure 3.6. Comparison of Os_i time series from the Songliao Basin SK1-S (green) and Demerara Rise ODP Site 1259 (blue). Time scales from Songliao Basin (Wu et al., 2013; Wang et al., 2016a; 2016b), Demerara Rise (Jones et al., 2018a; Chapter 2), and WIB (Joo and Sageman, 2014). Flood basalt emplacement in black (Wang et al., 2016a). Previously cited evidence for the Qingshankou Formation marine incursions in yellow shaded intervals for presence of marine biomarkers (Hu et al., 2015) and purple interval of $\delta^{34}S_{pyr}$ data (Huang et al., 2013).

One Os_i data point (1685 m) in the lower Songliao Os_i sample set is less radiogenic than other nearby horizons. This is also an interval where concentrations of 24-n-isopropylchlorestane spike (biomarker typically attributed to marine organisms, Hu et al., 2015) and XRF sulfur concentrations more than double for one data point. It is possible that this horizon indicates a minor seawater incursion. However, we consider that this is unlikely since the horizon is not associated with any spikes in euxinic-sensitive trace elements (e.g., Mo, V/V +Ni, Sect. 3.5.2) (Figure 3.3), TOC enrichments, or changes in lithology, and due to additional paleogeographic factors discussed below.

Our trace element and Os_i evidence contrary to a Songliao Basin-marine connection during deposition of Qingshankou Member 1 is consistent with many lines of previous observation such as: a lack of foraminifera, calcareous nannofossil, or marine macro-fossil preservation in the Qingshankou Formation of SK1-S (Wan et al., 2013; Xi et al., 2016), non-marine phytoplankton (Zhao et al., 2014), depleted non-marine $\delta^{18}O$ values (Chamberlain et al., 2013), plate tectonic reconstructions placing the nearest marine body at least 500 km away, and evidence for coastal mountain building between the Songliao Basin and Pacific Ocean (Yang, 2013) (Figure 3.1). Contrastingly, observations of $\delta^{34}S_{pyr}$ (Huang et al., 2013) and biomarkers (C_{30} steranes e.g., 24-isopropylchlorestane, Hu et al., 2015) have been interpreted as evidence for marine incursions. Additionally, a few poorly preserved foraminifera have been reported in Member 1 elsewhere in the basin (Xi et al., 2016), although no photographs or depths of occurrence are accessible to our knowledge, precluding verification, taxonomic identification, and correlation to horizons in the SK1-S core. It is possible to reconcile our geochemical datasets with enriched $\delta^{34}S_{pyr}$ data in Member 1 if a low sulfate lake water column inhibited sulfur isotope fractionation (Sect. 3.5.2). Explaining the presence of 24-n-isopropylchlorestane without invoking seawater incursions is more challenging, because the biomarker has been classified as an indicator of marine organic matter (Moldowan et al., 1990). However, we note that C_{30} steranes, including molecular precursors to 24-isopropylcholestane, have been detected in a modern French lake (Wunsche et al., 1987). If the biomarkers previously reported from the Songliao Basin (Hu et al., 2015) are instead derived from non-marine dinoflagellates, sponges or microbial symbionts producing C_{30} sterols, are detritally re-worked, or are the molecular diagenetic products of organic matter degradation in a thermally mature interval of the basin (cf. Feng et al., 2010), then their occurrences would be consistent with our interpretation of the Os_i record as that of an isolated lacustrine basin.

Alternatively, our Os_i record from the Songliao Basin could have been dominated by a high flux of continentally derived radiogenic Os_i from nearby catchments, masking a record of seawater incursions via mixing. A recent study of Holocene Os_i profiles in a transect off Greenland's coast demonstrated that Os_i records can be sensitive to local fluxes of weathered osmium (Rooney et al., 2016). However, we consider that this masking scenario is less likely in the Songliao Basin, since Members 2 and 3 lack evidence for marine incursions, but do not show evidence for extremely radiogenic Os_i values within the weathered catchments (Figure 3.6). Additionally, two strontium isotope measurements in the lower Qingshankou Formation (avg. $^{87}Sr/^{86}Sr = 0.70767$, 1σ SD ± 0.00005) are not extremely radiogenic, but are offset from coeval marine ratios (Chamberlain et al., 2013). Their values do not preserve evidence for marine incursions, nor do they indicate weathering of extremely radiogenic lithologies within the basin's catchment. This suggests that Os_i chemostratigraphy could resolve evidence of marine incursions if present. We note that it is possible that a brief marine incursion occurred in an unsampled interval, as temporal resolution of Os_i samples range from 100–300 kyr in Member 1. However, we selected samples from horizons with published proposed evidence (i.e., biomarker) for marine incursions (Figure 3.6). Additionally, we observe no abrupt lithologic alterations in SK1-S commonly associated with lacustrine-marine transitions in other basins (Calvert et al., 1996; Poirier and Hillaire-Marcel, 2011 and references therein).

In the younger OAE3 interval of Qingshankou Members 2 and 3, the Os_i data are less radiogenic, and approach values from the epicontinental marine WIB (Figure 3.6). Again, we do not interpret these data as evidence for a prolonged marine connection to the Songliao Basin, because little evidence exists of marine microfossils (Xi et al., 2016) or sulfate replete waters (Sect. 3.5.2; Figure 3.3) in this interval. Instead, we attribute the lower Os_i values in Qingshankou Members 2 and 3 to the weathering of the near contemporaneous mid-Coniacian flood basalts within the Songliao Basin (Wang et al., 2016a), which would possess mantle-like $^{187}Os/^{188}Os$ compositions (~0.13) mixing with lake waters (Figure 3.6). We also note that Os_i values are relatively stable through OAE3, suggesting muted changes in the weathering flux of osmium (Sect. 3.5.1).

3.5.4. Qingshankou Formation depositional model

Given limited evidence for incursions of saline marine waters in Member 1 (Sects. 3.5.2–3.5.3), we propose alternative mechanisms for lake stratification that could be responsible for enhanced anoxia (Sects. 3.5.1–3.5.2) and resulting enhanced organic matter burial. Based on modern and paleo analogs, we outline a new conceptual model characterizing bottom-water redox, biogeochemical cycling, and physical processes (stratification, mixing) for the lacustrine Songliao rift basin through the Qingshankou Formation interval (Figure 3.7). Sustained stratification of large meromictic lakes is critical in generating TOC-rich mudstone deposits, as settling organic matter from highly productive lacustrine surface waters is remineralized passing through isolated and progressively deoxygenated bottom-waters (Demaison and Moore, 1980). For any scenario of bottom-water anoxia, the depth of the stratified lake would need to exceed the wave-base mixing depth. This considerable minimum depth (e.g., ~100 m) on a large paleolake with an expansive fetch (~200–300 km) for generating waves, supports the assertion that the lake was deeper and more expansive during Member 1 than Members 2–3 (Feng et al., 2010), favoring meromixis within a deep lake.

Water column density stratification likely arose in Qingshankou Member 1 from gradients in temperature, salinity, temperature, and/or dissolved gases from organic matter remineralization (e.g., Boehrer and Schultze, 2008), inhibiting lake overturning and reoxygenation of bottom-waters (Figure 3.7). In the case of thermal stratification, most modern meromictic lakes do not occur outside the tropics (e.g., Lake Tanganyika), and are reinforced by additional density gradients. However, the mid-Cretaceous was a period of extreme greenhouse warmth. Intervals of high temperature and low seasonality (i.e., obliquity minima) would have inhibited the Songliao Basin water column overturning and reduced dissolved oxygen levels, and indeed palynological datasets indicate a semi-humid sub-tropical climate during deposition of Member 1 (Wang et al., 2013; Zhao et al., 2014). Although additional paleoclimate data are necessary to fully test this hypothesis, our idea that elevated temperatures would have inhibited lake overturning is consistent with general reconstructions for the warm mid-Cretaceous. Even though we do not detect seawater incursions in this study and no evaporites are associated with Member 1, evidence for elevated salinity is inferred from paleontological investigations that have documented slightly brackish algae, dinoflagellate, and ostracod assemblages (Zhao et al., 2014; Xi et al., 2016). Organic geochemical investigations have also detected salinity biomarkers (e.g., gammacerane, β-carotane) in Member 1 (Bechtel et al., 2012). Several ostracod $\delta^{18}O$ and $\delta^{13}C_{carb}$ values are enriched in Member 1 and lowermost Members 2 and 3 compared to overlying samples (Chamberlain et al., 2013), possibly related to enhanced evaporation rates and consistent with dolomite laminae preservation in the interval (Talbot, 1990; Gao et al., 2009; Wang et al., 2009). Further, authors interpret covariation between $\delta^{18}O$, $\delta^{13}C_{carb}$, Mg/Ca, and Sr/Ca as evidence for closed basin conditions throughout the Qingshankou Formation, signifying a lake basin sensitive to changing precipitation to evaporation (P/E) rates (Chamberlain et al., 2013). On the other hand, palynology suggests the climate was semi-humid during Member 1 (Wang et al., 2013) which would have limited evaporation and salinity's role in density stratification, although others report that diagenesis possibly biased palynological reconstructions (Zhao et al., 2014). A final process that we suspect contributed to elevated bottom-water density in Lake Songliao is the addition of dissolved biochemical products (e.g., HCO^{-3}, H_2S, CH_4, etc.) from remineralization of organic matter (Figure 3.7a). Evidence for methanogenesis, as well as heterotrophic biomarkers (e.g., hopanoids) (Bechtel et al., 2012), indicate microbial reworking of biomass in Member 1. This is consistent with increased bottom-water density via "biogenic meromixis", stratification from dissolved biochemical products (Boehrer and Schultze, 2008). Our combined model for Lake Songliao's stratification draws on many physical and geochemical processes, such as temperature gradients, biogenic meromixis, and elevated salinity. We hypothesize that these processes were controlled both by tectonic (i.e., lake depth) and climatic (e.g., P/E) conditions that contributed to a stagnant pool of anoxic bottom-water conducive to deposition of TOC-rich mudstones.

Conversely in Members 2 and 3, we propose that TOC-lean grey mudstones were the result of enhanced water column overturning and improved oxygenation of lake bottom-waters. During OAE3, the interval of lowest TOC in the Qingshankou Formation, factors such as, increased seasonality, freshening of bottom-waters, more vigorous wave mixing (i.e., higher surface wind velocity), and/or lake shallowing likely contributed to bottom-water reoxygenation and the demise of stratification (Figure 3.7b).

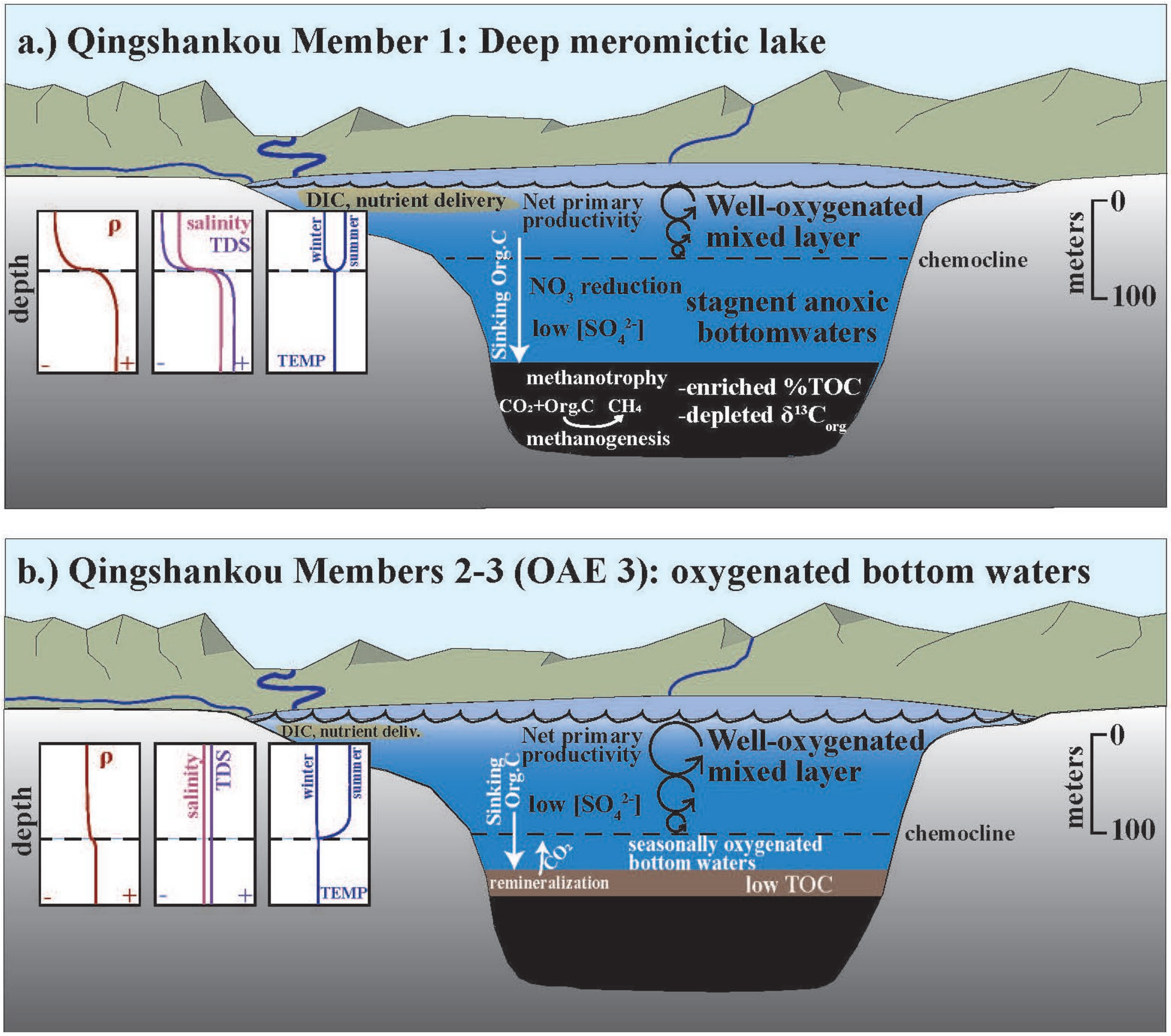

Figure 3.7. a.) Non-marine biogeochemical and depositional model of Qingshankou Member 1 also depicting theoretical plots of density (ρ), salinity, total dissolved substances (TDS), and winter and summer water temperature profiles. **b.)** Biogeochemical cycling and depositional model for Qingshankou Members 2 and 3 during OAE3 interval. See text for discussion.

3.6. Conclusions

Through geochemical analyses, we reconstruct local Late Cretaceous paleoclimate records and lacustrine carbon burial dynamics of the Qingshankou Formation in the Songliao Basin of northeast China. Correlation of Turonian–Coniacian $\delta^{13}C_{org}$ records from the Songliao Basin to the WIB confirms the presence of OAE3 in a low-TOC interval of Qingshankou Members 2 and

3, providing a unique record of the event in a lake system. The chemostratigraphic results from the Songliao Basin demonstrate that OAE2 and OAE3 did not trigger elevated organic carbon burial in an expansive East Asian lake. Furthermore, we attribute significant decreases in marine and lacustrine $\Delta^{13}C$ to a drawdown of pCO_2 and cooling through OAE3 and decreased soil productivity in the Songliao catchment. This finding is consistent with enhanced burial of organic carbon on a global scale and is analogous to interpretations for other prominent Cretaceous OAEs (Arthur et al., 1988; Barclay et al., 2010; Jarvis et al., 2011). However, Os_i stratigraphy records no evidence for significant changes in global volcanism though OAE3, which suggests an event trigger unique from OAE2 (i.e., LIP volcanism). We encourage future investigations, employing, for example, compound specific $\delta^{13}C$ chemostratigraphy and high-resolution paleoclimate proxies, to further resolve the robustness of $\delta^{13}C$ correlations and better elucidate the paleoclimatic response of the Songliao basin lacustrine units to OAE3.

Radiogenic Os_i values recorded through the TOC-rich Qingshankou Member 1 indicate that enhanced organic carbon burial and source rock formation occurred in a lacustrine basin isolated from the global ocean. Although our Os_i sample resolution is limited and marine incursions could have alluded detection in this initial survey, our higher resolution redox sensitive trace element data, as well as most existing paleogeographic, chemostratigraphic, and paleobiologic data, are also consistent with mudstone deposition in a low sulfate, lacustrine setting through Member 1. Our synthesis of existing stratigraphic datasets into a source rock depositional model for Qingshankou Member 1 outlines lacustrine stratification and biogeochemical cycling scenarios independent of marine incursions. This study underscores the potential to reconstruct Late Cretaceous paleoclimate, lake system responses to OAEs, and terrestrial carbon burial dynamics from lacustrine mudstone archives, such as those found in the Songliao Basin.

CHAPTER 4

Astronomical Pacing of Relative Sea Level during Oceanic Anoxic Event 2 from the Expanded SH#1 Core, Utah

Motivation: The SH#1 core was drilled in southern Utah in 2014 as part of an NSF-funded Earth Life-Transition project to better understand how paleo-environmental change across the Cenomanian-Turonian Boundary resulted in accelerated faunal turnover. Augmented by records from nearby outcrops, the core recovered a relatively continuous, expanded, and fossiliferous calcareous shale succession of OAE2 from the proximal western paleo-shoreline of the WIS.

Key findings:

- A $\delta^{13}C$ chemostratigraphy of the SH#1 core from the Kaiparowits Plateau (Utah) preserves the most expanded record of Oceanic Anoxic Event 2 (OAE2) from the central WIB;
- Horizons with relatively higher alteration of carbonate in proximal calcareous shales correspond to sequence stratigraphic surfaces (e.g., flooding surfaces), enabling reconstruction of relative sea level from proxies sensitive to diagenesis (i.e., $\delta^{13}C_{carb,}$ $\delta^{18}O_{carb}$);
- The $\delta^{13}C_{carb}$ chemostratigraphy in SH#1 records a dominant astronomical pacing of relative sea level, indicating terrestrial paleoclimate feedbacks to short eccentricity forcing drove sea level oscillations during OAE2, and potentially longer time intervals in the mid-Cretaceous greenhouse.

Note - A version of this work has been accepted for publication as:

Jones, M. M., Sageman B. B., Oakes R. L., Bralower T. J., Leckie R. M., Parker A. L., Sepúlveda, J., Fortiz, V., (in press), Astronomical Pacing of Relative Sea Level during Oceanic Anoxic Event 2: Preliminary Studies of the Expanded SH#1 Core, Utah, *GSA Bulletin*

CHAPTER 4

Astronomical Pacing of Relative Sea Level during Oceanic Anoxic Event 2 from the Expanded SH#1 Core, Utah

Abstract

Proximal marine strata of the North American Western Interior Basin (WIB) preserve a rich record of biotic turnover during Oceanic Anoxic Event 2 (OAE2 – 94 Ma), a pronounced Late Cretaceous carbon cycle perturbation interpreted to reflect global warming, widespread hypoxia, and possible ocean acidification. To develop a more robust synthesis of paleobiologic and geochemical datasets spanning this Earth-life transition, we drilled a 131-meter core (SH#1) on the Kaiparowits Plateau of southern Utah, recovering the Cenomanian-Turonian Boundary (CTB) interval in the Tropic Shale. A 17.5-meter positive excursion in high-resolution bulk carbon isotope chemostratigraphy ($\delta^{13}C_{org}$) of SH#1 characterizes the most expanded OAE2 record recovered from the central WIB.

Depleted values in a paired carbonate carbon isotope ($\delta^{13}C_{carb}$) chemostratigraphy cyclically punctuate the OAE2 excursion. These depletions correspond to intervals in the core with a higher degree of carbonate diagenesis and correlate well to an existing sequence stratigraphic framework of flooding surfaces in the shoreface facies of the Markagunt Plateau (~100 km west). We detect statistically significant evidence for astronomical cycles in the $\delta^{13}C_{carb}$ dataset, imparted by diagenesis at flooding surfaces, and develop a floating astronomical time scale (ATS) for the study interval. Stable eccentricity cycles (405 kyr) align with stratigraphic sequences and associated trends in sedimentation rate, and short eccentricity cycles (~100 kyr) pace nested parasequences. These results confirm an astronomical signal and, therefore, climatic forcing of

relative sea level during OAE2 in the WIB. Furthermore, cross-basin correlation of the ATS and expanded $\delta^{13}C$ chemostratigraphy of SH#1 suggests that these transgressive-regressive parasequences modulated siliciclastic sediment delivery in the seaway and contributed to deposition of prominent rhythmically-bedded CTB units across the WIB, including the Bridge Creek Limestone. The presented approach to analysis of these proximal offshore siliciclastic facies links early diagenetic influences on chemostratigraphy to astronomically modulated sequence stratigraphic horizons, and helps to resolve rates of paleobiologic and paleoenvironmental change during a significant Mesozoic carbon cycle perturbation.

CHAPTER 4

Astronomical Pacing of Relative Sea Level during Oceanic Anoxic Event 2 from the Expanded SH#1 Core, Utah

4.1. Introduction

Oceanic Anoxic Event 2 (OAE2), spanning the Late Cretaceous Cenomanian-Turonian Boundary (CTB; 93.9 Ma), represents a major perturbation to the Earth's carbon cycle, preserved as organic-rich black shales at deep marine sites in many basins globally (Schlanger and Jenkyns, 1976; Scholle and Arthur, 1980; Tsikos et al., 2004). Geochemical evidence indicates that large igneous province (LIP) volcanism impacted the ocean-atmosphere system (Bralower et al., 1997; Kerr, 1998; Turgeon and Creaser, 2008; Du Vivier et al., 2014) leading to significant shifts in global ocean chemistry, atmospheric pCO_2, climate, nutrient loading, primary production, and marine oxygen-deficiency (Adams et al., 2010; Owens et al., 2013). The resulting late Cenomanian faunal extinction event is among the most significant of the Cretaceous Period (Raup and Sepkoski, 1986), and represents a major Earth-life transition recorded in terrestrial (Eaton et al., 1997) and marine ecosystems (Leckie et al., 2002). Aragonitic marine organisms, such as ammonites (Harries and Little, 1999) and rudists (Philip and Airaud-Crumiere, 1991), were particularly susceptible to demise, and some studies indicate a pulsed character to the CTB extinction (Elder, 1989). Yet the precise mechanisms of marine extinction associated with OAE2, and OAEs in general, such as eutrophication and anoxia (e.g., Harries and Little, 1999; Parente et al., 2008), sea level fluctuations (Peters, 2008), or thermal stress and/or potentially ocean acidification (Du Vivier et al., 2015a), remain areas of active research.

The North American Western Interior Basin (WIB) preserves a rich stratigraphic and biotic record of OAE2, as the peak transgression of the Greenhorn Cyclothem (~93.5 Ma) occurs near the CTB interval, at a time when the expansive, shallow Western Interior Seaway inundated the North American craton and linked the proto-Gulf of Mexico to the polar Boreal sea (Kauffman and Caldwell, 1993; Arthur and Sageman, 2005) (Figures 4.1-4.2). Stratigraphic records spanning the CTB from the distal axial basin, such as in the Bridge Creek Limestone Member, are more condensed and calcareous than coeval units in the proximal foredeep, such as the Tropic Shale – the target of this study (Figure 4.2). The prominent, rhythmically-bedded limestone-marlstone couplets of the Bridge Creek Limestone occur over a massive area in the basin and suggest regular oscillations in sedimentation through time, hypothesized to be modulated by orbitally-controlled changes in global climate (Gilbert, 1895; Fischer et al., 1985). Later studies have attributed the interbedding to (1) siliciclastic dilution cycles, (2) carbonate productivity cycles, (3) redox cycles, or some combination of these models (Pratt, 1985; Eicher and Diner, 1989; Elderbak and Leckie, 2016 and refs therein). Regardless of depositional mechanism, the Bridge Creek interbeds preserve a robust record of Milankovitch orbital influence (Sageman et al., 1997a), which has been exploited to construct precise astronomical time scales (ATS) for the CTB interval and to quantify the duration of OAE2 (563-885 kyr depending on definition of the event: Sageman et al., 2006). These ATS, along with detailed biostratigraphy (Cobban et al., 2006; Corbett et al., 2014), datable bentonites (Meyers et al., 2012a), and traceable lithostratigraphic units (Elder et al., 1994), form a highly resolved chronostratigraphic framework for the WIB, which serves as a window to reconstruct paleoclimatic, paleobiotic, and geochemical changes through OAE2.

This study details results from a shallow continental drilling project of the CTB from the proximal foredeep of the WIB, near the western paleoshoreline of the epeiric seaway (Figures 4.1-4.2). We present litho-, bio-, chemo-, and sequence stratigraphic datasets from the SH#1 core, drilled through the fossiliferous Tropic Shale of the Kaiparowits Plateau in southern Utah, and

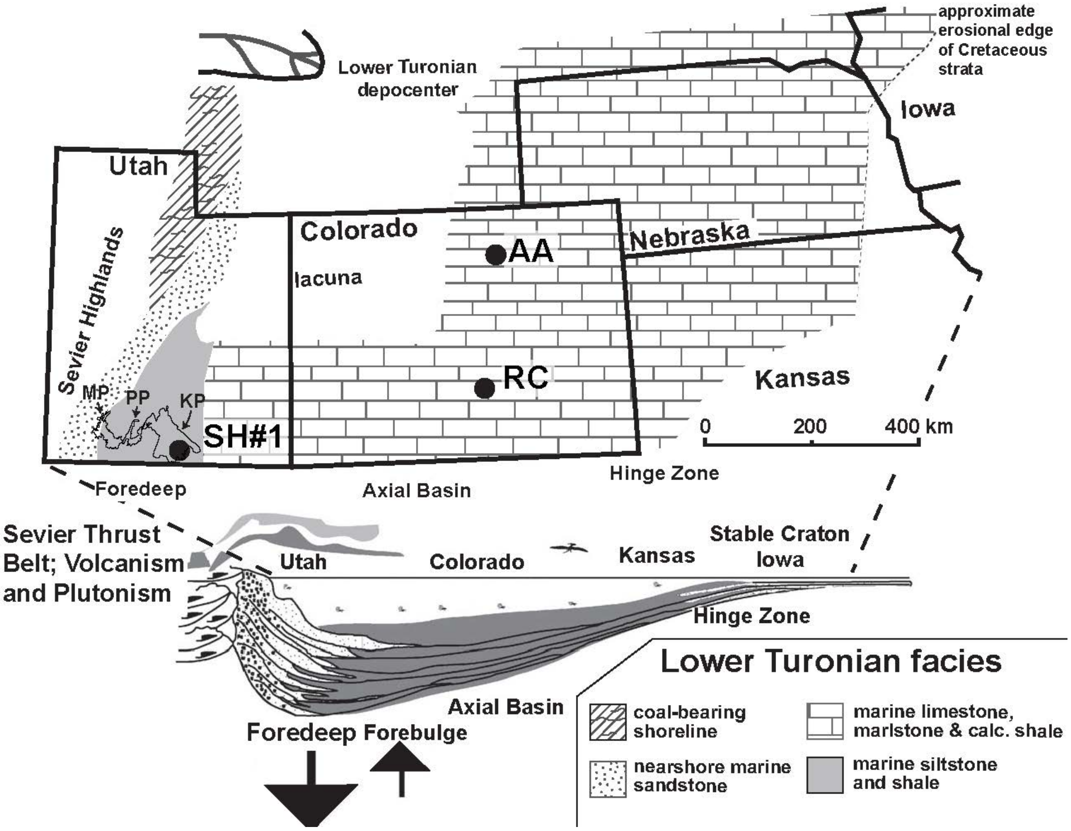

Figure 4.1. Top - Lower Turonian facies map (ca 93 Ma) of the central Western Interior Basin. Relevant Cenomanian-Turonian Boundary (CTB) sections abbreviated on map (SH#1: Smoky Hollow #1 core, this study; RC: Rock Canyon Anticline, Pueblo, CO, CTB global stratotype section and point; AA: Aristocrat Angus core, Denver Basin, CO). MP = Markagunt Plateau, PP = Paunsaugunt Plateau, KP = Kaiparowits Plateau. Bottom – west-east cross-sectional schematic of western interior foreland basin, including Sevier Thrust belt, proximal rapidly subsiding foredeep, forebulge, axial basin, and low accommodation stable craton (modified from Kauffman, 1984; White and Arthur, 2006).

uncover the most expanded $\delta^{13}C$ record of OAE2 for the central Western Interior, spanning this time of expanded net global marine anoxia and organic carbon burial. Using the stable isotope dataset, we test for astronomical periodicities to precisely resolve the timing of geochemical cycle perturbations, sea level fluctuations, and extinction horizons associated with OAE2 in the proximal setting of the WIB. The resulting SH#1 record and age model correlate to time-equivalent, astronomically-tuned CTB sections throughout the WIB and globally (e.g., Meyers et al., 2001; Li et al., 2017), and we utilize a proximal-distal correlation in the WIB to reevaluate the depositional model for the Bridge Creek Limestone, considering the influence of relative sea level oscillations on basinwide lithofacies patterns.

4.2 Geologic Material: SH#1 Core, KPS Outcrop, and Kaiparowits Plateau Stratigraphy

4.2.1 Western margin of the seaway

Stratigraphic successions along the western margin of the WIB, such as in the Kaiparowits, Paunsaugunt, and Markagunt plateaus of southern Utah, preserve a highly expanded, relatively continuous, siliciclastic CTB record ideal for higher temporal resolution reconstructions of OAE2 (Elder et al., 1994) (Figures 4.1-4.2). The rapidly subsiding, proximal foredeep of the foreland basin generated significant accommodation in the Late Cretaceous, which was filled with siliciclastic sediment supplied by the adjacent uplifted Sevier thrust belt (Jordan, 1981; Gardner, 1995). The Cenomanian-Turonian Tropic Shale in southern Utah, partially equivalent to the lower Mancos Shale (Leckie et al., 1997), consists of thick (210-275 m) dark-grey, fossiliferous (including aragonite), and bentonitic marine shale with intermittent, laterally traceable carbonate concretionary horizons (Gregory and Moore, 1931; Peterson, 1969; Elder, 1988; Leithold, 1994; Elder et al., 1994; Titus et al., 2005). The underlying Dakota Formation interfingers with the overlying Tropic Shale and consists of conglomerates, coals, sandstones, and sandy shales, deposited in a dynamic coastal depositional setting (Peterson, 1969; Elder et al., 1994). Use of the lithostratigraphic term "Dakota" was questioned by Young (1965), and recently Carpenter (2014) argued that the new name – "Naturita Formation" – be adopted in southern Utah; hereafter we employ the term "Naturita" for strata previously identified as Dakota.

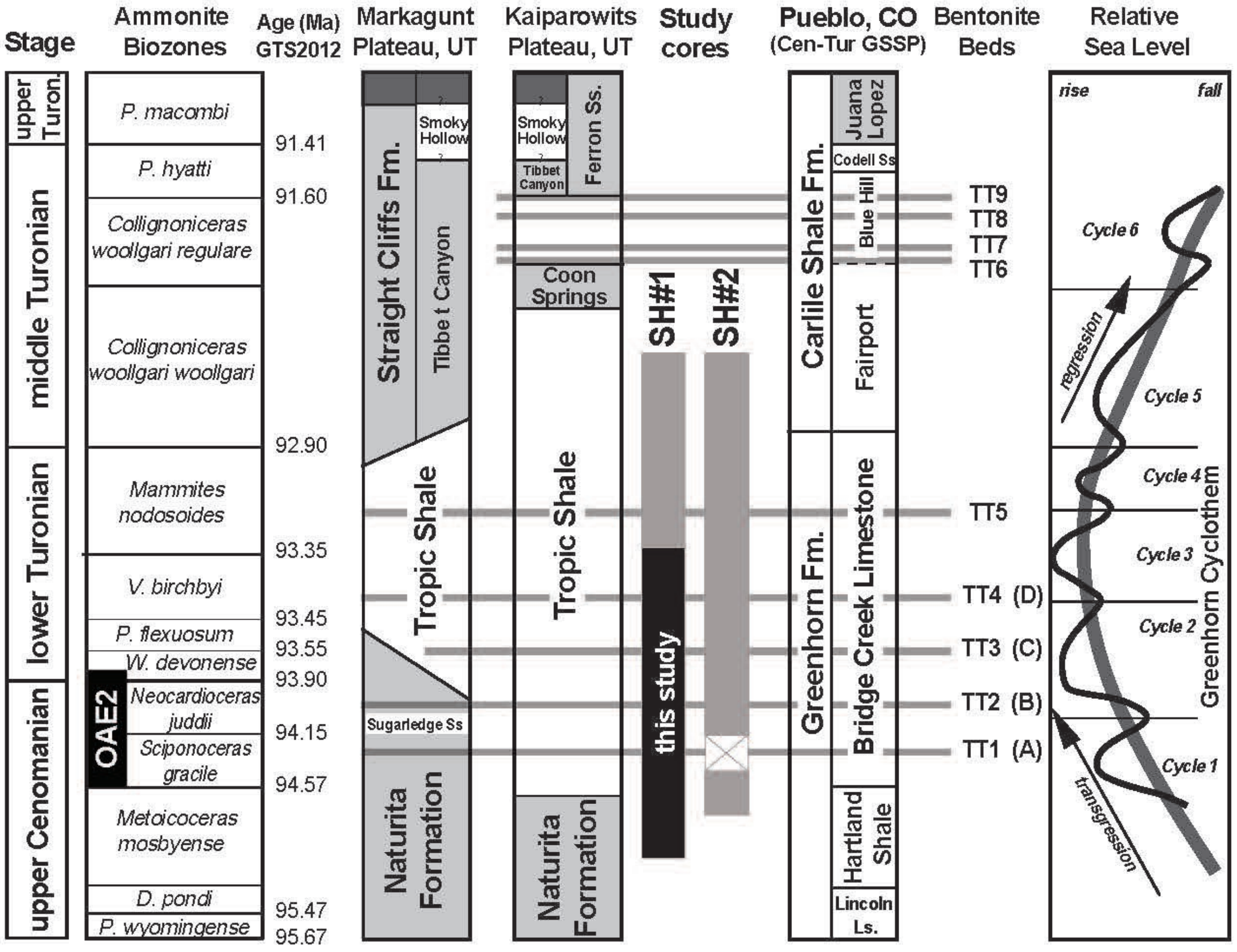

Figure 4.2. Generalized Cenomanian-Turonian lithostratigraphy, ammonite biostratigraphy, bentonite beds (A-D of Elder, 1988; TT1-TT9 of Leithold, 1994), and relative sea level framework (Cycle 1-6 of Leithold, 1994) of the Western Interior Basin (adapted from Tibert et al., 2003). Biozone ages from the 2012 Geologic Time Scale (Ogg and Hinnov, 2012 and refs. therein).

An interplay of subsidence, sedimentation, and eustasy formed distinct genetic sedimentary sequences in the Naturita and Tropic formations along the western coastal margin of the WIB in the Kaiparowits, Paunsaugunt, and Markagunt plateaus of southern Utah. A number of authors have hypothesized that distinct high frequency transgressive-regressive cycles along the WIB western margin resulted from astronomical forcing of Earth's climate – oscillating orbital eccentricity, axial obliquity, and precession (Elder et al., 1994; Leithold, 1994; Uličný, 1999; Tibert et al., 2003; Laurin and Sageman, 2007; Zhu et al., 2012), although spectral analysis techniques have not been applied in the proximal offshore facies previously. Alternative explanations for stratigraphic architecture, such as rapid subsidence and fault movement in the tectonically active foredeep, have also been proposed (Vakarelov et al., 2006; DeCelles, 2011) and surely played an important role in the history of WIB sedimentation, but would be unlikely to produce sedimentation patterns that match orbital periods.

Previous studies of macrofossil (Elder, 1987; Elder, 1989; Kirkland, 1991), foraminifera (Leckie et al., 1991, 1998; West et al., 1998; Tibert et al., 2003; Tibert and Leckie, 2013), and nannofossil (Watkins, 1985; Bralower, 1988; Corbett and Watkins, 2013; Corbett et al., 2014) biostratigraphy and $\delta^{13}C$ chemostratigraphy (Pratt and Threlkeld, 1984) of the Tropic and Mancos Shale Formations confirm the preservation of OAE2 along the western margin of the basin. Furthermore, four prominent and areally extensive bentonites are present in the lower Tropic Shale of southern Utah (Bentonites A-D), along with traceable carbonate-rich beds and concretions (Elder, 1988). These beds correlate over 600 km to the Bridge Creek Limestone at well-studied sites in the basin center (Elder et al., 1994), including the CTB Global Stratotype Section and Point (GSSP) at the Rock Canyon Anticline near Pueblo, CO (Kennedy et al., 2005; Sageman et al.,

2006) (Figure 4.2). These published biostratigraphic, chemostratigraphic, lithostratigraphic, and sequence stratigraphic investigations form the chronostratigraphic framework for this study, which utilizes the expanded thickness of sediments along the western margin of the WIB to develop a high-resolution $\delta^{13}C$ chemostratigraphy of OAE2 from the newly drilled SH#1 core.

4.2.2. SH#1 Core Drilling, Logging, and Curation

The USGS Water Resources Division was contracted to drill the Smoky Hollow #1 and #2 cores (SH#1, SH#2) in July 2014 on land within the Grand Staircase-Escalante National Monument (Figure 4.3: 37.158466°, -111.531947°; Figure 4.3). Drillers employed air rotary coring techniques to recover rock core in 10-foot barrels with 2.5-inch diameter. The total depth of SH#1 (TD = 131.15 m) was slightly deeper than SH#2 (TD = 128.26 m), with high recovery percentages in each core (SH#1: 96%, SH#2: 93%) (Table A3.3). For SH#2, drillers washed out to a depth of 94.72 m and recovered core from 94.72 to 128.26 m, to prioritize recovery of the OAE2 interval. However, an estimated 1.19 meters of rock was lost in SH#2 at the critical onset interval of OAE2 in the lowermost Tropic Shale, possibly due to the soft bentonitic nature of the sediments. Both cores penetrated the Tropic Shale/Naturita Formation contact and recovered fine-grained cross-bedded sandstones, coal beds, and flaser to lenticular bedding textures typical of the Upper Member, Naturita Formation (Peterson, 1969; Uličný, 1999) (see Sect. 4.4.1). Upon completion of drilling, electrical resistivity, conductivity, gamma ray, and caliper logs were measured in the SH#1 borehole (Figure A3.1).

Core from below 94.5 meters depth in both SH#1 and SH#2 was slabbed for description, sampling, and curation at Northwestern University. Guided by driller's notes and geophysical well logs, we identified core gaps and assigned an adjusted depth scale to core segments, aligning

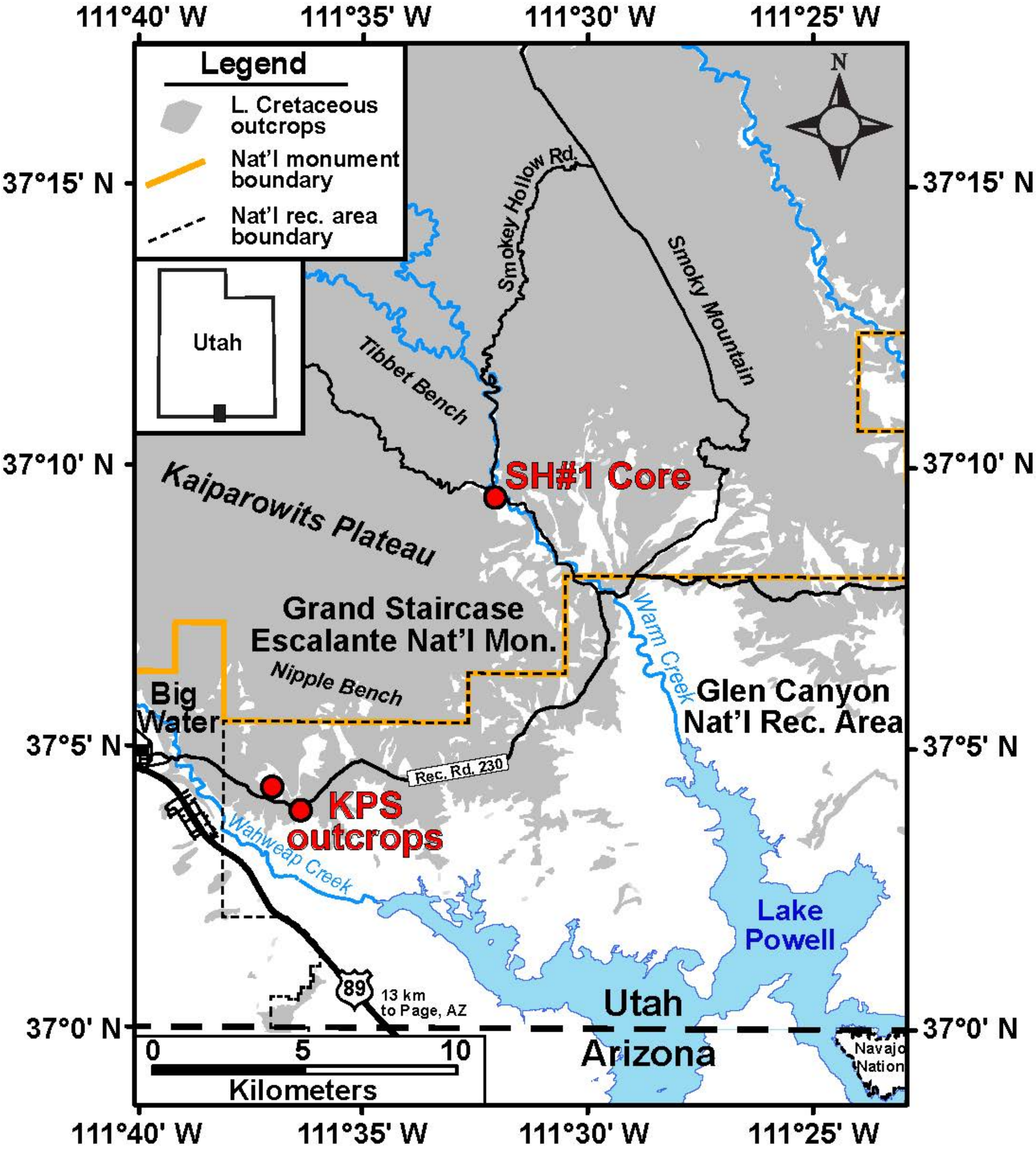

Figure 4.3. Map of the drilling sites for the SH#1 and SH#2 cores on Grand Staircase Escalante National Monument administered by the U.S. Bureau of Land Management (BLM), and the Kaiparowits Plateau Section outcrops (KPS) on National Park Service (NPS) land along the southernmost Kaiparowits Plateau east of Big Water, Utah. Note – fieldwork required NPS and BLM permits.

logging and core depth scales. Bentonites A-D were conspicuous in gamma ray, caliper, and conductivity logs and served as useful datums to align depth scales. After alignment, comparisons of depths of correlative marker beds in SH#1 and SH#2 yielded offsets of less than 8 cm, and offsets from logging depths of less than 18 cm. For curation, we marked adjusted depths (in feet) on SH#1 and SH#2, although scientific results are reported here in metric units.

4.2.3. Kaiparowits Plateau Section Outcrop

Larger volumes of sample were collected from the Kaiparowits Plateau Section (KPS) during fieldwork for ongoing organic geochemical and biostratigraphic research and to tie into existing OAE2 macrofossil extinction datums (Elder, 1989). The KPS outcrop is located 4 km east of Big Water, Utah in the Glen Canyon National Recreational Area, adjacent to Recreation Road 230 at the base of the southern escarpment of the Kaiparowits Plateau along Nipple Bench (Figures 4.3-4.4). Hand and backhoe trenching exposed two sections, KPS1 (lower: 37.06684°N 111.603946°W) and KPS2 (upper: 37.072083°N 111.615028°W), below the deep present-day weathering horizon of the lower Tropic Shale. Established regional litho- and bentonite stratigraphy permitted correlation of the composite KPS outcrop record to the nearby SH#1 core (Elder et al., 1994).

4.3. Methods

4.3.1. Geochemical Methods

Given higher recovery rates in SH#1 than SH#2, 146 samples were collected for geochemical analysis from SH#1 at 20-cm resolution spanning OAE2 in the Tropic Shale (94.5-124.97 m). Core samples were crushed in tungsten carbide containers on a Shatterbox® to a fine powder for geochemical analyses conducted at the Northwestern University Stable Isotope Laboratory.

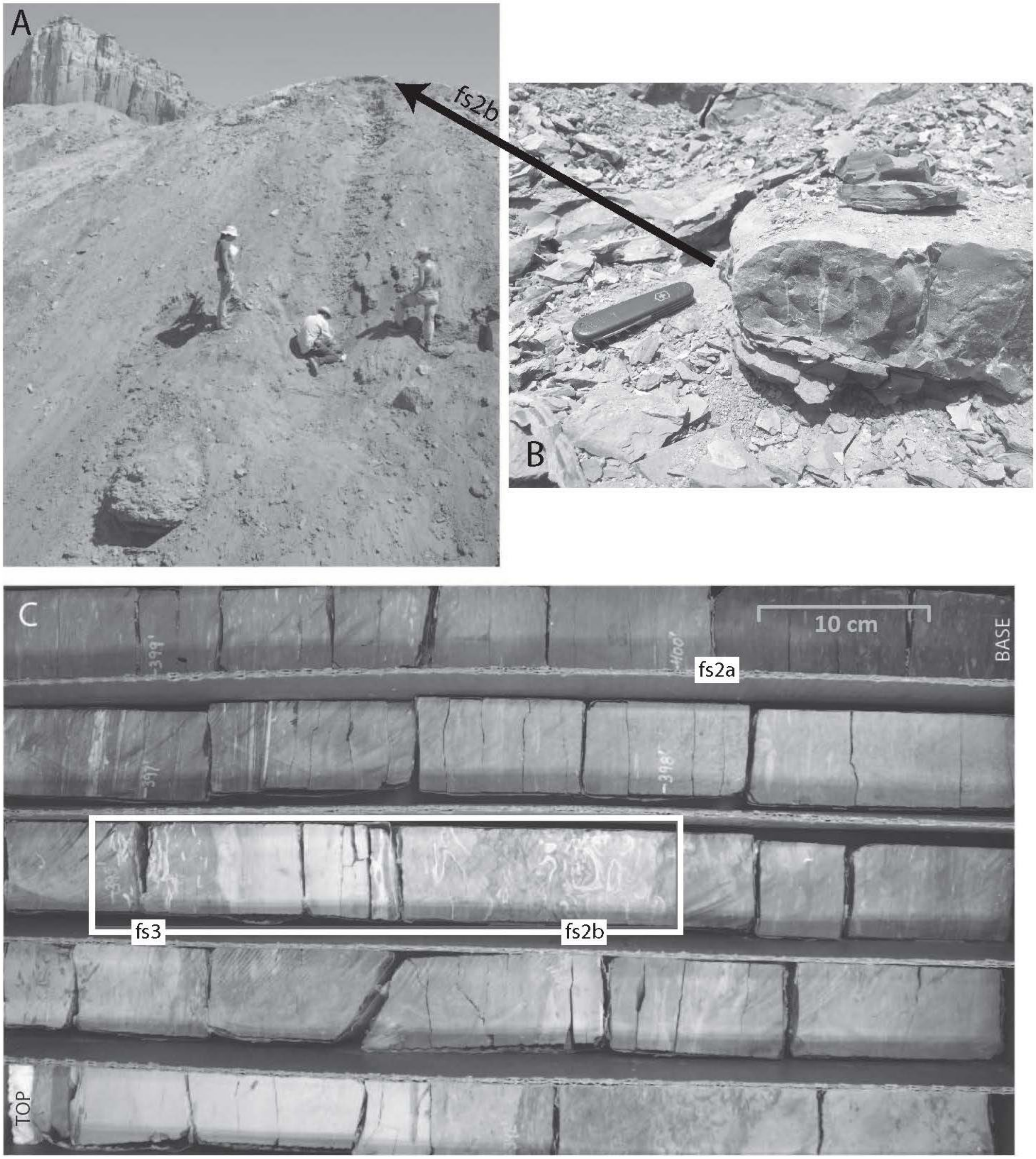

Figure 4.4. Photos illustrate: **A)** Lower outcrop section of study interval (KPS#1) pictured in Figure 4.5. **B)** Carbonate concretions at flooding surface fs2b at KPS#1 (*sensu* Elder et al., 1994). **C)** Details of the split SH#1 core showing Box 35 Sections 1-5 with rectangle highlighting the oyster-rich fs2b and fs3 flooding surfaces at ~396 ft and ~395 ft depth (120.7 m and 120.4 m), respectively. Note three light-colored bentonitic horizons that comprise the Bentonite A "swarm".

4.3.1.1. Carbonate Content, Total Organic Carbon -Weight percent carbonate content and weight percent total organic carbon (TOC) values were measured using coulometric titration on a UIC Coulometer. Two sigma analytical uncertainty for carbonate content and TOC calculated from 12 duplicate measurements was ±0.02%, after calibration with a UIC calcium carbonate standard (total carbon = 12.00%).

4.3.1.2. Bulk Organic Carbon Isotopes - Bulk organic carbon isotope ratios ($\delta^{13}C_{org}$) for samples collected from SH#1 were measured on powders with ≥0.10% TOC. Prior to analysis, samples were acidified in 2N HCl for 12 hours on a shaker table. Acidified samples were collected on filter paper and rinsed with 750 mL of deionized water to remove residual acid. Next, $\delta^{13}C_{org}$ values were measured on a Costech ECS4010 elemental analyzer coupled in continuous He flow to a Thermo Delta V Plus Isotope Ratio Mass Spectrometer (IRMS). Raw results were calibrated to the VPDB per mil scale using standards of acetanilide (Indiana University), urea (Indiana University), caffeine (IAEA), and cellulose (IAEA). In addition, an in-house reference material (Union Springs Shale) was measured throughout the run (n=15) with 1σ duplicate uncertainty of ±0.08‰. Average 1σ $\delta^{13}C_{org}$ uncertainty on 22 duplicate measurements of unknown samples was ±0.10‰.

4.3.1.3. Carbonate Carbon and Oxygen Isotopes - Bulk carbonate carbon ($\delta^{13}C_{carb}$) and oxygen ($\delta^{18}O_{carb}$) isotope ratios were measured from the same samples analyzed for $\delta^{13}C_{org}$ to compare chemostratigraphic signals. After purging the atmosphere of capped vials with He, roughly 400 μg of carbonate from oven-dried samples were acidified in vials with 1 mL of 103% H_3PO_4 for at least 6 hours. The $\delta^{13}C$ and $\delta^{18}O$ of evolved CO_2 gases from the carbonate fraction of samples were measured on a Thermo Gasbench II coupled in continuous flow with He carrier gas to a Thermo Delta V IRMS. Raw values were calibrated to the VPDB per mil scale using the NBS-18 standard and an in-house carbonate standard. Average 1σ analytical uncertainty of 11 duplicate $\delta^{18}O_{carb}$ and $\delta^{13}C_{carb}$ measurements was ±0.37‰ and ±0.06‰, respectively.

To evaluate carbonate diagenesis, we calculate covariation of the full $\delta^{13}C_{carb}$ and $\delta^{18}O_{carb}$ dataset, as well as of sliding stratigraphic depth intervals (25 consecutive samples), similar to the windowed approach of EHA spectral analysis (Meyers et al., 2001). Additionally, $\Delta^{13}C$ values ($\delta^{13}C_{carb}$ - $\delta^{13}C_{org}$) are calculated from paired $\delta^{13}C_{carb}$ and $\delta^{13}C_{org}$ values from a selection of the same sample powders (i.e., samples lacking evidence of diagenetic alteration). We use $\Delta^{13}C$ to assess for changes in isotopic fractionation associated with variations in marine productivity and carbon burial in samples where $\delta^{13}C$ values are not compromised by diagenesis.

4.3.2. Astrochronology Methods

The $\delta^{13}C_{carb}$ datasets were tested for astronomical frequencies using spectral analysis routines from the open-source Astrochron R software package (Meyers, 2014). Temporal uncertainty from previous $^{40}Ar/^{39}Ar$ and U/Pb age dating and astrochronologic time scales constrain maximum and minimum estimates for the duration between the deposition of Bentonites A-D in the WIB (Meyers et al., 2012a; Ma et al., 2014). Accounting for this temporal uncertainty and assuming linear sedimentation rates between the bentonitic horizons in SH#1, plausible sedimentation rates for the OAE2 interval range from 1.0 to 6.0 cm/kyr and guide identification of potential astronomical frequencies. Prior to implementing the astrochronologic analysis, $\delta^{13}C_{carb}$ data points suspected of severe diagenetic alteration, based on their depleted values well below the predominant range of variance for the study interval ($\delta^{13}C_{carb} < +1.0‰$), were filtered from the dataset.

Spectral power, as a function of spatial frequency, was calculated via the multi-taper method (MTM) of Fourier analysis (Thomson, 1982) for a given "window" of linearly interpolated (dZ=10 cm) and mean-subtracted $\delta^{13}C_{carb}$ data. The MTM algorithm also calculates an F-test to determine statistical significance for phase coherency of individual frequency bandwidths, which, when combined with autoregressive (AR) significance testing, provides definitive thresholds for detecting significant frequencies in stratigraphic datasets (Meyers, 2012). Evolutive harmonic analysis (EHA) (Meyers et al., 2001) techniques were applied to 5 m moving windows of $\delta^{13}C_{carb}$ data to probe for significant spatial frequencies as a function of depth. Evolutive average spectral misfit algorithms (ASM: Meyers and Sageman, 2007; Meyers et al., 2012b) were then applied to test for the degree of "misfit" between target astronomical periods (405.47, 126.98, 96.91, 48.54, 37.66, 22.42, 18.33 kyr; Laskar et al., 2004, 2011) and significant $\delta^{13}C_{carb}$ spatial frequencies (F-test > 80%). The ASM method iteratively calculates a temporal period for significant observed frequencies by assigning a range of sedimentation rates. Sedimentation rates that produce significant periods and minimize "misfit" with predicted astronomical periods indicate a higher probability Milankovitch signal. For each tested sedimentation rate, a Monte Carlo approach provides a statistical test to evaluate the degree to which observed periods are more consistent with astronomical periods, compared to randomly generated spectra (n=50,000). This approach enables calculation of a significance level (H_o) for decisively identifying Milankovitch cycles and estimating sedimentation rates for a given 5 m depth window. In evolutive ASM (e-ASM) (e.g., Meyers et al., 2012b), this process is implemented for each stratigraphic window of studied data to track sedimentation rates that exceed a specified H_o threshold of less than 0.1%. At this significance level, fewer than 10 of the 10,000 randomly generated spectra would have a lower misfit with target astronomical periods than the observed spectra from the stratigraphic dataset.

The primary ATS was constructed by frequency domain minimal tracing (Park and Herbert, 1987; Meyers et al., 2001) of the short eccentricity F-test peak following EHA (Table A3.2). A cycle duration of 96.9 kyr/cycle was assigned to convert from stratigraphic frequency to sedimentation rate and floating time. A second estimate for the ATS was produced from bandpass filtering the zero-padded (n=2,000) $\delta^{13}C_{carb}$ record for the bandwidth of the 96.9 kyr short eccentricity (0.17-0.50 cycle/m) as constrained by eASM and EHA results. A bandpass timescale was then constructed by assigning a half-cycle (48.5 kyr) duration between each minima and maxima of the bandpassed sinusoid (blue dots Figure 4.8). A third, final, eASM sedimentation rate estimate was calculated from horizons where results did not exceed an H_0 of 0.1%.

4.3.3. XRF Core Scanning

Slabbed surfaces of SH#1 were analyzed for semi-quantitative major and trace elemental abundances using an ITRAX X-ray fluorescence (XRF) core scanner at the University of Massachusetts-Amherst (UMass). Core-scanning XRF (CS-µXRF) is a low power, large chambered, non-vacuum XRF system. Itrax CS-µXRF was conducted with a molybdenum tube at 30 kV and 55 mA. Elements with atomic weights from Al to U were detected using a count time of 10 seconds per 2 mm step. The archived half of SH#1 was scanned at 2 mm resolution from 94.50 to 130.92 m with measurement positions recorded relative to the top of core boxes (see Table A3.3). Additional details about CS-µXRF at UMass can be found in Scroxton et al. (2018).

4.3.4. Biostratigraphy

Samples were collected for foraminifera from the KPS#1-2 outcrop and for calcareous nannofossil biostratigraphy from the SH#1 core. For foraminiferal biostratigraphy, sediment samples were soaked in 3% Quaternary-O for a week, disaggregated and washed over a 63-µm sieve, prior to picking at least 300 foraminifera for taxonomic identification. For nannofossil biostratigraphy, small chips of samples from SH#1 were placed in a pestle with a small amount of water and broken up gently with a mortar. The supernatant was poured into a beaker and ultrasonicated. The solution was dried on a coverslip on hot plate then attached to a glass slide using Norland Optical Adhesive #61 under an ultraviolet light. Slides were observed in a Zeiss Axio Imager A2 photomicroscope at a magnification of 1250x for a minimum of half an hour.

4.4. Results

4.4.1. Lithostratigraphy

4.4.1.1. Naturita Formation - The Naturita Formation in the SH#1 core (below 125.03 m) includes a lower interval of fine-grained sandstones and intermittent coal beds with sharp contacts and an upper interval with two coarsening-up packages grading from black coals to fine-grained sandstones (Figure 4.5). These packages (1.25 and 1.83 m thick, respectively) have sharp basal contacts above the underlying fine-grained sandstones and are similar to Naturita facies observed previously and interpreted as shallow marine sequences in the Upper Naturita (tentatively correlated to Units 4-5 of Uličný, 1999). They grade upward sequentially from coal or poorly laminated sandy shales, into sandy shales and muddy sandstones preserving heterolithic bedding structures (lenticular grading to flaser bedding), and finally into bioturbated very light-grey, fine-grained sandstones. Below these packages (>128.2 m), lithofacies are composed of more homogenous, fine-grained, medium to very thickly bedded, massive sandstones, with occasional terrestrial organic material and medium-thick coal beds (10's of cm) with sharp contacts.

4.4.1.2. Tropic Shale - Dark-grey calcareous shales with occasional marine macrofossils (i.e., inoceramids, oysters) characterize the overlying Tropic Shale in SH#1 (above 125.03 m) (Figure

4.4). Macrofossils are especially concentrated in thin shelly carbonate-rich horizons (less than 15 cm thick) that occur roughly every several meters. The fossiliferous horizons in SH#1 are consistent with concretionary carbonate beds observed in outcrops on the Kaiparowits Plateau by Elder et al. (1994) (Figure 4.4), who labeled these as flooding surfaces "fs0-fs7" and correlated them to limestone beds (LS1-7) in the Bridge Creek Limestone Member of central Colorado (Figures 4.5 and 4.11). Light-colored bentonites, or evidence for bentonites from geophysical logging and core gaps, are common in SH#1, and correlate with documented regional bentonite occurrences (Elder, 1988; Leithold, 1994; Elder et al., 1994; Tibert et al., 2003; Laurin and Sageman, 2007) (Figures 4.2 and 4.4). Bentonite A occurs as a zone of at least three distinct bentonites in the lowermost Tropic Shale (Kirkland, 1991) and is identified in SH#1 between 118.5-120.6 m.

The basal contact of the Tropic Shale was placed at a sharp lithologic shift at 125.03 m depth, delineating the highest well-defined fine-grained sandstone bed of the Naturita Formation and the overlying dark-grey marine shales (Peterson, 1969). The lowest studied interval of the Tropic Shale in SH#1, from Bentonite A to the base of the formation, preserves evidence for extensive bioturbation, coarser grain size, and lower carbonate content overall (Figure 4.5). Bioturbation in this interval varies from moderately laminated shales to non-calcareous bioturbated sandy shales (e.g., *Planolites*, *Chrondrites*) with occasional very light-grey sandy burrow infills. Above Bentonite A, bioturbation and coarser grained sandy horizons are rare, and the dark-grey shale lithologies are relatively homogenous.

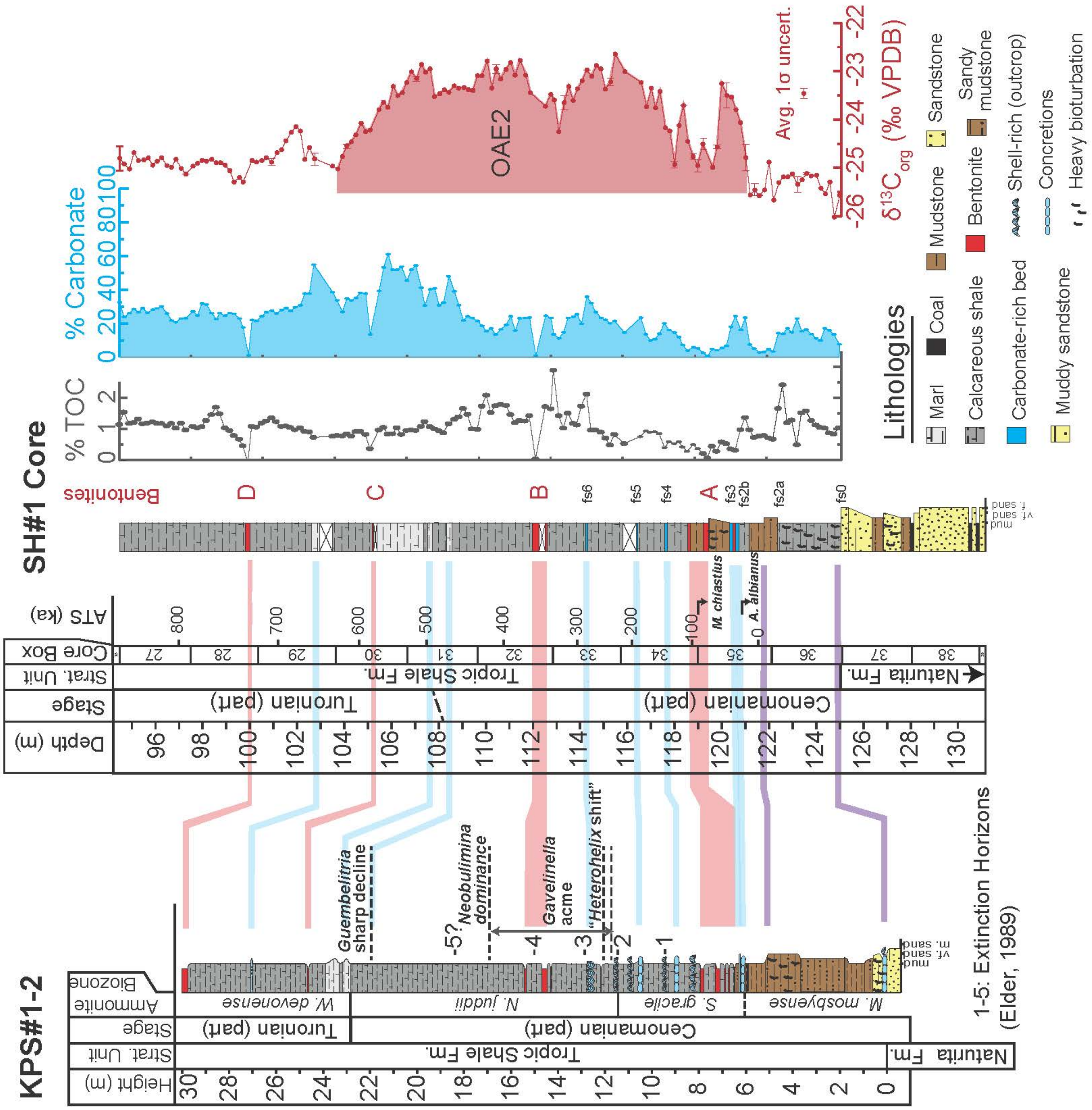
KPS#1-2
Height (m)
Strat. Unit
Stage
Ammonite Biozone
Naturita Fm.
Tropic Shale Fm.
Cenomanian (part)
Turonian (part)
M. mosbyense
S. gracile
N. juddii
W. devonense
mud
vf. sand
m. sand
Guembelitria sharp decline
Neobulimina dominance
Gavelinella acme
"Heterohelix shift"
-5?
-4
-3
-2
-1
1-5: Extinction Horizons (Elder, 1989)
SH#1 Core
Depth (m)
Core Box
ATS (ka)
M. chiastius
A. albianus
Bentonites
A
B
C
D
fs0
fs2a
fs2b
fs3
fs4
fs5
fs6
mud
vf. sand
f. sand
% TOC
% Carbonate
OAE2
Avg. 1σ uncert.
δ13Corg (‰ VPDB)
Lithologies
Marl
Coal
Mudstone
Sandstone
Calcareous shale
Bentonite
Sandy mudstone
Carbonate-rich bed
Shell-rich (outcrop)
Concretions
Muddy sandstone
Heavy bioturbation

Figure 4.5. (previous page) Lithostratigraphy and bentonite stratigraphy (bentonites A-D of Elder, 1988) allow correlation of the KPS#1-2 outcrops (left) to the SH#1 core (right). Terminology of flooding surfaces (e.g., fs0) from Elder et al. (1994). Ammonite biostratigraphy and macrofossil extinction horizons updated from Elder (1989) (see text). Foraminiferal events (KPS#1-2) and nannofossil datums (SH#1) from this investigation. Coulometry (TOC and %Carb) and bulk organic carbon isotope ($\delta^{13}C_{org}$) chemostratigraphy plotted at right. Floating astronomical time scale (ATS) combining evolutive average spectral misfit (eASM), bandpass filtering, and eccentricity tracing results plotted (see text for discussion). Colored bands mark correlation using bentonites (red), carbonate-rich beds (blue), and flooding surfaces (purple).

4.4.2. Biostratigraphy

Western Interior molluscan macrofossil biozones, characteristic of the OAE2 interval throughout the WIB (e.g., *S. gracile*, *N. juddii*, *W. devonense* biozones), were identified in the KPS outcrop section during earlier field studies (Elder, 1989; Elder et al., 1994; Sageman et al., 1997b), and are correlated to SH#1 using litho- and chemostratigraphic markers (Figures 4.5-4.6).

Typical open marine planktic foraminiferal species that globally serve as important datums associated with OAE2, including the last occurrences of *Rotalipora cushmani, R. greenhornensis,* and *Globigerinelloides bentonensis* (Leckie, 1985; Lowery et al., 2014; Elderbak and Leckie, 2016), were not found in the studied samples, most likely because the proximal setting of the Tropic Shale prohibited their colonization in the upper water column. However, foraminiferal biostratigraphy identified the first and last appearances of several regionally significant taxa; most important are those marking the onset of the 'Benthonic Zone' at the base of the *S. gracile* biozone (Eicher and Worstell, 1970; Eicher and Diner, 1985), and the '*Heterohelix* shift' (Figure 4.5), which approximates the *S. gracile/N. juddi* zonal boundary in the uppermost Cenomanian (Leckie, 1985; Leckie et al., 1998; Elderbak and Leckie, 2016). Other foraminiferal events observed elsewhere in the seaway appear to be diachronous, including the onset and end of the '*Gavelinella* acme', and the abrupt change to dominance of *Neobulimina* in benthic foraminiferal assemblages associated with the *N. juddi* ammonite zone (Leckie et al., 1998). Based on these results and refined ammonite and inoceramid biostratigraphy of the CTB at the GSSP (Kennedy et al., 2000; 2005), including the last occurrences of *Inoceramus pictus* and first occurrence of *Mytiloides opalensis*, we adjust the position of the CTB to 23 m above the base of the KPS section from its original position at ~19 m, which was determined based on secondary marker taxa (Elder, 1989) (Figure 4.5).

Two cosmopolitan nannofossil biostratigraphic datums were identified in SH#1, including the LADs (Last Appearance Datums) of *Microstaurus chiastius* (117.49 m) and *Axopodorhabus albianus* (119.445 m) (Figure 4.5). Above this interval, assemblages are dominated by boreal species (Fortiz, 2017) and few markers occur. Very rare specimens of *Quadrum gartneri* are observed at 109.1 and 103.6 meters but a range of this species could not be determined.

4.4.3. Geochemistry

4.4.3.1. Coulometry (TOC and Carbonate Content) - Weight percent carbonate content in SH#1 averages 23.4%, ranging from 0.8 to 61.2% in the Tropic Shale (Figures 4.5-4.6; Table A3.1). Carbonate content more than doubles from ~20% to ~50-60% above 108.5 m, spanning Bentonite C (102-109 m) and approaching the termination of the OAE2 carbon isotope excursion (CIE) (Figure 4.5). Aside from this sharp increase, carbonate content abruptly decreases at bentonitic horizons corresponding to Bentonites A-D. Two additional carbonate-lean (<10.0%) intervals bracket the onset of OAE2: the lower interval (121.20-122.19 m) corresponds to a shift to sandy shale facies; while the upper interval (118.35-120.20 m) consists of bentonitic shales near the

Bentonite A swarm. Some local maxima in carbonate content reflect shelly beds in SH#1, such as at 120.6 m and 120.4 m (Figure 4.4c).

The TOC values in SH#1 average 1.04%, ranging from 0 to 2.9% (Figure 4.5; Table A3.1). Values for TOC decline below 0.5% at bentonite layers, as well as in the carbonate-lean interval near Bentonite A (Figure 4.5). Above this interval, TOC values gradually increase up-core in two intervals: first from 121 m to 109 m where it peaks at 2.1%, above which TOC decreases abruptly to ~1.0%, and second, more subtly, from 109 m to 98.8 m.

4.4.3.2. Stable Isotopes ($\delta^{13}C_{org}$, $\delta^{13}C_{carb}$, $\delta^{18}O_{carb}$) - Carbon isotope chemostratigraphy from SH#1 exhibits a strong positive CIE in both $\delta^{13}C_{org}$ and $\delta^{13}C_{carb}$ (Figures 4.5-4.6; Table A3.1). Most prominently, OAE2 is recorded by a +2.6‰ $\delta^{13}C_{org}$ excursion from 121.2-103.7 m (17.5 m thick) in SH#1. The CIE can be subdivided into its finer-scale characteristic components, labelled as C2-C5 following the convention of Li et al. (2017) (Figure 4.6). Broadly, the OAE2 $\delta^{13}C_{org}$ excursion consists of two pulses, one lower CIE (C2) from 121.2-119.6 m, and a more extended positive CIE from 119.6-103.7 m (C3-C5). This upper sustained CIE preserves a fluctuating plateau (C4) of $\delta^{13}C_{org}$ values from roughly 116.6-106.0 m. Elevated $\delta^{13}C_{org}$ decreases from roughly 106.0-103.7 m to more depleted background values marking the termination of OAE2 (C5), and post-excursion $\delta^{13}C_{org}$ values are more enriched than pre-excursion values by +0.44‰.

The $\delta^{13}C_{carb}$ chemostratigraphy also preserves a robust +2.5‰ CIE characteristic of OAE2 between 120.4-103.5 m depth in SH#1 (Figure 4.6; Table A3.1). However, the $\delta^{13}C_{carb}$ curve reveals discrepancies with the $\delta^{13}C_{org}$ chemostratigraphy, including a higher onset of the OAE2 CIE (120.4 m) and a higher degree of apparent cyclicity, with intervals of highly variable and depleted values (e.g., 121.2-119.0 m). Below 122.2 m in the lowermost Tropic Shale, prior to OAE2, $\delta^{13}C_{carb}$ values are consistently more depleted (avg. $\delta^{13}C_{carb}$ = -0.23‰).

The covariance between $\delta^{13}C_{carb}$ and $\delta^{18}O_{carb}$ was tested to highlight potential carbonate diagenesis (Allan and Matthews, 1982). The full SH#1 datasets exhibit a weak, yet statistically significant positive covariation ($r = +0.45$, p-value < 0.01), which is opposite to the negative covariation observed in distal basin sites (e.g., Arthur and Dean, 1991; Pratt et al., 1993). Considered separately, the intervals of the lowermost Tropic Shale (125-122.4 m) and the main body of the Tropic Shale (above 122.2 m) show stronger $\delta^{13}C_{carb}$ and $\delta^{18}O_{carb}$ covariation with high statistical significance ($r = +0.91$ and $r = +0.66$, respectively: Figure 4.7). Applying a 25-point moving stratigraphic window for the correlation reveals some intervals of higher positive covariation (e.g., ~105-106 m, 109-110 m, 118-120 m) that correspond to parasequence-scale flooding surfaces (e.g., Elder et al., 1994), but also shows shifts toward lower covariation (from 119 to 116 m and 109 to 108 m) that coincide with major transgressions (Figure 4.6, right panel).

The average $\delta^{18}O_{carb}$ value of the SH#1 record (-8.11±1.82‰, 2σ) is comparable to values from previous studies elsewhere in the WIB (Pratt, 1985; Pratt et al., 1993; Keller et al., 2004). Relative to background $\delta^{18}O_{carb}$ values bracketing OAE2 (which extends from 104-121 m depth), the $\delta^{18}O_{carb}$ dataset displays a -2.5‰ negative excursion at the onset of OAE2 (C2-C3) and a +1‰ positive excursion in the upper segment of the event (C4). Several horizons with higher carbonate content and significant positive covariation of $\delta^{18}O_{carb}$ and $\delta^{13}C_{carb}$ preserve highly depleted $\delta^{18}O_{carb}$ values (>-2‰ shift) (e.g., 123.2, 121.0, 116.5, 111.4, 108.4 m) (Figures 4.6-4.7).

The $\Delta^{13}C$ values in SH#1 are lowest (avg. = 25.10‰) in the lowermost Tropic Shale (>122.2 m) and correspond to an interval of depleted $\delta^{13}C_{carb}$ values (Table A3.1; Figure 4.6).

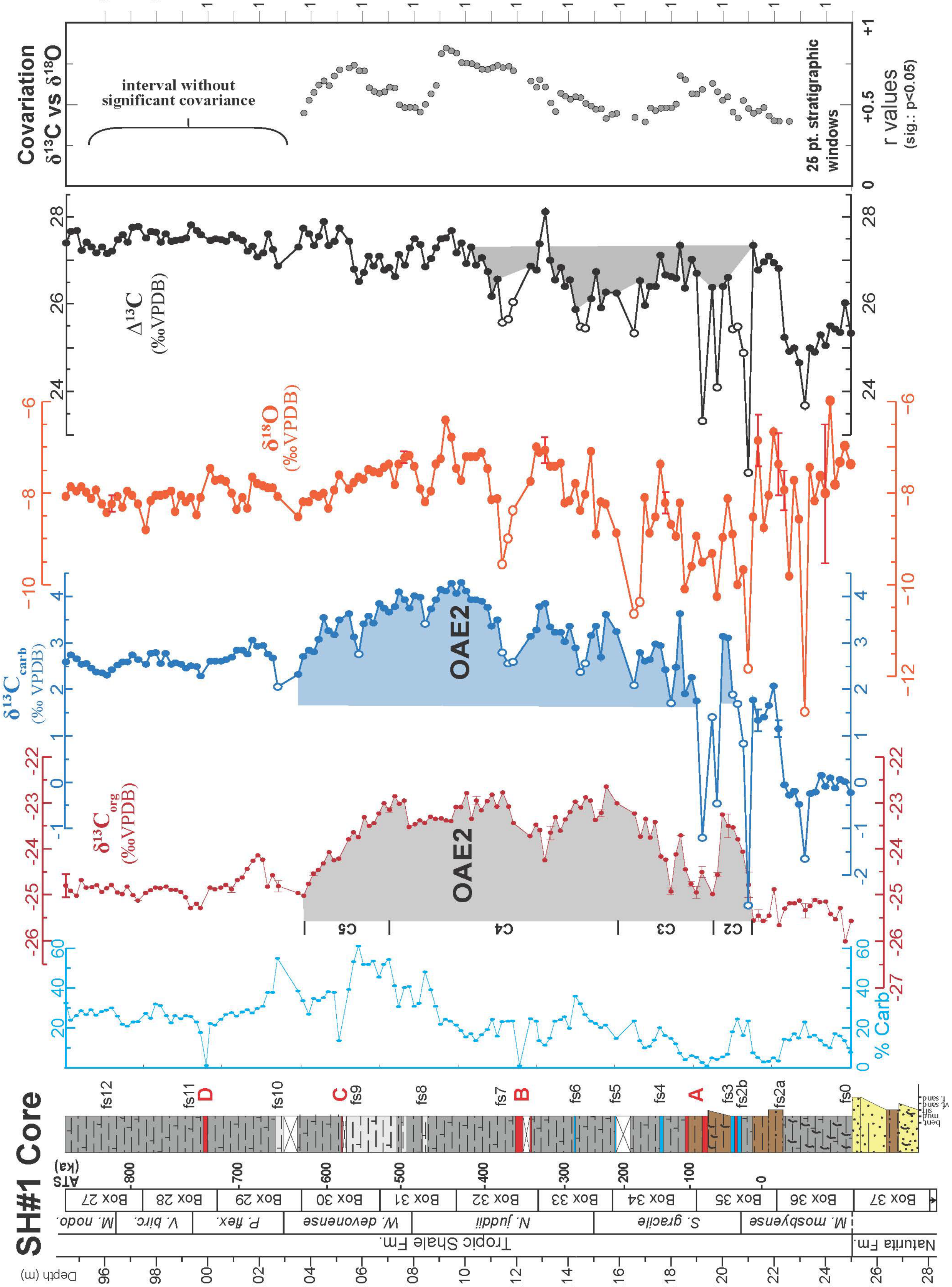
SH#1 Core
Depth (m)
Tropic Shale Fm.
Naturita Fm.
M. nodo.
V. birc.
P. flex.
W. devonense
N. juddii
S. gracile
M. mosbyense
Box 27
Box 28
Box 29
Box 30
Box 31
Box 32
Box 33
Box 34
Box 35
Box 36
Box 37
ATS (ka)
fs12
fs11
D
fs10
C
fs9
fs8
fs7
B
fs6
fs5
fs4
A
fs3
fs2b
fs2a
fs0
bent.
mud
silt
vf. sand
f. sand
% Carb
$\delta^{13}C_{org}$ (‰VPDB)
C5
C4
C3
C2
OAE2
$\delta^{13}C_{carb}$ (‰ VPDB)
OAE2
$\delta^{18}O$ (‰VPDB)
$\Delta^{13}C$ (‰VPDB)
Covariation $\delta^{13}C$ vs $\delta^{18}O$
interval without significant covariance
25 pt. stratigraphic windows
r values (sig.: p<0.05)
0
+0.5
+1

Figure 4.6. (previous page) Stratigraphic column and geochemical results from the SH#1 core. From left to right: carbonate content (%Carb), bulk organic carbon isotopes ($\delta^{13}C_{org}$), bulk carbonate carbon isotopes ($\delta^{13}C_{carb}$), oxygen isotopes ($\delta^{18}O_{carb}$), $\Delta^{13}C$ ($\delta^{13}C_{carb}$-$\delta^{13}C_{org}$), covariation (significant r values) of moving stratigraphic windows of $\delta^{13}C_{carb}$ and $\delta^{18}O_{carb}$ values (see Results). Open circles in plots of $\delta^{13}C_{carb}$, $\delta^{18}O_{carb}$, and $\Delta^{13}C$ indicate data suspected of carbonate diagenesis. Flooding surfaces (fs0-fs7) follow labeling scheme of Elder et al. (1994) and are expanded up-core in this study (fs8-fs12). Core box depths summarized in Table A3.3.

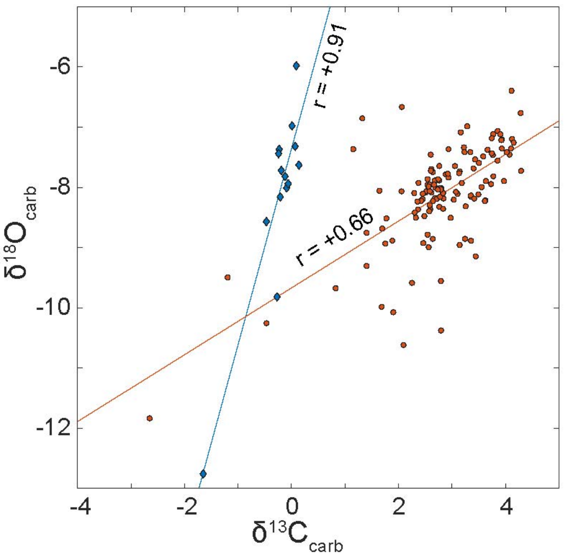

Figure 4.7. Scatterplot of gasbench $\delta^{13}C_{carb}$ and $\delta^{18}O_{carb}$ data. Lowermost Tropic Shale data (blue diamonds) preserve strong positive covariation and upper Tropic Shale data (red circles) preserve significant positive correlation.

Above this, $\Delta^{13}C$ increases to approximately 27‰, 80 cm below OAE2 (122.20 m). From the onset of the OAE2 CIE to ~1 m above Bentonite B (121.0-111.0 m), $\Delta^{13}C$ displays an excursion of -1‰ on average, but is as great as -3‰ at a few horizons with highly depleted $\delta^{13}C_{carb}$. Above the OAE2 CIE (~<105 m), $\Delta^{13}C$ values are 0.4‰ higher than the pre-OAE2 values above fs2b. The reliability of this proxy is later tested by assessing the role of diagenesis on $\delta^{13}C_{carb}$ (Sect. 4.5).

4.4.4. Astrochronology

Spectrograms from EHA analysis of the SH#1 $\delta^{13}C_{carb}$ dataset reveal frequencies with high amplitude and harmonic F-test values as a function of depth (Figure 4.8b-c). Between 116.5-97.0

m depth a continuous, high-amplitude (normalized), and significant (F-test>80%) peak occurs at low frequencies (<0.5 cycles/m). Additionally, multiple significant peaks smear to higher frequencies near 108.5 m, corresponding to a sharp increase in carbonate content in overlying strata (10-20% to 30-50%).

Several intervals throughout OAE2 in SH#1 exhibit ASM values below the established H_o threshold of 0.10% (see Methods) (Figure 4.8d). Therefore, we are able to reject the null hypothesis that the SH#1 $\delta^{13}C_{carb}$ chemostratigraphy does not preserve astronomical cycles (Figure 4.8d-e). Low H_o ASM sedimentation rate estimates average 2.9 cm/kyr (min. = 2.1 cm/kyr; max. = 5.0 cm/kyr) in the Tropic Shale of SH#1 between 119.01-97.01 m depth. Two potential eASM sedimentation rate solutions of 2.5 and 4.5 cm/kyr occur near Bentonite A. However, subsequent testing with an increased window size (7 m) substantiates the 2-3 cm/kyr estimate. Nevertheless, results from this lowermost OAE2 interval warrant caution during interpretation. The size of the EHA window (5 m) and the likelihood of diagenetically altered $\delta^{13}C_{carb}$ values in the lowermost Tropic Shale (see Figures 4.6-4.7) preclude extension of eASM analysis below 119.01 m. Higher in the core, near 104 m, two significant eASM sedimentation rate estimates are anomalously elevated (5.0 cm/kyr) compared to neighboring data points. However, no other trends in F-test spectrograms support a change in sedimentation rate, such as peak smearing. Some intervals within OAE2 do not exceed the H_o threshold from eASM analysis, and preserve equivocal evidence for astronomical cycles (116.41-114.81 m and 109.11-108.11 m).

Given statistically significant evidence for astronomical cycles in SH#1, we calculate additional sedimentation rate estimates using frequency domain minimal tuning and bandpass filtering methods (Figure 4.8c). The resulting sedimentation rate estimates from short eccentricity tracing of EHA results average 3.3 cm/kyr, ranging more than twofold from 1.9 to 5.0 cm/kyr. Similarly, but with more muted variability, the bandpass filtered sedimentation rate averages 2.9 cm/kyr. Combined, sedimentation rate curves from frequency domain minimal tuning, eASM, and bandpass filtering techniques record similar trends in sedimentation patterns in SH#1 through the OAE2 interval (Figure 4.8e). Notably, an abrupt shift to lower sedimentation rates at 108.5 m near the top of the OAE2 CIE separates two packages of sedimentation rate that increase up-core (117-108.5 m, 108.5-97.0 m) in a saw-toothed pattern (Figures 4.8e and 4.10). This change in sedimentation is also associated with F-test peak smearing to higher frequencies consistent with an abrupt decrease in sedimentation rate, and a local minimum in $\delta^{13}C_{carb}$ values. Smaller scale variations (i.e., several meters) in sedimentation rates nest within these broader trends, especially within the upper package. Herein, we label the two increasing up-core sedimentation rate packages after the transgressive-regressive Cycle 1 and 2 of Leithold (1994) given their correlation (Figures 4.8 and 4.10). The estimated temporal duration between Bentonites A and D from the ATS in SH#1 (679±25 kyr) is equivalent within uncertainty to the duration calculated from intercalibrated radioisotopic ages (610±350 kyr; Meyers et al., 2012a).

Our MTM analysis of the tuned SH#1 $\delta^{13}C_{carb}$ time series from EHA tracing of the short eccentricity cycle (interpolated to a spacing of 3 kyr, the minimum spacing of the uninterpolated timeseries) generates seven significant periods, following the criteria of Meyers (2012b) (F-test >90%, LOWSPEC confidence level >90%) (Table 4.1; Figure A3.2). Five of these cycles correspond to predicted astronomical periods with offsets of less than 2 kyr (Laskar et al., 2004; Laskar et al., 2011), including a short eccentricity, two obliquity, and two precession terms. Of the two unpredicted terms at 27 and 30 kyr, Ma et al. (2014) identified a similar significant period

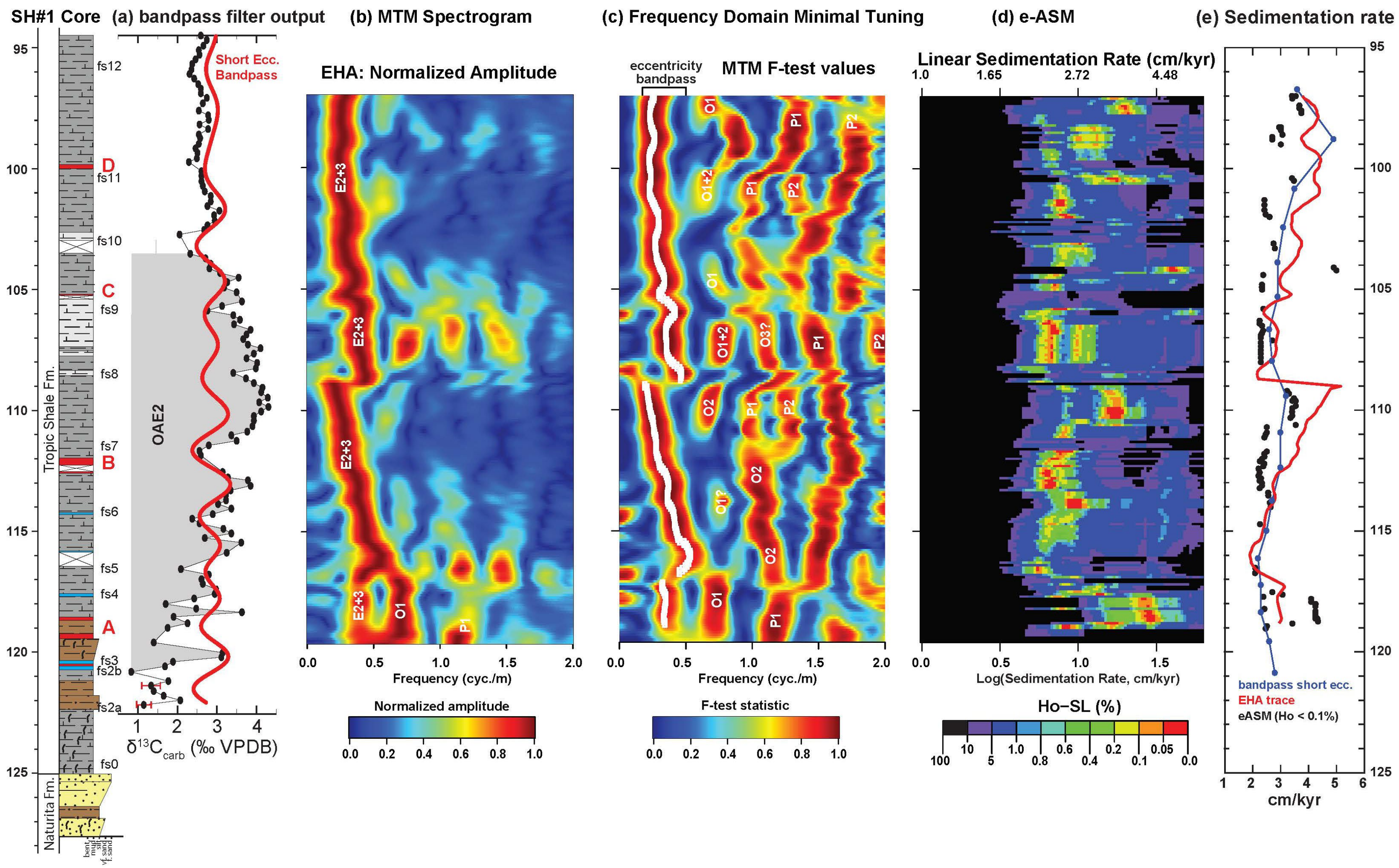

Figure 4.8. Astrochronologic analysis of the SH#1 core. (a) Bandpass filter of the $\delta^{13}C_{carb}$ dataset with heavily depleted values removed. (b) Multi-taper method (MTM) spectrogram of evolutive harmonic analysis (EHA) results, with short eccentricity labelled. (c) Frequency domain minimal tuning tracing (white circles) of spectrogram of F-test values. (d) Evolutive average spectral misfit (eASM) results as a function of simulated sedimentation rate versus depth with significance levels (H_o-SL). (e) Sedimentation rate estimates from various astrochronologic techniques. See text for methods and results.

(~28 kyr) in the Hartland Shale of the Angus core in Colorado, which they attribute to an additional short obliquity term.

4.4.5. XRF

High-resolution core scanning XRF calcium count data (Figure 4.9) track carbonate content values from coulometry and are used to refine carbonate sedimentation trends (see Figure 4.6). Spikes in Ca counts punctuate the continuous XRF dataset at macrofossil-bearing, carbonate-rich horizons (e.g., 120.6 m, 120.4, 117.7, 116.6, 114.4 etc.). Ratios of Ti/Al and Zr/Al, proximal-distal sediment proxies (Sageman et al., 2014b), preserve two cycles of increasing values up-core in the lower Tropic Shale below Bentonite B (maxima at 122.3, 116.6 m). Above ~109 m, Ti/Al and Zr/Al ratios are lower and generally more stable than below Bentonite B. In bentonitic intervals, Ti/Al ratios reach minima and Zr/Al ratios spike (e.g., 112.6 m).

4.5. Discussion

4.5.1 SH#1 Core Chemostratigraphy and OAE2 Onset

The $\delta^{13}C$ chemostratigraphy of the Tropic Shale in SH#1 reveals a relatively continuous CTB interval with a highly expanded (17.5 m) and characteristic, positive CIE that defines OAE2 (Figures 4.5-4.6). High sedimentation rates (Figures 4.8 and 4.10) enable an analysis of paleoenvironmental responses at a fine temporal resolution through OAE2 (avg. 35-kyr meter of strata), with no evidence for significant hiatuses in the form of sharp facies shifts, faults, or abrupt geochemical shifts and an ATS providing quantitative constraints on rates of change. Thus, the proximal offshore location of the SH#1 core is uniquely situated as it allows precise correlation of offshore facies and chemostratigraphic trends to the transgressive-regressive stratigraphic patterns

Table 4.1.: Significant (F-test confidence level (CL) >90%) astronomical periods detected in SH#1 from the interpolated (3 kyr) short eccentricity EHA-traced $\delta^{13}C_{carb}$ time series. Upper and lower bandwidth resolution periods are calculated as observed frequency plus/minus half the Rayleigh frequency (f_{ray} = 0.00141844 kyr^{-1}). Minimum temporal offsets in observed periods versus predicted astronomical periods at right (Laskar et al., 2004, 2011; Meyers et al., 2012b).

	Observed Frequency	**F-test harmonic CL (%)**	**LOWSPEC CL (%)**	**Observed Period (kyr)**	**Bandwidth resolution (kyr)**		**Target astronomical periods (kyr)**	**Minimum offset (kyr)**
1	0.010875	99.90	99.95	91.96	98.37	86.33	E3: 96.91 (101.13-93.03)	0
2	0.021513	99.98	73.08	46.48	48.07	45.00	O1: 48.54 (49.33-47.79)	0
3	0.028369	97.60	98.16	35.25	36.15	34.39	O2: 37.66 (37.95-37.38)	1.23
4	0.032624	95.76	97.58	30.65	31.33	30.00	O3? See text	-
5	0.036879	98.15	99.50	27.12	27.65	26.60	O3? See text	-
6	0.041371	96.53	98.88	24.17	24.59	23.76	P1: 22.42 (23.24-21.66)	0.52
7	0.0513	98.78	95.26	19.49	19.77	19.23	P2: 18.33 (18.40-18.26)	0.84

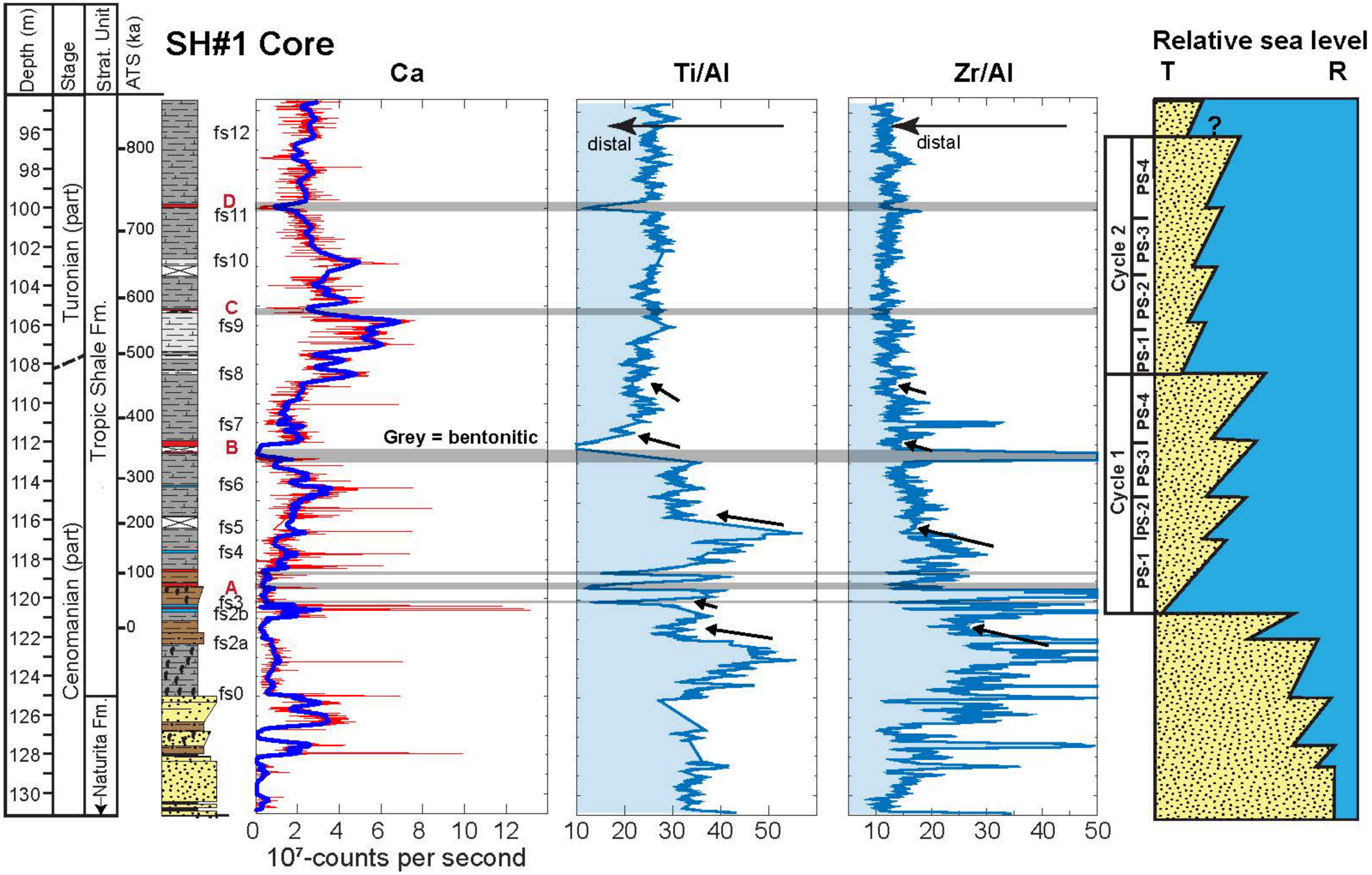

Figure 4.9. Select XRF elemental counts and ratios with 51-point smoothing from 94-131 m in SH#1. Shaded depths represent bentonitic intervals. Relative sea level derived from reconstructed sedimentation rates.

of nearby coeval shoreline facies (Elder et al., 1994; Leithold, 1994; Uličný, 1999; Tibert et al., 2003; Laurin and Sageman, 2007).

Although the Naturita-Tropic contact is located at 125 m in SH#1 based on lithostratigraphic convention, Uličný (1999) interpreted the lower 4 m of Tropic Shale as proximal offshore shale subunits of the Naturita Formation within the upper *M. mosbyense* biozone. These lithologies represent a transitional interval, with comparatively high-frequency stratigraphic packages recording ~10-20 m changes in relative sea level. In a west to east cross section including the KPS outcrop site, Uličný (1999) documented a set of basinward stacking parasequences (his units 4-6A) overlain by a notable amalgamated sequence boundary (with evidence of fluvial incision) and flooding surface (SB/FS). We correlate this flooding surface to surface "fs2a" of Elder et al. (1994) at ~122.2 m in SH#1 (Figures 4.4-4.5) and, based on the Elder et al. (1994) correlation to the GSSP in Pueblo, CO, the sequence boundary correlates to the pre-OAE2 hiatus lying just below the base of the Bridge Creek Limestone, first recognized by Pratt (1984). Just above the hiatus in Pueblo, predominantly laminated TOC-rich black shale facies shift to interbedded and bioturbated limestone-marlstone couplets, reflecting a major change in WIB sedimentation consistent with a major transgression (Figure 4.2). The "fs2b" flooding surface in Utah reflects this transgression, which Elder et al. (1994) correlated landward to a >150 km backstep of the shoreline and basinward to the condensed basal limestone of the Bridge Creek Member (Bed 63, Cobban and Scott, 1973; LS1, Elder et al., 1994). Ratios of Ti/Al and Zr/Al also shift to lower values through this interval (120-122 m) in SH#1, consistent with more distal facies above the transgression (Figure 4.9).

In the pre-OAE2 interval of the lowermost Tropic Shale in SH#1, carbonate contents decrease (<5.0%) and $\delta^{13}C_{carb}$ shifts to more enriched values (>0‰) above flooding surface fs2a at ~122 m, suggesting abrupt changes in carbonate sedimentation, preservation, or local carbon cycling (Figure 4.6). If the carbonate below fs2a is primary, the depleted $\delta^{13}C$ values could be the product of an estuarine or lagoonal depositional setting. Brackish water agglutinated benthic foraminifera and bivalve taxa support some degree of marine and fresh water mixing (Sageman et al., 1997b; Uličný, 1999; Tibert et al., 2003). However, strong positive covariance of $\delta^{13}C_{carb}$ and $\delta^{18}O_{carb}$ ($r = +0.91$, p-value < 0.01) and negative covariance of $\delta^{13}C_{carb}$ and carbonate content ($r = -0.65$, p-value $= 0.011$) in this interval are characteristic of diagenesis from meteoric waters and/or subaerial exposure (Figures 4.6-4.7) (Allan and Matthews, 1982). These geochemical observations are consistent with a relative sea level lowstand and associated carbonate diagenesis immediately preceding the onset of OAE2 along the western margin of the seaway.

Relative sea level lowstands and sequence boundaries have been interpreted in other upper Cenomanian successions just prior to initiation of OAE2, such as in the Anglo-Paris Basin (Robaszynski et al., 1998; Gale et al., 2008), Germany (Voigt et al., 2006; Richardt and Wilmsen, 2012), Egypt (Nagm, 2015), and Perú (Navarro-Ramirez et al., 2016). These findings, together with our observations from the SH#1 to Pueblo transect, suggest a eustatic origin for the pre-OAE2 lowstand. Additionally, the base of the OAE2 CIE lies 1.2 m above fs2a in SH#1. Extrapolating with a linear sedimentation rate below the ATS base, this represents a 41-kyr lag between the sea level fall prior to the event and the eventual carbon cycle perturbation (Figure 4.8). Globally, a lag of similar duration separates the earlier onset of LIP volcanism and the later onset of both the CIE (Turgeon and Creaser, 2008; Du Vivier et al., 2014) and indicators of anoxia (Ostrander et al., 2017), suggesting a prolonged (10's kyr) Earth System response to LIP volcanism (Adams et al., 2010).

4.5.2. Mechanism for $\delta^{13}C_{carb}$ Cyclicity in SH#1: Sea Level and Diagenesis

Lithofacies are more homogenous in the main body of the Tropic Shale above flooding surfaces fs2b and fs3 than in the underlying interval, and dominantly consist of black calcareous shale with occasional shell-rich or calcareous concretion horizons (Figure 4.4). However, the $\delta^{13}C_{carb}$ chemostratigraphy records notable variability in SH#1, with relatively depleted values cyclically punctuating the broader positive CIE of OAE2, exerting an influence on our astrochronologic analysis (Figures 4.6-4.8). Depletion of $\delta^{13}C_{carb}$ values that matches orbital rhythms could result from either of two processes (or a combination of both): 1) astronomical forcing of the global carbon cycle (e.g., Them et al., 2017), such as changes in global organic carbon burial rates; or 2) recurring diagenetic alteration of carbonate due to another process sensitive to orbitally-forced climatic oscillations (Arthur and Dean, 1991), such as relative sea level. Generally, carbonate diagenesis shifts $\delta^{13}C_{carb}$ and $\delta^{18}O_{carb}$ to more depleted values due to the incorporation of isotopically light, organically respired C and meteoric O into the lattice of carbonate minerals (Swart, 2015), as is observed in SH#1 at a number of carbonate-rich horizons (121.0, 119.8, 116.5, 111.4, 108.4, 103.5 m) (Figure 4.6). Accordingly, higher positive covariation of $\delta^{18}O_{carb}$ vs. $\delta^{13}C_{carb}$ in several of these intervals, as well as the common occurrence of carbonate concretions in the Tropic Shale below Bentonite B in the KPS outcrop, support the interpretation of carbonate diagenesis (109 and 105.5 m) (Figures 4.4 and 4.6).

In carbonate platform settings, intervals of depleted stable isotope values tend to correspond to sea level lowstands, subaerial exposure, weathering and remineralization of organic carbon, and meteoric diagenesis (Allan and Matthews, 1982; Mitchell et al., 1997). However, the calcareous shale facies of SH#1 preserve no evidence for subaerial exposure during OAE2.

Instead, the diagenetically altered intervals in the main body of the Tropic Shale correspond to carbonate-rich horizons interpreted as flooding surfaces that immediately overlie lowstands, based on westward correlation to transgressive lags that form the upper boundaries of siliciclastic parasequences (Elder et al., 1994). Similar relationships between carbonate diagenesis and flooding surfaces have been documented in more proximal siliciclastic shoreface successions (Al-Ramadan et al., 2005), including the Upper Cretaceous Book Cliffs of Utah (Taylor et al., 2000; Taylor and Machent, 2010).

Given the strong connection between astronomically forced $\delta^{13}C_{carb}$ minima and geochemical indicators of diagenesis, carbonate concretions, and flooding surfaces, along with the absence of similarly pulsed depletions in $\delta^{13}C_{org}$ (Figure 4.6), we do not attribute the short-lived negative shifts in $\delta^{13}C_{carb}$ in SH#1 to changes in the global carbon cycle. Instead, we propose that periodic shifts to depleted $\delta^{13}C_{carb}$ from carbonate diagenesis were driven by astronomically forced transgressions (i.e., flooding surfaces) during OAE2. At these condensed horizons, extended exposure of sediments at the seafloor allowed enhanced organic carbon remineralization and diagenetic recrystallization within the shell-rich beds, commonly resulting in the formation of carbonate concretions in outcrop (Figure 4.4) (Taylor et al., 1995; Klein et al., 1999). We hypothesize that freshwater influence during subsequent relative lowstands (e.g., submarine groundwater discharge) delivered isotopically depleted meteoric waters, which were progressively incorporated into diagenetic carbonate forming at more permeable, shell-rich flooding surfaces in the Tropic Shale (Carpenter et al., 1988; Taylor et al., 2000; Dale et al., 2014). Interestingly, the stratigraphic patterns of these flooding surfaces preserve a strong astronomical signal, highlighting an orbital, and therefore climatic, control on relative sea level patterns in the tectonically active foredeep of the WIB during OAE2.

4.5.3. Astronomically Forced Genetic Stratigraphic Sequences during OAE2

Sedimentation rate reconstructions of the SH#1 $\delta^{13}C_{carb}$ record provide additional direct evidence for astronomical forcing of relative sea level patterns through OAE2 (Figures 4.8-4.10). For example, we identify two specific amalgamated SB/FS in SH#1 that bound an interval of four parasequences, suggesting eccentricity bundling (i.e., PS-1 to PS-4 of Figure 4.10). One occurs at a major regional flooding surface (fs2b - 120.6 m) and a second at an abrupt decrease in ATS sedimentation rate (new fs8 - 108.5 m) (Figure 4.10). Distinct increases in carbonate content, depleted $\delta^{13}C_{carb}$ and $\delta^{18}O_{carb}$, and minima in Ti/Al and Zr/Al characterize these two horizons in SH#1, consistent with SB/FS of Cycle 1. Given the ~400 kyr duration of the sequence, hierarchical stacking (4:1) of minor sea level oscillations (~100 kyr), and the apparent repetition of these increasing up-core sedimentation rate cycles (Figure 4.8), we conclude that climate feedbacks from the stable 405-kyr long eccentricity cycle paced relative sea level sequences, and that nested parasequences correspond to the ~100 kyr short eccentricity cycle, as eASM testing confirms.

Shoreline trajectories in the nearby Markagunt Plateau (~100 km WNW of SH#1, Figures 1-2) preserve a well resolved sequence stratigraphy to further test the hypothesis of astronomically-forced transgressive-regressive cycles during OAE2 (Tibert et al., 2003; Laurin and Sageman, 2007). Maximum progradations of parasequence stacking sets there occur near Bentonites B (the Sugarledge Sandstone of Cashion, 1961) and D, and predictably correspond to increasing sedimentation rate estimates in SH#1 (Figure 4.10). Likewise, maximum flooding surfaces in the Markagunt, such as near Bentonite C, correlate to lower sedimentation rate estimates in SH#1.

These analogous relationships between shoreline trajectories from the Markagunt Plateau outcrops and parasequence stacking patterns from SH#1 (i.e., sedimentation rate estimates and geochemistry) support the interpretation that climate feedbacks to the stable eccentricity cycle paced sea level sequences through OAE2. Interestingly, the shale lithofacies of the Tropic Shale in SH#1 are visually homogenous, with subtle fossiliferous horizons, and we can best identify these key sequence stratigraphic surfaces only after astrochronologic and geochemical analysis.

At a finer resolution, a significant shoreline backstep is noted in the Markagunt underlying Bentonite B (Tibert et al., 2003; Laurin and Sageman, 2007) and is coeval with a decrease in Ti/Al values in SH#1, consistent with a major flooding surface (Figure 4.9). However, the stepwise decrease in sedimentation rates in the SH#1 ATS occurs one parasequence above Bentonite B, indicating that the most significant decreases in local sedimentation rate occurred at maximum flooding surface, as opposed to at the transgressive surface, likely due to basin hypsometry or other sediment transport processes.

Many authors have proposed that long (i.e., 2.4 Myr) and stable eccentricity forcing of the Late Cretaceous greenhouse climate system produced eustatic sea level cycles in the stratigraphic record, a potentially powerful tool for intercontinental correlation (Gale et al., 2002; 2008; Boulila et al., 2011; Haq, 2014; Wendler et al., 2014). Short and stable eccentricity cycles (i.e., 100, 405 kyr) have previously been proposed to correspond to relative sea level sequences along the western paleoshoreline of the WIB (Elder et al., 1994; Leithold, 1994; Uličný, 1999; Laurin and Sageman, 2007; Zhu et al., 2012). Using astrochronologic techniques that link modulations of sea level and associated carbonate diagenesis at flooding surfaces to the stable eccentricity cycle, the SH#1 record quantitatively validates a strong climatic, as opposed to tectonic, control on short-term trends (<1 Myr) in accommodation space regionally. These findings are consistent with eccentricity periodicities in the Cenomanian-Turonian sequences of the Levant Platform of Jordan (Wendler et al., 2014), and potentially in the Bohemian Basin (Uličný et al., 2014), and allude to a climatic control on mid-Cretaceous eustasy.

Although the OAE2 onset interval preserves minor evidence for obliquity amplification near the base of the ATS in SH#1 (Figure 4.8b), eccentricity forcing is dominant throughout the study interval, and especially robust above 117 m (Figure 4.10). Recent studies of proto-North Atlantic and Tethys sites alternatively indicate that the axial obliquity cycle dominated organic carbon burial, ocean circulation, and the hydrologic cycle during OAE2 and the Turonian Stage (Meyers et al., 2012b; Laurin et al., 2015; Kuhnt et al., 2017; Jones et al., 2018a; Charbonnier et al., 2018). Processes capable of driving Late Cretaceous eustatic cycles remain enigmatic and areas of research, such as aquifer eustasy (Wendler et al., 2016) and glacio-eustasy (Bornemann et al., 2008). However, the storage of water on continents inherently results from terrestrial climate conditions sensitive to orbital cycles. We therefore tentatively attribute the ~100 and ~405 kyr oscillations in sea level during OAE2 to terrestrial paleoclimate feedbacks from eccentricity forcing, and suggest that paleoceanographic proxies (e.g., redox) record amplified obliquity forcing due to changes in water mass circulation patterns, potentially originating at high latitudes (Meyers et al., 2012b).

4.5.4. SH#1 Paleoclimate and Paleocirculation Data

Recovery of fossils with aragonitic shell material from the Kaiparowits Plateau indicates retention of primary carbonate geochemistry, and thus potential for reliable paleoclimate data

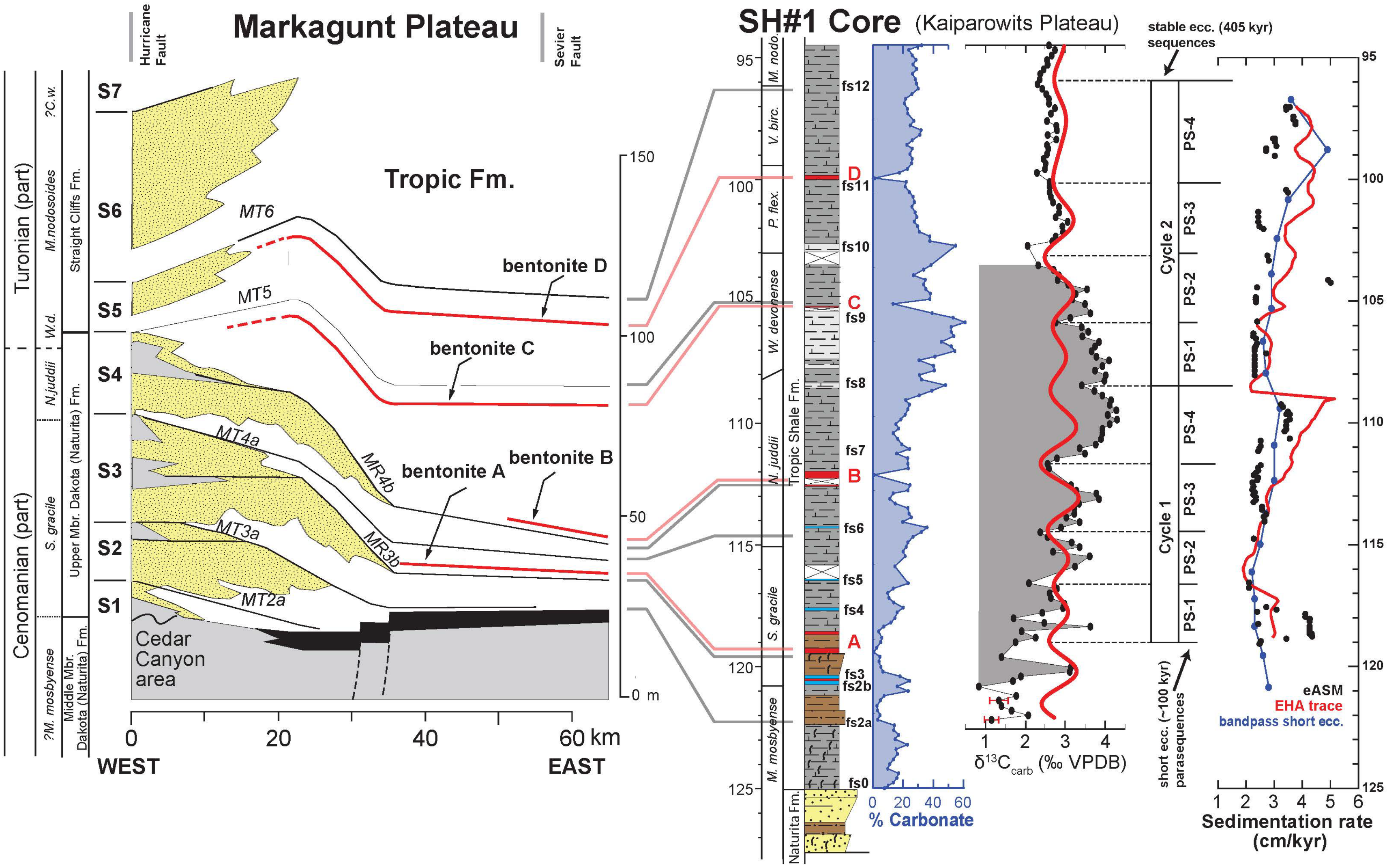

Figure 4.10. Correlation of Cenomanian-Turonian genetic sea level sequences (e.g., S4) of the Markagunt Plateau (left) (see Figure 4.1) to the OAE2 interval astrochronology and $\delta^{13}C_{carb}$ chemostratigraphy of the SH#1 core (right) via bentonite stratigraphy (figure modified from (Laurin and Sageman, 2007). Maximum transgressive surfaces (e.g., MT5), maximum regressive surfaces (e.g., MR3b), and sequences (S1-S7) of Laurin and Sageman (2007) indicated in Markagunt Plateau. In the

SH#1 core, sequences (e.g., Cycle 2; nomenclature from Leithold, 1994) and parasequences (e.g., PS-2) are assigned using flooding surfaces identified from short eccentricity bandpass and sedimentation rate estimates from astrochronology (right). Marker bed designation of SH#1 and biostratigraphy of Markagunt Plateau from Elder et al. (1994) and Tibert et al. (2003). See text for discussion.

during OAE2 (e.g., Pagani and Arthur, 1998). Flooding surfaces at specific horizons in SH#1 exhibit geochemical evidence for early carbonate diagenesis (see above) precluding paleoclimate interpretations. However, average $\delta^{18}O_{carb}$ values through OAE2 in SH#1 (-8.11±1.82‰), as well as $\delta^{18}O_{carb}$ values from intervals between flooding horizons, are similar to previously reported values from elsewhere in the basin (Pratt, 1985; Pratt et al., 1993; Keller et al., 2004; Caron et al., 2006), including the nearby Escalante core, which records minimal trace element evidence for diagenetic alteration of macrofossils (Pagani and Arthur, 1998). Additionally, the fact that nannofossils do not preserve calcite overgrowths, and isotopic values are not all extremely depleted (e.g., Taylor et al., 2000), nor do the values decrease with depth, suggests that carbonate from SH#1 and the Kaiparowits Plateau has not undergone pervasive burial diagenesis (e.g., Jenkyns et al., 1994).

The early phase of OAE2 in many European sections is characterized by evidence for cooling in an interval termed the Plenus Cold Event; it is marked by a distinctive positive shift in $\delta^{18}O$ and the appearance of faunal elements with Boreal affinities (Gale and Christensen, 1996; Jenkyns et al., 2017). Although a similar occurrence of positive $\delta^{18}O$ values was documented by Pratt (1985) in the distal offshore Bridge Creek Limestone of the WIB, they occur within an interval characterized by a significant influx of southern warm-water Tethyan taxa (Kauffman, 1984; Eicher and Diner, 1985). In contrast, the SH#1 record is characterized by more depleted $\delta^{18}O$ values in the early phase of OAE2 (Figure 4.6). We have argued that diagenetic alteration can explain depleted isotopic values in flooding surfaces, but that evidence for alteration between flooding surfaces is minimal. A possible explanation for the general depletion in $\delta^{18}O$ values is the influence of a lower salinity, isotopically light Boreal water mass along the western margin of the seaway. This circulation pattern is predicted by numerical models of the seaway (Slingerland et al., 1996), and supported by nannofossil stratigraphy (this study, see Biostratigraphy), macrofossil geochemistry (Pagani and Arthur, 1998), and microfaunal records (Eicher and Diner, 1985; Leckie et al., 1998; Tibert and Leckie, 2013; Elderbak and Leckie, 2016; Eldrett et al., 2017; Lowery et al., 2018). Alternatively, increased continental runoff could result in lighter $\delta^{18}O$ values in carbonates (e.g., Pratt et al., 1993; Petersen et al., 2016), but there is no definitive evidence for an increase in runoff at this time.

Additionally, $\Delta^{13}C$ values ($\delta^{13}C_{carb}$-$\delta^{13}C_{org}$) can be interpreted as a proxy for carbon isotope fractionation during photosynthesis (Freeman and Hayes, 1992; Hayes et al., 1999) (Figure 4.6). The values are sensitive to a variety of paleoenvironmental conditions, such as dissolved CO_2 levels and phytoplankton growth rates due to nutrient loading, although sedimentological factors, such as carbonate diagenesis or primary changes in organic matter type can potentially bias the proxy (Kump and Arthur, 1999). Discounting datapoints likely influenced by diagenesis (open symbols in Figure 4.6), the lower interval of the OAE2 in SH#1 shows a trend to lower $\Delta^{13}C$ values. This observation is consistent with other OAE2 records from Europe and Morocco, and has been interpreted as a signal of pCO_2 drawdown due to a global increase in organic carbon burial (Jarvis et al., 2011; Kuhnt et al., 2017). Reconstructions of pCO_2 based on fossil leaf stomata measurements in the coeval paralic facies of the Naturita (Dakota) Formation, to the west of SH#1 and KPS, also indicate a drawdown in pCO_2, although the measurements only correspond to the lowest portion of the OAE2 interval (Barclay et al., 2010). From these preliminary results it appears that the WIB records evidence of processes consistent with the Plenus Cold Event (i.e., pCO_2 drawdown), but there is neither direct geochemical or paleobiogeographic (e.g., Kauffman, 1984) evidence for cooling.

4.5.5. Regional and Global Correlation of SH#1 Record

Using traceable horizons, such as Bentonites A-D and characteristic segments of the CIE, we compare durations of OAE2 from short eccentricity bandpassed ATS of three central WIB cores: SH#1, the Angus core (Ma et al., 2014), and the Portland core near the CTB GSSP (Meyers et al., 2012a) (Figure 4.1) (Table 4.2). The lower OAE2 interval records the largest uncertainty ($1\sigma \pm 60$ kyr), possibly due to condensation at LS1 in Pueblo (Figure 4.11). However, the sites yield equivalent total durations for OAE2 of 600 ± 31 kyr (1σ), with the event's termination defined at the top of the main CIE. The distal limestone beds in the upper segment of OAE2 from the Portland core and GSSP in Colorado (Beds 79, 84, 86, 90, 97, 101) are time equivalent to proximal flooding surfaces in SH#1 in Utah (fs6-fs12), and both locations are dominantly paced by the short eccentricity cycle (Figure 4.11), confirming proximal-distal lithostratigraphic correlation schemes for the CTB interval in the WIB (Hattin, 1971; Elder et al., 1994; Elderbak and Leckie, 2016).

Workers have long debated depositional models for the traceable marlstone-limestone interbeds of the Bridge Creek Limestone (Pratt, 1981; Pratt, 1984; Barron et al, 1985; Eicher and Diner, 1989; Einsele and Ricken, 1991; Arthur and Dean, 1991; Elder et al., 1994; Meyers et al., 2001; Floegel et al., 2005; Eldrett et al., 2015b; Elderbak and Leckie, 2016), surmising that the couplets represent either: 1) carbonate productivity cycles, 2) oscillating siliciclastic dilution, or 3) a combination of these processes (Barron et al., 1985; Sageman et al., 1997a). Dynamic shoreline backstepping and flooding of coastal plains and estuaries, as the Markagunt Plateau and SH#1 records indicate, provides a direct mechanism to divert terrigenous sediment to the paralic foredeep and limit siliciclastic dilution basinward in the Bridge Creek Limestone. As a result, astronomically-forced shoreline parasequences detected along the Utah coastal margin, and associated fluctuations in siliciclastic dilution, may have been a key depositional mechanism behind the formation of rhythmically-bedded CTB strata traceable across the WIB (Elder et al., 1994; Meyers et al., 2001; Tibert et al., 2003; Laurin and Sageman, 2007).

Among other well-studied examples of OAE2, Gongzha, Tibet exhibits the most expanded section that also has an ATS (Li et al., 2017), preserving a similar CIE structure and an equivalent duration for the CIE plateau (C4) of OAE2 compared to SH#1 (Figure 4.12). However, the ATS estimates for the duration of OAE2 at SH#1 (619±39 kyr) and Gongzha (820±39 kyr) diverge, highlighting the challenge of precise intercontinental correlation and assignment of consistent durations to an event like OAE2, in part due to different approaches to the definition of its onset and termination. This offset decreases if we include the minor $\delta^{13}C$ enrichments below Bentonite D in SH#1 in the event's definition (scenario 2: OAE2 = 717±39 kyr and 21.5 m thick), as Sageman et al. (2006) propose in one scenario at the Pueblo GSSP. However, employing the "end of $\delta^{13}C$ plateau" definition for the OAE2 termination (sensu Tsikos et al., 2004) at the top of the C4 segment, estimated durations remain offset between SH#1 (517 kyr) and Gongzha (650 kyr). One possible explanation is that the OAE2 onset interval (C3) is significantly condensed in the fs2b-fs3 flooding horizons of the Kaiparowits Plateau, though a coeval expanded record from the Angus core (Denver Basin, WIB) (Ma et al., 2014) suggests that a maximum of 85 kyr could be missing. Alternatively, changes in sedimentation rates in the Gongzha CTB section might produce spurious eccentricity cycles, given that evolutive astrochronologic techniques were not used there (Li et al., 2017). One advantage of the WIB record in this regard is the presence of intercalated radioisotopic U/Pb and ^{40}Ar/^{39}Ar dates from bentonites (Meyers et al., 2012a), which support all three ATS results shown in Figure 4.11.

Table 4.2: Comparison of durations in kiloyears (kyr) between traceable horizons, such as bentonites (bent.) and the initiation of OAE2 CIE, in CTB interval of WIB from the SH#1 core (this study), the Angus core (Ma et al., 2014), and the Portland core near the GSSP (Meyers et al., 2012a).

Durations (kyr)	**CIE-Bent. A**	**Bent. A-B**	**CIE- Bent. B**	**Bent. B-C**	**Bent. C-D**	**OAE2**
SH#1 core	82	263	345	226	144	619
Angus core	167	143	310	255	-	565
Portland core	-	204	-	286	148	617
WIB average	125	203	328	256	146	600
st.dev. (+/-)	60	60	25	30	3	31

Figure 4.11. (next page): Correlation of astronomically tuned Cenomanian-Turonian Boundary sections (see Figure 4.1) across the WIB via bentonite stratigraphy and δ^{13}C chemostratigraphy. Short eccentricity bandpass filters of astrochronologic and δ^{13}C chemostratigraphic records presented in a proximal-distal transect from SH#1 (*this study*), Angus core (Joo and Sageman, 2014; Ma et al., 2014), and Portland core near the GSSP (Meyers et al., 2001; Sageman et al., 2006). Radioisotopic ages for bentonites and Portland core stratigraphic column from Meyers et al. (2012b), and bed numbering (e.g., LS1/Bed 63 in Portland and fs2b in SH#1) follows Cobban and Scott (1972) and Elder et al. (1994).

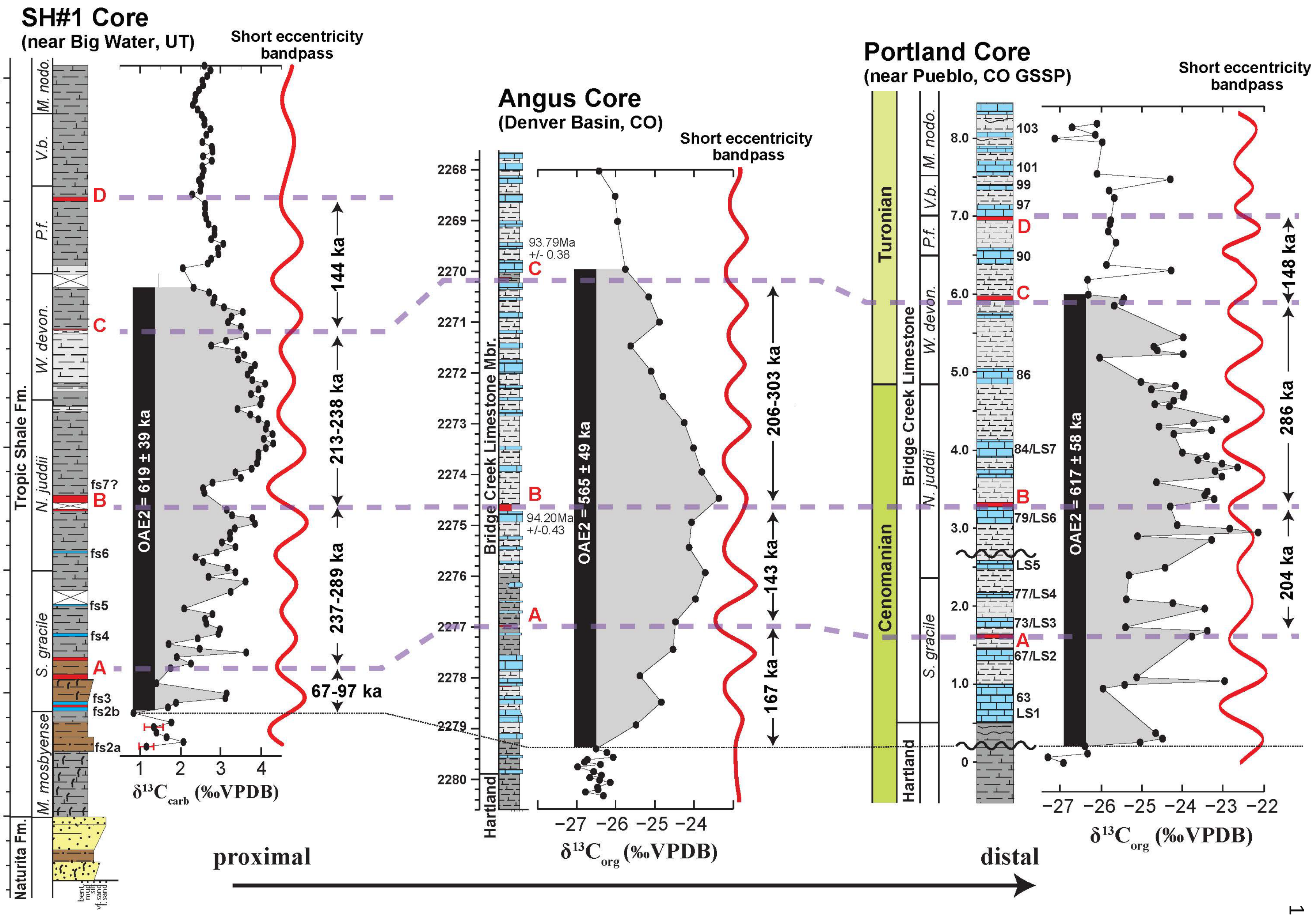
SH#1 Core
(near Big Water, UT)
Short eccentricity bandpass
95
100
105
110
115
120
125
Tropic Shale Fm.
Naturita Fm.
M. nodo.
V.b.
P.f.
W. devon.
N. juddii
S. gracile
M. mosbyense
D
C
B
A
fs7?
fs6
fs5
fs4
fs3
fs2b
fs2a
bent.
mud
silt
vf. sand
f. sand
OAE2 = 619 ± 39 ka
1 2 3 4
δ13Ccarb (‰VPDB)
144 ka
213-238 ka
237-289 ka
67-97 ka
Angus Core
(Denver Basin, CO)
Short eccentricity bandpass
2268
2269
2270
2271
2272
2273
2274
2275
2276
2277
2278
2279
2280
Bridge Creek Limestone Mbr.
Hartland
93.79Ma +/- 0.38
94.20Ma +/-0.43
OAE2 = 565 ± 49 ka
−27 −26 −25 −24
δ13Corg (‰VPDB)
206-303 ka
143 ka
167 ka
Portland Core
(near Pueblo, CO GSSP)
Short eccentricity bandpass
Turonian
Cenomanian
Bridge Creek Limestone
Hartland
8.0
7.0
6.0
5.0
4.0
3.0
2.0
1.0
0
103
101
99
97
90
86
84/LS7
79/LS6
LS5
77/LS4
73/LS3
67/LS2
63
LS1
OAE2 = 617 ± 58 ka
−27 −26 −25 −24 −23 −22
δ13Corg (‰VPDB)
148 ka
286 ka
204 ka
proximal
distal

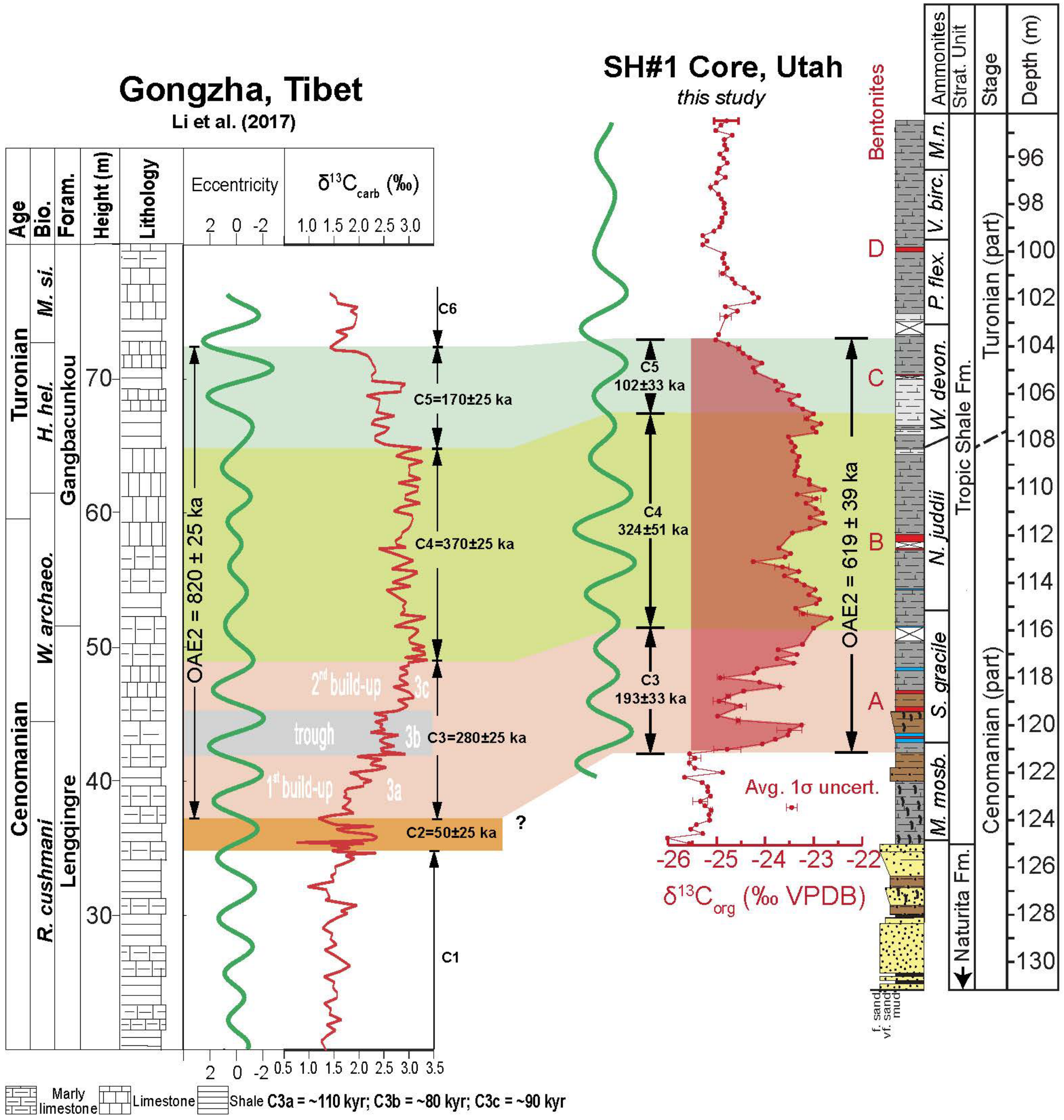

Figure 4.12. Correlation of highly expanded, astronomically tuned OAE2 sections from Gongzha, Tibet (left) (figure modified from Li et al., 2017) and SH#1 (right) via δ^{13}C chemostratigraphy subdivided into shaded segments titled C2-C5. See text for discussion.

4.6. Conclusions

The $\delta^{13}C$ chemostratigraphic results from the SH#1 core presented herein characterize the most expanded record of OAE2 to-date from the central North American WIB. Additionally, this study develops a stratigraphic technique to resolve astronomical forcing of relative sea level in calcareous shale successions by mechanistically linking periodic modifications of geochemical data due to diagenesis (e.g., $\delta^{13}C_{carb}$) with sequence stratigraphic surfaces. Repetitive horizons of diagenetic alteration in SH#1 punctuate the $\delta^{13}C_{carb}$ chemostratigraphy and correlate to flooding surfaces, which trace across the Kaiparowits and Markagunt Plateaus of southern Utah (Elder et al., 1994; Tibert et al., 2003; Laurin and Sageman, 2007). Spectral analyses of the $\delta^{13}C_{carb}$ dataset, via EHA, bandpass filtering, and eASM techniques, generate significant evidence for astronomical pacing of relative sea level oscillations through OAE2. The ATS sedimentation rates from SH#1 indicate that stable long eccentricity (405 kyr) defines sequences through OAE2 and modulates nested short eccentricity cycles (~100 kyr) of parasequences, linking climate and relative sea level. Although we must consider additional climate feedbacks that have could influenced local relative sea level and imparted sediment cyclicity, such as the regional hydrological cycle and sediment delivery, similar coeval patterns in Jordan suggest a eustatic origin to mid-Cretaceous relative sea level oscillations (Wendler et al., 2014).

Correlation of the SH#1 ATS to rhythmically bedded records in the axial basin of the central WIB, such as the CTB GSSP at Pueblo, CO and the Angus core, indicate a consistent duration for OAE2. The correlation also provides insights into the dynamic depositional processes that formed the marlstone-limestone couplets of the Bridge Creek Limestone. Given the lateral continuity of these beds across the WIB and their proximal manifestation as flooding surfaces, we interpret climatically (i.e., astronomically) forced sea level oscillations and associated variation in siliciclastic dilution to be a primary driver of interbedded CTB strata deposition. The ATS and $\delta^{13}C$ chemostratigraphy of SH#1 provide a temporally resolved framework, characterizing an expanded, relatively continuous, fossiliferous, shallow marine stratigraphic archive of OAE2. This record and sections along the greater Kaiparowits Plateau are ideal for future high-resolution analyses to reconstruct paleobiological and geochemical change across the notable Earth-life transition spanning the CTB.

CHAPTER 5

Regional Chronostratigraphic Synthesis of the Cenomanian-Turonian OAE2 Interval, Western Interior Basin: Astrochronology, Radioisotope Dating, and New Os and C Chemostratigraphy

Motivation: Understanding the timing of the triggers and cascading effects of episodes of climate change in Earth history requires age models with precision approaching the kiloyear resolution. The Western Interior Basin (U.S.) preserves a conformable stratigraphic record of the onset of Oceanic Anoxic Event 2 (OAE2) in the Angus core of Colorado, as well as the global stratotype section and point (GSSP) for the Cenomanian-Turonian Boundary (93.9±0.15 Ma) in Pueblo, Colorado. In this chapter, I present new osmium isotope (Os_i) chemostratigraphy from the Angus core and SH#1 core (Utah) to quantify the timing of large igneous province volcanism just prior to OAE2, along with the duration of a relatively brief hiatus at the base of OAE2 at the GSSP, utilizing existing precise astronomical time scales and radioisotopic ages of regional bentonites.

Key findings:

- Unradiogenic initial osmium isotope (Os_i) excursions, marking massive volcanism at onset of OAE2, are robustly preserved in Angus core (Denver Basin) and proximal SH#1 core (Utah) of the U.S. Western Interior.
- Conformable and astronomically-tuned Angus core interval quantifies 59±10 kyr lag between the Os_i excursion, recording volcanism, and carbon isotope excursion, recording net marine anoxia and org C burial globally.

- Conformable records in Western Interior Basin constrain duration of relatively brief hiatus at base of OAE2 in the uppermost Hartland Shale at the Cenomanian-Turonian Boundary GSSP in Pueblo, CO.

CHAPTER 5

Regional Chronostratigraphic Synthesis of the Cenomanian-Turonian OAE2 Interval, Western Interior Basin: Astrochronology, Radioisotope Dating, and New Os and C Chemostratigraphy

Abstract

Fluctuations in depositional conditions during the onset of severe climate events in Earth history predispose stratigraphic archives to hiatuses, often hindering complete reconstructions of these paleoclimate events and their triggers. Several studies have proposed that a hiatus of unknown duration exists in the uppermost Hartland Shale at the base of Oceanic Anoxic Event 2 (OAE2) in the North American Western Interior Basin (WIB) at the Cenomanian-Turonian Boundary (CTB) Global Stratotype Section and Point (GSSP) in Pueblo, Colorado, potentially influencing integrated radioisotopic, biostratigraphic, and astrochronologic age models. To quantify the duration of this hiatus, I utilize geochemical records of the marine osmium record (initial $^{187}Os/^{188}Os = Os_i$), which globally record prolific large igneous province (LIP) volcanic activity 10s kyr prior to the carbon isotope ($\delta^{13}C$) excursion of OAE2. The study presents a proximal-distal Os_i chemostratigraphic transect of the onset of OAE2 from three sites across the WIB: the SH#1 core (southern Utah), the Angus core (Denver Basin, CO), and the Portland core (near CTB GSSP from Du Vivier et al., 2014). The characteristic stratigraphic lag between Os_i and $\delta^{13}C$ excursions, although not present in the Portland core due to hiatus, occurs in the expanded and apparently continuous records of the onset of OAE2 in the SH#1 core and the Angus core. An existing astronomic time scale for the Angus core quantifies the temporal lag between LIP volcanism and the beginning of OAE2 (59±10 kyr) and constrains the duration of the hiatus in the

Portland core as geologically brief, indicating that the GSSP record is largely conformable through OAE2. This first astronomically-tuned, continuous Os_i record across the onset of OAE2 captures a geologically rapid onset of LIP volcanism, consistent with other records, such that the addition of CO_2 to the ocean-atmosphere system may have initially outpaced CO_2 consumption from silicate weathering, driving changes in marine carbonate chemistry and potentially shoaling the carbonate compensation depth above deep marine sites. Additionally, this refined chronostratigraphic resolution for OAE2 in the central WIB permits a critical evaluation of the hypothesis that significant amounts of time are lost in hiatus, and that the duration of OAE2 is substantially longer (~900 kyr) than early studies of the WIB document (~600-800 kyr), as proposed from recent records in the Eagle Ford of Texas. A detailed comparison and correlation between the CTB successions of Colorado and Texas finds that both regions preserve an equivalent number of short eccentricity cycles with minimal differences in the duration of OAE2, constrained by existing radioisotopic ages. It appears that the earlier reported offsets in event timing primarily arise from the usage of a minor short obliquity cycle (O1) for astrochronologic tuning of the Eagle Ford, and that records of OAE2 from central WIB sites, such as SH#1 and the Angus core, are relatively conformable through the event's initiation.

CHAPTER 5

Regional Chronostratigraphic Synthesis of the Cenomanian-Turonian OAE2 Interval, Western Interior Basin: Astrochronology, Radioisotope Dating, and New Os and C Chemostratigraphy

5.1. Introduction and Background

Resolving the causal mechanisms of major paleoclimate and paleobiotic events in Earth history is critical to understanding the vulnerabilities of modern and ancient ecosystems. However, the extreme changes in depositional environments associated with the onset of many mass extinction events and carbon cycle perturbations, such as sea level fluctuations or ocean acidification, may result in hiatal surfaces that obscure geological evidence of the processes initiating such events (Smith et al., 2001; Holland and Patzkowski, 2015, Baresel et al., 2017). Expanded, or at least relatively continuous, stratigraphic successions with robust time control are, therefore, key to reconstructing climate change in the geologic record. This study investigates the onset of Oceanic Anoxic Event 2 (OAE2, ~94 Ma), a significant Late Cretaceous carbon cycle perturbation lasting over half a million years, through a chemostratigraphic transect of the shallow marine Western Interior Basin (WIB) of North America. It assesses stratigraphic conformability at key reference sites such as the Cenomanian-Turonian Stage Global Boundary Stratotype Section and Point (GSSP) in Pueblo, Colorado, as well as refines the timing of major global geochemical cycles responses to OAE2 and reconstructs sea level across the event's onset.

Major events of volcanism (large igneous provinces - LIPs) commonly precede or are broadly contemporaneous with significant carbon cycle perturbations and mass extinctions through geologic time (Wignall, 2001; Kidder and Worsley, 2010). As a result, elemental and isotopic paleoceanographic proxies sensitive to volcanic fluxes may identify the initiation of such events, as well as elucidate a causal linkage between LIPs and perturbation of the carbon cycle. Moreover, they provide potential chemostratigraphic markers to constrain the relative expansion or condensation of stratigraphic intervals at the onset of these events. This is especially the case for isotopic systems with short marine residence times (τ) that capture rapid changes in geochemical fluxes (e.g., Kuroda et al., 2007). The osmium reservoir of the global ocean mixes over geologically brief timescales (τ << 30 kyr, Oxburgh, 2001; Rooney et al., 2016) and, at the time of deposition, initial marine osmium isotope ratios (^{188}Os/^{187}Os$_{(initial)}$ = Os$_{i}$) principally record changes in the relative fluxes of osmium from two isotopically distinct end members, continental weathering (Os$_{i}$ = ~1.4) and hydrothermal inputs (Os$_{i}$ = 0.13) (Peucker-Ehrenbrink and Ravizza, 2001). Consequently, the Os$_{i}$ proxy has resolved anomalous increases in volcanic activity across many Mesozoic climate transitions, including OAEs, the Triassic-Jurassic Boundary, and the Cretaceous-Paleogene Boundary (Ravizza and Peucker-Ehrenbrink, 2003; Kuroda et al., 2010; Bottini et al., 2012).

For OAE2 spanning the Late Cretaceous Cenomanian-Turonian Stage Boundary (CTB), the discovery of an abrupt unradiogenic Os$_{i}$ excursion (Turgeon and Creaser, 2008) provided strong evidence for the hypothesis that hydrothermal inputs, likely emanating from the Caribbean LIP and potentially the High Arctic LIP, triggered an Earth system response that ultimately led to expanded bottom water anoxia and elevated organic carbon burial (Sinton and Duncan, 1997; Kerr, 1998; Snow et al., 2005; Adams et al., 2010; Barclay et al., 2010; Owens et al., 2013). Subsequent chemostratigraphic records detected the OAE2 Os$_{i}$ excursion in numerous disparate basins, confirming the proxy as a globally correlative marine chemostratigraphic marker and highlighting the presence of a temporal lag, on the order of tens of kiloyear, between the onset of the Os$_{i}$

excursion and the younger carbon isotope ($\delta^{13}C$) excursion (Turgeon and Creaser, 2008; Du Vivier et al., 2014; 2015b). This lag records the response time of the Earth's carbon cycle to a massive pulse of CO_2 to the ocean-atmosphere system from LIP volcanism.

To assess potential explanations and implications of this lag, and to refine its duration, this chapter presents new high-resolution Os_i chemostratigraphy of the OAE2 onset interval of the WIB from the Angus core in north-central Colorado and the SH#1 core in southern Utah (Figure 5.1). Radioisotope geochronology, astrochronology, and $\delta^{13}C$ chemostratigraphy datasets provide tight age control for these locales and indicate a more continuous record than at the CTB GSSP in Pueblo, Colorado and the nearby Portland core (Ma et al., 2014; Joo and Sageman, 2014). The existing Os_i chemostratigraphy of the Portland core does not exhibit the characteristic lag between Os_i and $\delta^{13}C_{org}$ preserved in many other records (Du Vivier et al., 2014). This finding, along with sedimentological observations from Pueblo (Pratt, 1984; Eicher and Diner, 1989), suggests that a hiatus exists at the base of OAE2 in the GSSP. As a result, many recent studies have implicitly or explicitly questioned the stratigraphic completeness of the CTB and OAE2 records from the central WIB, suggesting that as much as hundreds of kyr of OAE2 may be missing at the GSSP (Eldrett et al., 2015a; 2017; Li et al., 2017; Jenkyns et al., 2017). Thus, expansion of Os_i chemostratigraphy in a transect of the WIB presents an opportunity to constrain the spatial extent, origin, and duration of this stratigraphic gap and to evaluate claims that a crucial interval of time is missing from sedimentary records of OAE2 in the central WIB, including at the GSSP. A second, proximal Os_i chemostratigraphy of the CTB from the Kaiparowits Plateau in southern Utah (SH#1 core) provides a new, expanded record within a framework of oscillating relative sea levels and biotic turnover through the onset of OAE2 (Jones et al., in press; Chapter 4).

5.2. Geologic Setting and Materials

The Late Cretaceous Greenhorn Cyclothem of the foreland Western Interior Basin preserves a ~10-Myr succession of shallow marine facies; OAE2, spanning the CTB, occurs just prior to the peak highstand of the cyclothem (Kauffman and Caldwell, 1993). This Early Turonian highstand (maximum transgression) of the seaway inundated the North American craton and linked the proto-Gulf of Mexico to the arctic Boreal Sea, spanning longitudinally from Iowa to central Utah (Figure 5.1). The uplifting Sevier thrust belt generated maximum subsidence in the proximal western foredeep of the basin, providing accommodation space and sediment supply that

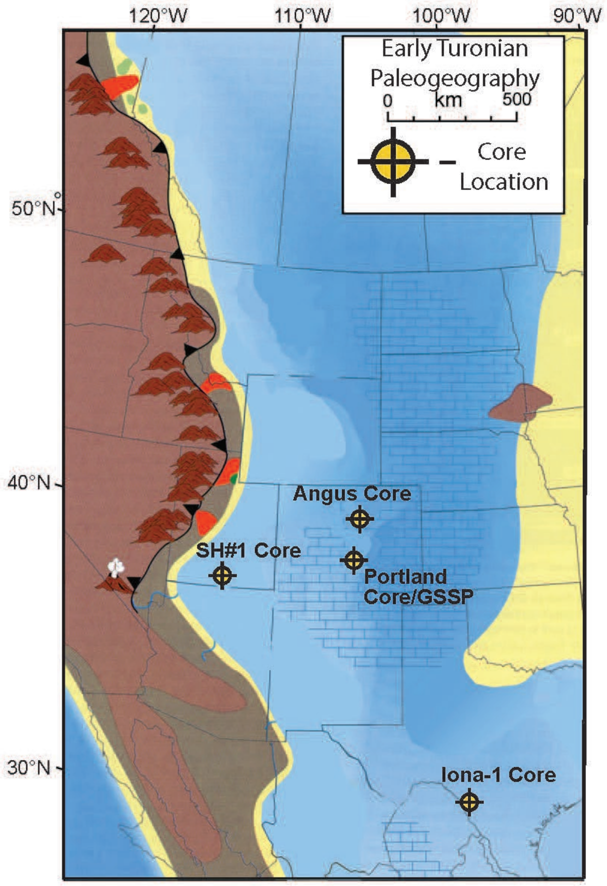

Figure 5.1: Early Turonian map of North American Western Interior Basin, marking localities of cores investigated or discussed in this study (basemap from Roberts and Kirschbaum, 1995 and Ma et al., 2014).

produced relatively expanded records of OAE2, such as in the Tropic Shale of the SH#1 core near Big Water, Utah (Jones et al., in press - see Chapter 4). Further east, in the more distal "axial basin" of Colorado to the "stable craton" of the central plains (*sensu* Kauffman, 1984), the hemipelagic sediments of the Bridge Creek Limestone accumulated more slowly and are more carbonate-rich, as is the case from the Angus core in the Denver Basin and the Portland core, near the CTB GSSP at the Rock Canyon Anticline in Pueblo, Colorado (Figure 5.1). A chronostratigraphic framework to correlate these proximal-distal regions of the WIB in detail consists of: areally expansive and radioisotopically dated bentonites (A-D, Elder, 1988; Obradovich, 1993; Meyers et al., 2012a; Ma et al., 2014); ammonite, inoceramid, and microfossil biostratigraphy (Elder, 1989, 1991; Leckie, 1985; Bralower, 1988; Kauffman et al., 1993; Keller and Prado, 2004; Kennedy et al., 2005; Caron et al., 2006; Corbett and Watkins, 2013), astrochronology from climatically sensitive lithologic patterns (Sageman et al., 1997a; Meyers et al., 2001; Ma et al., 2014; Jones et al., in press – Chapter 4), lithostratigraphy (Hattin, 1971; Cobban and Scott, 1972; Elder et al., 1994; Elderbak and Leckie, 2016), and carbon isotope chemostratigraphy (Pratt and Threlkeld, 1984; Pratt et al., 1993; Sageman et al., 2006; Joo and Sageman, 2014).

Prior to OAE2, during deposition of the Upper Cenomanian Hartland Shale in the axial basin, the seaway was relatively oxygen-depleted, restricted, and conducive to organic carbon burial (Eicher and Worstell, 1970; Sageman, 1985; 1989; Meyers et al., 2001; Du Vivier et al., 2014; Sageman et al., 2014b; Eldrett et al., 2017). Packages of skeletal limestone beds within the Greenhorn cyclothem correlate to shoreline lowstands overlain by transgressive intervals and reflect sediment winnowing from wave-base impingement on the seafloor, signifying the relatively shallow nature of the seaway (Sageman, 1996). The Bridge Creek Limestone overlies the Hartland Shale in the Angus and Portland cores of the axial basin. The shift to more calcareous, rhythmically bedded lithologies above this contact follows a transgression and pronounced backstepping of the basin's shoreline along the seaway's western margin in southern Utah (see Figure 4.2) (Kauffman, 1977; Laurin and Sageman, 2007). This deepening is associated with development of a more oxic watermass in the seaway during deposition of the lower Bridge Creek and OAE2 (Eicher and Worstell, 1970; Eicher and Diner, 1985, 1989; Arthur and Sageman, 1994; Sageman et al., 1997a; Meyers, 2007; Eldrett et al., 2014; 2017).

The Bridge Creek and uppermost Hartland Shale in the Portland core and GSSP exhibit evidence for hiatal surfaces at two horizons. The first, identified and quantified by spectral analyses to be <20 kyr, occurs near the base of the *Neocardioceras juddi* biozone (Meyers and Sageman, 2004). The second, a focus of this study, occurs at the base of the OAE2 CIE and 55 cm below the base of the thick lowermost Bridge Creek limestone bed (Bed 63 or LS1) (Pratt, 1984), which defines the members' contact (Figure 5.4) (Scott and Cobban, 1972; Elder, 1985). In the Angus core, LS1 expands to several couplets, indicating more continuous sedimentation and a higher fidelity record of the onset of OAE2 than at the GSSP (Ma et al., 2014).

Along the western paleo-margin of the seaway in southern Utah, the fossiliferous Tropic Shale overlies the Dakota Sandstone (Peterson, 1969; Elder et al., 1994; Leithold, 1994; Ulicny, 1999; Tibert et al., 2003; Laurin and Sageman, 2007). The SH#1 core drilled near Big Water, UT on the Kaiparowits Plateau records a largely continuous, proximal calcareous shale succession of the CTB and OAE2 (Jones et al., in press; Chapter 4). Thin carbonate-rich beds within the OAE2 interval of the lower Tropic Shale punctuate the thick shales. They preserve evidence of partial diagenetic alteration within the expanded $\delta^{13}C$ chemostratigraphy of the SH#1 core related to dominantly-eccentricity paced relative sea level cycles and flooding surfaces (Jones et al., in press;

Chapter 4), which grade eastward to the rhythmically-bedded limestones of the Bridge Creek in the axial basin (Elder et al., 1994; Laurin and Sageman, 2007). The combined astrochronology, expanded $\delta^{13}C$ chemostratigraphy, microfossil datums, and bentonite stratigraphy of the core (Jones et al., in press; Chapter 4) and ammonite biostratigraphy from outcrops on the Kaiparowits Plateau region (Elder, 1989) form a resolved chronostratigraphy for SH#1, which serves as age control for the Os_i chemostratigraphy of this study (Figure 4.11).

5.3. Re-Os Geochemical Methods

The existing $\delta^{13}C$ chemostratigraphic profiles guided high-resolution sampling for rhenium-osmium geochemical analyses through the onset of OAE2 from the SH#1 core (n=20, median spacing = 50 cm) and the Angus core (n=15, median spacing = 30 cm). Details on sample collection and alignment of the Angus core depth scale with previous studies are found in Table A4.1. Prior to analysis at Durham University, samples were powdered in ceramic containers using high-purity crushing techniques (Ottawa sand pre-clean) at Northwestern University. Following the methodology of Selby and Creaser (2003), sample powders were spiked with a $^{185}Re+^{190}Os$ tracer mixture and digested in sealed Carius tubes with 4N $CrO_3 \cdot H_2SO_4$ for ~48 hours at 200°C, principally leaching hydrogenous Re and Os (i.e., carbonates and organic matter). The Re fraction was isolated via NaOH-acetone extraction and anion column chromatography, while the Os fraction was isolated and purified via chloroform extraction with back reduction into HBr and $CrO_3 \cdot H_2SO_4$-HBr microdistillation. Isotopic ratios of samples and standards were measured on a Triton TIMS in negative ionization mode. Average 2σ precision for Os_i values was ± 0.014 (max = ± 0.057). Present-day measured $^{187}Os/^{188}Os$ values of samples were corrected to initial osmium ratios (Os_i) by accounting for post-depositional beta decay of ^{187}Re ($\lambda = 1.666\text{x}10^{-11}\text{yr}^{-1}$; Smoliar et al., 1996) using an age of 94.4 Ma for the onset of OAE2 (Meyers et al., 2012a; Du Vivier et al., 2015b). See Appendix 2.3 or the procedures of Jones et al. (2018b) for a detailed methodological summary.

5.4. Re-Os Geochemical Results

The records from the Angus and SH#1 cores reproduce an abrupt, unradiogenic Os_i excursion across the onset of OAE2 similar to the Portland core Os_i record (Du Vivier et al., 2014) at two new localities in the WIB. Unlike in the Portland core record, however, both the SH#1 and Angus cores preserve a stratigraphic lag between the initiation of the Os_i and $\delta^{13}C$ excursions, as is documented in other conformable records of OAE2, such as in the expanded Pont'd Issole section of southern France (Du Vivier et al., 2014). The Os_i excursion occurs below the base of the carbon isotope excursion (CIE) by 131±22 cm in the SH#1 core (122.29 m) and 80±25 cm in the Angus core (2279.98 m) (Figures 5.2-5.3). The unradiogenic Os_i shift occurs in the SH#1 core at the flooding surface "fs2a" of Elder et al. (1994) (see Figure 4.5) and in the Angus core in the uppermost calcareous shales of the Hartland Member.

Minimum values of Os_i at each Western Interior locality (SH#1 = 0.149 ± 0.006, Angus = 0.167 ± 0.002, Portland = 0.156 ± 0.003) approach the hydrothermal end member of the osmium isotope system ($^{187}Os/^{188}Os_{hydrothermal} = 0.12$; Peucker-Ehrenbrink and Ravizza, 2000). However, the magnitude of the Os_i excursion is significantly larger in the proximal SH#1 core ($\Delta Os_i = 1.30$) than in the Portland core ($\Delta Os_i = 0.78$; Du Vivier et al., 2014) and the Angus core ($\Delta Os_i = 0.74$), due to more radiogenic Os_i values preceding the event (max. Os_i in SH#1 = 1.446 ± 0.039 vs. Angus = 0.910 ± 0.027) (Figure 5.4).

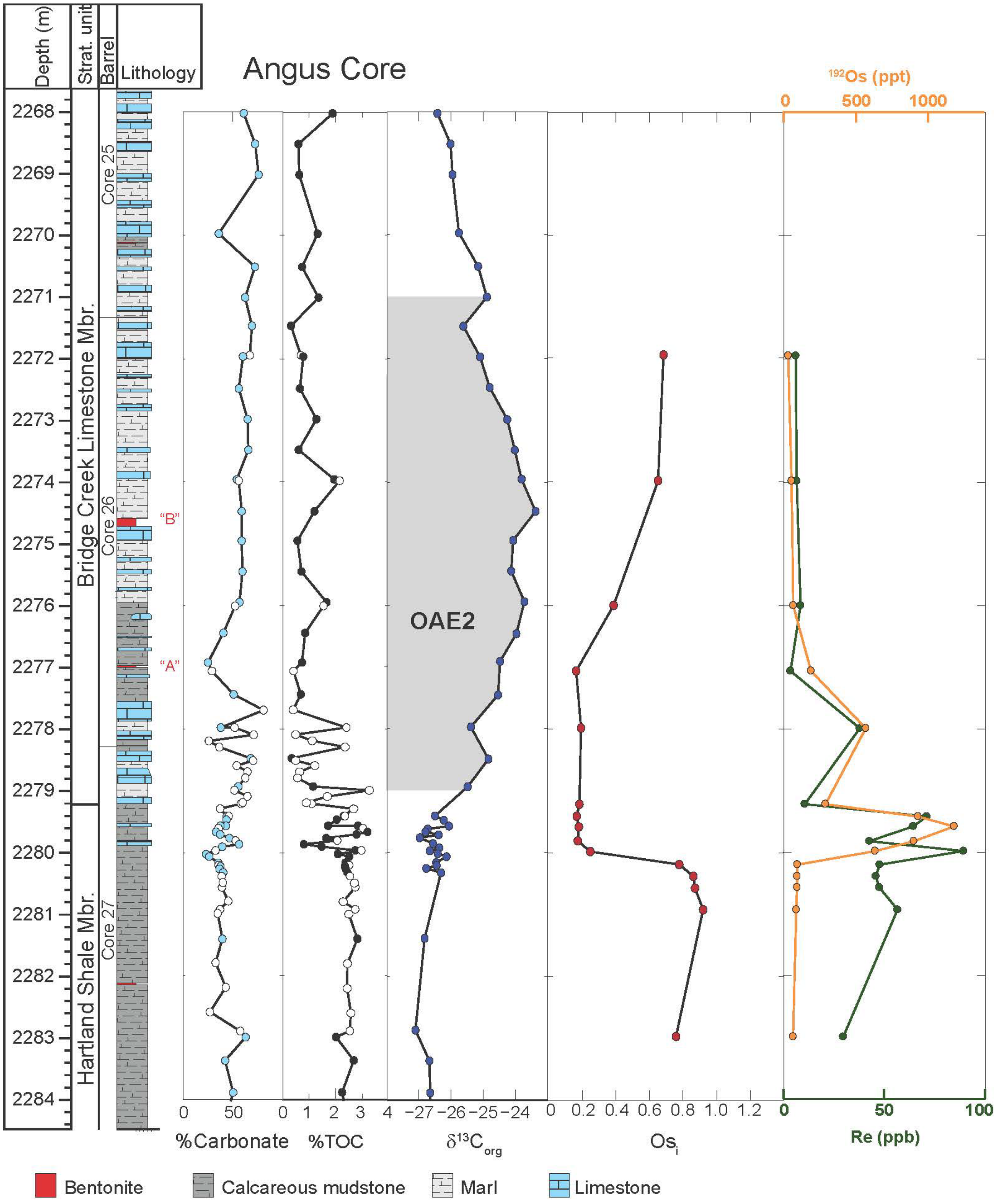

Figure 5.2: Chemostratigraphy of the Angus core. From left to right: wt.% carbonate content (open circles = new data – Table 5.1, blue circles from Joo and Sageman, 2014), wt.% TOC (open circles = new data – Table 5.1, black circles from Joo and Sageman, 2014), bulk organic carbon isotopic ratios $\delta^{13}C_{org}$ (Joo and Sageman, 2014), initial osmium isotope ratios Os_i (Table 5.2), rhenium concentrations (green), 192-osmium concentrations (orange).

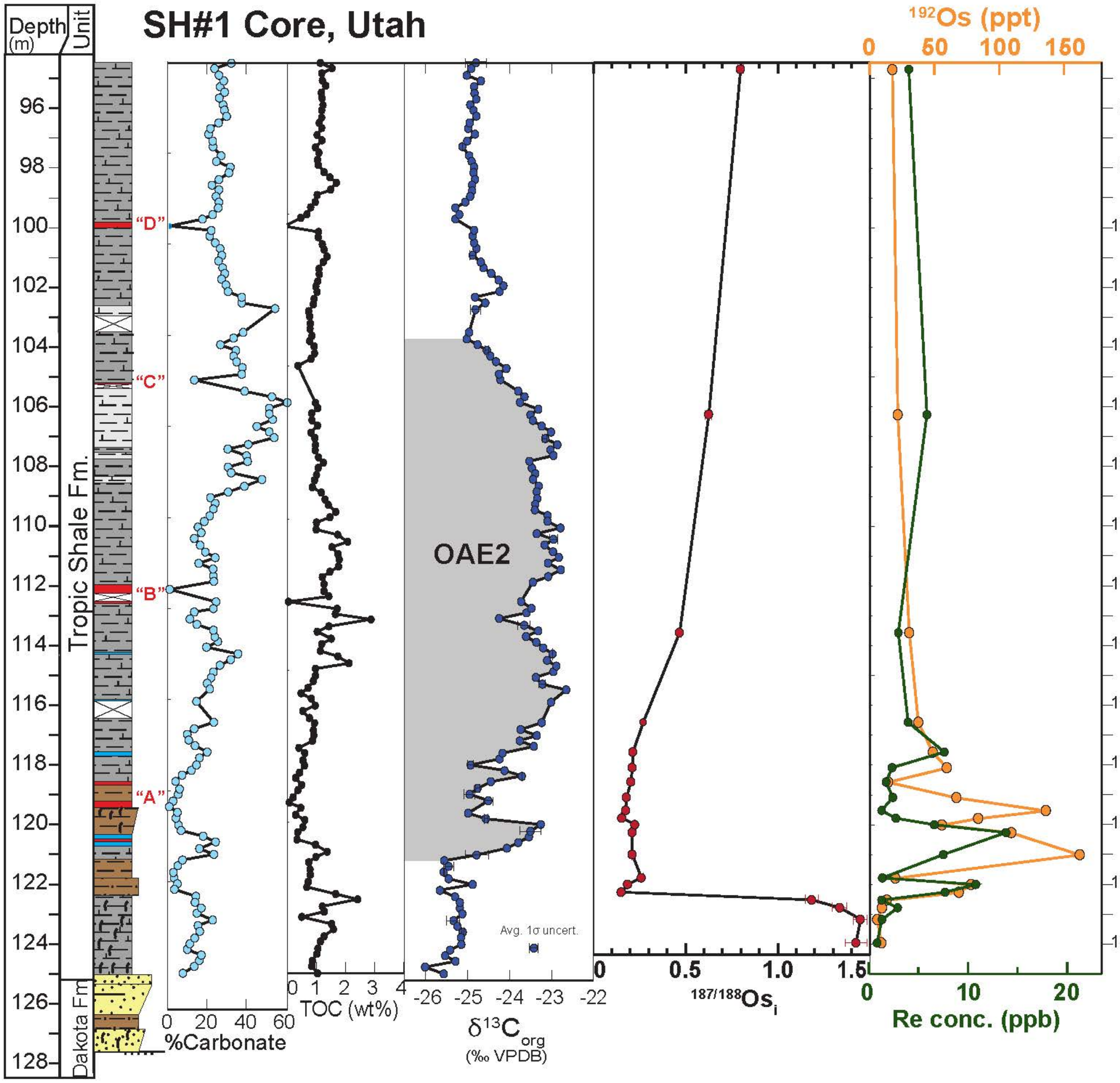

Figure 5.3: Chemostratigraphy of the SH#1 core in southern Utah. From left to right: wt.% carbonate content, %TOC, and $\delta^{13}C_{org}$ from Jones et al. in press; initial osmium isotope ratios (Os_i), rhenium concentrations (green), and 192-osmium concentrations (orange) from this study.

The astronomical time scale for the Angus core (Ma et al., 2014) constrains the duration of the lag between the Os_i excursion and the updated base of the OAE2 CIE to 2.9 ± 0.5 precessional cycles, equivalent to 59 ± 10 kiloyears (Figure 5.4). The observation that Os_i and $\delta^{13}C$

excursions are superimposed in the Portland core, but initiation of the $\delta^{13}C$ shift lags Os in the two other WIB sites, supports the hypothesis of a hiatus in the Pueblo area and permits the duration of missing time to be quantified. Equivalent to the duration of the lag, the hiatus represents ~60 kyr (see Discussion). Values of Os_i remain unradiogenic for 172-257 kiloyears spanning the *S. gracile* ammonite biozone at the beginning of OAE2 in the WIB.

Non-radiogenic Os enrichment, best represented by ^{192}Os concentration data, occurs through the onset of OAE2 in all sites (Figures 5.2-5.3, 5.5). Concentrations of ^{192}Os in the Angus core are significantly enriched (max $[^{192}Os] = 1183.9 \pm 4.3$ ppt) by roughly an order of magnitude compared to the SH#1 core (max $[^{192}Os] = 162.3 \pm 0.9$ ppt) (Table 5.2). Elevated ^{192}Os concentrations occur through the duration of the unradiogenic Os_i excursion.

Table 5.1: New %TOC and %Carb data from the Angus core spanning the onset of OAE2.

ID	Depth (m)	%CaCO3	%TOC
AA-18	2277.70	81.19	0.41
AA-18	2278.10	71.23	0.50
AA-18	2278.20	25.88	1.12
AA-18	2278.30	36.50	2.35
AA-18	2278.52	70.49	0.50
AA-18	2278.60	54.03	1.22
AA-18	2278.70	64.93	0.65
AA-18	2278.80	62.71	0.57
AA-18	2279.00	51.65	3.26
AA-18	2279.10	64.81	1.69
AA-18	2279.20	60.10	0.90
AA-18	2279.30	37.30	2.67
AA-18	2280.50	40.01	2.70
AA-18	2280.80	45.48	2.28
AA-18	2281.00	34.83	2.49
AA-18	2281.80	32.65	2.44
AA-18	2282.20	42.95	2.43
AA-18	2282.60	26.99	2.57

Concentrations of Re in the Angus core are highest in the uppermost Hartland Shale (max [Re] = 89.31 ± 0.22 ppb) in the ~60 kiloyears prior to OAE2 and exceed background levels in the unit (~50 ppb) (Table 5.2; Figure 5.3). Similar to records from the Portland core (Du Vivier et al., 2014), Re concentrations in the Angus core decrease markedly above the Hartland Shale-Bridge Creek Limestone contact and during the main body of the OAE2 CIE. Concentrations of Re are elevated in the central axial basin localities compared to the SH#1 core, where Re concentrations do not exceed 14 ppb, despite enrichment during the Os_i excursion.

5.5. Discussion

5.5.1. Refined chronostratigraphy of the CTB in the Western Interior Basin

An integrated chronostratigraphic framework of radioisotopic age dates, astrochronology, chemostratigraphy, and biostratigraphy at the Rock Canyon Anticline in Pueblo, Colorado defines the Global Stratotype Section and Point (GSSP) for the Cenomanian-Turonian Boundary (CTB) and constrains rates of change in geochemical and paleobiologic datasets from the Western Interior Seaway during OAE2 (Kennedy et al., 2005; Sageman et al., 2006 and refs therein). This high-resolution age control has aided in quantifying a cryptic 17 kyr hiatus above the LS5 bed of Elder et al. (1994) in the Bridge Creek Limestone Member (Meyers and Sageman, 2004) and has indicated the presence of a second hiatus at the base of OAE2 at the GSSP (Figure 5.4). Pioneering research of the CTB interval at Pueblo describes a distinct “thin wavy-bedded layer” in the uppermost Hartland Shale, along with phosphatized bones and scoured quartz sand (Pratt, 1984). These lithologic features, as well as a sharp influx of benthic foraminifera with Tethyan affinity in the overlying uppermost marlstone bed of the Hartland Shale, allude to a marked shift in paleoenvironmental conditions and are consistent with the presence of a hiatus (Eicher and Diner, 1989).

Table 5.2: Rhenium-osmium geochemistry of the Angus and SH#1 cores through Oceanic Anoxic Event 2. Initial osmium isotope ratios (Os$_i$) calculated from age of 94.4 Ma and floating time scales with t=0 placed at the base of the OAE2 carbon isotope excursion.

Angus Core Samples	**Depth (m)**	**Re (ppb)**	**±**	**Os (ppt)**	**±**	**192Os (ppt)**	**±**	**187Re/188Os**	**±**	**187/188Os**	**±**	**rho**	**Osi**	**±**	**Floating time (kyr)**
RO750-1_AA7454'-2.5cm	2271.95	6.15	0.02	71.8	0.4	25.3	0.2	483.7	3.3	1.444	0.012	0.673	0.683	0.017	475
RO745-1_AA7460'+17cm	2273.98	6.62	0.02	133.3	0.6	49.0	0.2	269.0	1.5	1.076	0.007	0.605	0.652	0.009	320
RO750-2_AA7467'+5.5cm	2276.00	8.54	0.02	161.0	0.7	60.9	0.3	279.0	1.7	0.827	0.006	0.633	0.388	0.009	186
RO750-3_AA7471'-10.5cm	2277.06	3.55	0.01	453.4	1.4	184.8	1.0	38.3	0.2	0.227	0.002	0.612	0.167	0.002	113
RO745-2_AA7474'-9cm	2277.99	37.88	0.09	1422.6	4.2	567.0	2.2	132.9	0.6	0.402	0.002	0.590	0.193	0.003	61
RO745-3_AA7477'+3cm	2279.22	10.66	0.03	708.1	2.3	285.9	1.5	74.2	0.4	0.300	0.002	0.627	0.184	0.003	-12
RO750-4_AA7478'-7cm	2279.42	71.09	0.18	2338.2	6.5	931.4	3.4	151.8	0.7	0.407	0.002	0.581	0.168	0.003	-25
RO750-5_AA7478'+9cm	2279.58	64.41	0.16	2951.0	7.8	1183.9	4.3	108.2	0.5	0.350	0.002	0.578	0.180	0.003	-35
RO745-4_AA7479'+2cm	2279.82	42.64	0.11	2241.1	6.2	902.2	3.6	94.0	0.4	0.323	0.002	0.594	0.175	0.002	-51
RO750-6_AA7479'+18cm	2279.98	89.31	0.22	1644.6	5.3	632.6	2.2	280.9	1.2	0.689	0.003	0.574	0.247	0.005	-59
RO745-5_AA7480'+9.5cm	2280.20	47.78	0.12	282.9	1.5	89.7	0.4	1059.1	5.2	2.439	0.014	0.627	0.772	0.022	-71
RO750-7_AA7481'-1.5cm	2280.39	45.86	0.12	278.4	1.5	87.9	0.4	1038.2	5.1	2.489	0.014	0.624	0.855	0.022	-81
RO745-6_AA7481'+16cm	2280.57	47.57	0.12	279.8	1.5	87.7	0.4	1079.5	5.3	2.562	0.015	0.628	0.863	0.023	-91
RO750-8_AA7483'-8.5cm	2280.93	56.60	0.14	274.9	1.6	82.0	0.3	1373.0	6.6	3.071	0.017	0.625	0.910	0.027	-108
RO745-7_AA7489'+14.5cm	2282.99	29.72	0.08	185.2	1.0	59.5	0.3	994.4	5.1	2.318	0.014	0.656	0.753	0.022	-235
SH#1 Core Samples	**Depth (m)**	**Re (ppb)**	**±**	**Os (ppt)**	**±**	**192Os (ppt)**	**±**	**187Re/188Os**	**±**	**87Os/188O**	**±**	**rho**	**Osi**	**±**	**Floating time (kyr)**
RO751-1_SH#1-94.66m	94.66	4.03	0.01	50.7	0.3	17.7	0.1	451.3	2.9	1.504	0.012	0.653	0.794	0.016	849
RO751-2_SH#1-106.27m	106.27	5.86	0.02	61.4	0.3	21.6	0.1	540.2	3.3	1.471	0.011	0.654	0.620	0.017	532
RO751-3_SH#1-113.58m	113.58	2.96	0.01	79.9	0.5	30.5	0.3	193.1	1.8	0.768	0.010	0.666	0.464	0.012	302
RO751-4_SH#1-116.58m	116.58	3.95	0.01	96.2	0.4	37.4	0.2	209.9	1.3	0.600	0.005	0.623	0.270	0.007	169
RO751-5_SH#1-117.58m	117.58	7.64	0.02	126.5	0.5	48.6	0.3	312.8	1.8	0.701	0.005	0.639	0.209	0.008	132
RO751-6_SH#1-118.08m	118.08	2.35	0.01	148.7	0.7	59.8	0.5	78.0	0.7	0.330	0.004	0.654	0.207	0.005	115
RO751-7_SH#1-118.58m	118.58	1.76	0.01	36.2	0.2	14.1	0.1	248.9	2.5	0.593	0.008	0.651	0.201	0.012	98
RO751-8_SH#1-119.08m	119.08	2.41	0.01	165.5	0.8	66.9	0.6	71.8	0.7	0.291	0.004	0.654	0.178	0.005	79
RO741-6_SH1: 119.53m	119.53	1.27	0.01	333.2	3.2	136.2	2.8	18.5	0.4	0.204	0.006	0.683	0.175	0.006	63
RO741-7_SH1: 119.79m	119.79	2.72	0.01	206.6	1.1	83.9	0.9	64.6	0.7	0.255	0.004	0.663	0.154	0.005	53
RO751-9_SH#1-120.03m	120.03	6.60	0.02	143.1	0.6	55.7	0.3	235.8	1.4	0.591	0.004	0.633	0.220	0.007	44
RO703-1_SH1-35:7	120.29	13.86	0.04	282.4	1.2	109.8	0.6	251.1	1.5	0.603	0.005	0.626	0.207	0.007	34
RO703-2_SH1-35:10	121.03	7.52	0.02	404.8	1.4	162.3	0.9	92.2	0.6	0.355	0.003	0.612	0.210	0.004	7
RO703-3_SH1-35:12	121.78	1.34	0.01	50.0	0.4	19.8	0.3	134.7	2.0	0.470	0.009	0.665	0.258	0.012	-21
RO741-8_SH1: 122.02m	122.02	10.79	0.03	201.6	0.8	78.2	0.4	274.2	1.7	0.615	0.005	0.634	0.183	0.007	-30
RO741-9_SH1: 122.29m	122.29	7.68	0.02	175.4	0.7	69.1	0.4	221.2	1.4	0.497	0.004	0.615	0.149	0.006	-40
RO741-10_SH1: 122.53m	122.53	1.30	0.01	38.0	0.4	13.3	0.2	193.9	2.9	1.488	0.029	0.670	1.183	0.034	-49
RO703-4_SH1-36:1	122.78	2.91	0.01	29.9	0.3	9.7	0.1	599.3	6.1	2.275	0.030	0.703	1.331	0.039	-59
RO751-10_SH#1-123.21m	123.21	1.32	0.01	18.2	0.2	6.0	0.1	438.9	5.4	2.137	0.030	0.707	1.446	0.039	-75
RO703-5_SH1-36:3	123.98	0.81	0.01	26.0	0.3	8.9	0.2	181.7	4.1	1.710	0.050	0.670	1.424	0.057	-103

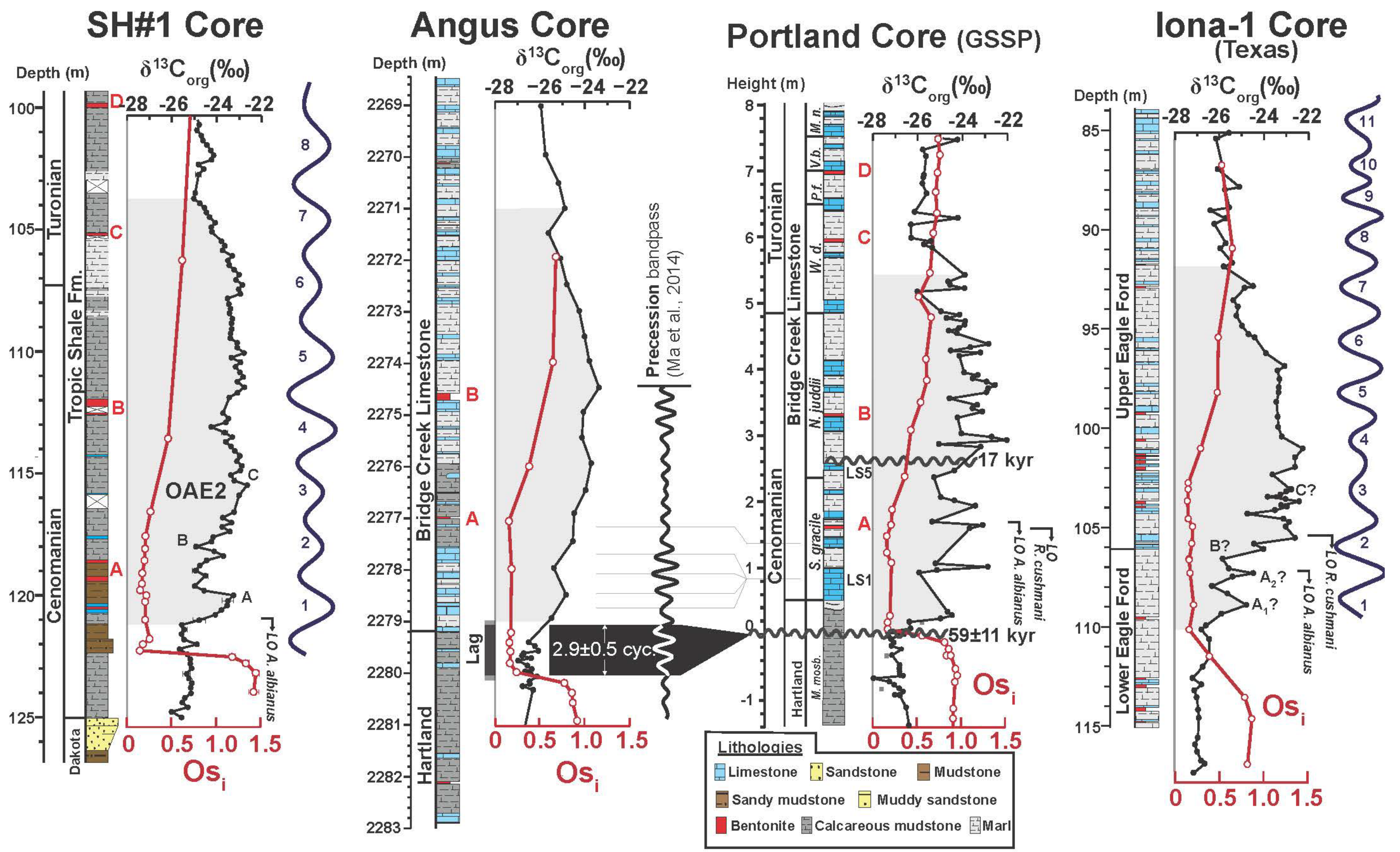

Figure 5.4: Initial osmium isotope records of the Western Interior Basin. Stratigraphic columns for the SH#1 core (Jones et al., in press; Chapter 4), Angus core (this study), Portland core near GSSP (Meyers et al., 2012a), and Iona-1 core from the Maverick Basin, Texas (from Eldrett et al., 2015a) (L-R). Bentonite labels A-D from Elder (1988) for central WIB sites; these bentonites may be present in the Iona-1 core of Texas as commonly indicated, however, Elder (1988) notes that these bentonites pinch out

(Figure 5.4 cont'd) in New Mexico before reaching Texas, complicating bentonite correlations to the Iona-1 core. Bandpass filters for SH#1 core (Jones et al., in press; Chapter 4), Angus core (Ma et al., 2014), and Iona-1 core (Eldrett et al., 2015a). Quantified durations of Portland core/GSSP hiatuses from Meyers and Sageman (2004) and this study (see text for discussion). Carbon isotope ($\delta^{13}C_{org}$) chemostratigraphy in black for SH#1 (Jones et al., in press; Chapter 4), Angus core (Joo and Sageman, 2014), Portland core (Sageman et al., 2006; Du Vivier et al., 2014), Iona-1 core (Eldrett et al., 2015a) define the OAE2 excursion (grey shading). Initial osmium isotope ratios (Os_i) (red) preserve unradiogenic (hydrothermal/LIP) excursion underlying OAE2 for SH#1 and Angus core (this study), Portland core (Du Vivier et al., 2014), and Iona-1 core (Wright, 2015).

More recently, Os_i chemostratigraphy of the nearby Portland core detected that the unradiogenic Os_i excursion preceding OAE2 directly underlies the base of the event's CIE and lacks the characteristic stratigraphic lag between Os_i and $\delta^{13}C$ excursions of the event globally (Figure 5.4) (Du Vivier et al., 2014). This confirmed the presence of a hiatus that has the potential to impact geochemical reconstructions of the critical OAE2 onset interval and the precise Earth system responses to the event's trigger (see discussion in Du Vivier et al., 2015a; Eldrett et al., 2017). However, the duration of the hiatus at the base of the OAE2 CIE at the GSSP remained unquantified prior to this study (see Results).

Lithostratigraphic correlations of the astronomically paced, hemipelagic marlstone-limestone couplets and widespread bentonite beds of the CTB interval in the central WIB reveal that the LS1 bed of the Bridge Creek at the GSSP and Portland core is condensed and expands into multiple couplets south and north of Pueblo at the Greenhorn Creek outcrop and in the Angus core of the Denver Basin, respectively (Figure 5.4) (Ma et al., 2014). Additionally, the new Os_i chemostratigraphy of the CTB interval from both the SH#1 core and the astronomically-tuned Angus core exhibit an expanded stratigraphic gap between the Os_i excursion and base of the OAE2 CIE (see Results). This signifies that more continuous sedimentation existed elsewhere in the region across the onset of OAE2 compared to the GSSP and constrains the duration of the hiatus at the GSSP to 59±10 kyr (Figure 5.4; see Results). Summing the quantified hiatuses above LS5 and at the base of OAE2, I estimate that the GSSP is missing 82±10 kiloyears in detectable hiatal surfaces (i.e., hiatuses of ≥10s kiloyear in duration). This suggests that the GSSP preserves ~90% of the temporal duration of OAE2 from the Os_i excursion to CIE termination. Although the GSSP is conformable spanning the CTB, adhering to criteria for GSSPs, the hiatus at the onset of OAE2 in this site omits a brief time interval. This interval, however, is represented in other sections within the basin that can be readily correlated to the GSSP site, such as the Angus and SH#1 cores.

5.5.2. CTB age model comparisons between central WIB and Texas

Oceanic Anoxic Event 2, first identified as a black shale succession spanning the Cenomanian-Turonian Boundary at many marine sites (Arthur et al., 1987), can be recognized globally in strata from a positive carbon isotope excursion (CIE) (Scholle and Arthur, 1980; Tsikos et al., 2004). Defining OAE2 from the base of this CIE to a return to stable background $\delta^{13}C$ values at the top of the event (the “long” definition compared to the “end of CIE plateau” termination), a recent study of the Eagle Ford Formation at the southern aperture of the WIS in the Maverick Basin, Texas argued for an expanded duration of OAE2 of 920±170 kyr (Eldrett et al., 2015a). This exceeds the value of 866±19 kyr determined in an earlier study from the central Western Interior Basin (Sageman et al., 2006). To reconcile the offset, Eldrett et al. (2017) note the occurrence of pre-cursor isotopic events in the Iona-1 core of Texas and invoke hiatuses at the base of the OAE2 CIE in the central WIB sites, suggesting a crucial interval of geologic time is missing in the Portland core and CTB GSSP (Figure 5.4). With the quantification of the hiatus at the base of the OAE2 CIE in the Portland core and the addition of more continuous Os_i records in the Angus and SH#1 cores, it is possible to assess this hypothesis more critically. Additionally, a recent rhenium-osmium geochemical study of the CTB succession in the Iona-1 core (Wright, 2015) provides a distinct chemostratigraphic marker to correlate and compare records from Utah and Colorado to Texas.

When the records from the central WIB and Texas are aligned and correlated using $\delta^{13}C$ and Os_i excursions, there is strong overlap between the short eccentricity bandpass astronomical time scales of OAE2 (Figure 5.6). Bandpass filtering and tracing of the short eccentricity spectral peak in both Texas and the central WIB preserves approximately seven cycles through the CIE (i.e., ~680 kyr), as do most other sites with relatively conformable records of OAE2 globally (Figures 5.4 and 5.7) (see Charbonnier et al., 2018). However, discrepancies in timing emerge when comparing the central WIB sites to the preferred time scale of Eldrett et al. (2015a), which traces the short obliquity cycle (O1: ~50 kyr) and reports a longer duration for OAE2. Thus, since eccentricity-based timescales correspond well among the sites, it is likely that the reported discrepancy between Texas and central WIB records of OAE2 primarily arises not from hiatuses, but from the usage of a less common obliquity cycle to tune the Iona-1 core record. This finding may indicate that, despite the increased amplitude of obliquity forcing during the CTB (Meyers et al., 2012b; Charbonnier et al., 2018), the O1 cycle is less reliable for astronomically tuning of mid-Cretaceous stratigraphic datasets, given significantly lower power in the La2004 and La2010 solutions than other eccentricity, obliquity and precession terms (Laskar et al., 2004; 2011; Wu et al., 2013). This hypothesis for the offset in durations of OAE2 records in the Eagle Ford and the central WIB, which originates from cyclostratigraphic techniques as opposed to hiatuses or significant differences in local stratigraphic preservation of the event, is consistent with the presented finding of a relatively short-lived hiatus at the base of the OAE2 CIE in the Portland core and GSSP and recent studies employing obliquity tuning of a CTB record in the Brianconnais Domain (Charbonnier et al., 2018) (Figure 5.7).

In addition, the Eagle Ford record preserves two ~+1-2‰ $\delta^{13}C$ excursions underlying the main body of OAE2 labelled as pre-cursor isotope events (PCEs; Eldrett et al., 2015a), which Wright (2015) confirms occur after and above the unradiogenic Os_i excursion (Figure 5.4). Similar $\delta^{13}C$ spikes occur prior to the main plateau of OAE2 in Morocco (Kuhnt et al., 2017) and at Demerara Rise (see Chapter 2). The occurrence of the PCEs above the new Os_i excursion in the Iona-1 core demonstrates that the Portland core does not preserve PCEs in the *M. mosbyense* zone underlying the Os_i excursion of OAE2, one possibility listed by Eldrett et al. (2015a) (Figure 5.4). The small spikes in $\delta^{13}C$ in the upper Hartland noted in Figure 11 of Eldrett et al. (2015a) are, instead, more likely artifacts of combining chemostratigraphic records from different datasets and laboratories with residual calibration offsets (i.e., Du Vivier et al., 2014; Joo and Sageman, 2014). Another possibility is that the PCEs in the Iona-1 core correspond to the “A” $\delta^{13}C$ peak for OAE2 of Pratt (1985), given the stratigraphic positions of the last occurrence (LO) datums of the foraminifera *Rotalipora Cushmani* and nannofossil marker *A. albianus* (Figure 5.4). The Iona-1 core may preserve two $\delta^{13}C$ peaks within the “A” interval due to a more detailed, expanded nature of the record compared to the Portland core and Pueblo GSSP. Nonetheless, additional high-resolution $\delta^{13}C$ chemostratigraphic studies of the onset of OAE2 in the central WIB, such as in the conformable Angus core (Figure 5.2), are needed to further test the hypothesis that the PCEs of Eldrett et al. (2015a) correlate to the “A” peak of Pratt (1985).

Although radioisotopic age estimates for the CTB are equivalent among records in Colorado (Meyers et al., 2012a), Texas (Eldrett et al., 2015a), and Canada (Barker et al., 2011), the numerical (i.e., absolute) age for the base of OAE2 is ~400 kyr older in the astronomical time scale of the Iona-1 core in the Eagle Ford of Texas (~94.8 Ma), anchored to U/Pb bentonite ages, than in the central WIB records (94.45±0.16 Ma), where astronomical time scales are anchored to radioisotopic ages dates for Bentonites A-D (Figure 5.8). This offset may result from the use of the O1 cycle for tuning the age-depth model in the Eagle Ford as discussed above. Another explanation may be that lead inheritance or pre-eruptive zircon crystallization biased ages in the Eagle Ford to older dates, as several ages do not obey stratigraphic superposition and produce anomalously old age estimates (Figure 5.8). Alternatively, discrepancies could arise from underlying offsets in the U/Pb and Ar/Ar geochronometers when applied to the Late Cretaceous (Schoene et al., 2006; Kuiper et al., 2008). However, this scenario is less likely given the equivalent age estimates for the base of the OAE2 CIE from Ar/Ar dates in the WIB and U/Pb dates from the Yezo Group of Japan (Figure 5.8) (Ma et al., 2014; Du Vivier et al., 2015b). More radioisotopic dating in the future utilizing techniques that lower temporal uncertainty, such as Ar/Ar Noblesse dating (Jicha et al., 2016), will continue testing and improving the current age models for OAE2.

5.5.3. Eustatic lowstand preceding OAE2

Spatial variability in the development of hiatuses locally in the WIB underscores an undulating nature to bathymetry of the epeiric seaway, even within the same structural zones of the basin, such as the “axial basin”. Wavy sedimentary structures and the missing time at Pueblo portend a shoaling of water column depth and susceptibility of the site to wave base impingement.

Notably, the Rock Canyon Anticline structure at Pueblo exposes the present-day CTB GSSP. Modern shallow marine foreland basins, such as the Persian Gulf Basin, exhibit analogous local variation in bathymetry linked to long-lived geologic structures (Kassler, 1973). Similarly, I posit that the Rock Canyon Anticline could have been active during the mid-Cretaceous and contributed to local shoaling, exposing the seafloor to wave base mixing and winnowing during sea level lowstands.

Regardless of the precise control on small-scale changes in Late Cenomanian bathymetry of the WIS, the wavy scoured bone bed indicates winnowing at the GSSP and, thus, a fall in relative sea level. This interval has previously been cited as a lowstand in the WIB (Sageman, 1985; CE-5 of Gale et al., 2008). Although the Angus core preserves no direct evidence for a lowstand or hiatus, in southern Utah a regression incising ~10 m of strata occurs within the *M. mosbyense* ammonite biozone along the western margin of the basin (Ulicny, 1999). The base of the unradiogenic Os_i excursion in SH#1 occurs in sandy mudstones overlying a flooding surface “fs2a” (Figure 5.3) (Jones et al., in press; Chapter 4), consistent with a pre-OAE2 lowstand and potentially a brief hiatus at this site. However, any putative hiatus at SH#1 would need to be geologically brief (<<59±10 kyr) given the preservation of the stratigraphic lag between Os_i and CIE (Figures 5.3-5.4). The *M. mosbyense* interval in Utah is coeval with the uppermost Hartland Shale in Colorado. Lower intervals in the Hartland Shale contain thin beds of winnowed skeletal limestones that correlate shoreward to a set of lowstands and shoreline progradation (Sageman, 1985; 1996). Thus, I attribute the hiatus in the uppermost Hartland Shale at Pueblo to Late Cenomanian winnowing of a bathymetric high during a minor lowstand in the basin.

Moreover, a compilation of global relative sea level records, constrained by ammonite biostratigraphy and/or $\delta^{13}C$ chemostratigraphy, reveals coeval sequence boundaries and lowstands underlying OAE2 at many localities, including: the English Chalk (Gale et al., 1993), the Paris Basin (Robaszynski et al., 1998), Germany (Voigt et al., 2006; Richardt et al., 2013), Czech Republic (Ulicny et al., 1997), Peru (Navarro-Ramirez et al., 2016), Mexico (Elrick et al., 2009), southern New Mexico (Mack et al., 2016), the northern Gulf of Mexico (Lowery et al., 2017b), Jordan (Wendler et al., 2014), Lebanon (Grosheny et al., 2017), Israel (Buchbinder et al., 2000), Egypt (Nagm et al., 2014), and Morocco (Kuhnt et al., 2009). Consistency among these global Upper Cretaceous relative sea level records ties the hiatus in the uppermost Hartland Shale in the WIB to an apparent eustatic lowstand preceding the onset of OAE2, coeval with or just preceding a major pulse of LIP volcanism (Figure 5.9). The link between LIP initiation and eustatic lowstand is consistent with original hypotheses of volcano-tectono-eustatic feedbacks at the onset of OAE2, followed by eustatic transgression with expanded shelfal area and organic carbon deposition (Arthur et al., 1987). However, robust eccentricity pacing of sea level through the event along the western margin of the seaway indicates at least a partial background control on sea level from climatic processes as well (Jones et al., in press; Chapter 4).

5.5.4. Refined timing of LIP volcanism and the OAE2 carbon cycle perturbation

The apparently conformable Os_i chemostratigraphy from the Angus core, with its high-resolution astronomical and radioisotopic timescale, provides a refined timeline of LIP volcanic activity in relation to the carbon cycle perturbation at the onset of OAE2 (Figures 5.5, 5.9). Each Os_i record spanning OAE2 from the WIB and, moreover, globally, indicates a geologically rapid increase in the flux of hydrothermal/volcanic osmium to the marine realm (Turgeon and Creaser,

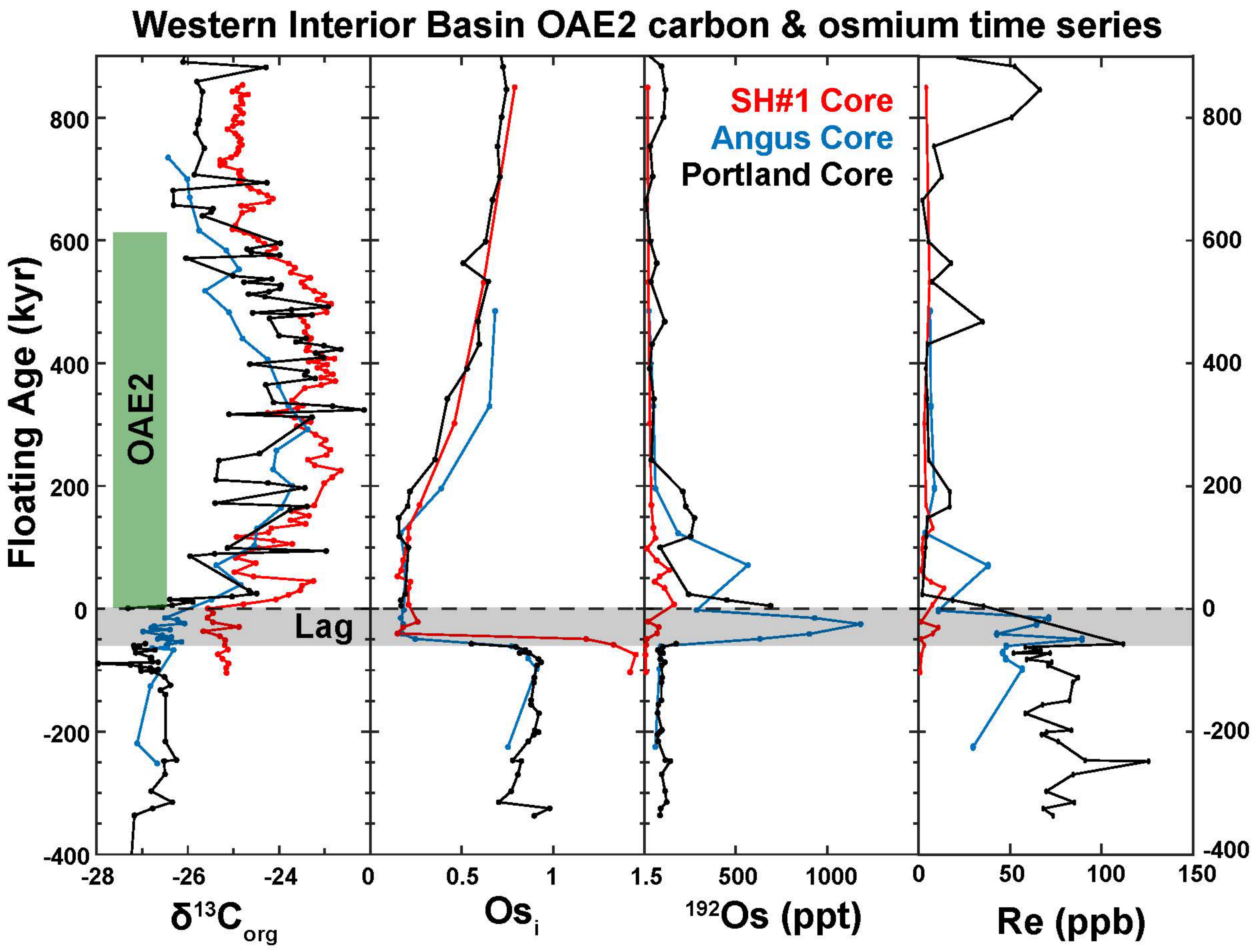
Western Interior Basin OAE2 carbon & osmium time series

Figure 5.5 (previous page): Timeseries of $\delta^{13}C_{org}$ and Re-Os geochemical records from the SH#1 core (red), Angus core (blue), and Portland core (black) through OAE2. Break in Portland core timeseries during lag (grey) signifies hiatus. From left to right, figure plots bulk carbon isotope ratios ($\delta^{13}C_{org}$), initial osmium isotope composition (Os_i), osmium-192 concentration, and rhenium concentration. Timeseries for Angus core from astrochronology (Ma et al., 2014), Portland core from astrochronology (Meyers et al., 2001) and linear interpolation of ammonite biozones below hiatus (this study), and SH#1 core from astrochronology (Jones et al., in press; Chapter 4) and linear interpolation of sedimentation rates below OAE2 CIE. See text for methods and discussion.

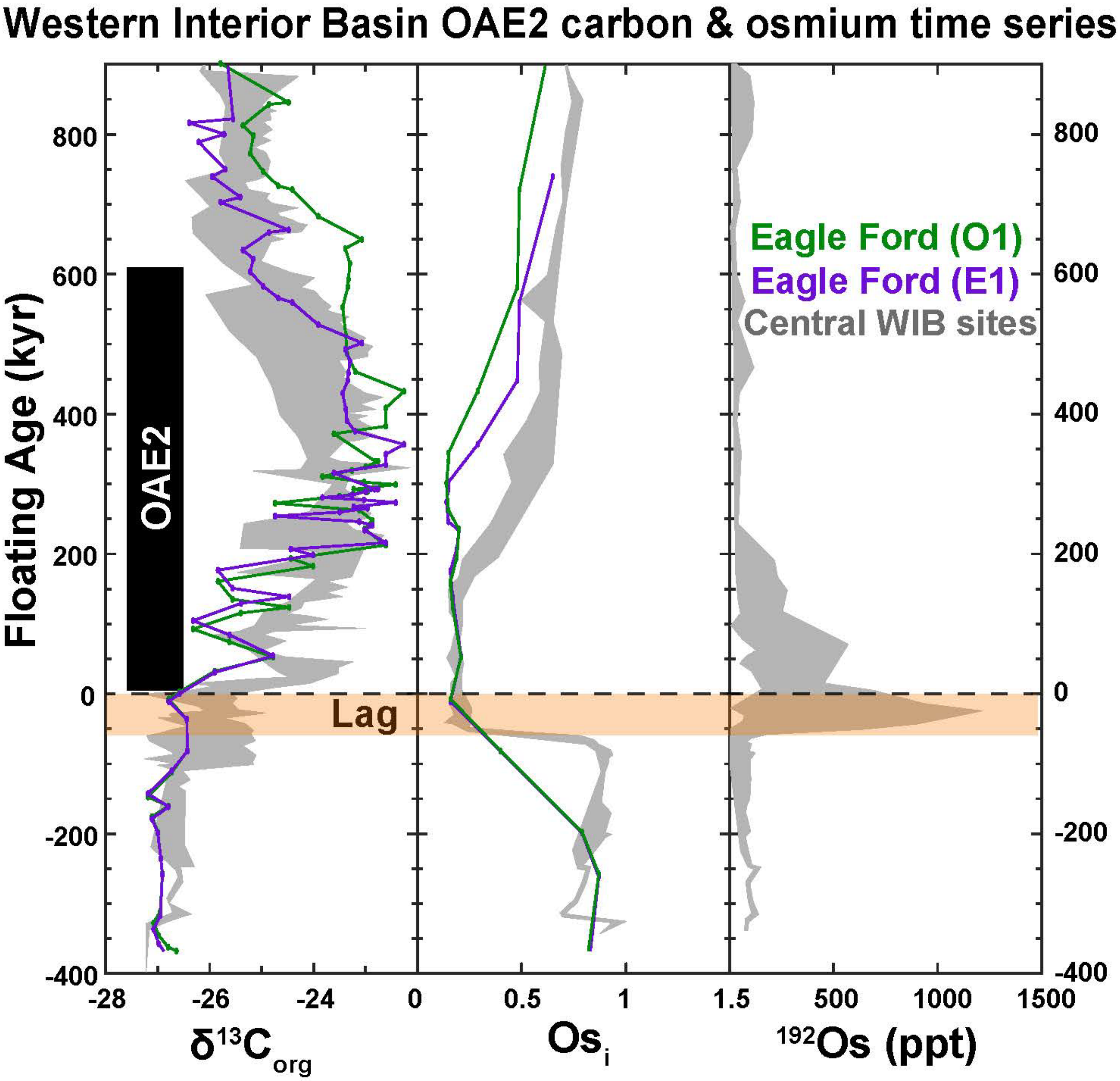

Figure 5.6 (previous page): Floating astronomically-tuned timeseries of geochemical data spanning OAE2 from the central Western Interior Basin (WIB) sites of this study compared with the Iona core of the Eagle Ford in Texas (Meyers et al., 2001; Ma et al., 2014; Eldrett et al., 2015a; Jones et al., in press). From left to right - carbon isotopic ratios ($\delta^{13}C_{org}$) (Sageman et al., 2006; Joo and Sageman, 2014; Eldrett et al., 2015a; Jones et al 2018 - Chapter 4), initial osmium isotope ratios (Os_i) (Wright, 2015; this study), and 192-osmium concentrations (this study). Different floating astronomical age models for Eagle Ford records from short eccentricity tuning (E1) and short obliquity tuning (O1) scenarios, the latter preferred by Eldrett et al. (2015a). Temporal lag between Os_i excursion and $\delta^{13}C$ excursion defining OAE2 shaded in orange. The E1 age model of the Eagle Ford strongly overlaps with age models from central WIB sites, whereas the O1 age model indicates a longer duration of OAE2.

2008; Du Vivier et al., 2014; 2015b). In the case of the astronomically tuned record from the Angus core, the precipitous unradiogenic Os_i excursion occurs abruptly in less than 20 kiloyears at most, with a subtle decrease in Os_i in the 20-40 kiloyears preceding the main excursion (Figures 5.2, 5.5, 5.9). Assuming that a massive increase in the hydrothermal/mantle C flux coincided with this rapid hydrothermal Os pulse (e.g., Kuroda et al., 2007), carbon release to the ocean-atmosphere system on this time scale would have occurred rapidly enough to potentially alter marine carbonate chemistry (Du Vivier et al. 2015b) and shoal the carbonate compensation depth (*cf.* Zachos et al., 2005) (Figure 5.9). This finding warrants future investigation of carbonate saturation state through OAE2 and its implication for marine biotas (see Chapter 6).

Although the onset of LIP volcanism prior to OAE2 occurred geologically rapidly, over the course of thousands of years, the positive carbon isotope excursion marking the onset of the event occurred only after a significant temporal lag, on the order of 10s of kiloyears. This study quantifies that lag at 59±10 kiloyears using the astronomical timescale in the Angus core (see Results, Figures 5.4-5.5, 5.9), a similar, though somewhat longer duration than previous estimates (Turgeon and Creaser, 2008; Du Vivier et al., 2014; 2015b). Fundamentally, this lag represents

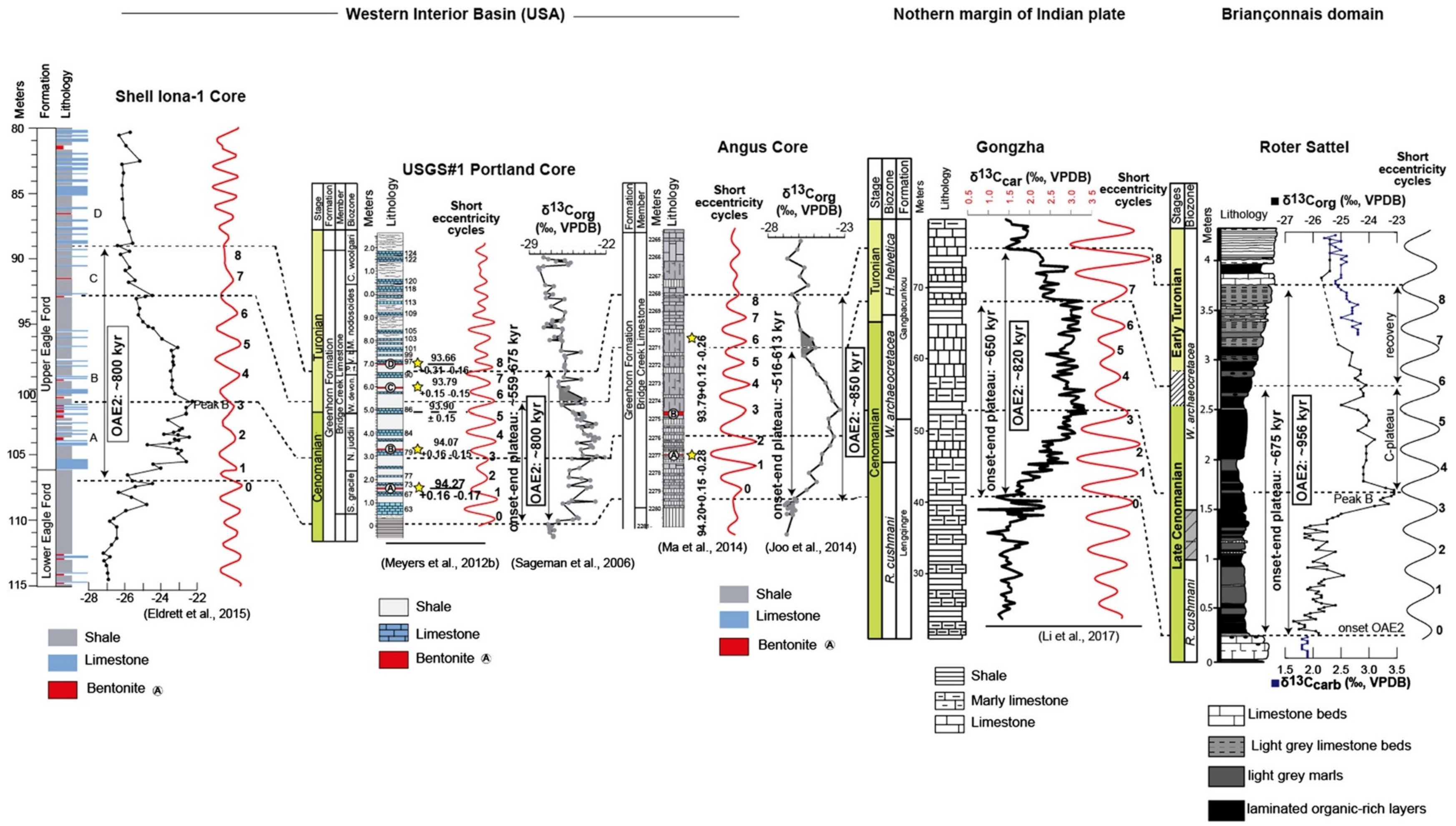

Figure 5.7: Compilation of astronomically-tuned stratigraphic records of Oceanic Anoxic Event 2 (OAE2), including some radioisotopic age dates (figure from Charbonnier et al., 2018). Most localities record a duration of OAE2 of 7-8 short eccentricity cycles, depending on definition of event.

the time between (1) the onset of massive submarine LIP volcanism, CO_2 degassing, and delivery of reduced metals to the marine realm; and (2) the carbon cycle perturbation of OAE2 recorded in $\delta^{13}C$ records, ultimately reflecting the spread in areal extent of anoxic and sulfidic marine bottom waters and burial/preservation of organic carbon (Scholle and Arthur, 1980; Adams et al., 2010; Owens et al., 2013).

The duration of the lag exceeds interpreted oceanic mixing timescales by an order of magnitude and, therefore, cannot solely represent the time needed to circulate water masses rich with biolimiting nutrients derived from submarine volcanic or continentally weathered sources, even in a sluggish mid-Cretaceous ocean (e.g., Turgeon and Creaser, 2008). It is possible that osmium cycle proxies (i.e., Os_i) are more sensitive to submarine LIP volcanism than carbon cycle proxies, and I have overestimated the pace of LIP CO_2 outgassing; tens of kiloyear could have been needed to accumulate CO_2 in the atmosphere. However, OAE2 preserves one of the longest unradiogenic Os_i excursions to-date from the Phanerozoic, suggesting an abruptly initiated and long-lived episode of prolific volcanism. Others place the exact timing of delayed anoxia at a maximum in the 405-kiloyear stable eccentricity cycle, invoking extreme seasonality (Batenburg et al., 2016). Although it is certainly plausible that phasing of astronomical cycles contributed to climatic conditions conducive to expanding marine anoxia, the lag between the abrupt onset of intensive LIP volcanism and anoxia is an order of magnitude briefer than the stable eccentricity cycle (405 kyr), suggesting additional factors were in play.

Alternatively, circulation of the marine dissolved oxygen reservoir typically provides a buffer against the prolonged expansion of anoxic bottom waters and organic carbon burial exhibited during OAEs. The inertia indicated by the lag between volcanic CO_2 input and widespread anoxia/carbon burial likely represents the globally-averaged drawdown of this substantial marine oxygen reservoir during OAE2. Accordingly, the presented duration of the Os-C lag is equivalent to the duration of a gradual drawdown of redox sensitive trace metals and bottom water oxygen levels at Demerara Rise (tropical Atlantic) which precedes OAE2 (Ostrander et al., 2017). The subsequent global-net enhanced burial and accumulation of organic carbon drove the OAE2 CIE only following this 10s of kyr deoxygenation process (Figure 5.9). This implies that the preservation of organic carbon due to anoxic/euxinic bottom and pore waters, mediated by organic matter sulfurization (Raven et al., 2018), was a key paleoceanographic feedback that ultimately triggered the OAE2 CIE (Mort et al., 2007), perhaps more so than the initial increases in marine primary productivity.

Multiple volcanic pulses: In addition to the pre-OAE2 lag, in the upper half of the OAE2 Os_i excursion above the first volcanic pulse, already unradiogenic Os_i values at each WIB site decrease further, subtly but consistently, and by more than analytical uncertainty (Table 5.2). Values of Os_i decrease in the SH#1, Angus, and Portland cores by 0.066, 0.026, and 0.053, respectively underlying Bentonite A (Table 5.2; Figures 5.2-5.4). Such small decreases in Os_i could relate locally to a basinward shift in facies associated with significant transgression at LS1-2 and shoreline backstepping increasing transport distance from radiogenic Os sources (Laurin and Sageman, 2007). However, Re and ^{192}Os concentrations increase at these horizons just underlying Bentonite A as well, consistent with a submarine volcanism source (Table 5.2). The WIB osmium chemostratigraphy indicates that the LIP emanated at least two pulses of volcanic activity that punctuated an elevated background rate of volcanism spanning the onset and the early interval of OAE2 (Figure 5.9). This scenario is consistent with observations of two pulses of anoxia during

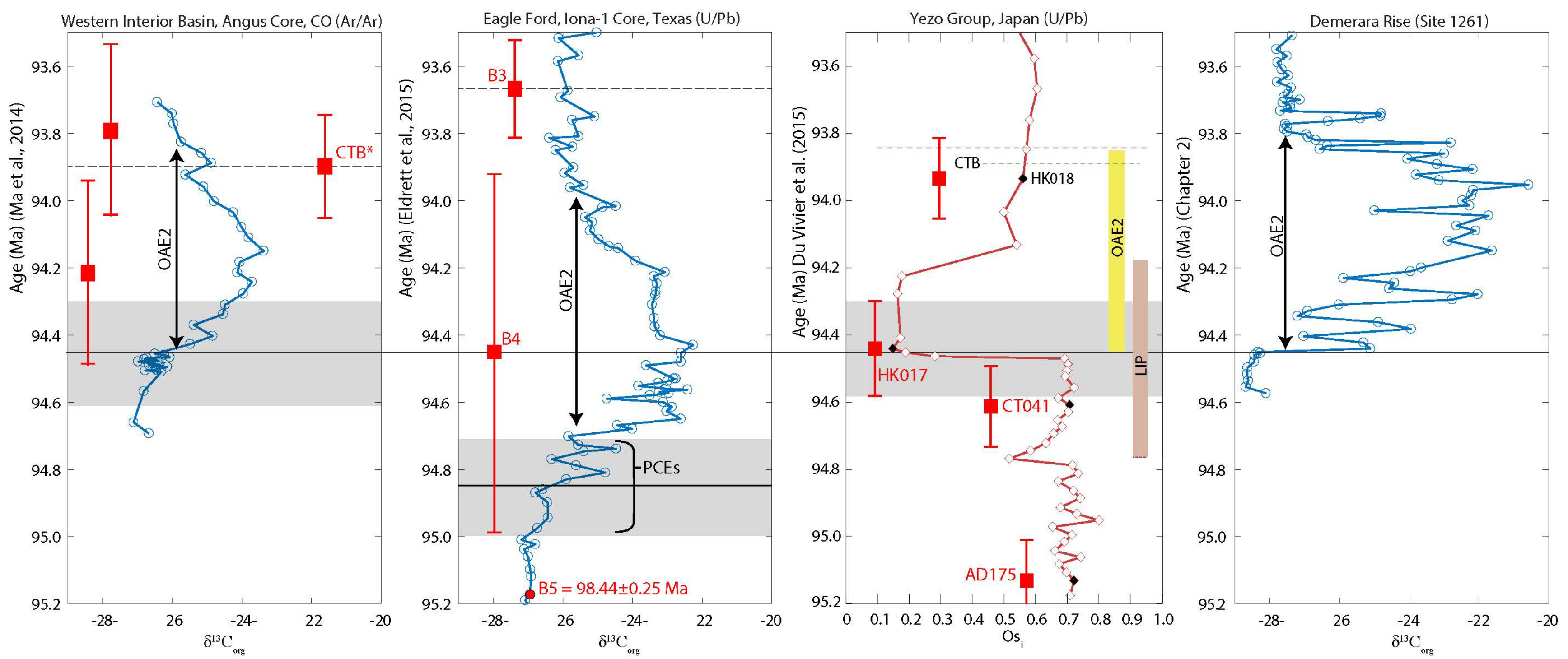

Figure 5.8: Numerical age models for Oceanic Anoxic Event 2 (OAE2) from Demerara Rise (see Chapter 2) and localities with radioisotopic age dates (Ar/Ar and U/Pb chronometers), including the Angus core (Ma et al., 2014), Iona-1 core (Eldrett et al., 2015a), and Yezo Group of Japan (Du Vivier et al., 2015b). Radioisotopic age estimates including temporal uncertainty (red) for the onset of the OAE2 carbon isotope excursion are shaded in grey. Records for the Angus core, Iona-1 core, and Site 1261 are astronomically-tuned. Pre-cursor events (PCE) in Iona-1 core (Eldrett et al., 2015a). *Age of the CTB noted in Angus core from the GSSP at Pueblo, Colorado (Meyers et al., 2012a).

the event from uranium isotopes (Clarkson et al., 2018) and temporally resolves a link between the intensity of volcanism and marine deoxygenation. Notably, the interval between these two deoxygenation events is identified as a cooling event – the Plenus Cold Event (Jenkyns et al., 2017). As a result, osmium concentration profiles may provide a chemostratigraphic marker to correlate sections and assess paleoclimate records of the Plenus Cold Event.

5.5.5. Osmium geochemical dynamics in a shallow epeiric seaway

The transect across the central WIB constrains spatial variability of Os_i chemostratigraphic records in a shallow continental seaway through a period of massive volcanism and transgression globally. Osmium chemostratigraphy of both Quaternary and Cenomanian-Turonian records exhibit a degree of spatial variability in Os_i composition among oceanic basins, highlighting the sensitivity of a given locality's record to water mass heterogeneity and the proximity of weathered sources of osmium (Du Vivier et al., 2014; Rooney et al., 2016). In the Western Interior Seaway, fluctuating sea levels through the Greenhorn cyclothem led to basin restriction at times recorded in geochemical and faunal records (Kauffman, 1984; Eicher and Diner, 1989). Despite this possibility, the unradiogenic Os_i excursion and enrichment in ^{192}Os at the onset of OAE2, heralding a pulse of LIP volcanism, is robustly preserved in each of the three sites transecting the basin (Figure 5.4).

Values of Os_i are equivalent across the basin during the syn- and post-OAE2 intervals, including at the most proximal locality - SH#1 (Figures 5.4-5.5). However, Os_i values in the SH#1 core are highly radiogenic prior to OAE2 compared to sites in the axial basin, at a time when the shoreline of the western margin of the seaway was closer to the site (~35 km, cf. Laurin and Sageman, 2007). The radiogenic values in this interval reflect the proximity of continentally

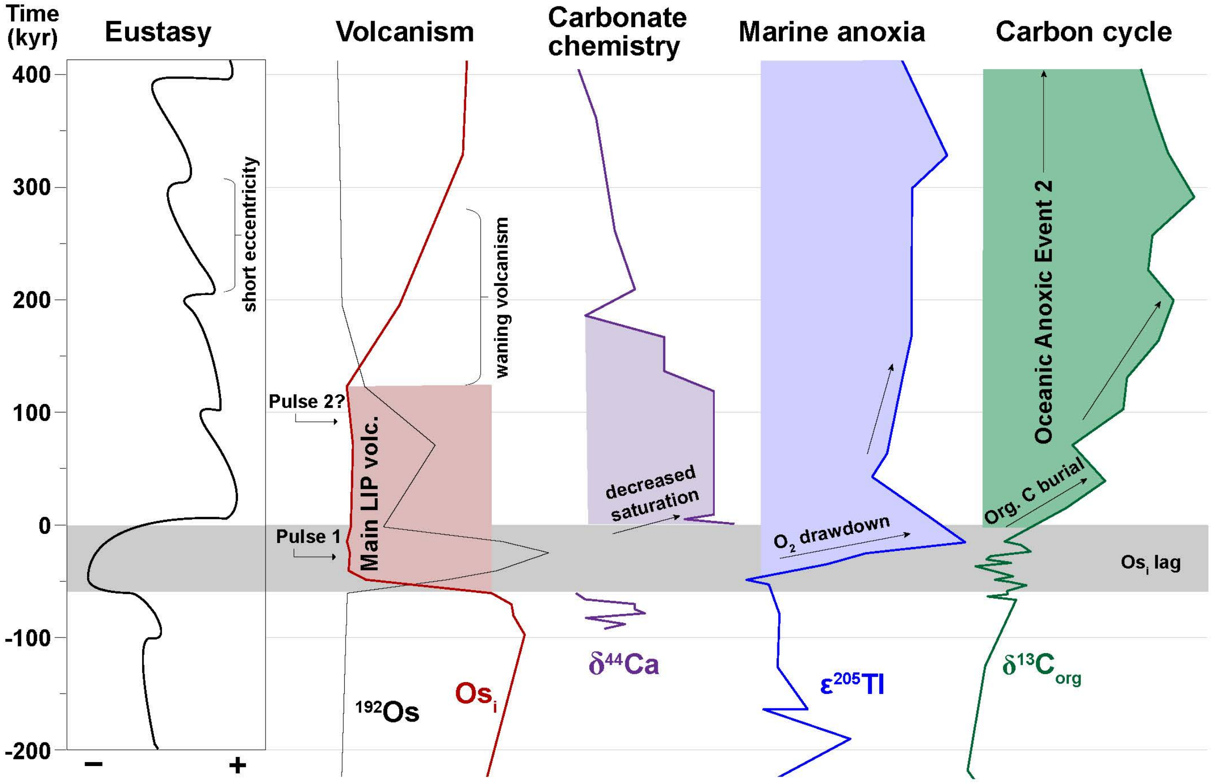

Figure 5.9: Refined conceptual timeline of OAE2. From left to right – conceptualized sea level history during OAE2 (Chapter 4; Jones et al., in press) and a record of osmium, calcium (Du Vivier et al., 2015a), thallium (Ostrander et al., 2017), and carbon (Joo and Sageman, 2014) isotopic signals as proxies for LIP volcanic activity, carbonate chemistry, marine deoxygenation, and carbon cycle response of organic carbon burial, respectively. See text for discussion**.**

weathered Os sources in the Sevier Belt. The values of Os$_i$ at SH#1 mimic those across the basin only above a major transgression near the base of OAE2 in SH#1, which reflects shoreline backstepping of ~150 km coeval with LS1 at the GSSP (Laurin and Sageman, 2007; Jones et al., in press). These patterns constrain the spatial sensitivity of the Os$_i$ proxy to runoff in the WIB. It appears that when the shoreline was within 10's of kilometers of the site, the Os$_i$ proxy is sensitive to runoff from the Sevier Belt, whereas when the shoreline is more than ~100 km away, the proxy tracks values of Os_i that characterize the seaway. Nonetheless, the pre-OAE2 interval at SH#1 exhibits a shift to unradiogenic values below the major Os_i excursion (Figures 5.3), similar to records globally (Du Vivier et al., 2014; 2015b). This suggests that the proxy remains sensitive to changes in the global fluxes of the marine Os cycle in settings proximal to shorelines, despite offsets in the absolute values of Os_i trends.

5.6. Conclusion

The presented Re-Os chemostratigraphy of the Angus core and SH#1 core transects the central Western Interior Basin, spanning the onset of OAE2 and adding a spatial dimension to an existing Os_i dataset from the Portland core (Du Vivier et al., 2014). This compilation of new Re-Os geochemistry along with existing geochemical, astrochronologic, and chronostratigraphic datasets from the Cenomanian-Turonian Boundary interval:

1.) defines the spatial variability and controls of Re-Os geochemical records in semi-restricted epeiric seaways during an interval of prolific LIP volcanism, finding a notable chemostratigraphic marker of volcanism preceding OAE2 extending into proximal settings in the form of a highly unradiogenic Os_i excursion;

2.) refines the duration of the temporal lag between the onset of LIP volcanic activity and widespread, globally-averaged marine anoxia at the onset of OAE2 to 59±10 kyr;

3.) suggests a second pulse of LIP volcanism emanated ~100 kyr after the onset of OAE2, consistent with earlier investigations;

4.) indicates that pre-cursor $\delta^{13}C$ excursions in in the Eagle Ford of Eldrett et al. (2017) corresponds to the “A” $\delta^{13}C$ peak of OAE2 in central WIB;

5.) constrains the duration of a hiatus in the Portland core and Pueblo (Cenomanian-Turonian Boundary GSSP) to the geologically brief temporal lag between volcanism and carbon cycle perturbation;

6.) suggests the hiatus results from a prominent eustatic lowstand recorded in many shallow marine setting globally preceding OAE2, potentially linked to climatic feedback from the onset of LIP volcanism;

7.) constrains a rapid onset of LIP volcanism and increased pCO_2, consistent with a scenario of altered marine carbonate chemistry and decreased aragonite/calcite saturation levels (Du Vivier et al., 2015a); and

8.) indicates that increased organic C preservation, following a gradual deoxygenation of the global ocean, was a highly significant factor behind the ultimate initiation of the OAE2 CIE.

CHAPTER 6

Volcanic Shoaling of the Marine Calcite Compensation Depth during OAE2

Motivation:

Evidence from Chapter 5 and prior investigations of OAE2 indicate that the event was triggered by prolific large igneous province (LIP) volcanism, which initiated abruptly ~60 kiloyear prior to the event. Given the associated volume and rate of CO_2 degassing from LIPs, I test the hypothesis that ocean acidification occurred as a response to volcanism during OAE2. Using isotope box modeling and compiling existing OAE2 literature, I reconstruct relative variation in the ocean's calcite compensation depth (CCD) and note morphological features of calcifying marine taxa that may result from lowered calcite/aragonite saturation states.

Key findings:

- A compilation of marine records of Oceanic Anoxic Event 2 (OAE2) reveals a shoaling of the CCD at pelagic sites due to some degree of ocean acidification.
- Osmium isotope box modeling indicates a 25-60x increase in volcanism pre-OAE2, consistent with ocean acidification, shoaled CCD, and declining carbonate saturation states.
- Ocean acidification in intermediate waters appears to be an additional paleoceanographic response to the volcanically-triggered anoxic event, likely stressing marine ecosystems.

CHAPTER 6

Volcanic Shoaling of the Marine Calcite Compensation Depth during OAE2

Abstract

Prolific large igneous province (LIP) volcanism at the onset of Oceanic Anoxic Event 2 (~94 Ma; OAE2) triggered a well-studied episode of widespread marine anoxia and rapid turnover of marine faunas. Given the interpreted rate and magnitude of CO_2 degassing from the LIP, it is reasonable to hypothesize that ocean acidification resulted from this large perturbation to the carbon cycle. To investigate carbonate sedimentation trends through OAE2, I compile global records of carbonate content from deep sea sediment cores and epicontinental locales and resolve a shoaling of the carbonate compensation depth (CCD) in marine basins. Employing a simple box model to reconstruct the unradiogenic marine osmium isotope excursion of OAE2, I calculate that the volcanic Os flux increased by 25-35x above pre-OAE2 levels, consistent with rapid CO_2 addition to the ocean-atmosphere system and observations of shoaling CCD. I hypothesize that the effects of this decrease in calcite saturation of oceanic waters, though apparently not severe enough to cause sustained dissolution in shallow surface waters, adversely impacted calcifying taxa in an ocean also experiencing deteriorating oxygen levels. Thus, ocean acidification, expressed via a shoaling CCD, was a noteworthy paleoceanographic response to LIP volcanism at the onset of OAE2, in addition to well-documented bottom water deoxygenation. Both of these processes likely contributed to elevated turnover rates associated with the Cenomanian-Turonian mass extinction event.

CHAPTER 6

Volcanic Shoaling of the Marine Calcite Compensation Depth during OAE2

6.1. Introduction

Episodes of ocean acidification in Earth history provide context for contemporary ocean acidification from anthropogenic carbon emissions, a phenomenon projected to result in undersaturation of aragonite in the surface waters of the Southern Ocean by 2100 (Orr et al., 2005; Ridgwell and Schmidt, 2010). Potential analogous acidification events have been identified during the Paleocene-Eocene Thermal Maximum (PETM), the end-Permian, and Mesozoic oceanic anoxic events (Zachos et al., 2005; Mehay et al., 2009; Erba et al., 2010; Payne et al., 2010; Hönisch et al., 2012). However, other case studies assert that some of these examples of prolific geologic releases of CO_2 occurred too slowly to significantly alter marine pH (Zeebe, 2012; Naafs et al., 2016), since the rate of CO_2 emission must outpace the delivery of alkalinity from silicate weathering, which buffers oceans on timescales of 10's of kiloyear (Kump et al., 2009; Andersson, 2014). Thus, precisely resolved relative timescales of paleoclimate events are requisite in assessing the plausibility of ocean acidification, and its effects on geochemical cycling and biotic responses. In this study, I assess a long-standing hypothesis that ocean acidification accompanied Oceanic Anoxic Event 2 (OAE2, ~94 Ma) (Kerr, 1998; Erba, 2004; Jenkyns, 2010; Du Vivier et al., 2015a) utilizing a global compilation of stratigraphic records from deep sea and outcrop sites measured over the past 50 years, along with recent findings from chemostratigraphic proxies for volcanic activity and a refined chronostratigraphy of the event (Chapter 5).

Ocean acidification is variously defined by different authors based on a set of interconnected measurements of marine carbonate chemistry, including carbonate mineral saturation states ($\Omega_{mineral}$) and pH (Equations 6.1-6.2). However, carbonate dissolution and sediment burndown commonly associated with ocean acidification are inherently erosive processes, potentially obscuring chemostratigraphic proxy records or sedimentological evidence of altered Ω and pH during geologic acidification events (Greene et al., 2012; Bralower et al., 2014). The stratigraphic record does robustly preserve an alternative marker of ocean acidification in the form of the calcite compensation depth (CCD) – the depth below which pelagic sediments contain low carbonate contents due to calcite undersaturation and dissolution in cold CO_2-replete deep and intermediate waters (Broecker, 2009). Rapid addition of CO_2 to the marine realm and acidification of the ocean forces the CCD to shoal, as is occurring in the modern ocean in response to oceanic uptake of anthropogenic CO_2 (Sulpis et al., 2018). Thus paleo-acidification events may be identified by the loss of carbonate in pelagic marine successions (Tyrrell and Zeebe, 2004; Zachos et al., 2005; Pälike et al., 2012). In order to evaluate ocean acidification and associated changes in marine carbonate chemistry during OAE2, this study tracks relative trends in the CCD based on a global compilation of carbonate contents and lithologies at 35 sites previously recognized to preserve the Cenomanian-Turonian interval (Figure 6.1; Table 6.1).

Equation 6.1: $\Omega_{mineral} = \frac{[Ca^{2+}][CO_3^{2-}]}{K_{sp}}$

Equation 6.2: $pH = -\log_{10}[H^+]$

6.2. OAE2 volcanism-acidification hypothesis and test

Widespread marine anoxia and euxinia during Oceanic Anoxic Event 2 (OAE2) led to the deposition of black shales in many basins globally (Schlanger and Jenkyns, 1976). Trace metal concentrations and isotopic ratios record enhanced volcanic activity from large igneous provinces (LIPs) during OAE2, such as the Caribbean, High Arctic, and possibly Madagascar LIPs, suggesting a volcanic trigger for the event (Kerr, 1998; Snow et al., 2005; Kuroda et al., 2007; Adams et al., 2010). In particular, initial osmium isotope (Os_i) chemostratigraphy exhibits a rapid shift (<20 kyr) to unradiogenic mantle values 60 kyr prior to the beginning of OAE2, which is defined by an abrupt positive excursion in carbon isotope values that persisted for >0.5 Myr (CIE) (Turgeon and Creaser, 2008; Du Vivier et al., 2014; 2015b; Chapter 5). Based on studies of volcanic CO_2 degassing associated with the Caribbean LIP, this rapid onset could have influenced marine carbonate chemistry (Kerr, 1998). Despite the fact that numerous localities include a carbonate-free shale interval at the onset of the event (e.g., Gubbio) and OAE2 has been implicated in general considerations of acidification through geologic time (Kump et al., 2009; Hönisch et al., 2012), only one recent study of Ca isotopes has shown direct geochemical evidence for altered calcite saturation states during OAE2 (Du Vivier et al., 2015a).

One complication for the study of ocean acidification during OAEs is that the spread of marine anoxia during OAE2 may have altered CO_2 levels in the ocean-atmosphere system. Carbon cycle models and proxies suggest a drawdown of pCO_2 due to the burial of vast quantities of organic carbon during the event (Arthur et al., 1988; Kuypers et al., 1999; Barclay et al., 2010). Similarly, paleoclimate reconstructions place the Plenus Cold Event – a transient episode of cooling and marine reoxygenation – after the onset of OAE2 (Jenkyns et al., 2017), consistent with lower pCO_2, and possibly minimizing any shift in marine carbonate chemistry. Nonetheless, sedimentological observations from pioneering studies of Cenomanian-Turonian deep-sea cores note carbonate barren intervals at many pelagic sites, portending a generally shallowed CCD (de Graciansky et al., 1985; Arthur and Dean, 1986; Herbin et al., 1986; Arthur et al., 1987).

Here, I seek to build on these studies and comprehensively test the OAE2-ocean acidification hypothesis by: 1.) compiling an updated dataset of marine carbonate content where quantitatively measured, 2.) assessing the timing of LIP volcanism in comparison to carbonate sedimentation, 3.) modeling the magnitude of volcanism to reconstruct the event's Os_i timeseries and test the possibility of acidification, 4.) considering alternative paleoceanographic influences on marine carbonate chemistry aside from volcanism, and 5.) evaluating how altered carbonate chemistry could influence shallower marine ecosystems and sedimentation patterns.

Relative changes in the paleodepth of the CCD at pelagic marine sites can be inferred from the abundance of carbonate (Zachos et al., 2005). Pelagic sediments with more than 20% carbonate are interpreted to have been deposited at a paleodepth shallower than the CCD, whereas sediments with carbonate content below this threshold are interpreted as deposited below the CCD (Broecker, 2009). This threshold is non-zero to account for sub-CCD settings where sulfate reduction during euxinic time intervals, such as OAEs, may have elevated porewater alkalinity locally and precipitated small amounts of authigenic carbonate, regardless of the primary water column chemistry (Schrag et al., 2013).

6.3. Results

6.3.1. OAE2 carbonate contents synthesis

Trends in carbonate sedimentation from the global compilation can be categorized into four responses to OAE2 (Figure 6.2). Nine pelagic sites preserve less than 20% $CaCO_3$ pre-, syn-, and post-OAE2, and, therefore, consistently remained below the CCD in abyssal settings. Thirteen epicontinental sites preserve 40-95% $CaCO_3$ prior to and during OAE2, of which seven record increases in carbonate content during OAE2, and therefore are interpreted to have remained consistently above the CCD. Notably, carbonate contents at eleven pelagic sites decrease 70-100%

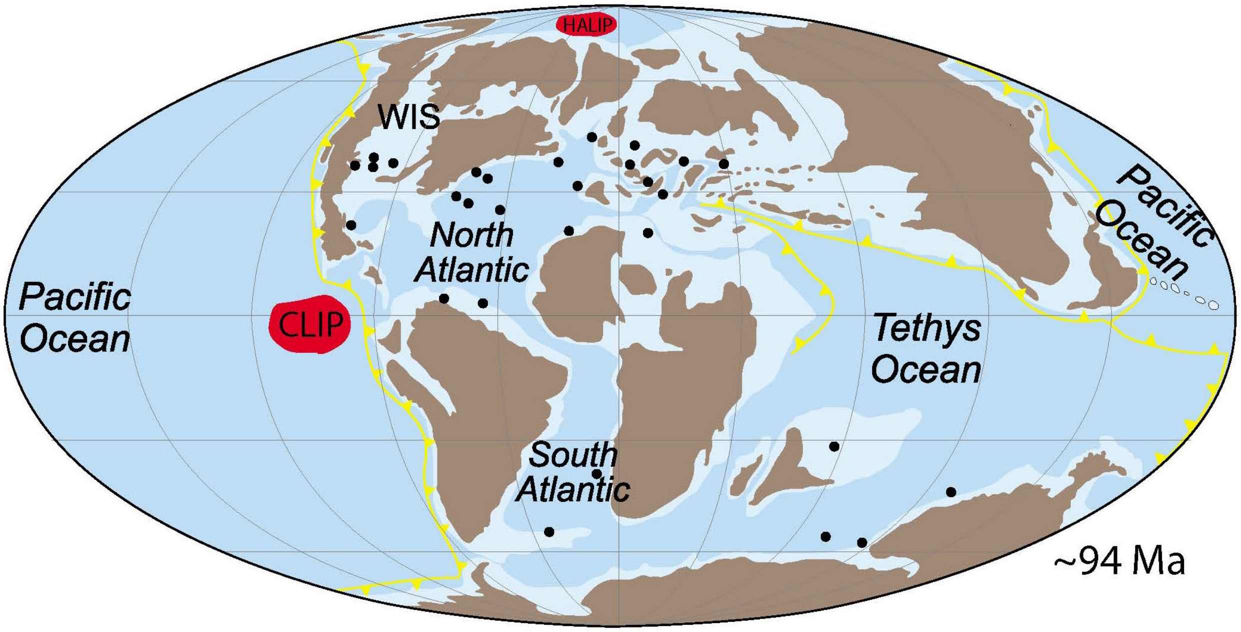

Figure 6.1: A palinspastic map during the Cenomanian-Turonian Boundary, including large igneous provinces (LIP) and sites (black dots) comprising the compilation of carbonate sedimentation through Oceanic Anoxic Event 2 (see Table 6.1) (modified from Jarvis et al., 2011 and Du Vivier et al., 2015a).

from pre-OAE2 values to sub-CCD values during OAE2, recording a pronounced shoaling of the CCD in multiple basins globally. The majority of these shoaled or sub-CCD pelagic sites are highly condensed through OAE2, decreasing temporal resolution of the event, and condensation may reflect either dissolution or impeded carbonate sedimentation (e.g., de Graciansky et al., 1984). Results from ODP Site 1138 on Kerguelen Plateau and from IODP Site U1516 in the Mentelle Basin of offshore SW Australia indicate that carbonate sedimentation was suspended on the order of several hundred kiloyear, assuming linear sedimentation rates (Dickson et al., 2017; Hasegawa et al., in prep.), equating to a shoaled CCD for the majority of the duration of OAE2. Two additional hemipelagic records remain below 30% $CaCO_3$ spanning OAE2. This could be consistent with a shoaled CCD, however these epicontinental sites are also comprised of significant quantities of terrigenous sediment, which likely served to dilute and reduce carbonate contents, independent of marine carbonate chemistry. Therefore, it is unlikely that the CCD shoaled through the two carbonate-lean shallow water sites at Bass River, NJ and the SH#1 core, Utah.

6.3.2. Osmium modeling of volcanism

To further assess a scenario of volcanically driven ocean acidification during OAE2, I employ a first-order osmium isotope box model to reconstruct volcanism rates, following the approach of Tejada et al. (2009) (see Model Parameters). The marine Os isotopic reservoir is highly sensitive to changes in unradiogenic volcanic fluxes ($^{187/188}$Os = 0.126) relative to radiogenic fluxes of continental weathering ($^{187/188}$Os = ~1.4, global average) (Peucker-Ehrenbrink and Ravizza, 2000). Moreover, the marine osmium reservoir has a short residence time (10's of kyr) and was relatively well mixed-during the mid-Cretaceous globally. As a result, Os_i chemostratigraphy can resolve rapid perturbations from LIPs, as has been demonstrated for OAE2, which preserves a pronounced unradiogenic Os_i excursion (Turgeon and Creaser, 2008; Du Vivier et al., 2014; 2015b). From box model output, I iteratively attempt to reconstruct the timeseries of the OAE2 Os_i excursion as it is recorded in a densely sampled, conformable, and astronomically-tuned dataset from the Angus core (Chapter 5).

To accurately generate the measured Os_i timeseries for OAE2, the model calculates that a 220 kyr perturbation of LIP volcanism with a flux between 25x and 35x greater than the background mantle flux is required (Figure 6.3). To better match the inflection of the Os_i excursion's onset and create multiple spikes in osmium concentrations during OAE2 (Chapter 5),

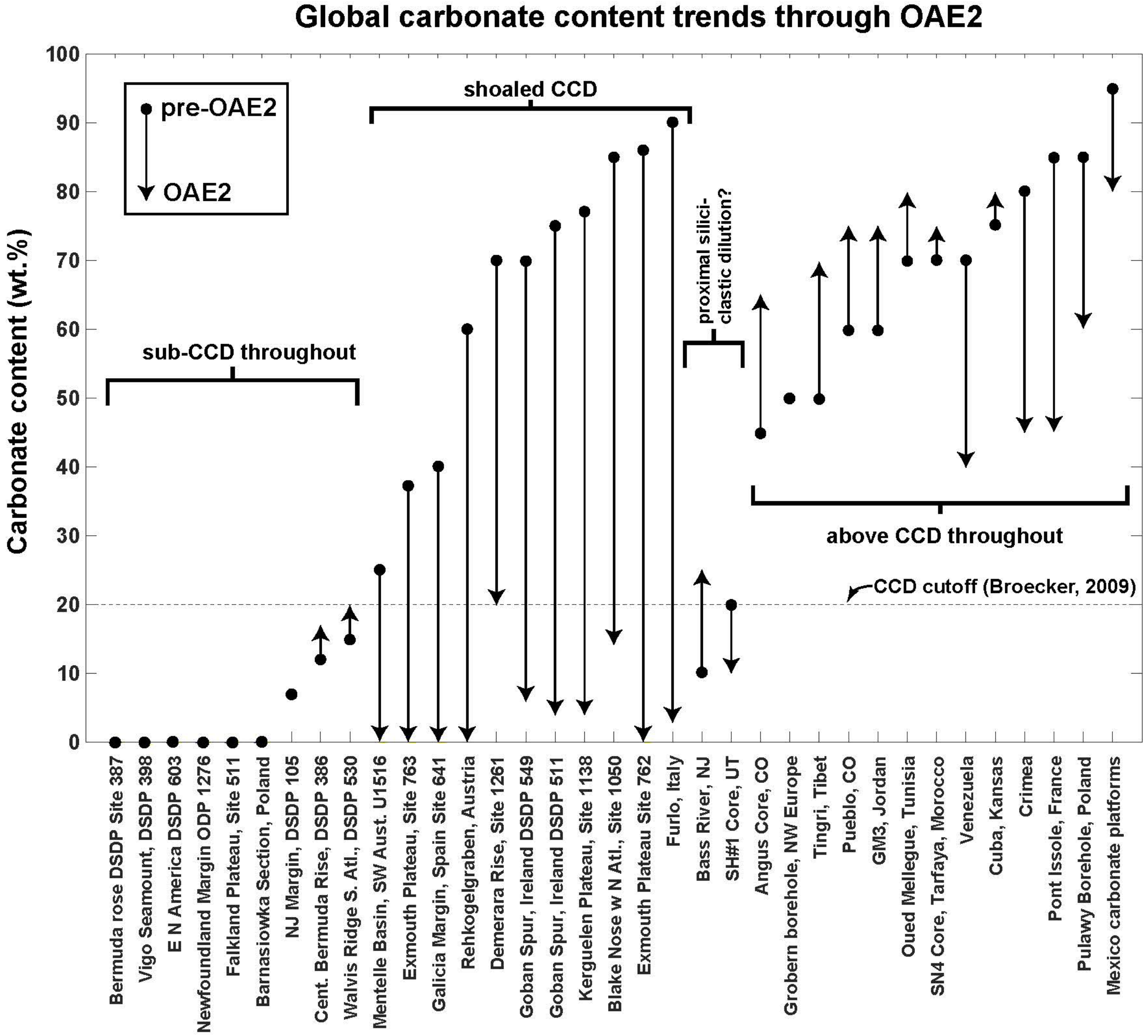

Figure 6.2: A global compilation of carbonate content in sediments (wt.%) prior to and during OAE2 (see Table 1 for data sources). Dotted line represents the cutoff for the calcite compensation depth (CCD) (Broecker, 2009). Sites with consistently less than 20% carbonate remained below the CCD (left), whereas sites with a precipitous decrease in carbonate during OAE2 record a shoaling CCD (center). Shallow water sites (right) remained above the CCD throughout OAE2 and some record increased carbonate contents in contrast to deeper water sites (see text for discussion).

I test a second scenario with two gaussian pulses of volcanism, which resembles the Os_i excursion well. The first of two gaussian pulses requires a 60x increase in the LIP Os flux above background within just 14 kyr (2σ) (Figure 6.3). Both scenarios of volcanism invoke considerably larger hydrothermal Os fluxes than proposed in a multi-isotope system model of OAE2 (Pogge von Strandmann et al., 2013), but are consistent with other prior Os_i studies and indicate a rapid pre-OAE2 onset of LIP volcanism (Turgeon and Creaser, 2008; Du Vivier et al., 2014).

The relationship between increasing emissions of Os and C as volcanic activity intensifies is poorly constrained and depends upon lithologies adjacent to a LIP during emplacement (Ganino and Arndt, 2009). However, if it is assumed that the fluxes scale linearly, a corollary 25-60x increase in CO_2 emission beyond background mantle/volcanic degassing would represent a major injection to the ocean-atmosphere carbon reservoir. Modern anthropogenic CO_2 emission rates are ~80-270x greater than background volcanic fluxes and are rapidly altering marine carbonate chemistry (Doney et al., 2009; Gerlach, 2011). Accordingly, a carbon release at a lower, yet similar order of magnitude and rate in the mid-Cretaceous would likely have affected marine carbonate chemistry. The result would be lower pH and calcite/aragonite saturation states, as is inferred from calcium isotope data at multiple sites (Du Vivier et al., 2015a), along with a shoaled marine CCD, as is observed in the new sedimentary carbonate content compilation through OAE2 (Figure 6.2).

6.4. Discussion

6.4.1. Ocean Acidification during OAE2

Oceanic Anoxic Event 2 has long been recognized as a deoxygenation event in many, though not all, marine basins, driving a substantial net increase in organic carbon burial and black shale deposition on a global scale (Arthur et al., 1987). The new compilation from sedimentology and geochemical modeling suggest that ocean acidification, in the form of a shoaling CCD at

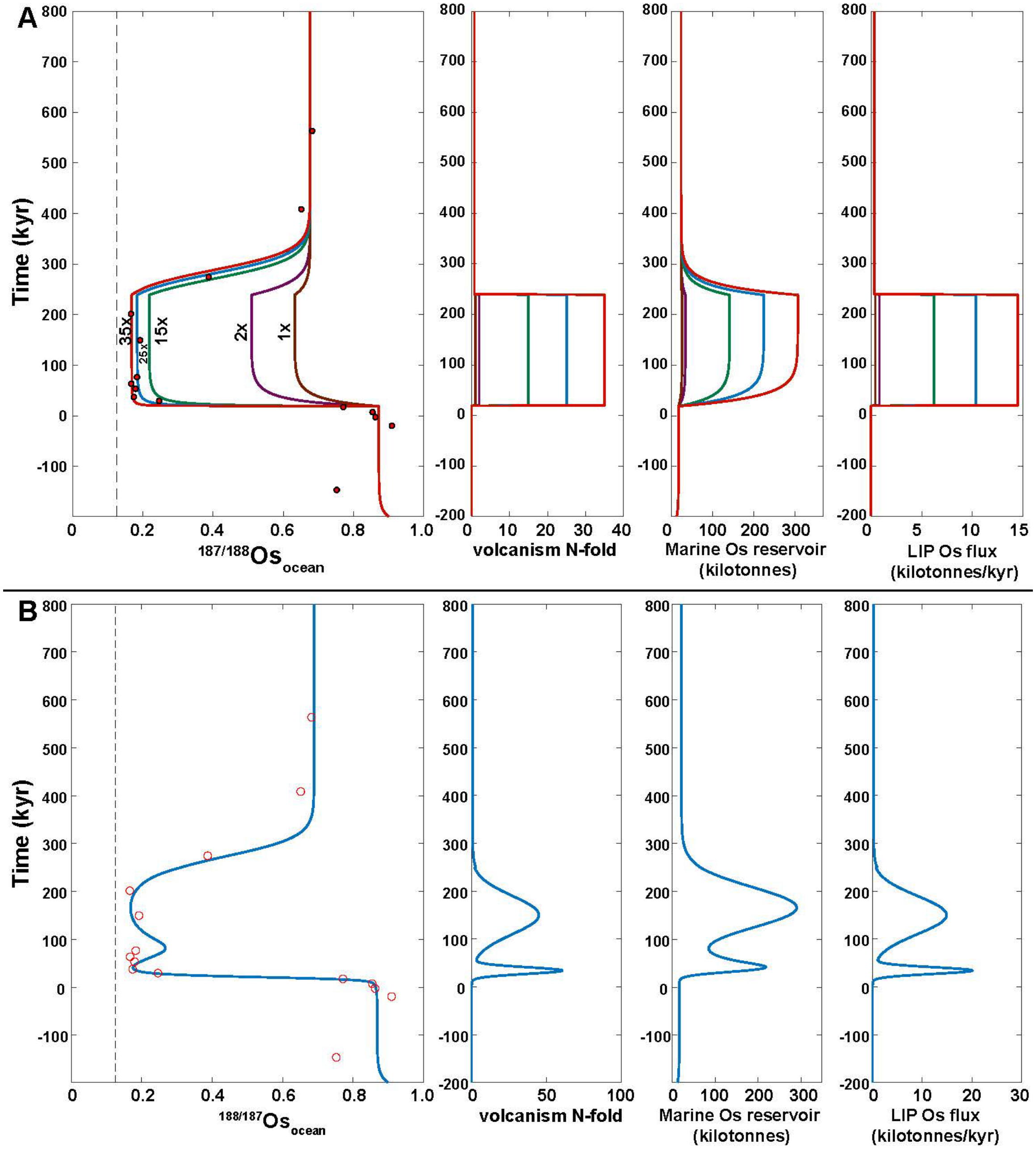

Figure 6.3: Box modeling results for the marine osmium geochemical cycle during OAE2. Top – Model results from a 220 kiloyear perturbation of increased volcanic Os flux. The magnitude of the increased volcanic flux relative to the background mantle Os flux ("N-fold" second panel) is varied iteratively from 1x (brown), 2x (purple), 15x (green), 25x (blue), and 35x (red) background. Model runs invoking LIP volcanism fluxes 25x to 35x the background mantle flux most closely (Figure 6.3 cont'd) reproduce the marine initial osmium isotope ratios (Os_i) measured from the astronomically-tuned Angus core (see Chapter 5). Bottom – This scenario perturbs the marine Os cycle with two gaussian pulses of increased volcanic Os flux. See Model Parameters for detailed discussion of model construction and parameters.

intermediate water depth sites, was an additional fundamental paleoceanographic response to this episode of LIP volcanism (Figure 6.2).

From sedimentological observations, however, shallow water carbonate deposition progressed during the event, and in many locales including epeiric seaways, carbonate concentrations increased (Figure 6.2). Sedimentation also continued in carbonate platform settings, which persisted through OAE2 (Elrick et al., 2009; Navarro-Ramirez et al., 2017), despite partial drowning and stress from nutrient loading (Jenkyns, 1991; Parente et al., 2008). Increases in carbonate content are particularly substantial in the Bridge Creek Limestone of the Western Interior Seaway, resulting from a pronounced global transgression at the onset of OAE2, which led to the inundation of continental margins, drowning of river valleys, and decreases in net siliciclastic dilution (Hancock and Kauffman, 1979; Sageman et al., 1997b; Chapter 4). Arthur et al. (1987) attributed the shoaling CCD to a shift in carbonate sedimentation from the pelagic realm to vastly expanded epicontinental seaways, although it is noted that pelagic carbonate sedimentation resumed following OAE2 even though continents remained inundated (e.g., Gambacorta et al., 2015). Nonetheless, transgression and increased shallow marine carbonate sedimentation during OAE2 may have augmented LIP emissions in decreasing the calcite saturation state of intermediate marine waters. It may have also prevented a post-OAE2 CCD "overshoot" to abyssal depths, as is observed post-PETM (Penman et al., 2016).

The prolonged shoaling of the CCD observed during OAE2, over several 100's of kiloyear, contrasts with conventional models of marine carbonate chemistry that predict more transient ocean acidification events during voluminous geologic CO_2 releases, terminated by the delivery of alkalinity from weathering within 10s of kyr (Zeebe, 2012; Hönisch et al., 2012). To reconcile model and observation, I hypothesize that the remineralization of ample organic carbon sinking from highly productive surfaces waters during OAE2 produced a significant flux of dissolved CO_2 to marine bottom waters, in addition to the mantle carbon flux from LIP volcanism (Arthur et al., 1987). This biogeochemical feedback, along with epicontinental carbonate deposition discussed above, would have prolonged shoaling of the CCD over longer timescales, possibly 100's of kyr. Such a scenario would explain why ocean acidification lasted longer during OAE2, and possibly other OAEs (Erba et al., 2010), than in conventionally modeled scenarios and during the PETM, an event lacking both pervasive black shale deposition and a positive CIE (McInerney and Wing, 2011).

Previous authors attributed localized CCD shoaling during OAE2 to regional increases in surface water productivity and subsequent organic carbon remineralization, producing CO_2 and reducing pH (Bralower, 1988; Vogt, 1989; Scopelliti et al., 2006). Although local organic carbon respiration likely contributed to a shoaling CCD locally and helped to prolong the phenomenon, it cannot explain shoaling of the CCD at other sites globally that do not preserve elevated TOC and were presumably oxic during portions of OAE2. For example, carbonate barren intervals without TOC enrichment occur at the Kerguelen Plateau and Mentelle Basin of Australia (Dickson et al., 2017; Hasegawa et al., in prep.), suggesting an inter-basinal control of global CCD trends, such as LIP volcanism (Figure 6.1).

Perhaps the Plenus Cold Event cooled bottom waters, increasing the solubility and concentration of dissolved CO_2 following the onset of OAE2 (Jenkyns et al., 2017). Cooled bottom waters in turn would have provided a deep marine sink for atmospheric CO_2, lowering pH, and inhibiting carbonate deposition, thus potentially also explaining decreased atmospheric CO_2 levels observed through the event in paleo pCO_2 proxies (Barclay et al., 2010). LIP volcanism appears to have initiated ocean acidification, but marine biogeochemical and paleoclimatic feedbacks to this trigger likely played an important role in sustaining a shoaled CCD in some locations.

Also puzzling, is the fact that the onset of OAE2 does not preserve a negative CIE, as is attributable to mass CO_2 emission during other candidate ocean acidification events like OAE1a and the PETM (Koch et al., 1992; Bauer et al., 2017). It is possible that a subtle, overlooked negative CIE does indeed occur at the base of OAE2 (Kuroda et al., 2007; Kidder and Worsley, 2010; Navarro-Ramirez et al., 2017), or that rapid marine deoxygenation and organic carbon burial prior to OAE2 (Ostrander et al., 2017) muted any negative CIE. Regardless, the pronounced Os_i excursion highlights the rapid onset of voluminous LIP volcanism capable of shoaling the CCD (Figure 6.3).

6.4.2. Biotic effects

Marine deoxygenation is hypothesized to have driven marine macro- and micro-faunal extinctions and accelerated turnover rates through OAE2 (Kauffman, 1984; Elder, 1989; Leckie et al., 2002). In addition to anoxia, findings of suppressed calcite and aragonite saturation states and a shoaling CCD due to LIP volcanism would have been a compounding stressor to marine ecosystems. Indeed, laboratory studies of modern calcifying organism commonly record significant declines in calcification rates at $\Omega_{aragonite}$ of less than three (Ries et al., 2009). Such conditions where surface waters are not yet undersaturated and would not generate outright dissolution, but Ω declines, would be consistent with epicontinental carbonate sedimentation trends of OAE2.

Biostratigraphic indicators of ocean acidification, such as dwarfing, thinning, and fragmentation of foraminifera and calcareous nannofossils, have been defined from other severe geologic acidification events, most strikingly the PETM (Kelly et al., 2010; Bralower et al., 2014; O'Dea et al., 2014; Gibbs et al., 2016). Some, but not all, of these features occur in the biostratigraphic record of OAE2. In particular, dwarfing of nannofossils and foraminifera has been reported from a number of both oxic and anoxic basins (Keller et al., 2001; Coccioni and Luciani, 2004; Faucher et al., 2017). These morphological shifts, along with the extinction of the deep-dwelling, keeled foraminifera *Rotalipora cushmani* following the initiation of LIP volcanism, are consistent with a scenario of volcanic CO_2 emission, decreased Ω, and biotic extinctions (Coccioni et al., 2016; Kuhnt et al., 2017). Further, records of demise in the mid-Cretaceous rudists reefs (Philip and Airaund-Crumiere, 1991) along with turnover of aragonitic ammonite (Elder, 1989) and calcitic microfossil taxa (Leckie et al., 2002) during OAE2 may, at least partially, record selection following changes in marine carbonate chemistry. However, the severity of surface water saturation changes during OAE2, as reflected in a positive calcium isotope excursion (Du Vivier et al., 2015a) and decreases in pelagic carbonate contents (Figure 5.2), along with its effect on marine biotas must still be investigated further and quantified.

6.5. Conclusions

Simple box modeling to reconstruct an abrupt unradiogenic Os_i excursion just preceding the onset of Oceanic Anoxic Event 2 requires a LIP volcanic flux of 25x-35x greater than the background mantle Os flux. Such a perturbation would release significant quantities of CO_2 on a timescale (10's of kyr) rapid enough to affect marine carbonate chemistry, decreasing pH and carbonate saturation states (Bauer et al., 2017). A compilation from marine Cenomanian-Turonian strata reveals that a carbonate barren interval punctuates several pelagic sites during OAE2, indicating that CO_2 delivery from LIP volcanism, possibly augmented by subsequent marine heterotrophy and cooling, triggered a transient shoaling of the CCD. Coeval epicontinental records, on the other hand, exhibit continued carbonate sedimentation through OAE2, demonstrating that prolonged undersaturation did not occur in surface waters during the event. However, dwarfing and fragmentation of microfossil morphologies may indicate that declining surface water saturation state, while still oversaturated with respect to calcite, adversely impacted marine ecosystems. Thus, I conclude that ocean acidification represented a notable component of environmental deterioration during OAE2 and other Mesozoic OAEs, triggered by episodes of massive CO_2 degassing associated with LIP emplacement, with fluxes that exceeded the buffering thresholds of the global ocean.

To further test this hypothesis of altered carbonate chemistry due to prolific LIP volcanism at the onset of OAE2, future investigations should focus on: 1.) evaluating potential indicators of biotic stress to declining Ω, 2.) refining the timing and duration of shoaled CCD within OAE2, and 3.) employing emerging geochemical proxies that may empirically record saturation states, pH, and/or dissolution, for example boron isotopes (e.g., Penman et al., 2014). For now, compiled sedimentological observations and isotope geochemical records across the mid-Cretaceous event are consistent with an interval of intense volcanism and CO_2 emission initiating ocean acidification and shoaling of the CCD. Although this geologic event likely does not match the pace of anthropogenic CO_2 emission, continued careful study of paleobiotic responses in benthic and planktic environments should provide predictive insights into the vulnerabilities and resiliencies of modern ecosystems as marine pH continues to decline.

Box model parameters

A simple isotope mass balance box model is used to reconstruct the unradiogenic initial $^{187/188}$Os (Os_i) excursion of OAE2, as recorded in an astronomically-tuned time series from the Angus core in the Denver Basin of Colorado (Chapter 5). The model calculates the mass (M_o) and isotopic composition (R_o) of the oceanic osmium reservoir following the approach of Tejada et al. (2009). It establishes input fluxes of unradiogenic cosmic (F_{cosmic}), unradiogenic mantle (F_{mantle}), and radiogenic continental weathering/riverine (F_{riv}) osmium to the ocean, along with an output sedimentary flux (F_{sed}). Unradiogenic and radiogenic osmium isotopic compositions are from Levasseur (1999). In addition, the model applies a perturbation flux representing Os delivery from large igneous province volcanism (F_{LIP}) for two different scenarios. The first scenario adds a pulse of constant unradiogenic Os flux from the LIP for a duration of 220 kyr. To reconstruct finer-scale inflections in the Os_i record, I also run a second scenario with two gaussian pulses of LIP volcanism. To reconstruct the pre-OAE2 Os_i steady-state value of ~0.9 in the Angus core, F_{mantle} is set at 331 tonnes/kyr (20% less than Tejada et al., 2009) and F_{riv} is set at 486 tonnes/kyr (65% higher than Tejada et al., 2009).

Equation A6.1: $dM_O = F_{riv} + F_{mantle} + F_{cosmic} + F_{LIP} - F_{sed}$

Eqn. A6.2: $dR_O = \frac{[(F_{riv}*(R_{riv}-R_O))+(F_{mantle}*(R_{mantle}-R_O))+(F_{LIP}*(R_{LIP}-R_O))+(F_{cosmic}(R_{cosmic}-R_O))]}{M_O}$

Initial conditions

Mass of marine Os reservoir: $M_o(0) = 13{,}000$ tonnes

Marine $^{187/188}$Os isotopic composition: $R_o(0) = 0.9$

Residence time: $\tau = 20{,}000$ years

End member isotopic compositions $^{187/188}$Os (Levasseur et al., 1999; Tejada et al., 2009):

$R_{riv} = 1.4$

$R_{mantle} = 0.126$

$R_{cosmic} = 0.126$

$R_{LIP} = 0.126$

Fluxes of osmium (tonnes Os/kyr) based on Tejada et al. (2009):

$F_{riv} = 486$

$F_{mantle} = 331$

$F_{cosmic} = 17.6$

$F_{sed} = M_o/\tau$

Perturbations

Box:

Duration/Constant LIP volcanism flux iterations – 220 kyr/F_{LIP} = 1, 2, 15, 25, 35 x F_{mantle}

Gaussian pulses:

1.) F_{LIP} / σ in kyr = $60 * F_{mantle}$ / 7 kyr
2.) F_{LIP} / σ in kyr = $40 * F_{mantle}$ / 40 kyr

Table 6.1: A compilation of carbonate contents (%$CaCO_3$) pre- and syn-OAE2 at 35 marine sites globally. See Figure 6.2 for visualization of carbonate sedimentation trends through OAE2.

Site	pre-OAE2 %CaCO3	OAE2 %CaCO3	% change	CCD classification	References
West Bermuda Rise DSDP Site 387	0	0	0%	sub-CCD	Tucholke and Vogt 1979
Vigo Seamount, offshore Iberian Peninsula DSDP Site 398	0	0	0%	sub-CCD	Arthur 1979
Continental Rise of Eastern N America DSDP Site 603	0	0	0%	sub-CCD	Meyers, 1987
Newfoundland Margin - NW Atlantic - ODP Site 1276	0	0	0%	sub-CCD	Sinninghe Damste et al 2010
Falkland Plateau S Atlantic DSDP Site 511	0	0	0%	sub-CCD	Huber et al 1995
Poland - Barnasiowka Section	0	0	0%	sub-CCD	Uchman et al 2008
W Atlantic - NJ Margin - DSDP Site 105	7	7	0%	sub-CCD	Herbin et al., 1987
Central Bermuda Rise DSDP Site 386	12	17	42%	sub-CCD	Cameron, 1979; van Helmond et al. 2014
Walvis Ridge S Atlantic - DSDP Site 530	15	20	33%	sub-CCD	Forster et al 2008
SW Australia - Mentelle Basin - IODP Sites U1513, U1516	25	0	-100%	shoaled CCD	Hasegawa in prep
Exmouth Plateau - Leg 122-Site 763C	38	0	-100%	shoaled CCD	Rullkotter et al 1992; Thurow et al. 1992
Galicia Margin N Atlantic offshore Spain - ODP Site 641	40	0	-100%	shoaled CCD	Thurow et al. 1988
Austria - Rehkogelgraben	60	0	-100%	shoaled CCD	Wagreich et al 2008
ODP Leg 207	70	20	-71%	shoaled CCD?	Ch. 2
Goban Sput Irish slope NE Atlantic DSDP Site 549	70	6	-91%	shoaled CCD	de Graciansky et al 1985; Waples & Cunningham, 1985
Goban Sput Irish slope NE Atlantic DSDP Site 551	75	4	-95%	shoaled CCD	de Graciansky et al 1985; Waples & Cunningham, 1985
Kerguelen Plateau ODP Site 1138	77	4	-95%	shoaled CCD	Meyers et al 2009
Blake Nose - subtrop western N Atlantic ODP Site 1050	85	14	-84%	shoaled CCD	Huber et al 1999
Exmouth Plateau, Australia - ODP Site 762	86	0	-100%	shoaled CCD	Exon et al., 1992; Rullkotter et al 1992
Furlo, Italy (Scaglia Bianca-Bonarelli)	90	3	-97%	shoaled CCD	Turgeon & Brumsack, 2006
ODP Leg 174x/Bass River Borehole, New Jersey	10	25	150%	above CCD	Bowman and Bralower, 2005
SH#1 Core, Utah	20	10	-50%	above CCD	Jones et al. (in press) Ch. 4
Angus Core, Colorado	45	65	44%	above CCD	Joo & Sageman, 2014; Ch. 5
NW Europe - Grobern borehole	50	50	0%	above CCD	Voigt et al 2006

Gongzha, Tingri Tibet	50	70	40%	above CCD	Bomou et al. 2013
Rock Canyon Anticline, Colorado	60	75	25%	above CCD	Sageman et al 1997; 2014
Jordan - GM3 basin margin	60	75	25%	above CCD	Wendler et al. 2010
Tunisia, Oued Mellegue	70	80	14%	above CCD	Nederbragt & Fiorentino 1999
Tarfaya Basin, Morocco - SN4 Core	70	75	7%	above CCD	Beil et al 2018
Venezuela	70	40	-43%	above CCD	Perez-Infante et al 1996
Cuba, Kansas	75	80	7%	above CCD	Bowman and Bralower, 2005
Crimea	80	45	-44%	above CCD	Fisher et al. 2005
Lambruisse & Pont Issole, France	85	45	-47%	above CCD	Takashima et al., 2009
Poland - Pulawy Borehole	85	60	-29%	above CCD	Peryt & Wyrwicka 1993
Mexico -carbonate platforms	95	80	-16%	above CCD	Elrick et al 2009

References

Adams, D. D., Hurtgen, M. T., and Sageman, B. B., 2010, Volcanic triggering of a biogeochemical cascade during Oceanic Anoxic Event 2: Nature Geoscience, v. 3, no. 3, p. 201-204.

Al-Ramadan, K., Morad, S., Proust, J. N., and Al-Aasm, I., 2005, Distribution of Diagenetic Alterations in Siliciclastic Shoreface Deposits within a Sequence Stratigraphic Framework: Evidence from the Upper Jurassic, Boulonnais, NW France: Journal of Sedimentary Research, v. 75, no. 5, p. 943-959.

Algeo, T. J., and Lyons, T. W., 2006, Mo–total organic carbon covariation in modern anoxic marine environments: Implications for analysis of paleoredox and paleohydrographic conditions: Paleoceanography, v. 21, no. 1.

Alin, S. R., and Johnson, T. C., 2007, Carbon cycling in large lakes of the world: A synthesis of production, burial, and lake-atmosphere exchange estimates: Global Biogeochemical Cycles, v. 21.

Allan, J. R., and Matthews, R. K., 1982, Isotope signatures associated with early meteoric diagenesis: Sedimentology, v. 29, no. 6, p. 797-817.

Amorosi, A., 1995, Glaucony and Sequence Stratigraphy - A Conceptual Framework of Distribution in Siliciclastic Sequences: Journal of Sedimentary Research Section B-Stratigraphy and Global Studies, v. 65, no. 4, p. 419-425.

Anderson, T. F., and Arthur, M. A., 1983, Stable Isotopes of Oxygen and Carbon and their Application to Sedimentologic and Paleoenvironmental Problems, *in* Arthur, M. A., Anderson, T. F., Kaplan, I. R., Veizer, J., and Land, L. S., eds., Stable Isotopes in Sedimentary Geology: Tulsa, OK, SEPM Short Course No. 10, p. 1-151.

Andersson, A. J., 2014, 8.19 - The Oceanic CaCO3 Cycle, *in* Holland, H. D., and Turekian, K. K., eds., Treatise on Geochemistry (Second Edition): Oxford, Elsevier, p. 519-542.

Ando, H., Huber, B. T., MacLeod, K. G., Ohta, T., and Khim, B., 2009, Blake Nose stable isotopic evidence against the mid-Cenomanian glaciation hypothesis: Geology, v. 37, no. 5, p. 451-454.

Arthur, M. A., 1979, North Atlantic Cretaceous Black Shales: The Record at Site 398 and a Brief Comparison with Other Occurrences, *in* Sibuet, J.-C., and Ryan, W. B. F., eds., Initial Reports of the Deep Sea Drilling Project, Volume 47: Washington, D.C., U.S. Government Printing Office, p. 719-751.

Arthur, M. A., and Schlanger, S. O., 1979, Cretaceous oceanic anoxic events as causal factors in development of reef-reservoired giant oil-fields: AAPG Bulletin, v. 63, no. 6, p. 870-885.

Arthur, M. A., and Dean, W. E., 1986, Cretaceous paleoceanography of the western North Atlantic Ocean, *in* Vogt, P. R., and Tucholke, B. E., eds., The Western North Atlantic Region, Geological Society of America.

Arthur, M. A., and Dean, W. E., 1991, A holistic geochemical approach to cyclomania; examples from Cretaceous pelagic limestone sequences, *in* Einsele, G. e., Ricken, W., and Seilacher, A., eds., Cycles and events in stratigraphy: Berlin, Federal Republic of Germany, Springer Verlag, p. 126.

Arthur, M. A., and Sageman, B. B., 1994, Marine Black Shales: Depositional Mechanisms and Environments of Ancient Deposits: Annual Review of Earth and Planetary Sciences, v. 22, no. 1, p. 499-551.

Arthur, M. A., and Sageman, B. B., 2005, Sea-level control on source-rock development: perspective from the Holocene Black Sea, the mid-Cretaceous Western Interior Basin of North America, and the Late Devonian Appalachian Basin, *in* Harris, N. B., ed., Deposition of Organic-Carbon-Rich Sediments: Models, Mechanisms, & Consequences, v. 82, p. 35-59.

Arthur, M. A., Dean, W. E., and Claypool, G. E., 1985, Anomalous C-13 enrichment in modern marine organic-carbon: Nature, v. 315, no. 6016, p. 216-218.

Arthur, M. A., Schlanger, S. O., and Jenkyns, H. C., 1987, The Cenomanian-Turonian Oceanic Anoxic Event, II. Palaeoceanographic controls on organic-matter production and preservation: Geological Society, London, Special Publications, v. 26, no. 1, p. 401-420.

Arthur, M. A., Dean, W. E., and Pratt, L. M., 1988, Geochemical and climatic effects of increased marine organic-carbon burial at the Cenomanian-Turonian Boundary: Nature, v. 335, no. 6192, p. 714-717.

Baddouh, M. b., Meyers, S. R., Carroll, A. R., Beard, B. L., and Johnson, C. M., 2016, Lacustrine 87Sr/86Sr as a tracer to reconstruct Milankovitch forcing of the Eocene hydrologic cycle: Earth and Planetary Science Letters, v. 448, p. 62-68.

Barclay, R. S., McElwain, J. C., and Sageman, B. B., 2010, Carbon sequestration activated by a volcanic CO2 pulse during Ocean Anoxic Event 2: Nature Geoscience, v. 3, no. 3, p. 205-208.

Baresel, B., Bucher, H., Bagherpour, B., Brosse, M., Guodun, K., and Schaltegger, U., 2017, Timing of global regression and microbial bloom linked with the Permian-Triassic boundary mass extinction: implications for driving mechanisms: Scientific Reports, v. 7, p. 43630.

Barker, I. R., Moser, D. E., Kamo, S. L., and Plint, A. G., 2011, High-precision U–Pb zircon ID–TIMS dating of two regionally extensive bentonites: Cenomanian Stage, Western Canada Foreland BasinThis article is one of a series of papers published in this Special Issue on the theme of Geochronology in honour of Tom Krogh: Canadian Journal of Earth Sciences, v. 48, no. 2, p. 543-556.

Barron, E. J., Arthur, M. A., and Kauffman, E. G., 1985, Cretaceous rhythmic bedding sequences: a plausible link between orbital variations and climate: Earth and Planetary Science Letters, v. 72, no. 4, p. 327-340.

Batenburg, S. J., De Vleeschouwer, D., Sprovieri, M., Hilgen, F. J., Gale, A. S., Singer, B. S., Koeberl, C., Coccioni, R., Claeys, P., and Montanari, A., 2016, Orbital control on the timing of oceanic anoxia in the Late Cretaceous: Climate of the Past, v. 12, no. 10, p. 1995-2009.

Bauer, K. W., Zeebe, R. E., and Wortmann, U. G., 2017, Quantifying the volcanic emissions which triggered Oceanic Anoxic Event 1a and their effect on ocean acidification: Sedimentology, v. 64, no. 1, p. 204-214.

Bechtel, A., Jia, J. L., Strobl, S. A. I., Sachsenhofer, R. F., Liu, Z. J., Gratzer, R., and Puttmann, W., 2012, Palaeoenvironmental conditions during deposition of the Upper Cretaceous oil shale sequences in the Songliao Basin (NE China): Implications from geochemical analysis: Organic Geochemistry, v. 46, p. 76-95.

Beil, S., Kuhnt, W., Holbourn, A. E., Aquit, M., Flögel, S., Chellai, E. H., and Jabour, H., 2018, New insights into Cenomanian paleoceanography and climate evolution from the Tarfaya Basin, southern Morocco: Cretaceous Research, v. 84, p. 451-473.

Berger, A., Loutre, M. F., and Laskar, J., 1992, Stability of the astronomical frequencies over the Earths history for paleoclimate studies: Science, v. 255, no. 5044, p. 560-566.

Berner, R. A., 1982, Burial of organic carbon and pyrite sulfur in the modern ocean – its geochemical and environmental significance: American Journal of Science, v. 282, no. 4, p. 451-473.

Bidigare, R. R., Fluegge, A., Freeman, K. H., Hanson, K. L., Hayes, J. M., Hollander, D., Jasper, J. P., King, L. L., Laws, E. A., Milder, J., Millero, F. J., Pancost, R., Popp, B. N., Steinberg, P. A., and Wakeham, S. G., 1997, Consistent fractionation of C-13 in nature and in the laboratory: Growth-rate effects in some haptophyte algae: Global Biogeochemical Cycles, v. 11, no. 2, p. 279-292.

Boehrer, B., and Schultze, M., 2008, Stratification of lakes: Reviews of Geophysics, v. 46, no. 2, p. 27.

Bomou, B., Adatte, T., Tantawy, A. A., Mort, H., Fleitmann, D., Huang, Y., and Föllmi, K. B., 2013, The expression of the Cenomanian–Turonian oceanic anoxic event in Tibet: Palaeogeography, Palaeoclimatology, Palaeoecology, v. 369, p. 466-481.

Bornemann, A., Norris, R. D., Friedrich, O., Beckmann, B., Schouten, S., Damste, J. S. S., Vogel, J., Hofmann, P., and Wagner, T., 2008, Isotopic evidence for glaciation during the Cretaceous supergreenhouse: Science, v. 319, no. 5860, p. 189-192.

Bosmans, J. H. C., Hilgen, F. J., Tuenter, E., and Lourens, L. J., 2015, Obliquity forcing of low-latitude climate: Climate of the Past, v. 11, no. 10, p. 1335-1346.

Bottini, C., Cohen, A. S., Erba, E., Jenkyns, H. C., and Coe, A. L., 2012, Osmium-isotope evidence for volcanism, weathering, and ocean mixing during the early Aptian OAE 1a: Geology, v. 40, no. 7, p. 583-586.

Boulila, S., Galbrun, B., Miller, K. G., Pekar, S. F., Browning, J. V., Laskar, J., and Wright, J. D., 2011, On the origin of Cenozoic and Mesozoic “third-order” eustatic sequences: Earth-Science Reviews, v. 109, no. 3, p. 94-112.

Bowman, A. R., and Bralower, T. J., 2005, Paleoceanographic significance of high-resolution carbon isotope records across the Cenomanian-Turonian boundary in the Western Interior and New Jersey coastal plain, USA: Marine Geology, v. 217, no. 3-4, p. 305-321.

Bralower, T. J., 1988, Calcareous nannofossil biostratigraphy and assemblages of the Cenomanian-Turonian Boundary interval: implications for the origin and timing of oceanic anoxia: Paleoceanography, v. 3, no. 3, p. 275-316.

Bralower, T. J., Fullagar, P. D., Paull, C. K., Dwyer, G. S., and Leckie, R. M., 1997, Mid-Cretaceous strontium-isotope stratigraphy of deep-sea sections: Geological Society of America Bulletin, v. 109, no. 11, p. 1421-1442.

Bralower, T. J., Kelly, D. C., Gibbs, S., Farley, K., Eccles, L., Lindemann, T. L., and Smith, G. J., 2014, Impact of dissolution on the sedimentary record of the Paleocene–Eocene thermal maximum: Earth and Planetary Science Letters, v. 401, p. 70-82.

Breitburg, D., Levin, L. A., Oschlies, A., Grégoire, M., Chavez, F. P., Conley, D. J., Garçon, V., Gilbert, D., Gutiérrez, D., Isensee, K., Jacinto, G. S., Limburg, K. E., Montes, I., Naqvi, S. W. A., Pitcher, G. C., Rabalais, N. N., Roman, M. R., Rose, K. A., Seibel, B. A., Telszewski, M., Yasuhara, M., and Zhang, J., 2018, Declining oxygen in the global ocean and coastal waters: Science, v. 359, no. 6371.

Broecker, W. S., 2009, Wally's Quest to Understand the Ocean's CaCO3 Cycle: Annual Review of Marine Science, v. 1, no. 1, p. 1-18.

Buchbinder, B., Benjamini, C., and Lipson-Benitah, S., 2000, Sequence development of Late Cenomanian-Turonian carbonate ramps, platforms and basins in Israel: Cretaceous Research, v. 21, no. 6, p. 813-843.

Burnett, J., Gallagher, L., and Hampton, M., 1998, Upper cretaceous: Calcareous nannofossil biostratigraphy, p. 132-199.

Calvert, S. E., Thode, H. G., Yeung, D., and Karlin, R. E., 1996, A stable isotope study of pyrite formation in the Late Pleistocene and Holocene sediments of the Black Sea: Geochimica et Cosmochimica Acta, v. 60, no. 7, p. 1261-1270.

Cameron, D. H., 1979, Grain-Size and Carbon/Carbonate Analyses, Leg43, Initial Reports of the Deep Sea Drilling Project, Volume 43: Washington, D.C., U.S. Government Printing Office, p. 1043-1047.

Caron, M., Dall'Agnolo, S., Accarie, H., Barrera, E., Kauffman, E. G., Amédro, F., and Robaszynski, F., 2006, High-resolution stratigraphy of the Cenomanian–Turonian boundary interval at Pueblo (USA) and wadi Bahloul (Tunisia): stable isotope and bio-events correlation: Geobios, v. 39, no. 2, p. 171-200.

Carpenter, S. J., Erickson, J. M., Lohmann, K. C., and Owen, M. R., 1988, Diagenesis of fossiliferous concretions from the Upper Cretaceous Fox Hills Formation, North Dakota: Journal of Sedimentary Research, v. 58, no. 4, p. 706-723.

Carpenter, K., 2014, Where the sea meets the land: the unresolved Dakota problem in Utah, *in* MacLean, J. S., Biek, R. F., and Huntoon, J. E., eds., Geology of Utah's Far South, Volume 43, Utah Geological Association, p. 357-372.

Catuneanu, O., Beaumont, C., and Waschbusch, P., 1997, Interplay of static loads and subduction dynamics in foreland basins: Reciprocal stratigraphies and the "missing" peripheral bulge: Geology, v. 25, no. 12, p. 1087-1090.

Chafetz, H. S., and Reid, A., 2000, Syndepositional shallow-water precipitation of glauconitic minerals: Sedimentary Geology, v. 136, no. 1-2, p. 29-42.

Chamberlain, C. P., Wan, X., Graham, S. A., Carroll, A. R., Doebbert, A. C., Sageman, B. B., Blisniuk, P., Kent-Corson, M. L., Wang, Z., and Wang, C., 2013, Stable isotopic evidence for climate and basin evolution of the Late Cretaceous Songliao basin, China: Palaeogeography Palaeoclimatology Palaeoecology, v. 385, p. 106-124.

Charbonnier, G., Boulila, S., Spangenberg, J. E., Adatte, T., Föllmi, K. B., and Laskar, J., 2018, Obliquity pacing of the hydrological cycle during the Oceanic Anoxic Event 2: Earth and Planetary Science Letters, v. 499, p. 266-277.

Clarkson, M. O., Stirling, C. H., Jenkyns, H. C., Dickson, A. J., Porcelli, D., Moy, C. M., Pogge von Strandmann, P. A. E., Cooke, I. R., and Lenton, T. M., 2018, Uranium isotope evidence for two episodes of deoxygenation during Oceanic Anoxic Event 2: Proceedings of the National Academy of Sciences, v. 115, no. 12, p. 2918-2923.

Cobban, W. A., and Scott, G. R., 1972, Stratigraphy and ammonite fauna of the Graneros Shale and Greenhorn Limestone near Pueblo, Colorado, USGS Numbered Series Report, Professional Paper 645., 108 p.

Cobban, W. A., Walaszczyk, I., Obradovich, J. D., and McKinney, K. C., 2006, A USGS Zonal Table for the Upper Cretaceous Middle Cenomanian--Maastrichtian of the Western Interior of the United States Based on Ammonites, Inoceramids, and Radiometric Ages, USGS Numbered Series, Open-File Report 2006-1250., 45 p.

Coccioni, R., and Luciani, V., 2004, Planktonic Foraminifera and Environmental Changes across the Bonarelli Event (OAE2, latest Cenomanian) in its Type Area: A High-Resolution Study from the Tethyan Reference Bottaccione Section (Gubbio, Central Italy): Journal of Foraminiferal Research, v. 34, no. 2, p. 109-129.

Coccioni, R., Sideri, M., Frontalini, F., and Montanari, A., 2016, The Rotalipora cushmani extinction at Gubbio (Italy): Planktonic foraminiferal testimonial of the onset of the Caribbean large igneous province emplacement?: Geol. Soc. Am. Special Paper, v. 524, p. 79-96.

Corbett, M. J., and Watkins, D. K., 2013, Calcareous nannofossil paleoecology of the mid-Cretaceous Western Interior Seaway and evidence of oligotrophic surface waters during OAE2: Palaeogeography, Palaeoclimatology, Palaeoecology, v. 392, no. Supplement C, p. 510-523.

Corbett, M. J., Watkins, D. K., and Pospichal, J. J., 2014, A quantitative analysis of calcareous nannofossil bioevents of the Late Cretaceous (Late Cenomanian–Coniacian) Western Interior Seaway and their reliability in established zonation schemes: Marine Micropaleontology, v. 109, p. 30-45.

Cumming, V. M., Selby, D., and Lillis, P. G., 2012, Re-Os geochronology of the lacustrine Green River Formation: Insights into direct depositional dating of lacustrine successions, Re-Os systematics and paleocontinental weathering: Earth and Planetary Science Letters, v. 359, p. 194-205.

Dakos, V., Scheffer, M., van Nes, E. H., Brovkin, V., Petoukhov, V., and Held, H., 2008, Slowing down as an early warning signal for abrupt climate change: Proceedings of the National Academy of Sciences, v. 105, no. 38, p. 14308-14312.

Dale, A., John, C. M., Mozley, P. S., Smalley, P. C., and Muggeridge, A. H., 2014, Time-capsule concretions: Unlocking burial diagenetic processes in the Mancos Shale using carbonate clumped isotopes: Earth and Planetary Science Letters, v. 394, p. 30-37.

de Graciansky, P. C., Deroo, G., Herbin, J. P., Montadert, L., Müller, C., Schaaf, A., and Sigal, J., 1984, Ocean-wide stagnation episode in the late Cretaceous: Nature, v. 308, p. 346.

de Graciansky, P. C., Poag, C. W., Cunningham, J. R., Loubere, P., Masson, D. G., Mazzullo, J. M., Montadert, L., Müller, C., Otsuka, K., Reynolds, L. A., Sigal, J., Snyder, S. W., Townsend, H. A., Vaos, S. P., and Waples, D., 1985, The Goban Spur transect: Geologic evolution of a sediment-starved passive continental margin: GSA Bulletin, v. 96, no. 1, p. 58-76.

DeCelles, P. G., 2011, Foreland Basin Systems Revisited: Variations in Response to Tectonic Settings, *in* Busby, C., and Azor, A., eds., Tectonics of Sedimentary Basins, John Wiley & Sons, Ltd, p. 405-426.

Demaison, G., and Moore, G. T., 1980, Anoxic environments and oil source bed genesis: Organic Geochemistry, v. 2, no. 1, p. 9-31.

Dickson, A. J., Saker-Clark, M., Jenkyns, H. C., Bottini, C., Erba, E., Russo, F., Gorbanenko, O., Naafs, B. D. A., Pancost, R. D., Robinson, S. A., Boorn, S. H. J. M., and Idiz, E., 2017, A Southern Hemisphere record of global trace-metal drawdown and orbital modulation of organic-matter burial across the Cenomanian–Turonian boundary (Ocean Drilling Program Site 1138, Kerguelen Plateau): Sedimentology, v. 64, no. 1, p. 186-203.

Doney, S. C., Fabry, V. J., Feely, R. A., and Kleypas, J. A., 2009, Ocean Acidification: The Other CO2 Problem: Annual Review of Marine Science, v. 1, no. 1, p. 169-192.

Donovan, A. D., Staerker, T. S., Pramudito, A., Weiguo, L., Corbett, M. J., Lowery, C. M., Miceli Romero, A., and Gardner, R., 2012, The Eagle Ford outcrops of West Texas: a laboratory for understanding heterogeneities within unconventional mudstone reservoirs: GCAGS J, v. 1, p. 162-185.

Du Vivier, A. D. C., Selby, D., Sageman, B. B., Jarvis, I., Groecke, D. R., and Voigt, S., 2014, Marine Os-187/Os-188 isotope stratigraphy reveals the interaction of volcanism and ocean circulation during Oceanic Anoxic Event 2: Earth and Planetary Science Letters, v. 389, p. 23-33.

Du Vivier, A. D. C., Jacobson, A. D., Lehn, G. O., Selby, D., Hurtgen, M. T., and Sageman, B. B., 2015a, Ca isotope stratigraphy across the Cenomanian–Turonian OAE 2: Links between volcanism, seawater geochemistry, and the carbonate fractionation factor: Earth and Planetary Science Letters, v. 416, p. 121-131.

Du Vivier, A. D. C., Selby, D., Condon, D. J., Takashima, R., and Nishi, H., 2015b, Pacific Os-187/Os-188 isotope chemistry and U-Pb geochronology: Synchroneity of global Os isotope change across OAE 2: Earth and Planetary Science Letters, v. 428, p. 204-216.

Eaton, J. G., Kirkland, J. I., Howard Hutchison, J., Denton, R., O'Neill, R. C., and Michael Parrish, J., 1997, Nonmarine extinction across the Cenomanian-Turonian boundary, southwestern Utah, with a comparison to the Cretaceous-Tertiary extinction event: Geological Society of America Bulletin, v. 109, no. 5, p. 560-567.

Eicher, D. L., and Worstell, P., 1970, Cenomanian and Turonian Foraminifera from the Great Plains, United States: Micropaleontology, v. 16, no. 3, p. 269-324.

Eicher, D. L., and Diner, R., 1985, Foraminifera as Indicators of Water Mass in the Cretaceous Greenhorn Sea, Western Interior, *in* Pratt, L. M., Kauffman, E. G., and Zelt, F. B., eds., Fine-Grained Deposits and Biofacies of the Cretaceous Western Interior Seaway: Evidence of Cyclic Sedimentary Processes; Midyear field trip guidebook 4: SEPM Society for Sedimentary Geology, p. 60-71.

Eicher, D. L., and Diner, R., 1989, Origin of the cretaceous bridge creek cycles in the western interior, United States: Palaeogeography, Palaeoclimatology, Palaeoecology, v. 74, no. 1, p. 127-146.

Einsele, G., Ricken, W., and Seilacher, A., 1991, Cycles and events in stratigraphy, New York.

Elder, W. P., 1987, The Paleoecology of the Cenomanian-Turonian (Cretaceous) Stage Boundary Extinctions at Black Mesa, Arizona: PALAIOS, v. 2, no. 1, p. 24-40.

Elder, W. P., 1988, Geometry of Upper Cretaceous bentonite beds: Implications about volcanic source areas and paleowind patterns, western interior, United States: Geology, v. 16, no. 9, p. 835-838.

Elder, W. P., 1989, Molluscan extinction patterns across the Cenomanian-Turonian Stage boundary in the Western Interior of the United States: Paleobiology, v. 15, no. 3, p. 299-320.

Elder, W. P., 1991, Molluscan paleoecology and sedimentation patterns of the Cenomanian-Turonian extinction interval in the southern Colorado Plateau region, *in* Nations, J. D., and Eaton, J. G., eds., Stratigraphy, depositional environments, and sedimentary tectonics of the Western Margin, Cretaceous Western Interior Seaway, Volume 260, Geological Society of America Special Paper, p. 113-137.

Elder, W. P., and Kirkland, J. I., 1985, Stratigraphy and Depositional Environments of the Bridge Creek Limestone Member of the Greenhorn Limestone at Rock Canyon Anticline Near Pueblo, Colorado, *in* Pratt, L. M., Kauffman, E. G., and Zelt, F. B., eds., Fine-Grained Deposits and Biofacies of the Cretaceous Western Interior Seaway: Evidence of Cyclic Sedimentary Processes; Midyear field trip guidebook 4: SEPM Society for Sedimentary Geology, p. 122-134.

Elder, W. P., Gustason, E. R., and Sageman, B. B., 1994, Correlation of basinal carbonate cycles to nearshore parasequences in the Late Cretaceous Greenhorn seaway, Western Interior U.S.A: Geological Society of America Bulletin, v. 106, no. 7, p. 892-902.

Elderbak, K., and Leckie, R. M., 2016, Paleocirculation and foraminiferal assemblages of the Cenomanian–Turonian Bridge Creek Limestone bedding couplets: Productivity vs. dilution during OAE2: Cretaceous Research, v. 60, p. 52-77.

Eldrett, J. S., Minisini, D., and Bergman, S. C., 2014, Decoupling of the carbon cycle during Ocean Anoxic Event 2: Geology, v. 42, no. 7, p. 567-570.

Eldrett, J. S., Ma, C., Bergman, S. C., Lutz, B., Gregory, F. J., Dodsworth, P., Phipps, M., Hardas, P., Minisini, D., Ozkan, A., Ramezani, J., Bowring, S. A., Kamo, S. L., Ferguson, K., Macaulay, C., and Kelly, A. E., 2015a, An astronomically calibrated stratigraphy of the Cenomanian, Turonian and earliest Coniacian from the Cretaceous Western Interior Seaway, USA: Implications for global chronostratigraphy: Cretaceous Research, v. 56, p. 316-344.

Eldrett, J. S., Ma, C., Bergman, S. C., Ozkan, A., Minisini, D., Lutz, B., Jackett, S.-J., Macaulay, C., and Kelly, A. E., 2015b, Origin of limestone–marlstone cycles: Astronomic forcing of organic-rich sedimentary rocks from the Cenomanian to early Coniacian of the Cretaceous Western Interior Seaway, USA: Earth and Planetary Science Letters, v. 423, p. 98-113.

Eldrett, J. S., Dodsworth, P., Bergman, S. C., Wright, M., and Minisini, D., 2017, Water-mass evolution in the Cretaceous Western Interior Seaway of North America and equatorial Atlantic: Climate of the Past, v. 13, no. 7, p. 855-878.

Elrick, M., Molina-Garza, R., Duncan, R., and Snow, L., 2009, C-isotope stratigraphy and paleoenvironmental changes across OAE2 (mid-Cretaceous) from shallow-water platform carbonates of southern Mexico: Earth and Planetary Science Letters, v. 277, no. 3, p. 295-306.

Erba, E., 2004, Calcareous nannofossils and Mesozoic oceanic anoxic events: Marine Micropaleontology, v. 52, no. 1, p. 85-106.

Erba, E., Bottini, C., Weissert, H. J., and Keller, C. E., 2010, Calcareous Nannoplankton Response to Surface-Water Acidification Around Oceanic Anoxic Event 1a: Science, v. 329, no. 5990, p. 428-432.

Erbacher, J., Friedrich, O., Wilson, P. A., Birch, H., and Mutterlose, J., 2005, Stable organic carbon isotope stratigraphy across Oceanic Anoxic Event 2 of Demerara Rise, western tropical Atlantic: Geochemistry Geophysics Geosystems, v. 6.

Exon, N. F., Borella, P. E., and Ito, M., 1992, Sedimentology of marine Cretaceous sequences in the central Exmouth Plateau (northwest Australia), *in* von Rad, U., and Haq, B. U., eds., Proceedings of the Ocean Drilling Program, Volume 122: Washington, D.C., U.S. Government Printing Office, p. 233-257.

Faucher, G., Erba, E., Bottini, C., and Gambacorta, G., 2017, Calcareous nannoplankton response to the latest Cenomanian Oceanic Anoxic Event 2 perturbation: Rivista Italiana di Paleontologia e Stratigrafia (Research In Paleontology and Stratigraphy), v. 123, no. 1.

Feng, Z.-q., Jia, C.-z., Xie, X.-n., Zhang, S., Feng, Z.-h., and Cross, T. A., 2010, Tectonostratigraphic units and stratigraphic sequences of the nonmarine Songliao basin, northeast China: Basin Research, v. 22, no. 1, p. 79-95.

Fischer, A. G., Herbert, T. D., and Premoli Silva, I., 1985, Carbonate bedding cycles in Cretaceous pelagic and hemipelagic sediments, *in* Pratt, L. M., Kauffman, E. G., and Zelt, F. B., eds., Fine-Grained Deposits and Biofacies of the Cretaceous Western Interior Seaway: Evidence of Cyclic Sedimentary Processes; Midyear field trip guidebook 4: SEPM Society for Sedimentary Geology, p. 1-10.

Fisher, C. G., Kauffman, E. G., and Wilhelm, L., 1985, The Niobrara Transgressive Hemicyclothem in central and eastern Colorado: The Anatomy of a Multiple Disconformity, *in* Pratt, L. M., Kauffman, E. G., and Zelt, F. B., eds., Fine-Grained Deposits and Biofacies of the

Cretaceous Western Interior Seaway: Evidence of Cyclic Sedimentary Proce-sses; Midyear field trip guidebook 4: SEPM Society for Sedimentary Geology, p. 184-198.

Flament, N., Gurnis, M., and Muller, R. D., 2013, A review of observations and models of dynamic topography: Lithosphere, v. 5, no. 2, p. 189-210.

Floegel, S., Hay, W. W., DeConto, R. M., and Balukhovsky, A. N., 2005, Formation of sedimentary bedding couplets in the Western Interior Seaway of North America—implications from climate system modeling: Palaeogeography, Palaeoclimatology, Palaeoecology, v. 218, no. 1, p. 125-143.

Forster, A., Sturt, H., Meyers, P. A., and Party, S. S., 2004, Molecular biogeochemistry of Cretaceous black shales from the Demerara Rise: preliminary shipboard results from Sites 1257 and 1258, Leg 207, *in* Erbacher, J., Mosher, D. C., and Malone, M. J., eds., Proc. ODP, Init. Repts., 207: College Station, TX (Ocean Drilling Program), p. 1-22.

Forster, A., Schouten, S., Moriya, K., Wilson, P. A., and Damste, J. S. S., 2007, Tropical warming and intermittent cooling during the Cenomanian/Turonian oceanic anoxic event 2: Sea surface temperature records from the equatorial Atlantic: Paleoceanography, v. 22, no. 1.

Forster, A., Kuypers, M. M. M., Turgeon, S. C., Brumsack, H.-J., Petrizzo, M. R., and Sinninghe Damsté, J. S., 2008, The Cenomanian/Turonian oceanic anoxic event in the South Atlantic: New insights from a geochemical study of DSDP Site 530A: Palaeogeography, Palaeoclimatology, Palaeoecology, v. 267, no. 3, p. 256-283.

Fortiz, V., 2017, Oceanic Anoxia Event 2 (93.9 Ma) in the Western Interior Seaway: High resolution calcareous nannofossil record from the Tropic Shale Formation [Masters thesis]: Pennsylvania State University.

Freeman, K. H., and Hayes, J. M., 1992, Fractionation of carbon isotopes by phytoplankton and estimates of ancient CO2 levels: Global Biogeochemical Cycles, v. 6, no. 2, p. 185-198.

Friedrich, O., Norris, R. D., Bornemann, A., Beckmann, B., Palike, H., Worstell, P., Hofmann, P., and Wagner, T., 2008, Cyclic changes in Turonian to Coniacian planktic foraminiferal assemblages from the tropical Atlantic Ocean: Marine Micropaleontology, v. 68, no. 3-4, p. 299-313.

Friedrich, O., Norris, R. D., and Erbacher, J., 2012, Evolution of middle to Late Cretaceous oceans—A 55 m.y. record of Earth's temperature and carbon cycle: Geology, v. 40, no. 2, p. 107-110.

Gale, A. S., and Christensen, W. K., 1996, Occurrence of the belemnite Actinocamax plenus in the Cenomanian of SE France and its significance: Bulletin of the Geological Society of Denmark, v. 43, p. 68-77.

Gale, A. S., Jenkyns, H. C., Kennedy, W. J., and Corfield, R. M., 1993, Chemostratigraphy versus biostratigraphy: data from around the Cenomanian–Turonian boundary: Journal of the Geological Society, v. 150, no. 1, p. 29-32.

Gale, A. S., Hardenbol, J., Hathway, B., Kennedy, W. J., Young, J. R., and Phansalkar, V., 2002, Global correlation of Cenomanian (Upper Cretaceous) sequences: Evidence for Milankovitch control on sea level: Geology, v. 30, no. 4, p. 291-294.

Gale, A. S., Voigt, S., Sageman, B. B., and Kennedy, W. J., 2008, Eustatic sea-level record for the Cenomanian (Late Cretaceous)-Extension to the Western Interior Basin, USA: Geology, v. 36, no. 11, p. 859-862.

Galeotti, S., Rusciadelli, G., Sprovieri, M., Lanci, L., Gaudio, A., and Pekar, S., 2009, Sea-level control on facies architecture in the Cenomanian-Coniacian Apulian margin (Western Tethys): A record of glacio-eustatic fluctuations during the Cretaceous greenhouse?: Palaeogeography Palaeoclimatology Palaeoecology, v. 276, no. 1-4, p. 196-205.

Gambacorta, G., Jenkyns, H., Russo, F., Tsikos, H., Wilson, P., Faucher, G., and Erba, E., 2015, Carbon-and oxygen-isotope records of mid-Cretaceous Tethyan pelagic sequences from the Umbria–Marche and Belluno Basins (Italy): Newsletters on Stratigraphy, v. 48, no. 3, p. 299-323.

Ganino, C., and Arndt, N. T., 2009, Climate changes caused by degassing of sediments during the emplacement of large igneous provinces: Geology, v. 37, no. 4, p. 323-326.

Gannoun, A., and Burton, K. W., 2014, High precision osmium elemental and isotope measurements of North Atlantic seawater: Journal of Analytical Atomic Spectrometry, v. 29, no. 12, p. 2330-2342.

Gao, Y., Ibarra, D. E., Wang, C., Caves, J. K., Chamberlain, C. P., Graham, S. A., and Wu, H., 2015, Mid-latitude terrestrial climate of East Asia linked to global climate in the Late Cretaceous: Geology, v. 43, no. 4, p. 287-290.

Gao, Y., Wang, P., Cheng, R., Wang, G., Wan, X., Wu, H., Wang, S., and Liang, W., 2009, Description of Cretaceous Sedimentary Sequence of the First Member of the Qingshankou Formation Recovered by CCSD-SK-Is Borehole in Songliao Basin: Lithostratigraphy, Sedimentary Facies, and Cyclic Stratigraphy: Earth Science Frontiers, v. 16, no. 2, p. 314-323.

Gardner, M. H., 1995, The stratigraphic hierarchy and tectonic history of the mid-Cretaceous foreland basin of Central Utah, *in* Dorobek, S. L., and Ross, R. M., eds., Stratigraphic Evolution of Foreland Basins, Volume SEPM Special Publication No 52, SEPM.

Gerlach, T., 2011, Volcanic versus anthropogenic carbon dioxide: Eos, Transactions American Geophysical Union, v. 92, no. 24, p. 201-202.

Gibbs, S. J., Bown, P. R., Ridgwell, A., Young, J. R., Poulton, A. J., and O'Dea, S. A., 2016, Ocean warming, not acidification, controlled coccolithophore response during past greenhouse climate change: Geology, v. 44, no. 1, p. 59-62.

Gilbert, G. K., 1895, Sedimentary Measurement of Cretaceous Time: The Journal of Geology, v. 3, no. 2, p. 121-127.

Glass, J. B., and Orphan, V. J., 2012, Trace Metal Requirements for Microbial Enzymes Involved in the Production and Consumption of Methane and Nitrous Oxide: Frontiers in Microbiology, v. 3, p. 61.

Glenister, L. M., and Kauffman, E. G., 1985, High resolution stratigraphy and depositional history of the Greenhorn Regressive Hemicyclothem, Rock Canyon Anticline, Pueblo, Colorado, *in* Pratt, L. M., Kauffman, E. G., and Zelt, F. B., eds., Fine-Grained Deposits and Biofacies of the Cretaceous Western Interior Seaway: Evidence of Cyclic Sedimentary Processes; Midyear field trip guidebook 4: SEPM Society for Sedimentary Geology, p. 170-183.

Gomes, M. L., and Hurtgen, M. T., 2013, Sulfur isotope systematics of a euxinic, low-sulfate lake: Evaluating the importance of the reservoir effect in modern and ancient oceans: Geology, v. 41, no. 6, p. 663-666.

Graham, S. A., Hendrix, M. S., Johnson, C. L., Badamgarav, D., Badarch, G., Amory, J., Porter, M., Barsbold, R., Webb, L. E., and Hacker, B. R., 2001, Sedimentary record and tectonic implications of Mesozoic rifting in southeast Mongolia: Geological Society of America Bulletin, v. 113, no. 12, p. 1560-1579.

Greene, S. E., Martindale, R. C., Ritterbush, K. A., Bottjer, D. J., Corsetti, F. A., and Berelson, W. M., 2012, Recognising ocean acidification in deep time: An evaluation of the evidence for acidification across the Triassic-Jurassic boundary: Earth-Science Reviews, v. 113, no. 1, p. 72-93.

Gregory, H. E., and Moore, R. C., 1931, The Kaiparowits Region: A Geographic and Geologic Reconnaissance of Parts of Utah and Arizona, 164.

Grosheny, D., Ferry, S., Lecuyer, C., Merran, Y., Mroueh, M., and Granier, B., 2017, The Cenomanian-Turonian Boundary Event (CTBE) in northern Lebanon as compared to regional data – Another set of evidences supporting a short-lived tectonic pulse coincidental with the event?: Palaeogeography, Palaeoclimatology, Palaeoecology, v. 487, p. 447-461.

Hancock, J. M., 1993, Sea-level changes around the Cenomanian-Turonian Boundary: Cretaceous Research, v. 14, no. 4-5, p. 553-562.

Hancock, J. M., and Kauffman, E. G., 1979, The great transgressions of the Late Cretaceous: Journal of the Geological Society, v. 136, no. 2, p. 175-186.

Haq, B. U., 2014, Cretaceous eustasy revisited: Global and Planetary Change, v. 113, p. 44-58.

Haq, B. U., and Huber, B. T., 2017, Anatomy of a eustatic event during the Turonian (Late Cretaceous) hot greenhouse climate: Science China Earth Sciences, v. 60, no. 1, p. 20-29.

Hardas, P., and Mutterlose, J., 2007, Calcareous nannofossil assemblages of Oceanic Anoxic Event 2 in the equatorial Atlantic: Evidence of an eutrophication event: Marine Micropaleontology, v. 66, no. 1, p. 52-69.

Harries, P. J., and Little, C. T. S., 1999, The early Toarcian (Early Jurassic) and the Cenomanian-Turonian (Late Cretaceous) mass extinctions: similarities and contrasts: Palaeogeography Palaeoclimatology Palaeoecology, v. 154, no. 1-2, p. 39-66.

Harris, N. B., Freeman, K. H., Pancost, R. D., White, T. S., and Mitchell, G. D., 2004, The character and origin of lacustrine source rocks in the Lower Cretaceous synrift Congo Basin, west Africa: AAPG Bulletin, v. 88, no. 8, p. 1163-1184.

Hasegawa, T., 1997, Cenomanian-Turonian carbon isotope events recorded in terrestrial organic matter from northern Japan: Palaeogeography Palaeoclimatology Palaeoecology, v. 130, no. 1-4, p. 251-273.

Hatch, J. R., and Leventhal, J. S., 1992, Relationship between inferred redox potential of the depositional environment and geochemistry of the Upper Pennsylvanian (Missourian) Stark Shale Member of the Dennis Limestone, Wabaunsee County, Kansas, U.S.A: Chemical Geology, v. 99, no. 1-3, p. 65-82.

Hattin, D. E., 1971, Widespread, synchronously deposited, burrow-mottled limestone beds in Greenhorn limestone (upper Cretaceous) of Kansas and southeastern Colorado: AAPG Bulletin, v. 55, no. 3, p. 412-431.

Hay, W. W., 2011, Can humans force a return to a ‘Cretaceous’ climate?: Sedimentary Geology, v. 235, no. 1, p. 5-26.

Hay, W. W., and Leslie, M. A., 1990, Could possible changes in global groundwater reservoir cause eustatic sea-level fluctuations?, Sea-level change: Washington, D.C., National Academy Press, p. 161-170.

Hay, W. W., DeConto, R. M., Wold, C. N., Wilson, K. M., Voigt, S., Schulz, M., Wold, A. R., Dullo, W.-C., Ronov, A. B., Balukhovsky, A. N., and Soding, E., 1999, Alternative global Cretaceous paleogeography, *in* Barrera, E., and Johnson, C. L., eds., Evolution of the Cretaceous ocean-climate system, Volume 332, GSA Special Paper, p. 1-47.

Hayes, J. M., Strauss, H., and Kaufman, A. J., 1999, The abundance of 13C in marine organic matter and isotopic fractionation in the global biogeochemical cycle of carbon during the past 800 Ma: Chemical Geology, v. 161, no. 1, p. 103-125.

Henderson, R. A., 1998, Eustatic and palaeoenvironmental assessment of the mid-Cretaceous Bathurst Island Group of the Money Shoals Platform, northern Australia: Palaeogeography Palaeoclimatology Palaeoecology, v. 138, no. 1-4, p. 115-138.

Herbin, J. P., Montadert, L., Müller, C., Gomez, R., Thurow, J., and Wiedmann, J., 1986, Organic-rich sedimentation at the Cenomanian-Turonian boundary in oceanic and coastal basins in the North Atlantic and Tethys: Geological Society, London, Special Publications, v. 21, no. 1, p. 389-422.

Herbin, J. P., Masure, E., and Roucache, J., 1987, Cretaceous Formations from the Lower Continental Rise off Cape Hatteras: Organic Geochemistry, Dinoflagellate Cysts, and the Cenomanian/Turonian Boundary Event at Sites 603 (Leg 93) and 105 (Leg 11), *in* van Hinte, J. E., and Wise, S. W., eds., Initial Reports of the Deep Sea Drilling Project, Volume 93: Washington, D.C., U.S. Government Printing Office, p. 1139-1162.

Hetzel, A., Boettcher, M. E., Wortmann, U. G., and Brumsack, H.-J., 2009, Paleo-redox conditions during OAE 2 reflected in Demerara Rise sediment geochemistry (ODP Leg 207): Palaeogeography Palaeoclimatology Palaeoecology, v. 273, no. 3-4, p. 302-328.

Hinnov, L. A., 2013, Cyclostratigraphy and its revolutionizing applications in the earth and planetary sciences: Geological Society of America Bulletin, v. 125, no. 11-12, p. 1703-1734.

Hinnov, L. A., and Hilgen, F. J., 2012, Cyclostratigraphy and Astrochronology: Geologic Time Scale 2012, Vols 1 & 2, p. 63-83.

Holland, S. M., and Patzkowsky, M. E., 2015, The stratigraphy of mass extinction: Palaeontology, v. 58, no. 5, p. 903-924.

Hollander, D. J., and Smith, M. A., 2001, Microbially mediated carbon cycling as a control on the delta C-13 of sedimentary carbon in eutrophic Lake Mendota (USA): New models for interpreting isotopic excursions in the sedimentary record: Geochimica Et Cosmochimica Acta, v. 65, no. 23, p. 4321-4337.

Holmden, C., Jacobson, A. D., Sageman, B. B., and Hurtgen, M. T., 2016, Response of the Cr isotope proxy to Cretaceous Ocean Anoxic Event 2 in a pelagic carbonate succession from the Western Interior Seaway: Geochimica Et Cosmochimica Acta, v. 186, p. 277-295.

Hönisch, B., Ridgwell, A., Schmidt, D. N., Thomas, E., Gibbs, S. J., Sluijs, A., Zeebe, R., Kump, L., Martindale, R. C., Greene, S. E., Kiessling, W., Ries, J., Zachos, J. C., Royer, D. L., Barker, S., Marchitto, T. M., Moyer, R., Pelejero, C., Ziveri, P., Foster, G. L., and Williams, B., 2012, The Geological Record of Ocean Acidification: Science, v. 335, no. 6072, p. 1058-1063.

Hou, D., Li, M., and Huang, Q., 2000, Marine transgressional events in the gigantic freshwater lake Songliao: paleontological and geochemical evidence: Organic Geochemistry, v. 31, no. 7–8, p. 763-768.

Hower, J., 1961, Some Factors Concerning the Nature and Origin of Glauconite: The American Mineralogist, v. 46, no. 3-4, p. 313-334.

Hu, J. F., Peng, P. A., Liu, M. Y., Xi, D. P., Song, J. Z., Wan, X. Q., and Wang, C. S., 2015, Seawater Incursion Events in a Cretaceous Paleo-lake Revealed by Specific Marine Biological Markers: Scientific Reports, v. 5, p. 9508.

Huang, Y. J., Yang, G. S., Gu, J., Wang, P. K., Huang, Q. H., Feng, Z. H., and Feng, L. J., 2013, Marine incursion events in the Late Cretaceous Songliao Basin: Constraints from sulfur geochemistry records: Palaeogeography Palaeoclimatology Palaeoecology, v. 385, p. 152-161.

Huber, B. T., Hodell, D. A., and Hamilton, C. P., 1995, Middle–Late Cretaceous climate of the southern high latitudes: Stable isotopic evidence for minimal equator-to-pole thermal gradients: GSA Bulletin, v. 107, no. 10, p. 1164-1191.

Huber, B. T., Leckie, R. M., Norris, R. D., Bralower, T. J., and CoBabe, E., 1999, Foraminiferal assemblage and stable isotopic change across the Cenomanian-Turonian boundary in the subtropical North Atlantic: Journal of Foraminiferal Research, v. 29, no. 4, p. 392-417.

Huber, B. T., MacLeod, K. G., Watkins, D. K., and Coffin, M. F., 2018, The rise and fall of the Cretaceous Hot Greenhouse climate: Global and Planetary Change, v. 167, p. 1-23.

Huffman, E. W. D., 1977, Performance of a new automatic carbon-dioxide coulometer: Microchemical Journal, v. 22, no. 4, p. 567-573.

Ibarra, D. E., Jones, M. M., Floor, G., Caves Rugenstein, J. K., Sageman, B. B., Graham, S. A., Chamberlain, C. P., and von Blanckenburg, F., in prep., Congruent weathering of North America across Oceanic Anoxic Event 2.

Jarvis, I., Gale, A. S., Jenkyns, H. C., and Pearce, M. A., 2006, Secular variation in Late Cretaceous carbon isotopes: a new delta C-13 carbonate reference curve for the Cenomanian-Campanian (99.6-70.6 Ma): Geological Magazine, v. 143, no. 5, p. 561-608.

Jarvis, I., Lignum, J. S., Groecke, D. R., Jenkyns, H. C., and Pearce, M. A., 2011, Black shale deposition, atmospheric CO2 drawdown, and cooling during the Cenomanian-Turonian Oceanic Anoxic Event: Paleoceanography, v. 26.

Jarvis, I., Trabucho-Alexandre, J., Gröcke, D. R., Uličný, D., and Laurin, J., 2015, Intercontinental correlation of organic carbon and carbonate stable isotope records: evidence of climate and sea-level change during the Turonian (Cretaceous): The Depositional Record, v. 1, no. 2, p. 53-90.

Jenkyns, H. C., 1991, Impact of Cretaceous Sea Level Rise and Anoxic Events on the Mesozoic Carbonate Platform of Yugoslavia: AAPG Bulletin, v. 75, no. 6, p. 1007-1017.

Jenkyns, H. C., 2010, Geochemistry of oceanic anoxic events: Geochemistry Geophysics Geosystems, v. 11.

Jenkyns, H. C., Gale, A. S., and Corfield, R. M., 1994, Carbon- and oxygen-isotope stratigraphy of the English Chalk and Italian Scaglia and its palaeoclimatic significance: Geological Magazine, v. 131, no. 1, p. 1-34.

Jenkyns, H. C., Dickson, A. J., Ruhl, M., and van den Boorn, S. H. J. M., 2017, Basalt-seawater interaction, the Plenus Cold Event, enhanced weathering and geochemical change: deconstructing Oceanic Anoxic Event 2 (Cenomanian–Turonian, Late Cretaceous): Sedimentology, v. 64, no. 1, p. 16-43.

Jicha, B. R., Singer, B. S., and Sobol, P., 2016, Re-evaluation of the ages of 40Ar/39Ar sanidine standards and supereruptions in the western U.S. using a Noblesse multi-collector mass spectrometer: Chemical Geology, v. 431, p. 54-66.

Jiménez Berrocoso, Á., MacLeod, K. G., Martin, E. E., Bourbon, E., Londoño, C. I., and Basak, C., 2010, Nutrient trap for Late Cretaceous organic-rich black shales in the tropical North Atlantic: Geology, v. 38, no. 12, p. 1111-1114.

Jones, M. M., Sageman, B. B., and Meyers, S. R., 2018a, Turonian Sea Level and Paleoclimatic Events in Astronomically Tuned Records from the Tropical North Atlantic and Western Interior Seaway: Paleoceanography and Paleoclimatology, v. 33, no. 5, p. 470-492.

Jones, M. M., Ibarra, D. E., Gao, Y., Sageman, B. B., Selby, D., Chamberlain, C. P., and Graham, S. A., 2018b, Evaluating Late Cretaceous OAEs and the influence of marine incursions on organic carbon burial in an expansive East Asian paleo-lake: Earth and Planetary Science Letters, v. 484, p. 41-52.

Jones, M. M., Sageman, B. B., Oakes, R. L., Parker, A. L., Leckie, R. M., Bralower, T. J., Sepúlveda, J., and Fortiz, V., in press, Astronomical pacing of relative sea level during Oceanic Anoxic Event 2: Preliminary studies of the expanded SH#1 Core, Utah: GSA Bulletin.

Joo, Y. J., and Sageman, B. B., 2014, Cenomanian to Campanian carbon isotope chemostratigraphy from the Western Interior Basin, USA: Journal of Sedimentary Research, v. 84, no. 7, p. 529-542.

Jordan, T. E., 1981, Thrust loads and foreland basin evolution, Cretaceous, western United States: AAPG Bulletin, v. 65, no. 12, p. 2506-2520.

Junium, C. K., and Arthur, M. A., 2007, Nitrogen cycling during the cretaceous, Cenomanian-Turonian oceanic anoxic event II: Geochemistry Geophysics Geosystems, v. 8.

Junium, C. K., Meyers, S. R., and Arthur, M. A., 2018, Nitrogen cycle dynamics in the mid-Cretaceous Greenhouse: Earth and Planetary Science Letters, v. 481, p. 404-411.

Kassler, P., 1973, The Structural and Geomorphic Evolution of the Persian Gulf, *in* Purser, B. H., ed., The Persian Gulf: Holocene Carbonate Sedimentation and Diagenesis in a Shallow Epicontinental Sea: Berlin, Heidelberg, Springer-Verlag, p. 10-32.

Kauffman, E. G., 1977, Geological and biological overview: Western Interior Cretaceous Basin: The Mountain Geologist, v. 13, p. 75-99.

Kauffman, E. G., 1984, Paleobiogeography and evolutionary response dynamic in the Cretaceous Western Interior Seaway of North America, *in* Westermann, G. E. G., ed., Jurassic-Cretaceous Biochronology and Paleogeography of North America, Geological Association of Canada.

Kauffman, E. G., 1988, Concepts and methods of high-resolution event stratigraphy: Annual Review of Earth and Planetary Sciences, v. 16, no. 1, p. 605-654.

Kauffman, E. G., and Caldwell, W. G. E., 1993, The Western Interior Basin in space and time, *in* Caldwell, W. G. E., and Kauffman, E. G., eds., Evolution of the Western Interior Basin, Volume Special Paper 39, Geological Association of Canada, p. 1-30.

Kauffman, E. G., Sageman, B. B., Kirkland, J. I., Elder, W. P., Harries, P. J., and Villamil, T., 1993, Molluscan Biostratigraphy of the Cretaceous Western Interior Basin, North America, *in* Caldwell, W. G. E., and Kauffman, E. G., eds., Evolution of the Western Interior Basin, Volume 39, Geological Association of Canada, p. 397-434.

Keeling, R. F., Körtzinger, A., and Gruber, N., 2010, Ocean Deoxygenation in a Warming World: Annual Review of Marine Science, v. 2, no. 1, p. 199-229.

Keller, G., and Pardo, A., 2004, Age and paleoenvironment of the Cenomanian–Turonian global stratotype section and point at Pueblo, Colorado: Marine Micropaleontology, v. 51, no. 1, p. 95-128.

Keller, G., Han, Q., Adatte, T., and Burns, S. J., 2001, Palaeoenvironment of the Cenomanian–Turonian transition at Eastbourne, England: Cretaceous Research, v. 22, no. 4, p. 391-422.

Keller, G., Berner, Z., Adatte, T., and Stueben, D., 2004, Cenomanian–Turonian and δ13C, and δ18O, sea level and salinity variations at Pueblo, Colorado: Palaeogeography, Palaeoclimatology, Palaeoecology, v. 211, no. 1, p. 19-43.

Kelly, D. C., Nielsen, T. M. J., McCarren, H. K., Zachos, J. C., and Röhl, U., 2010, Spatiotemporal patterns of carbonate sedimentation in the South Atlantic: Implications for carbon cycling during the Paleocene–Eocene thermal maximum: Palaeogeography, Palaeoclimatology, Palaeoecology, v. 293, no. 1, p. 30-40.

Kennedy, W. J., Walaszczyk, I., and Cobban, W. A., 2000, Pueblo, Colorado, USA, candidate Global Boundary Stratotype Section and Point for the base of the Turonian Stage of the Cretaceous, and for the base of the Middle Turonian Substage, with a revision of the Inoceramidae (Bivalvia): Acta Geologica Polonica, v. 50, no. 3, p. 295-334.

Kennedy, W. J., Walaszczyk, I., and Cobban, W. A., 2005, The global boundary stratotype section and point for the base of the Turonian stage of the cretaceous: Pueblo, Colorado, USA: Episodes, v. 28, no. 2, p. 93-104.

Kerr, A. C., 1998, Oceanic plateau formation: a cause of mass extinction and black shale deposition around the Cenomanian-Turonian boundary?: Journal of the Geological Society, v. 155, p. 619-626.

Kerr, A. C., Tarney, J., Marriner, G. F., Nivia, A., and Saunders, A. D., 1997, The Caribbean-Colombian Cretaceous igneous province: The internal anatomy of an oceanic plateau: Geophysical monograph-American Geophysical Union, v. 100, p. 123-144.

Kidder, D. L., and Worsley, T. R., 2010, Phanerozoic Large Igneous Provinces (LIPs), HEATT (Haline Euxinic Acidic Thermal Transgression) episodes, and mass extinctions: Palaeogeography Palaeoclimatology Palaeoecology, v. 295, no. 1-2, p. 162-191.

Kirkland, J. I., 1991, Lithostratigraphic and biostratigraphic framework for the Mancos Shale (Late Cenomanian to Middle Turonian) at Black Mesa, northeastern Arizona, *in* Nations, J. D., and Eaton, J. G., eds., Stratigraphy, depositional environments; and sedimentary tectonics of the western margin, Cretaceous Western Interior Seaway, Volume 260, Geological Society of America Special Paper, p. 85-111.

Klein, J. S., Mozley, P., Campbell, A. R., and Cole, R., 1999, Spatial distribution of carbon and oxygen isotopes in laterally extensive carbonate-cemented layers; implications for mode of growth and subsurface identification: Journal of Sedimentary Research, v. 69, no. 1, p. 184-201.

Koch, P. L., Zachos, J. C., and Gingerich, P. D., 1992, Correlation between isotope records in marine and continental carbon reservoirs near the Palaeocene/Eocene boundary: Nature, v. 358, p. 319.

Kolonic, S., Wagner, T., Forster, A., Damste, J. S. S., Walsworth- Bell, B., Erba, E., Turgeon, S., Brumsack, H. J., Chellai, E. I., Tsikos, H., Kuhnt, W., and Kuypers, M. M. M., 2005, Black shale deposition on the northwest African Shelf during the Cenomanian/Turonian oceanic anoxic event: Climate coupling and global organic carbon burial: Paleoceanography, v. 20, no. 1.

Kraal, P., Slomp, C. P., Forster, A., and Kuypers, M. M. M., 2010, Phosphorus cycling from the margin to abyssal depths in the proto-Atlantic during oceanic anoxic event 2: Palaeogeography Palaeoclimatology Palaeoecology, v. 295, no. 1-2, p. 42-54.

Kuhnt, W., Holbourn, A., Gale, A., Chellai, E. H., and Kennedy, W. J., 2009, Cenomanian sequence stratigraphy and sea-level fluctuations in the Tarfaya Basin (SW Morocco): Geological Society of America Bulletin, v. 121, no. 11-12, p. 1695-1710.

Kuhnt, W., Holbourn, A. E., Beil, S., Aquit, M., Krawczyk, T., Flogel, S., Chellai, E. H., and Jabour, H., 2017, Unraveling the onset of Cretaceous Oceanic Anoxic Event 2 in an extended sediment archive from the Tarfaya-Laayoune Basin, Morocco: Paleoceanography, v. 32, no. 8, p. 923-946.

Kuiper, K. F., Deino, A., Hilgen, F. J., Krijgsman, W., Renne, P. R., and Wijbrans, J. R., 2008, Synchronizing Rock Clocks of Earth History: Science, v. 320, no. 5875, p. 500-504.

Kump, L. R., and Arthur, M. A., 1999, Interpreting carbon-isotope excursions: carbonates and organic matter: Chemical Geology, v. 161, no. 1-3, p. 181-198.

Kump, L. R., Bralower, T. J., and Ridgwell, A., 2009, Ocean Acidification in Deep Time: Oceanography, v. 22, no. 4, p. 94-107.

Kuroda, J., Hori, R. S., Suzuki, K., Gröcke, D. R., and Ohkouchi, N., 2010, Marine osmium isotope record across the Triassic-Jurassic boundary from a Pacific pelagic site: Geology, v. 38, no. 12, p. 1095-1098.

Kuroda, J., Jiménez-Espejo, F. J., Nozaki, T., Gennari, R., Lugli, S., Manzi, V., Roveri, M., Flecker, R., Sierro, F. J., Yoshimura, T., Suzuki, K., and Ohkouchi, N., 2016, Miocene to Pleistocene osmium isotopic records of the Mediterranean sediments: Paleoceanography, v. 31, no. 1, p. 148-166.

Kuroda, J., Ogawa, N. O., Tanimizu, M., Coffin, M. F., Tokuyama, H., Kitazato, H., and Ohkouchi, N., 2007, Contemporaneous massive subaerial volcanism and late cretaceous Oceanic Anoxic Event 2: Earth and Planetary Science Letters, v. 256, no. 1-2, p. 211-223.

Kuypers, M. M. M., Pancost, R. D., and Damste, J. S. S., 1999, A large and abrupt fall in atmospheric CO2 concentration during Cretaceous times: Nature, v. 399, no. 6734, p. 342-345.

Kuypers, M. M. M., Pancost, R. D., Nijenhuis, I. A., and Damste, J. S. S., 2002, Enhanced productivity led to increased organic carbon burial in the euxinic North Atlantic basin during the late Cenomanian oceanic anoxic event: Paleoceanography, v. 17, no. 4.

Kuypers, M. M. M., Lourens, L. J., Rijpstra, W. R. C., Pancost, R. D., Nijenhuis, I. A., and Damste, J. S. S., 2004, Orbital forcing of organic carbon burial in the proto-North Atlantic during oceanic anoxic event 2: Earth and Planetary Science Letters, v. 228, no. 3-4, p. 465-482.

Larson, R. L., 1991, Latest pulse of Earth: Evidence for a mid-Cretaceous superplume: Geology, v. 19, no. 6, p. 547-550.

Laskar, J., Robutel, P., Joutel, F., Gastineau, M., Correia, A. C. M., and Levrard, B., 2004, A long-term numerical solution for the insolation quantities of the Earth: Astronomy & Astrophysics, v. 428, no. 1, p. 261-285.

Laskar, J., Fienga, A., Gastineau, M., and Manche, H., 2011, La2010: a new orbital solution for the long-term motion of the Earth: Astronomy & Astrophysics, v. 532.

Laurin, J., and Sageman, B. B., 2007, Cenomanian-Turonian coastal record in SW Utah, USA: Orbital-scale transgressive-regressive events during oceanic anoxic event II: Journal of Sedimentary Research, v. 77, no. 9-10, p. 731-756.

Laurin, J., Cech, S., Ulicny, D., Staffen, Z., and Svobodova, M., 2014, Astrochronology of the Late Turonian: implications for the behavior of the carbon cycle at the demise of peak greenhouse: Earth and Planetary Science Letters, v. 394, p. 254-269.

Laurin, J., Meyers, S. R., Uličný, D., Jarvis, I., and Sageman, B. B., 2015, Axial obliquity control on the greenhouse carbon budget through middle- to high-latitude reservoirs: Paleoceanography, v. 30, no. 2, p. 133-149.

Leckie, R. M., 1985, Foraminifera of the Cenomanian-Turonian Boundary Interval, Greenhorn Formation, Rock Canyon Anticline, Pueblo, Colorado, *in* Pratt, L. M., Kauffman, E. G., and Zelt, F. B., eds., Fine-Grained Deposits and Biofacies of the Cretaceous Western Interior Seaway: Evidence of Cyclic Sedimentary Processes; Midyear field trip guidebook 4: SEPM Society for Sedimentary Geology, p. 139-149.

Leckie, R. M., Schmidt, M. G., Finkelstein, D., and Yuretich, R., 1991, Paleoceanographic and paleoclimatic interpretations of the Mancos Shale (Upper Cretaceous), Black Mesa Basin, Arizona, *in* Nations, J. D., and Eaton, J. G., eds., Stratigraphy, depositional environments; and sedimentary tectonics of the western margin, Cretaceous Western Interior Seaway, Geological Society of America.

Leckie, R., Kirkland, J., and Elder, W., 1997, Stratigraphic framework and correlation of a principal reference section of the Mancos Shale (Upper Cretaceous), Mesa Verde, Colorado, *in* Proceedings New Mexico Geological Society Guidebook, 48th Field Conference, Mesozoic Geology and Paleontology of the Four Corners Region, p. 163-216.

Leckie, R. M., Yuretich, R. F., West, O. L. O., Finkelstein, D., and Schmidt, M., 1998, Paleoceanography of the southwestern Western Interior Sea during the time of the Cenomanian-Turonian Boundary (Late Cretaceous), *in* Dean, W. E., and Arthur, M. A., eds., Stratigraphy and paleoenvironments of the Cretaceous Western Interior Seaway, USA, Volume 6, SEPM, p. 101-126.

Leckie, R. M., Bralower, T. J., and Cashman, R., 2002, Oceanic anoxic events and plankton evolution: Biotic response to tectonic forcing during the mid-Cretaceous: Paleoceanography, v. 17, no. 3.

Lees, J. A., 2008, The calcareous nannofossil record across the late cretaceous Turonian/Coniacian boundary, including new data from Germany, Poland, the Czech Republic and England: Cretaceous Research, v. 29, no. 1, p. 40-64.

Leithold, E. L., 1994, Stratigraphical architecture at the muddy margin of the Cretaceous Western Interior Seaway, southern Utah: Sedimentology, v. 41, no. 3, p. 521-542.

Li, Y.-X., Montañez, I. P., Liu, Z., and Ma, L., 2017, Astronomical constraints on global carbon-cycle perturbation during Oceanic Anoxic Event 2 (OAE2): Earth and Planetary Science Letters, v. 462, p. 35-46.

Liu, S., and Nummedal, D., 2004, Late Cretaceous subsidence in Wyoming: Quantifying the dynamic component: Geology, v. 32, no. 5, p. 397-400.

Locklair, R. E., and Sageman, B. B., 2008, Cyclostratigraphy of the Upper Cretaceous Niobrara Formation, Western Interior, USA: A Coniacian-Santonian orbital timescale: Earth and Planetary Science Letters, v. 269, no. 3-4, p. 539-552.

Locklair, R., Sageman, B., and Lerman, A., 2011, Marine carbon burial flux and the carbon isotope record of Late Cretaceous (Coniacian-Santonian) Oceanic Anoxic Event III: Sedimentary Geology, v. 235, no. 1-2, p. 38-49.

Loutit, T. S., Hardenbol, J., Vail, P. R., and Baum, G. R., 1988, Condensed Sections: the Key to Age Determination and Correlation of Continental Margin Sequences, *in* Wilgus, C. K., Hastings, B. S., Posamentier, H., Van Wagoner, J., Ross, C. A., and Kendall, C. G., eds., Sea-Level Changes - An Integrated Approach, Volume No. 42, SEPM Special Publication, p. 183-213.

Lowery, C. M., Corbett, M. J., Leckie, R. M., Watkins, D., Miceli Romero, A., and Pramudito, A., 2014, Foraminiferal and nannofossil paleoecology and paleoceanography of the Cenomanian–Turonian Eagle Ford Shale of southern Texas: Palaeogeography, Palaeoclimatology, Palaeoecology, v. 413, no. Supplement C, p. 49-65.

Lowery, C. M., Leckie, R. M., and Sageman, B. B., 2017a, Micropaleontological evidence for redox changes in the OAE3 interval of the US Western Interior: Global vs. local processes: Cretaceous Research, v. 69, p. 34-48.

Lowery, C. M., Cunningham, R., Barrie, C. D., Bralower, T., and Snedden, J. W., 2017b, The Northern Gulf of Mexico During OAE2 and the Relationship Between Water Depth and Black Shale Development: Paleoceanography, v. 32, no. 12, p. 1316-1335.

Lowery, C. M., Mark Leckie, R., Bryant, R., Elderbak, K., Parker, A., Polyak, D. E., Schmidt, M., Snoeyenbos-West, O., and Sterzinar, E., 2018, The Late Cretaceous Western Interior Seaway as a model for oxygenation change in epicontinental restricted basins: Earth-Science Reviews, v. 177, p. 545-564.

Ludvigson, G. A., Joeckel, R. M., González, L. A., Gulbranson, E. L., Rasbury, E. T., Hunt, G. J., Kirkland, J. I., and Madsen, S., 2010, Correlation of Aptian-Albian Carbon Isotope Excursions in Continental Strata of the Cretaceous Foreland Basin, Eastern Utah, U.S.A: Journal of Sedimentary Research, v. 80, no. 11, p. 955.

Ma, C., Meyers, S. R., Sageman, B. B., Singer, B. S., and Jicha, B. R., 2014, Testing the astronomical time scale for oceanic anoxic event 2, and its extension into Cenomanian strata of the Western Interior Basin (USA): Geological Society of America Bulletin, v. 126, no. 7-8, p. 974-989.

Maberly, S. C., Barker, P. A., Stott, A. W., and De Ville, M. M., 2013, Catchment productivity controls CO2 emissions from lakes: Nature Climate Change, v. 3, no. 4, p. 391-394.

Machlus, M. L., Ramezani, J., Bowring, S. A., Hemming, S. R., Tsukui, K., and Clyde, W. C., 2015, A strategy for cross-calibrating U–Pb chronology and astrochronology of sedimentary sequences: An example from the Green River Formation, Wyoming, USA: Earth and Planetary Science Letters, v. 413, p. 70-78.

Mack, G. H., Hook, S., Giles, K. A., and Cobban, W. A., 2016, Sequence stratigraphy of the Mancos Shale, lower Tres Hermanos Formation, and coeval middle Cenomanian to middle Turonian strata, southern New Mexico, USA: Sedimentology, v. 63, no. 4, p. 781-808.

MacLeod, K. G., Martin, E. E., and Blair, S. W., 2008, Nd isotopic excursion across Cretaceous ocean anoxic event 2 (Cenomanian-Turonian) in the tropical North Atlantic: Geology, v. 36, no. 10, p. 811-814.

MacLeod, K. G., Huber, B. T., Jimenez Berrocoso, A., and Wendler, I., 2013, A stable and hot Turonian without glacial delta O-18 excursions is indicated by exquisitely preserved Tanzanian foraminifera: Geology, v. 41, no. 10, p. 1083-1086.

Mancini, E. A., Obid, J., Badali, M., Liu, K., and Parcell, W. C., 2008, Sequence-stratigraphic analysis of Jurassic and Cretaceous strata and petroleum exploration in the central and eastern Gulf coastal plain, United States: AAPG Bulletin, v. 92, no. 12, p. 1655-1686.

Martin, E. E., MacLeod, K. G., Berrocoso, A. J., and Bourbon, E., 2012, Water mass circulation on Demerara Rise during the Late Cretaceous based on Nd isotopes: Earth and Planetary Science Letters, v. 327, p. 111-120.

McInerney, F. A., and Wing, S. L., 2011, The Paleocene-Eocene Thermal Maximum: A Perturbation of Carbon Cycle, Climate, and Biosphere with Implications for the Future: Annual Review of Earth and Planetary Sciences, v. 39, no. 1, p. 489-516.

Méhay, S., Keller, C. E., Bernasconi, S. M., Weissert, H., Erba, E., Bottini, C., and Hochuli, P. A., 2009, A volcanic CO2 pulse triggered the Cretaceous Oceanic Anoxic Event 1a and a biocalcification crisis: Geology, v. 37, no. 9, p. 819-822.

Merewether, E. A., and Cobban, W. A., 1986, Biostratigraphic units and tectonism in the mid-Cretaceous foreland, Colorado and adjacent areas, *in* Peterson, J. A., ed., Paleotectonics and sedimentation in the Rocky Mountain region, United States, Volume AAPG Memoir 41, p. 443-468.

Meyers, P. A., 1987, Appendix II. Organic carbon and calcium carbonate analyses, Deep Sea Drilling Project Leg 93, North American continental rise, *in* van Hinte, J. E., and Wise, S. W., eds., Initial Reports, DSDP, 93, Volume 93: Washington, D.C., U.S. Government Printing Office, p. 465-469.

Meyers, P. A., 1994, Preservation of Elemental and Isotopic Source Identification of Sedimentary Organic-Matter: Chemical Geology, v. 114, no. 3-4, p. 289-302.

Meyers, P. A., Bernasconi, S. M., and Forster, A., 2006, Origins and accumulation of organic matter in expanded Albian to Santonian black shale sequences on the Demerara Rise, South American margin: Organic Geochemistry, v. 37, no. 12, p. 1816-1830.

Meyers, P. A., Yum, J.-G., and Wise, S. W., 2009, Origins and maturity of organic matter in mid-Cretaceous black shales from ODP Site 1138 on the Kerguelen Plateau: Marine and Petroleum Geology, v. 26, no. 6, p. 909-915.

Meyers, S. R., 2007, Production and preservation of organic matter: The significance of iron: Paleoceanography, v. 22, no. 4.

Meyers, S. R., 2012, Seeing red in cyclic stratigraphy: Spectral noise estimation for astrochronology: Paleoceanography, v. 27, no. 3, p. n/a-n/a.

Meyers, S. R., 2014, Astrochron: An R Package for Astrochronology.

Meyers, S. R., and Sageman, B. B., 2004, Detection, quantification, and significance of hiatuses in pelagic and hemipelagic strata: Earth and Planetary Science Letters, v. 224, no. 1-2, p. 55-72.

Meyers, S. R., and Sageman, B. B., 2007, Quantification of deep-time orbital forcing by average spectral misfit: American Journal of Science, v. 307, no. 5, p. 773-792.

Meyers, S. R., and Hinnov, L. A., 2010, Northern Hemisphere glaciation and the evolution of Plio-Pleistocene climate noise: Paleoceanography, v. 25, no. 3.

Meyers, S. R., Sageman, B. B., and Hinnov, L. A., 2001, Integrated quantitative stratigraphy of the Cenomanian-Turonian bridge creek limestone member using evolutive harmonic analysis and stratigraphic modeling: Journal of Sedimentary Research, v. 71, no. 4, p. 628-644.

Meyers, S. R., Siewert, S. E., Singer, B. S., Sageman, B. B., Condon, D. J., Obradovich, J. D., Jicha, B. R., and Sawyer, D. A., 2012a, Intercalibration of radioisotopic and astrochronologic time scales for the Cenomanian-Turonian boundary interval, Western Interior Basin, USA: Geology, v. 40, no. 1, p. 7-10.

Meyers, S. R., Sageman, B. B., and Arthur, M. A., 2012b, Obliquity forcing of organic matter accumulation during Oceanic Anoxic Event 2: Paleoceanography, v. 27.

Miller, K. G., Sugarman, P. J., Browning, J. V., Kominz, M. A., Olsson, R. K., Feigenson, M. D., and Hernández, J. C., 2004, Upper Cretaceous sequences and sea-level history, New Jersey Coastal Plain: Geological Society of America Bulletin, v. 116, no. 3-4, p. 368-393.

Miller, K. G., Kominz, M. A., Browning, J. V., Wright, J. D., Mountain, G. S., Katz, M. E., Sugarman, P. J., Cramer, B. S., Christie-Blick, N., and Pekar, S. F., 2005, The Phanerozoic Record of Global Sea-Level Change: Science, v. 310, no. 5752, p. 1293.

Mitchell, R. N., Bice, D. M., Montanari, A., Cleaveland, L. C., Christianson, K. T., Coccioni, R., and Hinnov, L. A., 2008, Oceanic anoxic cycles? Orbital prelude to the Bonarelli Level (OAE 2): Earth and Planetary Science Letters, v. 267, no. 1-2, p. 1-16.

Mitchell, S. F., Ball, J. D., Crowley, S. F., Marshall, J. D., Paul, C. R. C., Veltkamp, C. J., and Samir, A., 1997, Isotope data from Cretaceous chalks and foraminifera: Environmental or diagenetic signals?: Geology, v. 25, no. 8, p. 691-694.

Moldowan, J. M., Fago, F. J., Lee, C. Y., Jacobson, S. R., Watt, D. S., Slougui, N.-E., Jeganathan, A., and Young, D. C., 1990, Sedimentary 24-n-Propylcholestanes, Molecular Fossils Diagnostic of Marine Algae: Science, v. 247, no. 4940, p. 309-312.

Molenaar, C. M., and Cobban, W. A., 1991, Middle Cretaceous stratigraphy on the south and east sides of the Uinta Basin, northeast Utah and northwestern Colorado, *in* Survey, U. S. G., ed., Volume Bulletin 1787, p. 1-34.

Mort, H. P., Adatte, T., Foellmi, K. B., Keller, G., Steinmann, P., Matera, V., Berner, Z., and Stueben, D., 2007, Phosphorus and the roles of productivity and nutrient recycling during oceanic anoxic event 2: Geology, v. 35, no. 6, p. 483-486.

Moucha, R., Forte, A. M., Mitrovica, J. X., Rowley, D. B., Quéré, S., Simmons, N. A., and Grand, S. P., 2008, Dynamic topography and long-term sea-level variations: There is no such thing as a stable continental platform: Earth and Planetary Science Letters, v. 271, no. 1–4, p. 101-108.

Naafs, B. D. A., Castro, J. M., De Gea, G. A., Quijano, M. L., Schmidt, D. N., and Pancost, R. D., 2016, Gradual and sustained carbon dioxide release during Aptian Oceanic Anoxic Event 1a: Nature Geoscience, v. 9, p. 135.

Nagm, E., El-Qot, G., and Wilmsen, M., 2014, Stable-isotope stratigraphy of the Cenomanian–Turonian (Upper Cretaceous) boundary event (CTBE) in Wadi Qena, Eastern Desert, Egypt: Journal of African Earth Sciences, v. 100, p. 524-531.

Nagm, E., 2015, Stratigraphic significance of rapid faunal change across the Cenomanian–Turonian boundary in the Eastern Desert, Egypt: Cretaceous Research, v. 52, p. 9-24.

Navarro-Ramirez, J. P., Bodin, S., and Immenhauser, A., 2016, Ongoing Cenomanian — Turonian heterozoan carbonate production in the neritic settings of Peru: Sedimentary Geology, v. 331, p. 78-93.

Navarro-Ramirez, J. P., Bodin, S., Consorti, L., and Immenhauser, A., 2017, Response of western South American epeiric-neritic ecosystem to middle Cretaceous Oceanic Anoxic Events: Cretaceous Research, v. 75, p. 61-80.

Nederbragt, A. J., and Fiorentino, A., 1999, Stratigraphy and palaeoceanography of the Cenomanian-Turonian Boundary Event in Oued Mellegue, north-western Tunisia: Cretaceous Research, v. 20, no. 1, p. 47-62.

Nederbragt, A. J., Thurow, J., and Pearce, M. A., 2007, Sediment composition and cyclicity in the mid-Cretaceous at Demerara Rise, ODP Leg 207, *in* Mosher, D. C., Erbacher, J., and Malone, M. J., eds., Proc. ODP, Sci. Results, 207: College Station, TX (Ocean Drilling Program), p. 1-31.

Nesbitt, H. W., and Young, G. M., 1982, Early Proterozoic Climates and Plate Motions Inferred from Major Element Chemistry of Lutites: Nature, v. 299, no. 5885, p. 715-717.

O'Dea, S. A., Gibbs, S. J., Bown, P. R., Young, J. R., Poulton, A. J., Newsam, C., and Wilson, P. A., 2014, Coccolithophore calcification response to past ocean acidification and climate change: Nature Communications, v. 5, p. 5363.

Obradovich, J. D., 1993, A Cretaceous Time Scale, *in* Caldwell, W. G. E., and Kauffman, E. G., eds., Evolution of the Western Interior Basin, Volume Special Paper 39, Geological Association of Canada, p. 379-396.

Ogg, J. G., Hinnov, L. A., and Huang, C., 2012, Cretaceous: Geologic Time Scale 2012, Vols 1 & 2, p. 793-853.

Orr, J. C., Fabry, V. J., Aumont, O., Bopp, L., Doney, S. C., Feely, R. A., Gnanadesikan, A., Gruber, N., Ishida, A., Joos, F., Key, R. M., Lindsay, K., Maier-Reimer, E., Matear, R., Monfray, P., Mouchet, A., Najjar, R. G., Plattner, G.-K., Rodgers, K. B., Sabine, C. L., Sarmiento, J. L., Schlitzer, R., Slater, R. D., Totterdell, I. J., Weirig, M.-F., Yamanaka, Y., and Yool, A., 2005, Anthropogenic ocean acidification over the twenty-first century and its impact on calcifying organisms: Nature, v. 437, p. 681.

Oster, J. L., and Kelley, N. P., 2016, Tracking regional and global teleconnections recorded by western North American speleothem records: Quaternary Science Reviews, v. 149, p. 18-33.

Ostrander, C. M., Owens, J. D., and Nielsen, S. G., 2017, Constraining the rate of oceanic deoxygenation leading up to a Cretaceous Oceanic Anoxic Event (OAE-2: ~94 Ma): Science Advances, v. 3, no. 8.

Owens, J. D., Gill, B. C., Jenkyns, H. C., Bates, S. M., Severmann, S., Kuypers, M. M. M., Woodfine, R. G., and Lyons, T. W., 2013, Sulfur isotopes track the global extent and dynamics of euxinia during Cretaceous Oceanic Anoxic Event 2: Proceedings of the National Academy of Sciences of the United States of America, v. 110, no. 46, p. 18407-18412.

Oxburgh, R., 2001, Residence time of osmium in the oceans: Geochemistry, Geophysics, Geosystems, v. 2, no. 6, p. n/a-n/a.

Pagani, M., and Arthur, M. A., 1998, Stable isotopic studies of Cenomanian-Turonian proximal marine fauna from the US Western Interior seaway, *in* Dean, W. E., and Arthur, M. A., eds., Stratigraphy and Paleoenvironments of the Cretaceous Western Interior Seaway USA, Volume 6, SEPM Concepts in Sedimentology and Paleontology, p. 201-225.

Pagani, M., Huber, M., and Sageman, B., 2014, Greenhouse Climates, *in* Turekian, K. K., ed., Treatise on Geochemistry (Second Edition): Oxford, Elsevier, p. 281-304.

Pälike, H., Lyle, M. W., Nishi, H., Raffi, I., Ridgwell, A., Gamage, K., Klaus, A., Acton, G., Anderson, L., Backman, J., Baldauf, J., Beltran, C., Bohaty, S. M., Bown, P., Busch, W., Channell, J. E. T., Chun, C. O. J., Delaney, M., Dewangan, P., Dunkley Jones, T., Edgar, K. M., Evans, H., Fitch, P., Foster, G. L., Gussone, N., Hasegawa, H., Hathorne, E. C., Hayashi, H., Herrle, J. O., Holbourn, A., Hovan, S., Hyeong, K., Iijima, K., Ito, T., Kamikuri, S.-i., Kimoto, K., Kuroda, J., Leon-Rodriguez, L., Malinverno, A., Moore Jr, T. C., Murphy, B. H., Murphy, D. P., Nakamura, H., Ogane, K., Ohneiser, C., Richter, C., Robinson, R., Rohling, E. J., Romero, O., Sawada, K., Scher, H., Schneider, L., Sluijs, A., Takata, H., Tian, J., Tsujimoto, A., Wade, B. S., Westerhold, T., Wilkens, R., Williams, T., Wilson, P. A., Yamamoto, Y., Yamamoto, S., Yamazaki, T., and Zeebe, R. E., 2012, A Cenozoic record of the equatorial Pacific carbonate compensation depth: Nature, v. 488, p. 609.

Parente, M., Frijia, G., Di Lucia, M., Jenkyns, H. C., Woodfine, R. G., and Baroncini, F., 2008, Stepwise extinction of larger foraminifers at the Cenomanian-Turonian boundary: A shallow-water perspective on nutrient fluctuations during Oceanic Anoxic Event 2 (Bonarelli Event): Geology, v. 36, no. 9, p. 715-718.

Park, J., and Herbert, T. D., 1987, Hunting for paleoclimatic periodicities in a geologic time-series with an uncertain time scale: Journal of Geophysical Research-Solid Earth and Planets, v. 92, no. B13, p. 14027-14040.

Payne, J. L., Turchyn, A. V., Paytan, A., DePaolo, D. J., Lehrmann, D. J., Yu, M., and Wei, J., 2010, Calcium isotope constraints on the end-Permian mass extinction: Proceedings of the National Academy of Sciences, v. 107, no. 19, p. 8543-8548.

Penman, D. E., Hönisch, B., Zeebe, R. E., Thomas, E., and Zachos, J. C., 2014, Rapid and sustained surface ocean acidification during the Paleocene-Eocene Thermal Maximum: Paleoceanography, v. 29, no. 5, p. 357-369.

Penman, D. E., Turner, S. K., Sexton, P. F., Norris, R. D., Dickson, A. J., Boulila, S., Ridgwell, A., Zeebe, R. E., Zachos, J. C., and Cameron, A., 2016, An abyssal carbonate compensation depth overshoot in the aftermath of the Palaeocene–Eocene Thermal Maximum: Nature Geoscience, v. 9, no. 8, p. 575.

Perch-Nielsen, K., 1985, Mesozoic calcareous nannofossils, *in* Bolli, H. M., Saunders, J. B., and Perch-Nielsen, K., eds., Plankton Stratigraphy, Volume 1, p. 329-426.

Perez-Infante, J., Farrimond, P., and Furrer, M., 1996, Global and local controls influencing the deposition of the La Luna Formation (Cenomanian-Campanian), western Venezuela: Chemical Geology, v. 130, no. 3, p. 271-288.

Peryt, D., and Wyrwicka, K., 1993, The Cenomanian/Turonian boundary event in Central Poland: Palaeogeography, Palaeoclimatology, Palaeoecology, v. 104, no. 1, p. 185-197.

Peters, S. E., 2008, Environmental determinants of extinction selectivity in the fossil record: Nature, v. 454, no. 7204, p. 626-629.

Petersen, K. D., Nielsen, S. B., Clausen, O. R., Stephenson, R., and Gerya, T., 2010, Small-Scale Mantle Convection Produces Stratigraphic Sequences in Sedimentary Basins: Science, v. 329, no. 5993, p. 827-830.

Petersen, S. V., Tabor, C. R., Lohmann, K. C., Poulsen, C. J., Meyer, K. W., Carpenter, S. J., Erickson, J. M., Matsunaga, K. K. S., Smith, S. Y., and Sheldon, N. D., 2016, Temperature and salinity of the Late Cretaceous Western Interior Seaway: Geology, v. 44, no. 11, p. 903-906.

Peterson, F., 1969, Cretaceous sedimentation and tectonism in the southeastern Kaiparowits region, Utah, 69-202.

Peucker-Ehrenbrink, B., and Ravizza, G., 2000, The marine osmium isotope record: Terra Nova, v. 12, no. 5, p. 205-219.

Philip, J. M., and Airaudcrumiere, C., 1991, The Demise of the Rudist-Bearing Carbonate Platforms at the Cenomanian Turonian Boundary – A Global Control: Coral Reefs, v. 10, no. 2, p. 115-125.

Pogge von Strandmann, P. A. E., Jenkyns, H. C., and Woodfine, R. G., 2013, Lithium isotope evidence for enhanced weathering during Oceanic Anoxic Event 2: Nature Geoscience, v. 6, p. 668.

Poirier, A., and Hillaire-Marcel, C., 2011, Improved Os-isotope stratigraphy of the Arctic Ocean: Geophysical Research Letters, v. 38, no. 14, L14607.

Pratt, L. M., 1981, A paleo-oceanographic interpretation of the sedimentary structures, clay minerals, and organic matter in a core of the Middle Cretaceous Greenhorn Formation near Pueblo, Colorado [PhD Dissertation]: Princeton University, 176 p.

Pratt, L. M., 1984, Influence of paleoenvironmental factors on preservation of organic matter in Middle Cretaceous Greenhorn Formation, Pueblo, Colorado: AAPG Bulletin, v. 68, no. 9, p. 1146-1159.

Pratt, L. M., 1985, Isotopic studies of organic matter and carbonate in rocks of the Greenhorn Marine Cycle, *in* Pratt, L. M., Kauffman, E. G., and Zelt, F. B., eds., Fine-grained deposits and biofacies of the Cretaceous Western Interior Seaway: Evidence of cyclic sedimentary processes; Midyear field trip guidebook 4: SEPM Society for Sedimentary Geology, p. 38-48.

Pratt, L., and Threlkeld, C., 1984, Stratigraphic significance of 13C/12C ratios in mid-Cretaceous rocks of the Western Interior, USA, *in* Stott, D. F., and Glass, D. J., eds., The Mesozoic of middle North America, Volume 9, Canadian Society of Petroleum Geologists Memoir, p. 305-312.

Pratt, L. M., Arthur, M. A., Dean, W. E., and Scholle, P. A., 1993, Paleoceanographic cycles and events during the Late Cretaceous in the Western Interior Seaway of North America, *in* Caldwell, W. G. E., and Kauffman, E. G., eds., Evolution of the Western Interior Basin, Volume Special Paper 39, Geological Association of Canada, p. 333-354.

Raup, D. M., and Sepkoski, J. J., 1986, Periodic Extinction of Families and Genera: Science, v. 231, no. 4740, p. 833-836.

Raven, M. R., Fike, D. A., Gomes, M. L., Webb, S. M., Bradley, A. S., McClelland, H. L. O., 2018, Organic carbon burial during OAE2 driven by changes in the locus of organic matter sulfurization: Nature Communications, v. 9, no. 1, p. 3409

Ravizza, G., and Peucker-Ehrenbrink, B., 2003, Chemostratigraphic Evidence of Deccan Volcanism from the Marine Osmium Isotope Record: Science, v. 302, no. 5649, p. 1392-1395.

Raymo, M. E., Mitrovica, J. X., O'Leary, M. J., DeConto, R. M., and Hearty, P. L., 2011, Departures from eustasy in Pliocene sea-level records: Nature Geoscience, v. 4, no. 5, p. 328-332.

Rehfeld, K., Marwan, N., Heitzig, J., and Kurths, J., 2011, Comparison of correlation analysis techniques for irregularly sampled time series: Nonlinear Processes in Geophysics, v. 18, no. 3, p. 389-404.

Richardt, N., and Wilmsen, M., 2012, Lower Upper Cretaceous standard section of the southern Münsterland (NW Germany): carbon stable-isotopes and sequence stratigraphy: Newsletters on Stratigraphy, v. 45, no. 1, p. 1-24.

Richardt, N., Wilmsen, M., and Niebuhr, B., 2013, Late Cenomanian–Early Turonian facies development and sea-level changes in the Bodenwöhrer Senke (Danubian Cretaceous Group, Bavaria, Germany): Facies, v. 59, no. 4, p. 803-827.

Ridgwell, A., and Schmidt, D. N., 2010, Past constraints on the vulnerability of marine calcifiers to massive carbon dioxide release: Nature Geoscience, v. 3, p. 196.

Ries, J. B., Cohen, A. L., and McCorkle, D. C., 2009, Marine calcifiers exhibit mixed responses to CO2-induced ocean acidification: Geology, v. 37, no. 12, p. 1131-1134.

Robaszynski, F., Gale, A. S., Juignet, P., Amedro, F., and Hardenbol, J., 1998, Sequence stratigraphy in the Upper Cretaceous Series of the Anglo-Paris Basin: exemplified by the Cenomanian Stage, *in* de Graciansky, P., Hardenbol, J., Jacquin, T., and Vail, P. R., eds., Mesozoic and Cenozoic Sequence Stratigraphy of European Basins, Volume 60, SEPM Special Publication, p. 363-386.

Roberts, L. N. R., and Kirschbaum, M. A., 1995, Paleogeography of the Late Cretaceous of the Western Interior of Middle North America–Coal distribution and sediment accumulation: U.S. Geological Survey Professional Paper 1561, 115 p.

Rooney, A. D., Selby, D., Lloyd, J. M., Roberts, D. H., Lückge, A., Sageman, B. B., and Prouty, N. G., 2016, Tracking millennial-scale Holocene glacial advance and retreat using osmium isotopes: Insights from the Greenland ice sheet: Quaternary Science Reviews, v. 138, p. 49-61.

Rovere, A., Raymo, M. E., Mitrovica, J. X., Hearty, P. J., O'Leary, M. J., and Inglis, J. D., 2014, The Mid-Pliocene sea-level conundrum: Glacial isostasy, eustasy and dynamic topography: Earth and Planetary Science Letters, v. 387, p. 27-33.

Rullkotter, J., Littke, R., Radke, M., Disko, U., Horsfield, B., and Thurow, J., 1992, Petrography and geochemistry of organic matter in Triassic and Cretaceous deep-sea sediments from the Wombat and Exmouth plateaus and nearby abyssal plains off northwest Australia, *in* Von Rad, U., and Haq, B. U., eds., Proceedings of the Ocean Drilling Program, Scientific Results, Volume 122: College Station, TX, Ocean Drilling Program, p. 317-333.

Sageman, B. B., 1985, High-resolution stratigraphy and paleobiology of the Hartland Shale Member: analysis of an oxygen-deficient epicontinental sea, *in* Pratt, L. M., Kauffman, E. G., and Zelt, F. B., eds., Fine-Grained Deposits and Biofacies of the Cretaceous Western Interior Seaway: Evidence of Cyclical Sedimentary Processes; Midyear field trip guidebook 4: SEPM Society for Sedimentary Geology, p. 110-121.

Sageman, B. B., 1989, The benthic boundary biofacies model: Hartland Shale member, greenhorn formation (Cenomanian), western interior, North America: Palaeogeography, Palaeoclimatology, Palaeoecology, v. 74, no. 1, p. 87-110.

Sageman, B. B., 1996, Lowstand tempestites: Depositional model for cretaceous skeletal limestones, Western Interior basin: Geology, v. 24, no. 10, p. 888-892.

Sageman, B. B., and Bina, C. R., 1997, Diversity and species abundance patterns in Late Cenomanian black shale biofacies, Western Interior, US: Palaios, v. 12, no. 5, p. 449-466.

Sageman, B. B., Rich, J., Arthur, M. A., Birchfield, G. E., and Dean, W. E., 1997a, Evidence for Milankovitch periodicities in Cenomanian-Turonian lithologic and geochemical cycles, western interior USA: Journal of Sedimentary Research, v. 67, no. 2, p. 286-302.

Sageman, B. B., Kauffman, E., Harries, P., and Elder, W., 1997b, Cenomanian/Turonian bioevents and ecostratigraphy in the Western Interior Basin: contrasting scales of local, regional, and global events, Paleontological events: stratigraphic, ecological, and evolutionary implications. Columbia University Press, New York, p. 520-570.

Sageman, B. B., Meyers, S. R., and Arthur, M. A., 2006, Orbital time scale and new C-isotope record for Cenomanian-Turonian boundary stratotype: Geology, v. 34, no. 2, p. 125-128.

Sageman, B. B., Singer, B. S., Meyers, S. R., Siewert, S. E., Walaszczyk, I., Condon, D. J., Jicha, B. R., Obradovich, J. D., and Sawyer, D. A., 2014a, Integrating Ar-40/Ar-39, U-Pb, and astronomical clocks in the Cretaceous Niobrara Formation, Western Interior Basin, USA: Geological Society of America Bulletin, v. 126, no. 7-8, p. 956-973.

Sageman, B. B., Lyons, T. W., and Joo, Y. J., 2014b, Geochemistry of Fine-Grained, Organic Carbon-Rich Facies A2 - Holland, Heinrich D, *in* Turekian, K. K., ed., Treatise on Geochemistry (Second Edition): Oxford, Elsevier, p. 141-179.

Sahagian, D., Pinous, O., Olferiev, A., and Zakharov, V., 1996, Eustatic curve for the Middle Jurassic-Cretaceous based on Russian platform and Siberian stratigraphy: Zonal resolution: AAPG Bulletin, v. 80, no. 9, p. 1433-1458.

Schlanger, S. O., and Jenkyns, H. C., 1976, Cretaceous Oceanic Anoxic Events: Causes and Consequences: Geologie en Mijnbouw, v. 55, no. 3-4, p. 6.

Schlanger, S. O., Arthur, M. A., Jenkyns, H. C., and Scholle, P. A., 1987, The Cenomanian-Turonian Oceanic Anoxic Event, I. Stratigraphy and distribution of organic carbon-rich beds and the marine $\delta^{13}C$ excursion: Geological Society of London, Special Publications, v. 26, no. 1, p. 371-399.

Schoene, B., Crowley, J. L., Condon, D. J., Schmitz, M. D., and Bowring, S. A., 2006, Reassessing the uranium decay constants for geochronology using ID-TIMS U–Pb data: Geochimica et Cosmochimica Acta, v. 70, no. 2, p. 426-445.

Schoene, B., Condon, D. J., Morgan, L., and McLean, N., 2013, Precision and Accuracy in Geochronology: Elements, v. 9, no. 1, p. 19-24.

Scholle, P. A., and Arthur, M. A., 1980, Carbon isotope fluctuations in Cretaceous pelagic limestones - potential stratigraphic and petroleum exploration tool: AAPG Bulletin, v. 64, no. 1, p. 67-87.

Schrag, D. P., Higgins, J. A., Macdonald, F. A., and Johnston, D. T., 2013, Authigenic Carbonate and the History of the Global Carbon Cycle: Science, v. 339, no. 6119, p. 540-543.

Scopelliti, G., Bellanca, A., Neri, R., Baudin, F., and Coccioni, R., 2006, Comparative high-resolution chemostratigraphy of the Bonarelli Level from the reference Bottaccione section (Umbria–Marche Apennines) and from an equivalent section in NW Sicily: Consistent and contrasting responses to the OAE2: Chemical Geology, v. 228, no. 4, p. 266-285.

Scott, C., and Lyons, T. W., 2012, Contrasting molybdenum cycling and isotopic properties in euxinic versus non-euxinic sediments and sedimentary rocks: Refining the paleoproxies: Chemical Geology, v. 324, p. 19-27.

Scroxton, N., Burns, S., Dawson, P., Rhodes, J. M., Brent, K., McGee, D., Heijnis, H., Gadd, P., Hantoro, W., and Gagan, M., 2018, Rapid measurement of strontium in speleothems using core-scanning micro X-ray fluorescence: Chemical Geology, v. 487, p. 12-22.

Selby, D., and Creaser, R. A., 2003, Re-Os geochronology of organic rich sediments: an evaluation of organic matter analysis methods: Chemical Geology, v. 200, no. 3-4, p. 225-240.

Shackleton, N. J., 1987, Oxygen isotopes, ice volume and sea level: Quaternary Science Reviews, v. 6, no. 3, p. 183-190.

Sharp, Z., 2017, Principles of Stable Isotope Geochemistry.

Shipboard Scientific Party, 2004, Proc. ODP, Init. Repts., 207, College Station, TX (Ocean Drilling Program).

Sinninghe-Damste, J. S., van Bentum, E. C., Reichart, G.-J., Pross, J., and Schouten, S., 2010, A CO2 decrease-driven cooling and increased latitudinal temperature gradient during the mid-Cretaceous Oceanic Anoxic Event 2: Earth and Planetary Science Letters, v. 293, no. 1-2, p. 97-103.

Sinton, C. W., and Duncan, R. A., 1997, Potential links between ocean plateau volcanism and global ocean anoxia at the Cenomanian-Turonian boundary: Economic Geology, v. 92, no. 7-8, p. 836-842.

Slingerland, R., Kump, L. R., Arthur, M. A., Fawcett, P. J., Sageman, B. B., and Barron, E. J., 1996, Estuarine circulation in the Turonian Western Interior seaway of North America: Geological Society of America Bulletin, v. 108, no. 8, p. 941-952.

Smith, A. B., Gale, A. S., and Neale, E. A. M., 2001, Sea-Level Change and Rock-Record Bias in the Cretaceous: A Problem for Extinction and Biodiversity Studies: Paleobiology, v. 27, no. 2, p. 241-253.

Smoliar, M. I., Walker, R. J., and Morgan, J. W., 1996, Re-Os ages of group IIA, IIIA, IVA, and IVB iron meteorites: Science, v. 271, no. 5252, p. 1099-1102.

Snow, L. J., Duncan, R. A., and Bralower, T. J., 2005, Trace element abundances in the Rock Canyon Anticline, Pueblo, Colorado, marine sedimentary section and their relationship to Caribbean plateau construction and oxygen anoxic event 2: Paleoceanography, v. 20, no. 3.

Spicer, R. A., and Herman, A. B., 2010, The Late Cretaceous environment of the Arctic: A quantitative reassessment based on plant fossils: Palaeogeography, Palaeoclimatology, Palaeoecology, v. 295, no. 3, p. 423-442.

Sprovieri, M., Sabatino, N., Pelosi, N., Batenburg, S. J., Coccioni, R., Iavarone, M., and Mazzola, S., 2013, Late Cretaceous orbitally-paced carbon isotope stratigraphy from the Bottaccione Gorge (Italy): Palaeogeography Palaeoclimatology Palaeoecology, v. 379, p. 81-94.

Stoll, H. M., and Schrag, D. P., 2000, High-resolution stable isotope records from the Upper Cretaceous rocks of Italy and Spain: Glacial episodes in a greenhouse planet?: Geological Society of America Bulletin, v. 112, no. 2, p. 308-319.

Sulpis, O., Boudreau, B. P., Mucci, A., Jenkins, C., Trossman, D. S., Arbic, B. K., and Key, R. M., 2018, Current $CaCO_3$ dissolution at the seafloor caused by anthropogenic CO_2: Proceedings of the National Academy of Sciences.

Sundaram, R., Henderson, R. A., Ayyasami, K., and Stilwell, J. D., 2001, A lithostratigraphic revision and palaeoenvironmental assessment of the Cretaceous System exposed in the onshore Cauvery Basin, southern India: Cretaceous Research, v. 22, no. 6, p. 743-762.

Swart, P. K., 2015, The geochemistry of carbonate diagenesis: The past, present and future: Sedimentology, v. 62, no. 5, p. 1233-1304.

Takashima, R., Nishi, H., Hayashi, K., Okada, H., Kawahata, H., Yamanaka, T., Fernando, A. G., and Mampuku, M., 2009, Litho-, bio- and chemostratigraphy across the Cenomanian/Turonian boundary (OAE 2) in the Vocontian Basin of southeastern France: Palaeogeography, Palaeoclimatology, Palaeoecology, v. 273, no. 1, p. 61-74.

Talbot, M. R., 1990, A review of the palaeohydrological interpretation of carbon and oxygen isotopic ratios in primary lacustrine carbonates: Chemical Geology: Isotope Geoscience section, v. 80, no. 4, p. 261-279.

Talbot, M. R., Jensen, N. B., Laerdal, T., and Filippi, M. L., 2006, Geochemical responses to a major transgression in giant African lakes: Journal of Paleolimnology, v. 35, p. 467-489.

Taylor, K. D., Gawthorpe, R. L., and Van Wagoner, J. C., 1995, Stratigraphic control on laterally persistent cementation, Book Cliffs, Utah: Journal of the Geological Society, v. 152, no. 2, p. 225-228.

Taylor, K. D., Gawthorpe, R. L., Curtis, C. D., Marshall, J. D., and Awwiller, D. N., 2000, Carbonate Cementation in a Sequence-Stratigraphic Framework: Upper Cretaceous Sandstones, Book Cliffs, Utah-Colorado: Journal of Sedimentary Research, v. 70, no. 2, p. 360-372.

Taylor, K. G., and Machent, P. G., 2010, Systematic sequence-scale controls on carbonate cementation in a siliciclastic sedimentary basin: Examples from Upper Cretaceous shallow marine deposits of Utah and Coloradao, USA: Marine and Petroleum Geology, v. 27, no. 7, p. 1297-1310.

Tejada, M. L. G., Suzuki, K., Kuroda, J., Coccioni, R., Mahoney, J. J., Ohkouchi, N., Sakamoto, T., and Tatsumi, Y., 2009, Ontong Java Plateau eruption as a trigger for the early Aptian oceanic anoxic event: Geology, v. 37, no. 9, p. 855-858.

Tessin, A., Hendy, I., Sheldon, N., and Sageman, B., 2015, Redox-controlled preservation of organic matter during “OAE 3” within the Western Interior Seaway: Paleoceanography, v. 30, no. 6, p. 702-717.

Them, T. R., Gill, B. C., Caruthers, A. H., Gröcke, D. R., Tulsky, E. T., Martindale, R. C., Poulton, T. P., and Smith, P. L., 2017, High-resolution carbon isotope records of the Toarcian Oceanic Anoxic Event (Early Jurassic) from North America and implications for the global drivers of the Toarcian carbon cycle: Earth and Planetary Science Letters, v. 459, p. 118-126.

Thomson, D. J., 1982, Spectrum estimation and harmonic-analysis: Proceedings of the Ieee, v. 70, no. 9, p. 1055-1096.

Thurow, J., Moullade, M., Brumsack, H. J., Masure, E., Taugourdeau-Lantz, J., and Dunham, K., 1988, The Cenomanian/Turonian Boundary Event (CTBE) at Hole 641A, ODP Leg 103 (Compared with the CTBE interval at Site 398), *in* Boillot, G., and Winterer, E. L., eds., Proceeding of the Ocean Drilling Program, Scientific Results, Volume 103: College Station, TX, Ocean Drilling Program, p. 587-634.

Thurow, J., Brumsack, H. J., Rullkotter, J., Littke, R., and Meyers, P. A., 1992, The Cenomanian-Turonian Boundary event in the Indian Ocean - a key to understand the global picture, *in* Duncan, R. A., Rea, D. K., Kidd, R. B., von Rad, U., and Weissel, J. K., eds., Synthesis of

Results from Scientific Drilling in the Indian Ocean, Volume 70: Washington, D.C., American Geophysical Union, p. 253-274.

Tibert, N. E., Leckie, R. M., Eaton, J. G., Kirkland, J. I., Colin, J.-P., Leithold, E. L., and Mccormic, M. E., 2003, Recognition of relative sea-level change in Upper Cretaceous coal-bearing strata: a paleoecological approach using agglutinated Foraminifera and ostracodes to detect key stratigraphic surfaces, *in* C, O. H., and Leckie, R. M., eds., Micropaleontologic proxies for sea-level change and stratigraphic discontinuities, Volume 75, Society for Sedimentary Geology, p. 263-299.

Tibert, N. E., and Leckie, R. M., 2013, Cenomanian-Turonian (Upper Cretaceous) foraminifera from the westernmost Colorado Plateau, southwest Utah, USA: Micropaleontology, v. 59, no. 6, p. 555-578.

Titus, A. L., Powell, J. D., Roberts, E. M., Sampson, S. D., Pollock, S. L., Kirkland, J. I., and Albright, B. L., 2005, Late Cretaceous stratigraphy, depositional environments, and macrovertebrate paleontology of the Kaiparowits Plateau, Grand Staircase–Escalante National Monument, Utah, *in* Pederson, J., and Dehler, C. M., eds., Interior Western United States, Volume 6, Geological Society of America Field Guide, p. 101-128.

Trabucho-Alexandre, J., Tuenter, E., Henstra, G. A., van der Zwan, K. J., van de Wal, R. S. W., Dijkstra, H. A., and de Boer, P. L., 2010, The mid-Cretaceous North Atlantic nutrient trap: Black shales and OAEs: Paleoceanography, v. 25.

Tribovillard, N., Algeo, T. J., Lyons, T., and Riboulleau, A., 2006, Trace metals as paleoredox and paleoproductivity proxies: An update: Chemical Geology, v. 232, no. 1-2, p. 12-32.

Tsikos, H., Jenkyns, H. C., Walsworth-Bell, B., Petrizzo, M. R., Forster, A., Kolonic, S., Erba, E., Silva, I. P., Baas, M., Wagner, T., and Damste, J. S. S., 2004, Carbon-isotope stratigraphy recorded by the Cenomanian-Turonian Oceanic Anoxic Event: correlation and implications based on three key localities: Journal of the Geological Society, v. 161, p. 711-719.

Tucholke, B. E., and Vogt, P. R., 1979, Western North Atlantic: sedimentary evolution and aspects of tectonic history, *in* Tucholke, B. E., and Vogt, P. R., eds., Initial Reports of the Deep Sea Drilling Project, Volume 43: Washington, D.C., U.S. Government Printing Office, p. 791-825.

Turgeon, S., and Brumsack, H.-J., 2006, Anoxic vs dysoxic events reflected in sediment geochemistry during the Cenomanian–Turonian Boundary Event (Cretaceous) in the Umbria–Marche Basin of central Italy: Chemical Geology, v. 234, no. 3, p. 321-339.

Turgeon, S. C., and Creaser, R. A., 2008, Cretaceous oceanic anoxic event 2 triggered by a massive magmatic episode: Nature, v. 454, no. 7202, p. 323-U329.

Tyrrell, T., and Zeebe, R. E., 2004, History of carbonate ion concentration over the last 100 million years: Geochimica et Cosmochimica Acta, v. 68, no. 17, p. 3521-3530.

Uchman, A., Bąk, K., and Rodríguez-Tovar, F. J., 2008, Ichnological record of deep-sea palaeoenvironmental changes around the Oceanic Anoxic Event 2 (Cenomanian–Turonian boundary): An example from the Barnasiówka section, Polish Outer Carpathians: Palaeogeography, Palaeoclimatology, Palaeoecology, v. 262, no. 1, p. 61-71.

Uličný, D., 1999, Sequence stratigraphy of the Dakota Formation (Cenomanian), southern Utah: interplay of eustasy and tectonics in a foreland basin: Sedimentology, v. 46, no. 5, p. 807-836.

Ulicny, D., Hladikova, J., Attrep, M. J., Cech, S., Hradecka, L., and Svobodova, M., 1997, Sea-level changes and geochemical anomalies across the Cenomanian-Turonian boundary: Pecinov quarry, Bohemia: Palaeogeography Palaeoclimatology Palaeoecology, v. 132, no. 1-4, p. 265-285.

Ulicny, D., Jarvis, I., Groecke, D. R., Cech, S., Laurin, J., Olde, K., Trabucho-Alexandre, J., Svabenicka, L., and Pedentchouk, N., 2014, A high-resolution carbon-isotope record of the Turonian stage correlated to a siliciclastic basin fill: Implications for mid-Cretaceous sea-level change: Palaeogeography Palaeoclimatology Palaeoecology, v. 405, p. 42-58.

Vakarelov, B. K., Bhattacharya, J. P., and Nebrigic, D. D., 2006, Importance of high-frequency tectonic sequences during greenhouse times of Earth history: Geology, v. 34, no. 9, p. 797-800.

van Helmond, N. A. G. M., Ruvalcaba Baroni, I., Sluijs, A., Sinninghe Damsté, J. S., and Slomp, C. P., 2014, Spatial extent and degree of oxygen depletion in the deep proto-North Atlantic basin during Oceanic Anoxic Event 2: Geochemistry, Geophysics, Geosystems, v. 15, no. 11, p. 4254-4266.

Van Wagoner, J., Posamentier, H., Mitchum, R., Vail, P., Sarg, J., Loutit, T., and Hardenbol, J., 1988, An overview of the fundamentals of sequence stratigraphy and key definitions, Sea-Level Changes - An Integrated Approach, Volume SEPM Special Publication No. 42, The Society of Economic Paleontologists and Mineralogists.

Vogt, P. R., 1989, Volcanogenic upwelling of anoxic, nutrient-rich water: A possible factor in carbonate-bank/reef demise and benthic faunal extinctions?: GSA Bulletin, v. 101, no. 10, p. 1225-1245.

Voigt, S., and Hilbrecht, H., 1997, Late Cretaceous carbon isotope stratigraphy in Europe: Correlation and relations with sea level and sediment stability: Palaeogeography Palaeoclimatology Palaeoecology, v. 134, no. 1-4, p. 39-59.

Voigt, S., and Wiese, F., 2000, Evidence for Late Cretaceous (Late Turonian) climate cooling from oxygen-isotope variations and palaeobiogeographic changes in Western and Central Europe: Journal of the Geological Society, v. 157, p. 737-743.

Voigt, S., Gale, A. S., and Voigt, T., 2006, Sea-level change, carbon cycling and palaeoclimate during the Late Cenomanian of northwest Europe; an integrated palaeoenvironmental analysis: Cretaceous Research, v. 27, no. 6, p. 836-858.

Wagreich, M., 2012, "OAE 3" - regional Atlantic organic carbon burial during the Coniacian-Santonian: Climate of the Past, v. 8, no. 5, p. 1447-1455.

Wagreich, M., Bojar, A.-V., Sachsenhofer, R. F., Neuhuber, S., and Egger, H., 2008, Calcareous nannoplankton, planktonic foraminiferal, and carbonate carbon isotope stratigraphy of the Cenomanian–Turonian boundary section in the Ultrahelvetic Zone (Eastern Alps, Upper Austria): Cretaceous Research, v. 29, no. 5, p. 965-975.

Walaszczyk, I., Wood, C. J., Lees, J. A., Peryt, D., Voigt, S., and Wiese, F., 2010, The Salzgitter-Salder Quarry (Lower Saxony, Germany) and Slupia Nadbrzezna river cliff section (central Poland): a proposed candidate composite Global Boundary Stratotype Section and Point for the Coniacian Stage (Upper Cretaceous): Acta Geologica Polonica, v. 60, no. 4, p. 445-477.

Walaszczyk, I., Kopaevich, L. F., and Beniamovski, V. N., 2013, Inoceramid and foraminiferal record and biozonation of the Turonianand Coniacian (Upper Cretaceous) of the Mangyshlak Mts., western Kazakhstan: Acta Geologica Polonica, v. 63, no. 4, p. 469-+.

Walaszczyk, I., Shank, J. A., Plint, A. G., and Cobban, W. A., 2014, Interregional correlation of disconformities in Upper Cretaceous strata, Western Interior Seaway: Biostratigraphic and sequence-stratigraphic evidence for eustatic change: Geological Society of America Bulletin, v. 126, no. 3-4, p. 307-316.

Wan, X., Zhao, J., Scott, R. W., Wang, P., Feng, Z., Huang, Q., and Xi, D., 2013, Late Cretaceous stratigraphy, Songliao Basin, NE China: SK1 cores: Palaeogeography Palaeoclimatology Palaeoecology, v. 385, p. 31-43.

Wang, P., Gao, Y., Cheng, R., Wang, G., Wu, H., Wan, X., Yang, G., and Wang, Z., 2009, Description of Cretaceous Sedimentary Sequence of the Second and Third Member of the Qingshankou Formation Recovered by CCSD-SK-Is Borehole in Songliao Basin: Lithostratigraphy, Sedimentary Facies and Cyclic Stratigraphy: Earth Science Frontiers, v. 16, no. 2, p. 288-313.

Wang, C. S., Feng, Z. G., Zhang, L. M., Huang, Y. J., Cao, K., Wang, P. J., and Zhao, B., 2013, Cretaceous paleogeography and paleoclimate and the setting of SKI borehole sites in Songliao Basin, northeast China: Palaeogeography Palaeoclimatology Palaeoecology, v. 385, p. 17-30.

Wang, P. J., Mattern, F., Didenko, N. A., Zhu, D. F., Singer, B., and Sun, X. M., 2016a, Tectonics and cycle system of the Cretaceous Songliao Basin: An inverted active continental margin basin: Earth-Science Reviews, v. 159, p. 82-102.

Wang, T., Ramezani, J., Wang, C., Wu, H., He, H., and Bowring, S. A., 2016b, High-precision U–Pb geochronologic constraints on the Late Cretaceous terrestrial cyclostratigraphy and geomagnetic polarity from the Songliao Basin, Northeast China: Earth and Planetary Science Letters, v. 446, p. 37-44.

Waples, D. W., and Cunningham, R., 1985, Leg 80 Shipboard Organic Geochemistry, *in* de Graciansky, P. C., and Poag, C. W., eds., Initial Reports Deep Sea Drilling Program, Volume 80: Washington, D.C., U.S. Government Printing Office, p. 949-968.

Watkins, D. K., 1985, Biostratigraphy and Paleoecology of Calcareous Nannofossils in the Greenhorn Marine Cycle, *in* Pratt, L. M., Kauffman, E. G., and Zelt, F. B., eds., Fine-Grained Deposits and Biofacies of the Cretaceous Western Interior Seaway: Evidence of Cyclic Sedimentary Processes; Midyear field trip guidebook 4: SEPM Society for Sedimentary Geology, p. 151-156.

Wedepohl, K. H., 1971, Environmental influences on the chemical composition of shales and clays: Physics and Chemistry of the Earth, v. 8, p. 307-333.

Wendler, I., 2013, A critical evaluation of carbon isotope stratigraphy and biostratigraphic implications for Late Cretaceous global correlation: Earth-Science Reviews, v. 126, p. 116-146.

Wendler, J. E., Lehmann, J., and Kuss, J., 2010, Orbital time scale, intra-platform basin correlation, carbon isotope stratigraphy and sea-level history of the Cenomanian–Turonian Eastern Levant platform, Jordan, *in* Homberg, C., and Bachmann, M., eds., Evolution of the Levant Margin and Western Arabia Platform since the Mesozoic, Geological Society of London.

Wendler, J. E., Meyers, S. R., Wendler, I., and Kuss, J., 2014, A million-year-scale astronomical control on Late Cretaceous sea-level: Newsletters on Stratigraphy, v. 47, no. 1, p. 1-19.

Wendler, J. E., Wendler, I., Vogt, C., and Kuss, J., 2016, Link between cyclic eustatic sea-level change and continental weathering: Evidence for aquifer-eustasy in the Cretaceous: Palaeogeography Palaeoclimatology Palaeoecology, v. 441, p. 430-437.

West, O. L., Leckie, R. M., and Schmidt, M., 1998, Foraminiferal Paleoecology and Paleoceanography of the Greenhorn Cycle Along the Southwestern Margin of the Western Interior Sea, Stratigraphy and Paleoenvironments of the Cretaceous Western Interior Seaway, USA, Volume 6, SEPM Concepts in Sedimentology and Paleontology, p. 79-99.

White, T., Furlong, K., and Arthur, M., 2002, Forebulge migration in the Cretaceous Western Interior basin of the central United States: Basin Research, v. 14, no. 1, p. 43-54.

White, T., and Arthur, M. A., 2006, Organic carbon production and preservation in response to sea-level changes in the Turonian Carlile Formation, U.S. Western Interior Basin: Palaeogeography, Palaeoclimatology, Palaeoecology, v. 235, no. 1, p. 223-244.

Wiese, F., 1999, Stable isotope data (delta C-13, delta O-18) from the Middle and Upper Turonian (Upper Cretaceous) of Liencres (Cantabria, northern Spain) with a comparison to northern Germany (Sohlde & Salzgitter-Salder): Newsletters on Stratigraphy, v. 37, no. 1-2, p. 37-62.

Wignall, P. B., 2001, Large igneous provinces and mass extinctions: Earth-Science Reviews, v. 53, no. 1, p. 1-33.

Wright, S. C., 2015, Applications of the Rhenium-osmium Isotopic System, and Platinum and Iridium Abundances in Organic-rich Mud Rocks: A Geochronology, Geochemistry, and Redox Study [Doctoral Dissertation]: University of Houston, 302 p.

Wu, H., Zhang, S., Jiang, G., Hinnov, L., Yang, T., Li, H., Wan, X., and Wang, C., 2013, Astrochronology of the Early Turonian-Early Campanian terrestrial succession in the Songliao Basin, northeastern China and its implication for long-period behavior of the Solar System: Palaeogeography Palaeoclimatology Palaeoecology, v. 385, p. 55-70.

Wunsche, L., Gulacar, F. O., and Buchs, A., 1987, Several Unexpected Marine Sterols in a Fresh-Water Sediment: Organic Geochemistry, v. 11, no. 3, p. 215-219.

Xi, D. P., Cao, W. X., Huang, Q. H., Do Carmo, D. A., Li, S., Jing, X., Tu, Y. J., Jia, J. Z., Qu, H. Y., Zhao, J., and Wan, X. Q., 2016, Late Cretaceous marine fossils and seawater incursion events in the Songliao Basin, NE China: Cretaceous Research, v. 62, p. 172-182.

Xu, W., Ruhl, M., Jenkyns, H. C., Hesselbo, S. P., Riding, J. B., Selby, D., Naafs, B. D. A., Weijers, J. W. H., Pancost, R. D., Tegelaar, E. W., and Idiz, E. F., 2017, Carbon sequestration in an expanded lake system during the Toarcian oceanic anoxic event: Nature Geosci, v. advance online publication.

Yang, Y. T., 2013, An unrecognized major collision of the Okhotomorsk Block with East Asia during the Late Cretaceous, constraints on the plate reorganization of the Northwest Pacific: Earth-Science Reviews, v. 126, p. 96-115.

Young, R. G., 1965, Type section of Naturita Formation: AAPG Bulletin, v. 49, no. 9, p. 1512-1516.

Zachos, J. C., Röhl, U., Schellenberg, S. A., Sluijs, A., Hodell, D. A., Kelly, D. C., Thomas, E., Nicolo, M., Raffi, I., Lourens, L. J., McCarren, H., and Kroon, D., 2005, Rapid Acidification of the Ocean During the Paleocene-Eocene Thermal Maximum: Science, v. 308, no. 5728, p. 1611-1615.

Zeebe, R. E., 2012, History of Seawater Carbonate Chemistry, Atmospheric CO2, and Ocean Acidification: Annual Review of Earth and Planetary Sciences, v. 40, no. 1, p. 141-165.

Zelterman, D., 2015, Applied multivariate statistics with R, Switzerland, Springer-Verlag.

Zhao, J., Wan, X. Q., Xi, D. P., Jing, X., Li, W., Huang, Q. H., and Zhang, J. Y., 2014, Late Cretaceous palynology and paleoclimate change: Evidence from the SK1 (South) core, Songliao Basin, NE China: Science China-Earth Sciences, v. 57, no. 12, p. 2985-2997.

Zhu, Y., Bhattacharya, J. P., Li, W., Lapen, T. J., Jicha, B. R., and Singer, B. S., 2012, Milankovitch-scale sequence stratigraphy and stepped forced regressions of the Turonian Ferron Notom Deltaic Complex, south-central Utah, USA: Journal of Sedimentary Research, v. 82, no. 9-10, p. 723-746.

Appendices

Appendix 1: Supplemental Material for Chapter 2 and Jones et al. (2018a)

Turonian Sea Level and Paleoclimatic Events in Astronomically Tuned Records from the Tropical North Atlantic and Western Interior Seaway

Contents

This file contains supporting information for Jones et al. (2018a) including details on depth scale corrections, age uncertainty calculations, spectral analysis techniques and results, geochemical datasets, and carbon isotope chemostratigraphic correlations.

Text A1.1.

MCD to MBSF-log depth scale correction

The Initial Report of ODP Leg 207 reported a 12.1m discrepancy between logging and coring depth scales (Shipboard Sci. Party, 2004) which was corrected before development of the Site 1261 astronomical time scale (Meyers et al., 2012b). Astronomical tuning of strata at Site 1261 was performed via spectral analysis of geophysical well logs (Formation MicroScanner - FMS) while samples for bulk carbon isotope analyses were collected from core stored in the ODP Bremen Repository. Geophysical logging depths were reported using the meters below sea floor logging depth scale (MBSF-log), and geochemical sample depths were recorded in meters composite depth (MCD) (Shipboard Sci. Party, 2004). However, offsets between FMS log depths (MBSF-log) and core depths (MCD) were noted when comparing depths of traceable limestone beds. Since the goal of the study was to link high resolution $\delta^{13}C_{org}$ records with astronomical tuning, it was necessary to correct for discrepancies between the two depth scales. Tie points between the depth scales were determined using three marker beds noted in archived lithologic logs, core photos, and FMS logs (Table A1.1). A bentonite rich horizon (MCD depth = 633.67–634.36m) was detected as a conspicuous spike in FMS logs (Meyers et al., 2012b) while low conductivity cemented limestone beds from Site 1261 Hole A Core 46R and Hole B Core 13R were assigned as shallow and deep marker bed tie points respectively.

Offsets between MCD and MBSF-log were assessed at the three tie points and offsets for sample horizons were interpolated from the nearest two tie points. Since some samples were studied from horizons above the highest tie point and below the lowest tie point, these samples were assumed to have an offset equal to the nearest tie point. The following equations were used to calculate sample depth in MBSF-log to align sample depths (MCD_{sample}) with log depths for the highest accuracy in astronomical tuning of $\delta^{13}C$ records.

Table A1.1. (next page) Depth offset relationships between meters composite depth (MCD) and corrected meters below sea floor-logging (MBSF-log) depth scales at Site 1261. All MCD depth values for samples were transformed to MBSF-log values for consistent comparison with the astronomical time scale derived from FMS logs of the well. These formulas were used to transform previously published bio- and chemostratigraphic data and new $\delta^{13}C_{org}$, %TOC, %Carb, and C/N data from MCD to MBSF-log depth scales (see Text A1.1 and Table A1.3 and A1.7). A similar correction was not necessary for Site 1259 records since astrochronologic analyses were conducted on geochemical data (%Carb) recorded on the meters composite depth scale.

MCD depth/range	**MBSF-log**	**Offset: [MBSF-log = $\text{MCD}_{\text{sample}}$ + Offset]**
< 611.26 m	613.98 m	= 2.72 m
611.26 – 633.67 m		= 2.72 m – [(1.08 m – 2.72 m) / (633.67 m – 611.26 m)] x (MCD – 611.26 m)
633.67-634.36 m	634.75 – 635.44 m	= 1.08 m
634.36 – 638.70 m		= 1.08 m – [(1.35 m – 1.08 m) / (638.70 m – 634.36 m)] x (MCD – 634.36 m)
638.70 m	640.05 m	= 1.35 m
> 638.70 m		= 1.35 m

Text A1.2.

Age uncertainty for stratigraphic horizons at Sites 1261 and 1259 was calculated from a variety of sources for both "floating" and "anchored" time scales. Multiple sources of uncertainty were combined in quadrature. For the spliced floating astronomical time scale, sources of uncertainty include: cross-site stratigraphic correlation[1a], uncertainty in calculating the ATS at Site 1259[1b] and Site 1261[1c], and the conversion of sample depths ($\delta^{13}C$) from MCD to MBSF-log depth scales[1d] (Text A1.1). After testing various kernel smoothing bandwidths, uncertainty in the $\delta^{13}C$ cross-site stratigraphic correlation for splicing Site 1259 and Site 1261 was estimated to be ±30 kyr. Uncertainty in development of floating astronomical time scales arises from variation in user specified parameters of spectral analysis such as EHA window size, zero-padding, window step size, etc. Sageman et al. (2014a) estimated ATS uncertainty at ¼ the duration of the traced or bandpassed astronomical frequency. Since the Site 1261 and Site 1259 ATS are constructed from tracing of the short and long eccentricity cycle respectively, uncertainty estimates for these components of the time scale are ±25 kyr and ±100 kyr respectively. The conversion from MCD to MBSF-log depth scales (see Text A1.1) imparted a temporal uncertainty (±30 kyr) at Site 1261 which was calculated by dividing the estimated converted depth uncertainty (50 cm) by sedimentation rate (1.75 cm/kyr).

Additional temporal uncertainty was accounted for in placing the Turonian-Coniacian (TCB) and Cenomanian-Turonian (CTB) stage boundaries at Site 1259 and 1261. Stratigraphic uncertainty in assigning the TCB at Site 1259 (based on the identification of the Navigation CIE) was ±85 kyr due to sampling resolution[2a]. Near the CTB at Site 1261, sampling resolution in identifying the onset of the OAE2 CIE (the stratigraphic marker for anchoring the ATS) was much higher and temporal uncertainty was estimated at ±5 kyr[2b].

We anchor the spliced ATS at Demerara Rise to a numerical age for the base of the OAE2 CIE, a globally detected chemostratigraphic marker and robust tie point below the Cenomanian-Turonian Boundary. The numerical age for the base of OAE2 is derived from the central Western Interior Basin, where radioisotopically-dated bentonites (Ar/Ar and U/Pb geochronology), $\delta^{13}C$ chemostratigraphy, ammonite biostratigraphy, and astrochronology have been integrated to calculate an age of 93.90±0.15 Ma for the CTB at the global stratotype section and point (GSSP) near Pueblo, Colorado (Kennedy et al., 2005; Sageman et al., 2006; Meyers et al., 2012a). However, a hiatus on the order of 10s of kiloyear is present at the base of Bed 63 in Pueblo (Eicher and Diner, 1989; Ma et al., 2014; Du Vivier et al., 2014). Therefore, we splice the record from the GSSP to the more complete record in the Angus core in the Denver Basin (Ma et al., 2014) to calculate the age of the base of the OAE2 CIE. There, Bed 63 from the GSSP is expanded and represented by multiple precessional couplets which permit high-resolution chronometry at the onset of OAE2. Using the astronomical time scale, $\delta^{13}C$ chemostratigraphy, and lithostratigraphy from the Angus core, we calculate the duration between the onset of the OAE2 CIE and the CTB (525-565 kyr), considering sources of temporal uncertainty in the floating astrochronology[3b] and radioisotopic age[3a] for the CTB (Meyers et al., 2012a) (Table A1.2). As a result, we determine the age of the onset of OAE2 to be 94.45±0.16 Ma. This age estimate is within uncertainty of two recent high resolution astrochronology studies of the onset of OAE2 (Eldrett et al., 2015a; Kuhnt et al., 2017).

Eldrett et al. (2017) expand the definition of OAE2 in the Eagle Ford of Texas to include lower amplitude excursions in $\delta^{13}C_{org}$ chemostratigraphy there that they identify as pre cursor events (PCEs). Using U/Pb geochronology and astrochronology, they place the onset of OAE2, including the PCEs, at 95.01±0.12 Ma. The PCE enrichments in $\delta^{13}C_{org}$ in the Iona-1 core of Texas could be a local phenomenon (local productivity, changing organic material, etc.) since they have not been documented elsewhere globally yet. Alternatively, the occurrence of these PCEs may represent a uniquely expanded record of the onset of OAE2 and noteworthy perturbations to the global carbon cycle that precede the main high-amplitude CIE that traditionally defines OAE2. This underscores the importance of additional high-resolution chemostratigraphic investigations of expanded OAE2 records in the future. However, the absence of PCEs at Demerara Rise suggests that the onset age of OAE2 more closely aligns with estimates for the main body of the CIE derived from existing datasets discussed above. Moreover, chemostratigraphy of the initial osmium isotope proxy, which preserves a sharp unradiogenic excursion 10s of kyr prior to the base of the OAE2 CIE (Turgeon and Creaser, 2008), occurs at similar horizons in the central WIB (Angus, Portland, SH#1 cores) and Demerara Rise (Du Vivier et al., 2014; Chapter 5).

	Sources of temporal uncertainty								
	Combined uncertainty (kyr)	**Cross-well splicing[1a]** (±30kyr)	**ATS 1259[1b]** (±100kyr)	**ATS 1261[1c]** (±25kyr)	**MCD-MBSF calc.[1d]** (±30kyr)	**TCB δ^{13}C stratigraphy[2a]** (±85kyr)	**OAE2 δ^{13}C onset[2b]** (±5kyr)	**CTB age uncert. GSSP[3a]** (±150kyr)	**OAE2 δ13C onset WIB[3b]** (±40kyr)
Site 1261 floating time uncertainty	±39			X	X				
Site 1261 anchored age uncertainty	±160			X	X		X	X	X
Site 1259 floating time uncertainty	±100		X						
Spliced **Site 1259 and Site 1261** floating time uncertainty	±111	X	X	X	X				
Site 1259 Anchored age uncertainty	±191	X	X	X	X		X	X	X
Turonian-Coniacian Boundary Age estimate (from anchored and spliced ATS)	±209	X	X	X	X	X	X	X	X
Turonian Stage duration floating time	±146	X	X	X	X	X	X		X

Table A1.2. Summary of uncertainty in floating, spliced, and anchored astronomical time scales from Demerara Rise. Column headers correspond to footnotes in text detailing sources of uncertainty.

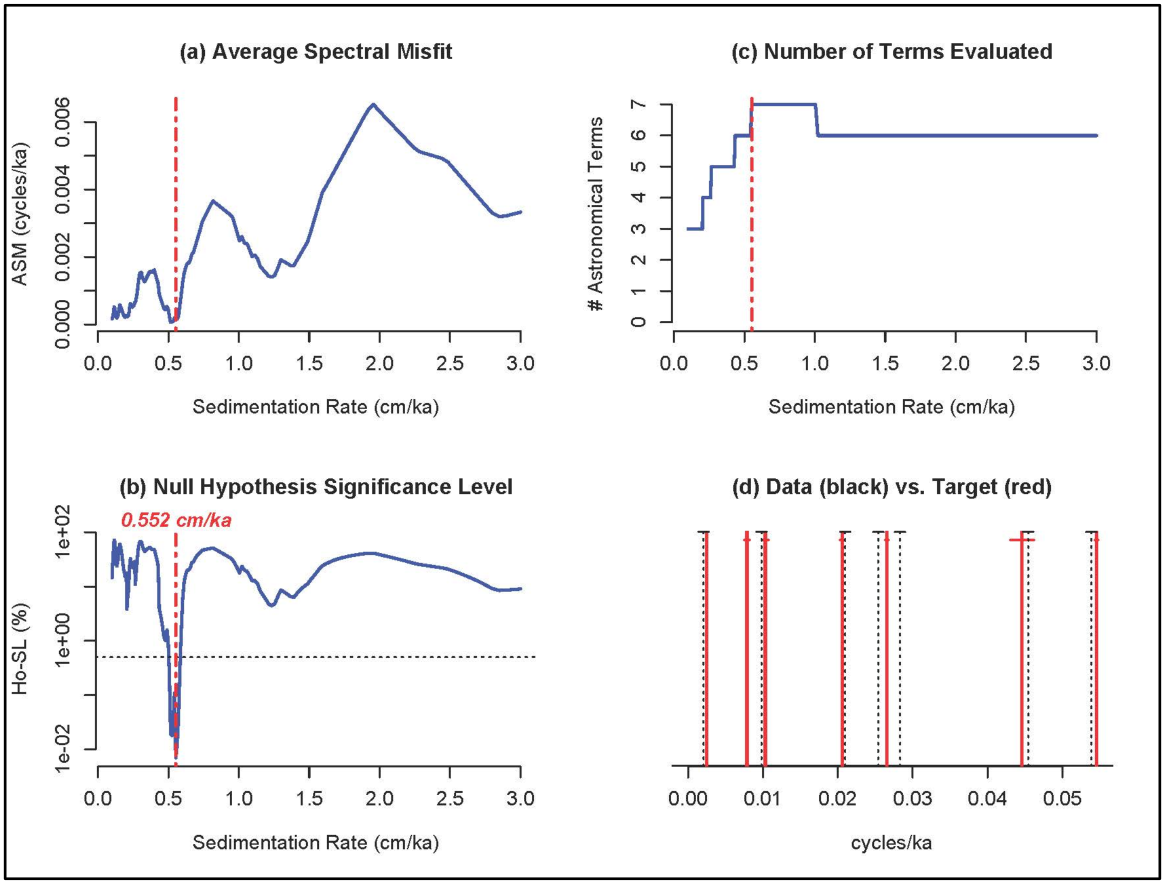

Figure A1.1. Example of average spectral misfit (ASM) (Meyers and Sageman, 2007) null hypothesis significance level results for Site 1259 (from Junium et al., 2018). These results are for the 4-meter %Carb (Friedrich et al., 2008) evolutive harmonic analysis (EHA) (Meyers et al., 2001) window centered on 526.5 mcd, identifying an optimal sedimentation rate of 0.552 cm/kyr (null significance level=0.008%; ASM=0.0001595397 cycles/kyr). **(a)** average spectral misfit in cycles/kyr, **(b)** Null hypothesis significance level (dotted line at 0.5% is the critical significance level), **(c)** the number of astronomical terms available for evaluation at each sedimentation rate, **(d)** the observed frequencies (black dotted lines) versus predicted astronomical target frequencies (red lines) given the optimal calibration of 0.552 cm/kyr. Horizontal lines at the top of panel "**d**" indicate uncertainties employed in the ASM analysis (Meyers et al., 2012b).

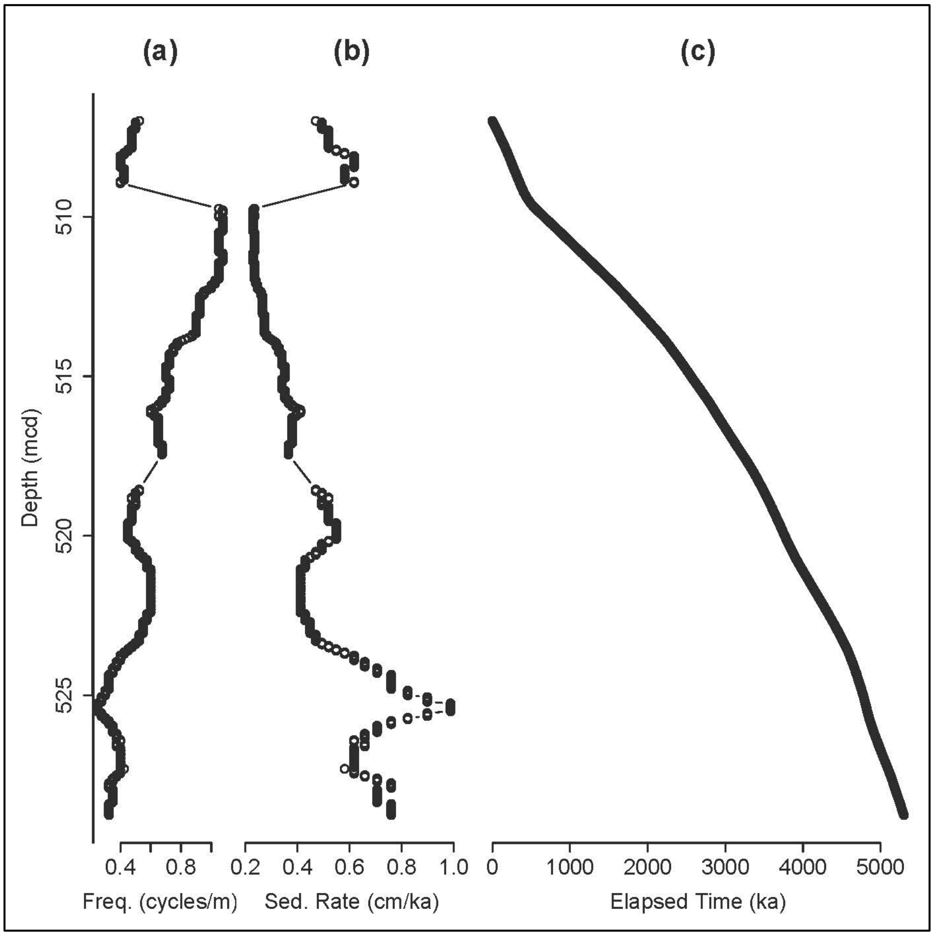

Figure A1.2. Frequency domain minimal tuning and the floating astronomical time scale for 1259A. **(a)** Spatial frequency drift of the long eccentricity signal (405 kyr) as observed in the EHA plots of Figure A1.1. An 80% F-test confidence level threshold was used to identify significant frequencies for tuning. Identification of the long eccentricity cycle is based upon the evolutive ASM results presented in Figure 2.4 and Figure A1.1. **(b)** Sedimentation rate derived from panel **"a"**, given a temporal period of 405 kyr for the spatial cycle. **(c)** Floating astro-nomical time scale derived by numerically integrating the sedimentation rate curve in panel **"b"**.

Table A1.3. (next page) Geochemical data from Demerara Rise Site 1261 and Site 1259 is recorded versus depth and time. Depth is recorded in MBSF-log for samples from Site 1261 from correction applied for offset between logging and MCD depth scales (see Text A1.1). Depth for samples from Site 1259 are recorded in MCD. Age corresponds to floating astronomical time scales developed by Meyers et al. (2012a) (Site 1261) and this study (Site 1259) spliced together by a Gaussian kernel smoothing stratigraphic correlation technique (Sect. 2.3.3) and anchored to the onset of the positive OAE2 carbon isotope excursion (94.45±0.16 Ma) (Meyers et al., 2001; Sageman et al., 2006; Meyers et al., 2012a; Ma et al., 2014). C/N is reported as atomic ratios. Average 1σ of $\delta^{13}C_{org}$ is less than 0.15‰.

Age (kyr)	Depth (MCD)	$\delta^{13}C_{org}$	%TOC	C/N	Carbonate%	%TOC (carbonate free)	Site
88451	508.40	-25.79	16.8	34.2	43.6	29.9	1259
88485	508.60	-27.87	10.5	31.9	57.9	24.9	1259
88519	508.80	-27.68	9.8	32.3	51.8	20.4	1259
88553	509.00	-23.84	22.6	39.6	35.9	35.3	1259
88589	509.20	-27.32	9.2	35.3	43.8	16.4	1259
88634	509.40	-27.55	7.7	33.3	55.4	17.2	1259
88691	509.60	-27.93	8.2	30.9	52.2	17.1	1259
88768	509.80	-27.60	6.1	33.5	68.8	19.6	1259
88854	510.00	-26.46	3.2	38.4	86.2	23.0	1259
88941	510.20	-27.00	11.0	37.0	51.8	22.9	1259
89028	510.40	-27.67	12.3	30.4	35.3	19.0	1259
89114	510.60	-27.69	10.7	31.2	53.1	22.7	1259
89199	510.80	-27.20	6.2	31.4	68.0	19.2	1259
89284	511.00	-28.10	1.0	31.0	92.9	14.6	1259
89370	511.20	-21.74	20.8	42.6	44.3	37.2	1259
89453	511.39	-22.35	18.8	43.8	44.0	33.6	1259
89542	511.60	-23.48	5.4	32.1	82.6	31.3	1259
89627	511.80	-23.18	12.8	37.2	62.4	34.1	1259
89873	512.40	-28.41	2.4	29.1	7.3	2.6	1259
89949	512.60	-27.23	12.4	32.8	49.9	24.6	1259
90024	512.80	-27.53	3.6	31.4	84.4	23.3	1259
90099	513.00	-27.47	9.6	33.3	47.8	18.4	1259
90173	513.20	-28.35	6.1	27.7	43.3	10.7	1259
90245	513.40	-26.28	16.8	35.1	40.7	28.3	1259
90318	513.60	-28.04	4.0	27.7	32.9	6.0	1259
90400	513.83	-27.55	6.2	32.5	76.8	26.6	1259
90452	513.99	-27.68	1.3	32.2	95.2	27.9	1259
90513	514.19	-27.82	12.7	31.6	48.7	24.8	1259
90573	514.39	-28.01	9.6	32.0	47.8	18.5	1259
90632	514.59	-27.98	12.0	33.0	46.3	22.4	1259
90692	514.80	-28.00	11.5	32.4	49.7	22.7	1259
90749	515.00	-28.28	10.7	32.0	50.7	21.7	1259
90807	515.20	-28.58	10.7	30.9	42.1	18.4	1259
90865	515.40	-28.78	3.1	30.1	82.3	17.3	1259
91132	516.40	-27.91	10.1	33.2	46.3	18.7	1259
91182	516.59	-28.16	11.5	36.8	49.5	22.7	1259
91238	516.80	-27.93	8.7	35.8	38.6	14.2	1259
91290	517.00	-28.62	10.2	33.5	49.4	20.2	1259
91344	517.20	-28.80	2.0	31.6	89.1	18.5	1259

Age (kyr)	Depth (MCD)	$\delta^{13}C_{org}$	%TOC	C/N	Carbonate%	%TOC (carbonate free)	Site
91398	517.40	-26.41	16.9	37.6	43.3	29.8	1259
91450	517.59	-28.39	9.7	30.7	51.2	19.8	1259
91504	517.80	-28.26	7.9	26.9	66.9	23.7	1259
91553	518.00	-28.27	8.9	30.0	57.4	20.9	1259
91599	518.20	-28.21	5.1	29.6	29.2	7.2	1259
91644	518.40	-28.19	12.4	31.9	41.4	21.1	1259
91687	518.60	-28.15	10.8	32.0	53.9	23.3	1259
91728	518.80	-28.26	9.3	31.7	35.3	14.4	1259
91767	519.00	-28.21	6.0	28.8	20.7	7.5	1259
91805	519.19	-28.30	11.9	31.7	33.8	17.9	1259
91845	519.40	-25.92	12.3	34.4	48.3	23.7	1259
91883	519.60	-27.26	9.1	32.1	41.1	15.4	1259
91920	519.80	-28.34	8.2	33.3	33.0	12.2	1259
91956	520.00	-27.36	1.2	25.0	63.1	3.3	1259
91992	520.19	-26.62	4.3	27.7	62.5	11.3	1259
92036	520.41	-27.47	1.2	24.8	43.1	2.1	1259
92078	520.61	-27.29	1.2	26.6	60.8	3.0	1259
92121	520.80	-26.86	3.4	32.3	77.9	15.3	1259
92167	521.00	-26.38	9.4	36.5	46.5	17.5	1259
92216	521.20	-27.70	9.3	30.5	41.9	16.0	1259
92262	521.39	-24.90	14.4	37.2	46.2	26.7	1259
92313	521.60	-24.95	12.3	40.2	47.5	23.3	1259
92361	521.80	-26.04	12.1	36.6	57.8	28.6	1259
92432	522.09	-27.44	1.7	32.2	89.3	15.7	1259
92459	522.20	-27.67	9.6	30.0	44.5	17.3	1259
92507	522.40	-27.34	6.5	30.8	69.1	20.9	1259
92554	522.60	-27.78	9.1	29.0	44.3	16.4	1259
92599	522.80	-27.60	11.8	32.3	44.4	21.2	1259
92644	523.00	-27.59	10.4	32.0	52.3	21.7	1259
92687	523.20	-27.61	8.7	31.5	48.5	17.0	1259
92729	523.40	-27.77	8.5	32.2	52.0	17.8	1259
92765	523.59	-27.75	6.7	31.3	67.5	20.7	1259
92799	523.79	-27.66	0.7	31.4	96.7	20.5	1259
92831	523.99	-27.72	8.8	28.7	53.0	18.7	1259
92836	609.50	-27.14	11.0	30.7	31.9	16.2	1261
92849	609.71	-27.50	1.4	39.4	91.9	17.5	1261
92860	609.91	-26.98	1.0	32.1	94.3	16.8	1261
92862	524.20	-27.80	4.1	29.3	79.8	20.4	1259
92872	610.11	-27.75	7.7	39.9	39.1	12.7	1261

Age (kyr)	Depth (MCD)	$\delta^{13}C_{org}$	%TOC	C/N	Carbonate%	%TOC (carbonate free)	Site
92884	610.31	-27.24	8.7	33.0	46.1	16.2	1261
92888	524.39	-27.71	5.5	31.3	66.9	16.6	1259
92896	610.51	-27.84	7.9	37.4	40.0	13.1	1261
92909	610.71	-27.57	7.6	30.0	55.1	16.9	1261
92916	524.60	-27.68	1.8	30.1	74.8	7.2	1259
92925	610.97	-27.94	7.7	36.8	35.1	11.9	1261
92934	611.11	-27.58	4.2	31.8	69.2	13.6	1261
92942	524.80	-27.89	6.9	31.1	44.0	12.4	1259
92946	611.31	-27.13	1.6	40.1	91.7	19.2	1261
92958	611.51	-27.21	6.8	29.9	51.5	14.1	1261
92967	525.00	-27.78	10.7	32.9	39.3	17.6	1259
92969	611.71	-27.73	9.6	36.4	28.2	13.4	1261
92980	611.91	-27.30	9.3	33.6	47.0	17.6	1261
92989	525.20	-27.92	10.8	30.9	40.1	18.0	1259
92992	612.11	-27.41	8.4	29.7	45.9	15.5	1261
92992	612.12	-27.69	9.1	31.2	37.8	14.7	1261
93003	612.31	-27.70	9.8	37.8	35.5	15.3	1261
93011	525.41	-27.66	8.5	29.6	47.1	16.0	1259
93014	612.51	-27.19	6.9	37.8	35.0	10.5	1261
93024	612.69	-27.45	2.7	38.6	72.1	9.5	1261
93031	525.60	-27.22	9.9	30.7	44.5	17.9	1259
93037	612.92	-27.58	1.1	26.6	95.5	24.0	1261
93055	525.80	-27.28	8.0	32.9	51.0	16.4	1259
93057	613.29	-27.32	8.6	-	47.5	16.4	1261
93080	613.69	-27.88	6.2	44.0	50.0	12.4	1261
93082	526.00	-27.30	9.1	31.7	50.6	18.5	1259
93110	526.20	-26.97	10.2	32.3	50.5	20.6	1259
93123	614.49	-27.30	7.5	43.9	52.5	15.7	1261
93141	526.40	-27.46	9.9	32.0	36.2	15.6	1259
93145	614.89	-26.44	3.9	-	77.9	17.6	1261
93167	615.29	-27.13	9.9	-	43.7	17.5	1261
93172	526.60	-27.11	5.2	35.9	69.3	16.9	1259
93189	615.69	-27.04	9.2	41.3	43.0	16.2	1261
93204	526.80	-27.26	3.7	33.8	77.4	16.6	1259
93212	616.09	-27.52	9.5	39.1	33.4	14.2	1261
93223	616.29	-26.73	8.8	33.8	29.2	12.5	1261
93234	616.49	-27.09	1.7	39.6	80.7	8.8	1261
93237	527.00	-26.28	1.4	37.4	95.5	30.5	1259
93245	616.69	-27.28	8.7	34.0	41.4	14.8	1261

Age (kyr)	Depth (MCD)	$\delta^{13}C_{org}$	%TOC	C/N	Carbonate%	%TOC (carbonate free)	Site
93256	616.89	-24.95	3.4	-	79.1	16.1	1261
93269	527.20	-25.37	1.1	35.9	96.7	33.7	1259
93302	527.40	-27.06	5.1	35.0	69.9	16.9	1259
93333	527.60	-27.53	5.5	36.6	40.4	9.3	1259
93360	527.80	-27.44	10.3	30.4	41.6	17.6	1259
93387	619.40	-27.84	9.4	36.1	31.1	13.6	1261
93387	528.00	-27.35	10.1	32.8	45.3	18.4	1259
93398	619.60	-27.65	9.9	34.9	28.0	13.8	1261
93408	619.80	-27.85	11.0	35.2	33.7	16.6	1261
93416	528.20	-27.13	10.7	33.1	43.2	18.8	1259
93418	620.00	-26.02	7.4	37.2	59.6	18.2	1261
93427	620.17	-27.55	12.3	-	7.4	13.3	1261
93444	528.40	-27.08	10.1	33.8	54.1	22.0	1259
93449	620.60	-27.71	1.7	36.6	85.8	11.9	1261
93468	620.98	-27.33	8.0	34.9	47.3	15.2	1261
93470	528.60	-27.26	5.2	33.2	67.5	15.8	1259
93489	621.39	-28.03	12.0	33.3	7.3	12.9	1261
93509	621.79	-27.36	4.0	36.8	71.3	13.9	1261
93550	622.59	-27.80	11.2	31.0	5.5	11.8	1261
93570	622.99	-27.50	3.8	32.4	72.1	13.4	1261
93589	623.39	-27.77	7.1	31.8	43.5	12.5	1261
93609	623.79	-27.65	9.5	32.0	38.0	15.4	1261
93628	624.19	-27.46	9.1	33.9	37.6	14.5	1261
93647	624.59	-27.78	9.5	31.9	38.4	15.5	1261
93664	624.97	-27.38	6.1	28.8	58.1	14.5	1261
93683	625.37	-27.46	7.3	35.4	56.6	16.9	1261
93692	625.57	-27.59	9.9	34.7	24.2	13.1	1261
93700	625.77	-27.13	9.1	36.7	32.8	13.5	1261
93708	625.97	-27.62	11.7	35.5	33.4	17.6	1261
93717	626.19	-27.40	9.4	32.4	32.8	14.0	1261
93725	626.39	-27.39	5.8	35.6	57.6	13.8	1261
93733	626.59	-27.69	2.8	33.1	76.0	11.7	1261
93741	626.79	-24.80	2.9	39.9	88.4	24.6	1261
93748	626.99	-24.82	1.1	36.3	95.2	23.8	1261
93756	627.19	-25.40	1.6	38.8	92.3	20.8	1261
93764	627.39	-26.32	2.5	38.6	84.5	16.3	1261
93772	627.62	-27.55	8.2	35.9	51.5	16.9	1261
93779	627.80	-27.49	7.8	37.9	46.8	14.6	1261
93787	628.00	-27.58	11.0	36.5	22.3	14.2	1261

Age (kyr)	Depth (MCD)	$\delta^{13}C_{org}$	%TOC	C/N	Carbonate%	%TOC (carbonate free)	Site
93795	628.20	-27.49	10.8	40.7	28.6	15.1	1261
93804	628.41	-26.94	9.6	34.4	28.3	13.4	1261
93812	628.60	-26.89	10.3	35.1	22.5	13.2	1261
93820	628.80	-26.67	11.8	35.9	22.9	15.3	1261
93828	629.00	-22.80	14.9	48.1	48.8	29.0	1261
93837	629.20	-26.34	4.8	38.0	68.2	15.0	1261
93847	629.40	-26.56	9.3	37.6	48.2	18.0	1261
93860	629.60	-22.99	17.1	43.3	29.7	24.3	1261
93876	629.80	-24.04	13.3	43.0	18.3	16.3	1261
93892	630.00	-23.20	14.5	45.5	46.5	27.0	1261
93907	630.20	-22.17	13.2	-	51.7	27.4	1261
93923	630.40	-23.80	17.4	42.6	17.9	21.2	1261
93940	630.62	-23.14	9.9	43.9	50.0	19.8	1261
93953	630.79	-20.57	16.8	49.7	48.5	32.5	1261
93969	630.99	-22.16	17.2	44.5	33.3	25.8	1261
93984	631.19	-22.21	14.0	46.4	38.9	22.9	1261
94000	631.39	-22.47	17.5	-	34.4	26.6	1261
94015	631.59	-22.27	17.9	48.5	31.6	26.1	1261
94030	631.79	-24.99	11.8	40.3	19.4	14.7	1261
94045	631.99	-21.72	2.1	43.4	90.9	23.4	1261
94075	632.39	-22.64	13.9	44.9	36.1	21.8	1261
94090	632.59	-22.09	11.5	-	59.6	28.3	1261
94120	632.99	-22.88	8.4	43.6	60.0	21.1	1261
94149	633.39	-21.62	5.3	-	64.6	14.9	1261
94200	634.06	-23.65	17.0	46.3	17.6	20.6	1261
94211	634.21	-23.96	10.2	43.8	20.7	12.9	1261
94231	634.46	-25.88	14.8	41.1	19.5	18.4	1261
94245	634.62	-24.42	15.5	43.0	11.1	17.4	1261
94262	634.82	-24.57	9.7	44.2	38.9	15.9	1261
94279	635.02	-22.03	16.6	52.1	43.8	29.5	1261
94295	635.22	-22.76	26.3	54.6	0.5	26.4	1261
94310	635.39	-26.01	15.3	39.9	17.7	18.6	1261
94329	635.62	-26.91	13.7	36.2	22.2	17.6	1261
94344	635.79	-27.20	8.2	34.9	21.6	10.5	1261
94362	635.99	-24.88	12.0	40.3	51.7	24.8	1261
94382	636.19	-23.94	3.7	35.4	89.4	34.9	1261
94404	636.42	-27.02	4.0	34.9	73.4	15.0	1261
94423	636.62	-25.30	9.0	36.4	63.1	24.4	1261
94441	636.81	-25.11	12.5	38.0	45.5	22.9	1261

Age (kyr)	Depth (MCD)	$\delta^{13}C_{org}$	%TOC	C/N	Carbonate%	%TOC (carbonate free)	Site
94451	636.91	-28.33	9.7	31.8	12.7	11.1	1261
94455	636.96	-28.27	10.0	32.0	48.2	19.3	1261
94460	637.01	-28.43	8.5	31.9	20.2	10.7	1261
94480	637.22	-28.44	8.9	35.2	55.6	20.0	1261
94497	637.40	-28.63	8.7	33.7	53.3	18.6	1261
94517	637.60	-28.64	7.4	32.1	50.4	14.9	1261
94536	637.80	-28.61	6.6	32.5	63.4	18.0	1261
94555	638.00	-28.68	4.9	32.8	69.3	16.0	1261
94574	638.20	-28.10	3.0	32.2	82.0	16.7	1261

Astronomical term	**E1**	**E2**	**E3**	**O1**	**O2**	**P1**	**P2**
Duration (kyr)	405.47	126.98	96.91	48.54	37.66	22.42	18.33

Table A1.4. Theoretical target periods used in the ASM analyses, based on the time domain astronomical model of (Laskar et al., 2004; 2011). Please see (Meyers et al., 2012b) for additional information on estimation of the target periods and their uncertainties.

r	δ^{13}C	%TOC	C/N	%Carb	%TOC-*cf*
δ^{13}C	1				
%TOC	**0.43**	1			
C/N	**0.67**	**0.52**	1		
%Carb	0.08	**-0.57**	0.03	1	
%TOC-*cf*	**0.61**	**0.57**	**0.67**	**+0.26**	1

Table A1.5. Correlation coefficients (r) of raw geochemical data from Site 1259. Significantly correlated (P-value < 0.01; Sect. 2.5.1) geochemical datasets are **bolded**.

r	δ^{13}C	TOC	C/N	Carb	TOC-*cf*
δ^{13}C	1				
TOC	+0.46	1			
C/N	**+0.80**	**+0.54**	1		
Carb	-0.01	**-0.79**	-0.17	1	
TOC-cf	**+0.74**	+0.39	**+0.52**	+0.19	1

Table A1.6. Correlation coefficients (r) of raw geochemical data from Site 1261. Significantly correlated (P-value < 0.01; Sect. 2.5.1) geochemical datasets are **bolded**.

Age (Ma)	**Depth (MCD)**	**Site**	**Geologic events**	**Type (*F.O./L.O.*)**	**Reference**
89.90	512.45	1259	base of CC13 Nannofossil Zone	F.O.	(Bornemann et al., 2008)
91.96-92.08	520.00-520.61	1259	Glauconite-rich bed	n/a	(Shipboard Sci. Party, 2004)
92.23	521.26	1259	positive $\delta^{18}O_{foram}$ excursion	n/a	(Bornemann et al., 2008)
92.28	521.45	1259	base of CC12 Nannofossil Zone	F.O.	(Bornemann et al., 2008)
93.80	628.29	1261	*E. eptapetalus*	F.O.	(Hardas and Mutterlose, 2007)
94.18	633.76	1261	*Q. gartneri*	F.O.	(Hardas and Mutterlose, 2007)
94.18	633.86	1261	*Q. intermedium*	F.O.	(Hardas and Mutterlose, 2007)
94.32	635.55	1261	*A. albianus*	L.O.	(Hardas and Mutterlose, 2007)

Table A1.7. Several previously published biostratigraphic depth horizons (Hardas and Mutterlose, 2007; Bornemann et al., 2008) were converted from depth to numerical time using the composite Demerara Rise anchored astrochronology (Meyers et al., 2012b; this study). Litho-/paleoclimatic events such as the positive $\delta^{18}O$ excursion from planktic foraminifera are reported. Numerical age uncertainty is ±191 kyr at Site 1259 and ±163 kyr at Site 1261 (see Text A1.2).

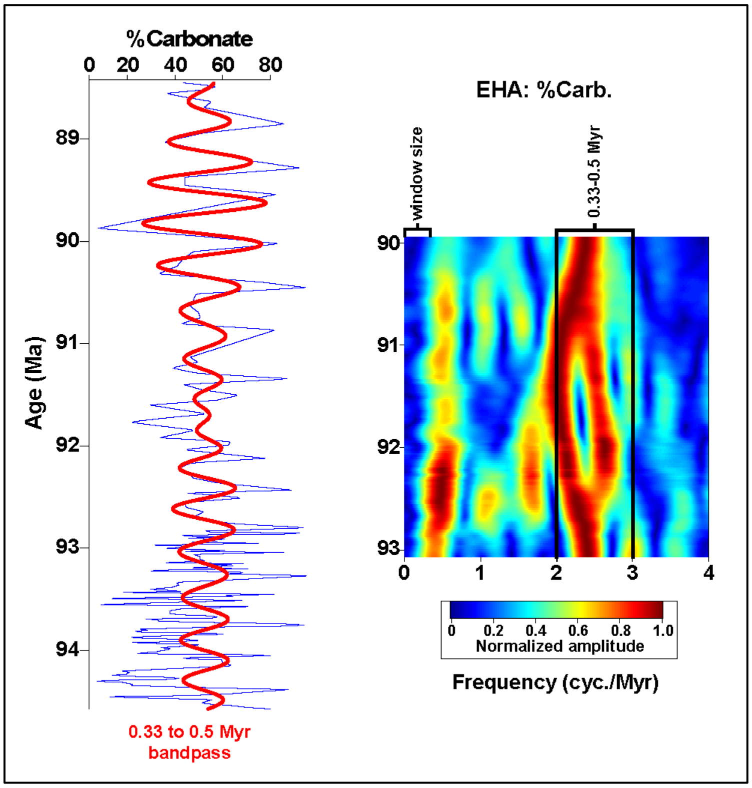

Figure A1.3. Bandpass filter (left) and EHA (right) results of weight percent carbonate time series from Site 1259 and Site 1261. High spectral amplitudes are recorded in the 2-3 cycle/Myr frequency band, suggesting influence from the stable 405 kyr eccentricity cycle.

A	B	C	D	E	F	G	H	I	J	K
Named CIE	**DR Age (Ma)** (±191 kyr)	**DR duration (kyr) to CTB** (< ±111 kyr)	**EF duration to CTB (kyr)**	**Difference (DR-EF)**	**WIB duration to CTB (kyr)**	**Difference (DR-WIB)**	**Bohemian Basin[a]**	**Difference (BB-DR)**	**Umbria-Marche Basin (Italy)**	**Difference (DR-UMB)**
White Fall or light point?	88.52	5379			5444	-65				
unnamed	88.73	5173			5091	82				
Light point?	88.88	5019			4854	165				
Navigation[a]	89.09	4810			4585	**225**				
Hitchwood #3[b]	89.45	4450					4435	-15		
F.O. *M. scupini*[c]	89.84	4062					4015	-47		
Hitchwood #1	90.25	3646	3527	119	3458	**188**	3719	73	3100	**546**
Bridgewick	90.93	2974	3288	**-314**	2932	42	3454	**480**		
Pewsey	?		2369		2149					
Glynde	91.60	2300	2057	**243**	1853	**447**				
Round Down	92.30	1601	1265	**336**	1617	-16			1370	**231**
Lulworth	92.68	1223	973	**250**	1217	6				
Holywell	93.25	647	*773*	*126*	*407*	***240***				
Unnamed	93.55	348	427	-79	392	-44				
OAE 2	94.05	-147	-183	36	-100	-47				
Median absolute difference (kyr)				185		74		60		**389**

Table A1.8. Gaussian kernel smoothed (1σ = ±75 kyr) $\delta^{13}C_{org}$ chemostratigraphic records from Turonian intervals globally (DR = Demerara Rise (this study), Tropical N. Atlantic; EF = Eagle Ford Fm. Iona-1 core Maverick Basin, Texas (Eldrett et al., 2015a); WIB = Western Interior Basin composite record (Joo and Sageman, 2014)), as well as astronomically tuned CIE timing relative to the CTB (BB = Bohemian Basin, Czech Republic (Laurin et al., 2014); UMB = Umbria Marche Basin, Italy (Batenburg et al., 2016)). Time scales for the various localities are constructed by various authors as follows: DR – astrochronology anchored to carbon isotope excursion (CIE); EF – astrochronology and radioisotope geochemistry; WIB – linear interpolation of biozone ages constrained by at least one of the methods of radioisotopic dating, astrochronology, or spline fitting; BB – astrochronology & biostratigraphy; UMB – astrochronology anchored by CIE. Carbon isotope excursions (CIEs) are detected from maxima values of the smoothed $\delta^{13}C_{org}$ time series which have a prominence of 0.5‰ greater than the adjacent minima. Positive CIEs are in black text and negative CIEs are in **red** text. A numerical age (col. B) for named Late Cretaceous CIEs (col. A (Jarvis et al., 2006)) detected at Demerara Rise is estimated from the astronomical time scales presented by (Meyers et al., 2012b) and this study which are anchored by assigning the onset of the OAE2 CIE to 94.45±0.16 Ma (Sageman et al., 2006; Meyers et al., 2012a; Ma et al., 2014). These ages for CIEs at DR (col. C), EF (col. D), WIB (col. F), BB (col. H), and UMB (col. J) are presented as the elapsed time from the Cenomanian-Turonian Boundary (CTB) at 93.90±0.15 Ma (Meyers et al., 2012a). The differences in timing of CIEs from the CTB are reported in columns E, G, I, and K. Differences greater than half a long stable eccentricity cycle (405 kyr/2) are **bolded** to indicate substantial discrepancies in CIE duration estimation. [a]Since the CTB is absent in the Bohemian Basin record, the relative ages of BB CIEs are calculated assuming that the Navigation CIE is equivalent in age to that determined at DR (4810 kyr) and other BB CIEs are calculated relative to this age anchor. [b]The F.O. of *P. germani* approximates the Hitchwood #2 CIE in the BB (Laurin et al., 2014). [c]The F.O. of *M. scupini* approximates the unnamed minimum in $\delta^{13}C_{org}$ between the Hitchwood#1 and Hitchwood#2 CIEs. [d]Estimated temporal uncertainty from: astronomical time scales from Sites 1259 and 1261, splicing of records, and MCD to MBSF-log conversion (see Text S2). [e]Estimated uncertainty of age of CTB from GSSP (Meyers et al., 2012a). [f]Estimated temporal uncertainty of the OAE2 CIE onset in WIB and at Demerara Rise (see Text A1.2). Discrepancies among records are attributed to: sampling resolution, uncertainty in sedimentation rates from astrochronology and radioisotope geochemical analyses/methods, undetected hiatuses in study intervals, selection of standard deviation of the kernel smoother, local environmental variability in bulk $\delta^{13}C_{org}$ values (e.g. type of organic matter, algal growth rates, etc.), and analytical uncertainty of bulk $\delta^{13}C_{org}$ measurements.

Appendix 2: Supplemental Material for Chapter 3 and Jones et al. (2018b)

Evaluating Late Cretaceous OAEs and the Influence of Marine Incursions on Organic Carbon Burial in an Expansive East Asian Paleo-lake

Contents

A2.1) Carbon geochemistry analytical procedures

A2.2) XRF analytical procedures

A2.3) Re-Os isotope analytical procedures

A2.4) SK1-S time scale

A2.5) Cross-correlating Songliao Basin and Western Interior Basin $\delta^{13}C_{org}$ time series

A2.6) $\Delta^{13}C$ of the SK1-S core, Songliao Basin

A2.7) $\Delta^{13}C$ Angus Aristocrat core (WIB)

A2.8) Geochemical data tables:

  Table A2.1.: Turonian-Coniacian Re-Os geochemistry of the SK1-S core, Angus core, and Demerara Rise

  Table A2.2.: Carbon chemistry of the SK1-S core

  Table A2.3.: Angus core (Denver Basin) $\delta^{13}C$ chemostratigraphy

A2.1) Carbon geochemistry analytical procedures

Samples collected from SK1-S were powdered in tungsten carbide crushing containers in a shatterbox and analyzed via coulometric titration on a UIC Coulometer to measure weight percent carbonate content and weight percent total organic carbon (TOC) at the Northwestern University Integrated Laboratory for Earth and Planetary Sciences (Huffman, 1977). Powders were acidified in 2N HCl for 12 hours on a shaker table to degas carbonate-bound carbon. After filtering acidified samples to remove salts with 750 mL of deionized water, bulk organic carbon isotope ratios ($\delta^{13}C_{org}$) and carbon to nitrogen (C/N) ratios were measured on a continuous flow Costech ECS4010 Elemental Analyzer coupled to a Thermo Delta V Plus Mass Spectrometer. Average 1σ uncertainty on duplicates (n=12) of unknown $\delta^{13}C$ measurements is ±0.05‰ (max = ±0.20‰). To correct for instrument mass fractionation and adjust to the VPBD per mil scale, raw results were calibrated using caffeine (IAEA) and acetanilide (Indiana University) standards.

Powders from samples of the Angus Aristocrat (AA) core from the Western Interior Basin (WIB) of North America (Weld County, Denver Basin, Colorado) were analyzed for bulk carbonate carbon isotopes ($\delta^{13}C_{carb}$) spanning OAE3 (n=80). OAE3 in the AA core and much of the WIB is preserved in the Lower Shale to Middle Shale sub-members of the Smoky Hill Member of the Niobrara Formation (Joo and Sageman, 2014; Tessin et al., 2015). These powders were previously analyzed for $\delta^{13}C_{org}$ (Joo and Sageman, 2014), permitting precise comparison of $\delta^{13}C_{carb}$ and $\delta^{13}C_{org}$ values from the same horizon, and therefore a more accurate calculation of $\Delta^{13}C$ ($\delta^{13}C_{carb}$- $\delta^{13}C_{org}$). For $\delta^{13}C_{carb}$ analysis, roughly 400µg of carbonate was added to cleaned glass vials. Vials were capped, and atmospheric CO_2 was purged from the vials using vacuum pumps and He displacement. Several drops of 103% H_3PO_4 were added to each purged vial to acidify samples and evolve CO_2 gas from the sample. The CO_2 gas was then analyzed on a continuous flow Thermo Gasbench II – Delta-V-Plus IRMS at Northwestern University. To correct for instrument mass fractionation and adjust to the VPBD per mil scale, raw results were calibrated using the NBS-18 and NBS-19 (NIST) standards and an in-house carbonate standard. Typically, internal precision is <±0.05‰ and ±0.15‰ for standard duplicates.

A2.2) XRF Analytical Procedures

To measure the powdered bulk samples (n=84) for major and trace element concentrations, we use a Spectro Xepos He ED-XRF Spectrometer at Stanford University calibrated with USGS, NIST and internal standards, with replicate analyses of NIST SRM 2711 (Montana Soil) used to ensure calibration accuracy. To assess precision, replicates of NIST SRM 2711 (n=9) and sample triplicates (n=5) indicate 1σ relative uncertainty of less than ±5% on all elements except Co, Mo, Ba and Ce, which indicate uncertainty of less than ±15%.

We report Mo, Fe, and V+Cr concentration data normalized to aluminum (Figure 3.3). This minimizes the effect of fluctuating detrital contributions and tests for authigenic enrichment above crustal values (Tribovillard et al., 2006). Additionally, Mo and S concentrations are normalized to TOC to evaluate trace metal inventories in the water column (Algeo and Lyons, 2006).

A2.3) Re-Os Isotope Analytical Procedures

Ten samples from the SK1-S core in the Songliao Basin were analyzed for rhenium-osmium (Re-Os) geochemistry in the Source Rock and Sulfide Geochronology and Geochemistry Laboratory at Durham University in February-March of 2016. Re-Os isotope analytical procedures implemented in this study followed those refined by Selby and Creaser (2003), and more recently implemented in chemostratigraphic applications (Du Vivier et al., 2014; Du Vivier et al., 2015b). At least 30 grams of mudstone per sample was crushed in a shatterbox using ceramic containers and pucks which had been purified with standard Ottawa Sand beforehand. Any visible markings on the core were filed away prior to crushing.

Given the high value nature of the Re abundance in organic-rich sedimentary units, the Re abundance of the sample set pre-determined prior to the full Re-Os analysis. The pre-determined Re abundances were obtained via ID-ICP-MS on a Thermo X-Series Mass Spectrometer. The full Re-Os protocol was determined using between ~0.3-1.0g of sample powder. The sample powders were spiked with a known volume of a mixed ^{185}Re + ^{190}Os tracer solution and were digested in 8mL of 4N $CrO_3 \cdot H_2SO_4$ in a sealed Carius tube for ~48 hours at 220°C. This digestion principally leaches the hydrogenous fraction (i.e. carbonates and organics) of osmium and rhenium from the sediments (Selby and Creaser, 2003). The Re and Os were then separated to eliminate isobaric interference during final thermal ionization mass spectrometry (TIMS) analysis. Osmium was isolated using chloroform extraction, with back extraction into 9N HBr. The Os was further purified by CrO_3-H_2SO_4-HBr microdistillation. The Re fraction was isolated from the 4N $CrO_3 \cdot H_2SO_4$ solution via NaOH-acetone extraction and further purified via standard anion column chromatography.

The purified Re and Os extracts were loaded to Ni and Pt filaments, respectively, together with $Ba(NO_3)_2$ and $Ba(OH)_2$/NaOH activator solution. The isotope compositions of the Re and Os fractions were analyzed on a Thermo Triton TIMS in negative ionization mode (Creaser et al., 1991; Volkening et al., 1991) using secondary electron multiplier (SEM) to measure osmium counts and multiple Faraday cups for rhenium measurements. In-house Re and Os solutions were continuously analyzed during the course of this study to ensure and monitor long-term mass spectrometry reproducibility. The Re standard solution (125pg) and DROsS Os standard solution (50 pg) yield ^{185}Re/^{187}Re values of 0.5984 ± 0.003 (1 SD, n = 4) and ^{187}Os/^{188}Os values of 0.16088 ± 0.0006 (1SD, n = 8), respectively; both were identical to previously reported values. The measured difference in ^{185}Re/^{187}Re values for the Re standard solution and the accepted ^{185}Re/^{187}Re value (0.5974) is used for mass fractionation correction of the Re sample data. All Re and Os data were oxide and blank corrected. Procedural blanks for Re and Os in this study were 12 ± 3 pg/g and 0.07 ± 0.05 pg/g, respectively, with an ^{187}Os/^{188}Os value of 0.25 ± 0.15 (n = 4). The ^{187}Re/^{188}Os and ^{187}Os/^{188}Os uncertainties were determined through full propagation of uncertainties, including those in weighing, mass spectrometer measurements, spike calibrations, blank abundances and reproducibility of standard values. The osmium isotope ratios were corrected for ^{187}Re decay ($\lambda = 1.666 * 10^{-11}$ yr^{-1}; Smoliar et al., 1996) to derive the initial (i.e. syn-depositional) osmium isotope ratios (Os_i) using equation A2.1:

$$\mathbf{Os_i = {}^{187/188}Os - {}^{187}Re/{}^{188}Os \times e^{(\lambda t - 1)}} \qquad \textbf{(Equation A2.1)}$$

A2.4) SK1-S time scale and uncertainty

In this study, we utilize existing radioisotope geochronology of bentonites and a published floating astronomical time scale (ATS) from SK1-S as a numerical time scale for the Qingshankou Formation. In an effort to resolve the precision of the SK1-S time scale, we quantify the sources of uncertainty in the anchored SK1-S time scale (e.g., radioisotopic, astrochronologic, stratigraphic) (Eqn. A2). This approach evaluates the robustness of intercontinental correlations of $\delta^{13}C$ chemostratigraphic records, especially between terrestrial and marine basins like the Songliao Basin and the Western Interior Basin, where traditional biostratigraphic correlations are not possible.

Wu et al. (2013) construct a floating ATS (relative numeric time) for SK1-S via spectral analysis and bandpass filtering of the 405-kyr stable eccentricity cycle preserved in geophysical well logs. Wang et al. (2016b) report uranium-lead (U/Pb) zircon age dates from four bentonite horizons in SK1-S using a high-precision chemical abrasion-isotopic dilution-thermal ionization mass spectrometer (CA-ID-TIMS) analytical technique. Three of these U/Pb ages, with low total analytical uncertainty ($2\sigma = \pm 120$ kyr), originate from bentonite horizons in the Turonian Qingshankou Member 1 (1673, 1705, 1780 m), and one from the Santonian Nenjiang Formation (1019 m). Following the calibrated stratigraphy approach of Wang et al. (2016b), we anchor the floating ATS to each of the horizons in the Qingshankou with U/Pb numerical ages to test consistency among the 3 possible tie points. The 2σ standard deviation of the three scenarios for anchoring the ATS in Qingshankou Member 1 is ±90 kyr, and the mean numerical age-model is equivalent to anchoring the ATS to the bentonite S1705 bentonite (1705 m = 90.974, $2\sigma = \pm 0.12$ Ma). We did not attempt to anchor the ATS to the fourth U/Pb dated bentonite in the Nenjiang Formation, since there is regional evidence for a hiatus in the underlying Yaojia Formation which adds significant uncertainty to the ATS in the interval above the Qingshankou (Figure 3.2) (Feng et al., 2010; Wang et al., 2016b). Lastly, we consider uncertainty from the development of the ATS. Currently there are few techniques to quantify uncertainties associated with astrochronologic analysis. However, Sageman et al. (2014a) estimate that sources of uncertainty in ATS (e.g. orbital target period, depositional noise, etc.) sum to roughly one quarter of the bandpassed cycle. In the case of SK1-S, the 405-kyr stable eccentricity cycle tunes the ATS (Wu et al., 2013); therefore, uncertainty is estimated at ±101 kyr. We calculate a total uncertainty of ±181 kyr for the SK1-S time scale when we combine each source of uncertainty in quadrature (Eqn. A2):

$$\textbf{total time scale uncertainty} = \sqrt{a^2 + b^2 + c^2} \qquad \textbf{(Equation A2.2)}$$

Where: a is the U/Pb analytical uncertainty (120 kyr, 2σ),

b is the bentonite tie point uncertainty (90 kyr, 2σ), and

c is the floating astrochronology uncertainty (101 kyr, 2σ). We report the total time scale uncertainty at two standard deviations (2σ).

With sources of uncertainty quantified, we calculate temporal durations between bentonite horizons using the independent methods of astrochronology and radioisotopic dating to test for consistency between the geochronometers and accuracy of the age model. In an approach similar to Wang et al. (2016b) (their Figure 3), we find that the estimated durations between bentonites S1673 and S1780 in SK1-S are equivalent using astrochronologic (1261±101 kyr) and radioisotopic (1350±120 kyr) techniques and that the offset (89 kyr) is within the range of uncertainty specified above.

A2.5) Cross-correlating Songliao Basin and Western Interior Basin $\delta^{13}C_{org}$ time series

A carbon isotope correlation of excursions (CIEs) recorded in the Songliao Basin (this study) and the Western Interior Basin of North America (Joo and Sageman, 2014), served to identify the Oceanic Anoxic Event 3 CIE in the Songliao Basin (see Sect. 3.5.1). Astrochronologic analyses of the SK1-S core (Wu et al., 2013) and the Western Interior record (Locklair and Sageman, 2008), along with radioisotopic age dates for bentonites in the respective basins (Sageman et al., 2014a; Wang et al., 2016b), provide high-resolution anchored astronomical time scales to develop continuous $\delta^{13}C$ records for comparison.

In addition to a visual correlation of these time series, a quantitative analysis to determine lags and correlative horizons between records was implemented (see Figure 3.4), via a Gaussian kernel smoothing cross-correlation technique (Jones et al., 2018a; Chapter 2). In this approach, the irregularly sampled raw $\delta^{13}C$ time series were smoothed using a Gaussian kernel smoother which robustly (Rehfeld et al., 2011) calculates a continuous interpolated time series by weighting nearby raw data points as a function of distance and user specified Gaussian standard deviation (σ) (e.g., Dakos et al., 2008; Gao et al., 2015; Oster and Kelley, 2016). Resulting kernel smoothed time series were then cross-correlated to determine horizons of best alignment. In the cross-correlation, one time series is iteratively lagged relative to the other record. At each lag (τ), the Pearson's correlation coefficient (ρ) is calculated to quantify correlation of the time series (e.g., Mitchell et al., 2008). The resulting Gaussian kernel smoothed cross-correlation of Turonian-Coniacian records from the Western Interior Basin and Songliao Basin produced an optimal correlation with a lag of +333 kyr (Figure A2.1). This indicates that the anchored time scales of the WIB and Songliao Basin have a robust correlation ($\rho_{max} = +0.85$) and are offset by 333 kyr (either Songliao shifted younger by 333 kyr or WIB record shifted older by 333 kyr). This offset, although resolvable using the Gaussian kernel smoothing cross-correlation technique, is less than the temporal uncertainty of each time series (Sect. 3.5.1 and A2.4).

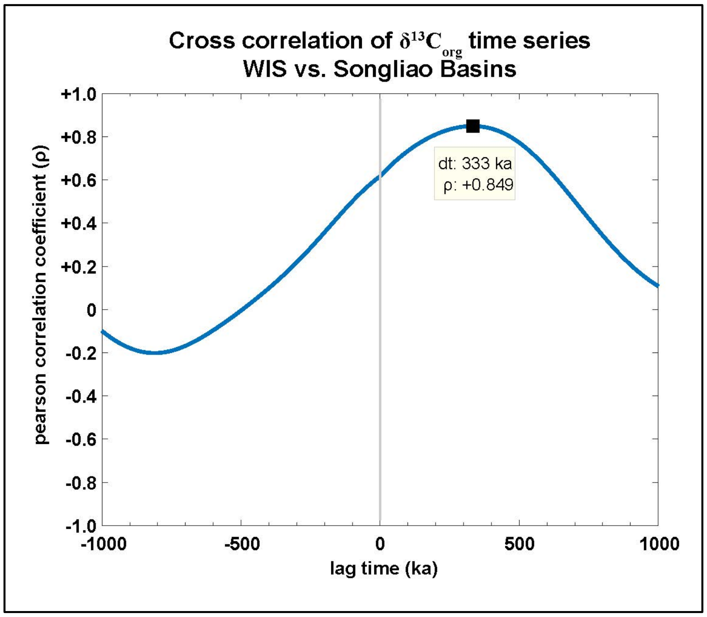

Figure A2.1.: Cross correlation of Gaussian kernel smoothed time series from the Songliao Basin and Western Interior Basin. Maximum correlation (pearson correlation coefficient, ρ) occurs when the Songliao Basin record is shifted 333 kyr younger (or WIB record shifted 333 kyr older).

A2.6) $\Delta^{13}C$ Songliao Basin SK1-S Core

The various $\delta^{13}C$ chemostratigraphic records of the SK1-S core were measured from samples at different horizons for ostracod $\delta^{13}C_{carb}$ (Chamberlain et al., 2013) and bulk organic $\delta^{13}C_{org}$ (this study; Hu et al., 2015). This precludes direct calculation of $\Delta^{13}C$ from identical horizons, such as in the Angus core (see A2.1). Therefore, $\delta^{13}C_{carb}$ values were estimated for ages of corresponding $\delta^{13}C_{org}$ values, by Gaussian kernel smoothing ($1\sigma = 50$ kyr) the $\delta^{13}C_{carb}$ dataset to produce a continuous $\delta^{13}C_{carb}$ chemostratigraphy and calculate $\Delta^{13}C$ (see A2.3).

A2.7) $\Delta^{13}C$ Angus Aristocrat Core (WIB)

The $\Delta^{13}C$ ($\delta^{13}C_{carb}$-$\delta^{13}C_{org}$) values through OAE3 in the Angus core (Denver Basin, CO) were calculated using $\delta^{13}C_{org}$ (Joo and Sageman, 2014) and $\delta^{13}C_{carb}$ values (see A2.1, Sect. 3.4.2) of powders from identical stratigraphic horizons. Smoothed $\Delta^{13}C$ values decrease by ~-0.5‰ through OAE3 (Figure 3.5, Table A2.1). We interpret this as a signal of decreasing carbon isotope fractionation between marine dissolved inorganic carbon (DIC) and photosynthate due to pCO_2 draw down through OAE3.

A nearby $\Delta^{13}C$ record from the Portland core, roughly 200 km south of the Angus core, does not record a similar trend through OAE3 (Tessin et al., 2015). The authors attribute their $\Delta^{13}C$ record to changes in the type of organic matter preserved and preferential degradation of organic compounds through thermal maturation, and therefore a diagentically altered $\delta^{13}C_{org}$ record. They also record a spike in weight percent total organic carbon (TOC) at the onset of OAE3. This TOC spike (<1% to 3-6%), along with changing C/N and hydrogen index values, indicates a dramatic shift in organic carbon burial dynamics and organic matter type. This highlights the susceptibility of $\Delta^{13}C$ records to diagenesis of organic matter or carbonate.

In the Angus core however, we believe the $\Delta^{13}C$ signal in the OAE3 interval is not significantly diagentically altered, and can be interpreted as a proxy for carbon isotope fractionation between DIC and photosynthate. The $\delta^{13}C_{carb}$ values (~+2‰) are not significantly depleted compared to other time equivalent records in the WIB (Pratt et al., 1993; Tessin et al., 2015), in the English Chalk (Jarvis et al., 2006), or elsewhere (Wagreich, 2012 and references therein). Additionally, $\delta^{13}C_{carb}$ and $\delta^{18}O$ do not covary ($r^2 = 0.04$) (Figure A2.2). These observations suggest minimal diagenetic overprinting of the primary bulk $\delta^{13}C_{carb}$. Likewise, we do not interpret $\delta^{13}C_{org}$ data from the Angus core (Joo and Sageman, 2014) as diagenetically altered. There are no major changes in TOC in the Angus core across OAE3, and $\delta^{13}C_{org}$ and TOC do not covary ($r^2 = 0.001$). Since neither $\delta^{13}C_{org}$ or $\delta^{13}C_{carb}$ exhibit geochemical indications of diagenetic alteration, we interpret the $\Delta^{13}C$ record as primary and thus, in the framework of Kump and Arthur (1999).

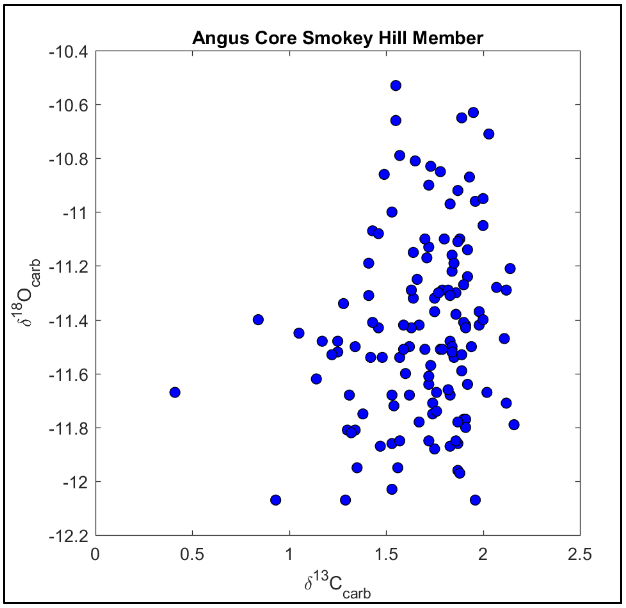

Figure A2.2.: Cross plot of bulk $\delta^{13}C_{carb}$ and $\delta^{18}O$ (r^2=0.04) from the Smoky Hill Member of the Angus core, including the OAE3 interval.

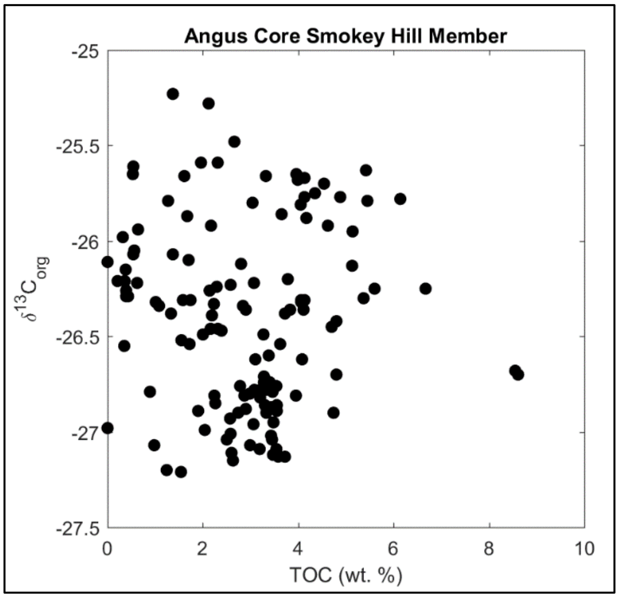

Figure A2.3.: Cross plot of bulk $\delta^{13}C_{carb}$ and weight percent total organic carbon (TOC) (r^2=0.001) from the Smoky Hill Member of the Angus core, including the OAE3 interval.

Table A2.1.: Re-Os geochemistry of select intervals in the Turonian-Coniacian Stages from the SK1-S core, Angus core, and Demerara Rise (see text for discussion). Measured at Durham University in 2016.

Batch/Sample	Core	Depth	Age	Re (ppb)	±	Os (ppt)	±	192Os (ppt)	±	187Re/188Os	±	187Os/188Os	±	rho	Osi	±
RO743-1_SK1s-1325.0m	SK1-S	1325	86.878	5.04	0.01	40.8	0.3	13.8	0.1	726.3	4.9	1.821	0.015	0.674	0.769	0.022
RO743-2_SK1s-1365.0m	SK1-S	1365	87.306	1.11	0.01	27.0	0.3	10.0	0.2	220.7	4.8	0.982	0.029	0.685	0.660	0.035
RO743-3_SK1s-1395.0m	SK1-S	1395	87.627	0.99	0.01	36.1	0.4	13.5	0.3	145.3	3.1	0.941	0.027	0.677	0.729	0.032
RO743-4_SK1s-1405m	SK1-S	1405	87.734	0.23	0.01	18.1	0.4	6.9	0.3	67.3	3.3	0.822	0.047	0.600	0.723	0.052
RO743-5_SK1s-1455m	SK1-S	1455	88.269	1.13	0.01	33.3	0.4	12.4	0.3	182.3	3.9	0.973	0.028	0.684	0.705	0.034
RO741-1_SK1-s 1665m	SK1-S	1665	90.516	3.26	0.01	38.9	0.3	13.4	0.2	484.4	6.3	1.640	0.027	0.707	0.909	0.036
RO741-2_SK1-s 1685m	SK1-S	1685	90.731	2.18	0.01	30.5	0.3	10.8	0.1	399.6	5.0	1.365	0.022	0.691	0.761	0.029
RO741-3_SK1-s 1715m	SK1-S	1715	91.052	3.60	0.01	41.7	0.4	14.4	0.2	496.6	6.3	1.627	0.026	0.705	0.874	0.036
RO741-4_SK1-s 1740m	SK1-S	1740	91.319	3.85	0.01	48.0	0.4	16.7	0.2	458.5	4.6	1.564	0.020	0.689	0.866	0.027
RO741-5_SK1-s 1750.54m	SK1-S	1750.54	91.432	3.94	0.02	44.0	0.4	15.0	0.2	523.2	6.6	1.755	0.029	0.704	0.958	0.039

Batch/Sample	Site	Depth (MCD)	ATS Age (Ma) Jones et al 2017	Re (ppb)	±	Os (ppt)	±	192Os (ppt)	±	187Re/188Os	±	187Os/188Os	±	rho	Osi	±
RO743-6_DR511.6MCD	1259	511.60	89.542	48.17	0.12	205.1	1.2	61.4	0.3	1561.9	7.9	3.041	0.018	0.650	0.709	0.030
RO743-7_DR513.99MCD	1259	513.99	90.452	12.38	0.03	91.1	0.5	31.1	0.2	792.7	5.1	1.747	0.014	0.677	0.551	0.021
RO743-8_DR515.2MCD	1259	515.20	90.807	79.71	0.20	890.3	3.6	317.7	1.1	499.2	2.1	1.331	0.007	0.579	0.575	0.010
RO743-9_DR518.4MCD	1259	518.40	91.644	142.36	0.35	1081.9	4.9	366.1	1.3	773.6	3.3	1.814	0.009	0.572	0.632	0.014
RO743-10_DR523.0MCD	1259	523.00	92.644	77.66	0.19	676.1	3.0	233.9	0.8	660.5	2.9	1.609	0.008	0.584	0.589	0.013

Batch/Sample	Core	Depth (m)	Age (Ma) Joo & Sageman (2014)	Re (ppb)	±	Os (ppt)	±	192Os (ppt)	±	187Re/188Os	±	187Os/188Os	±	rho	Osi	±
RO750-9_AA7213'+24cm	Angus	2198.76	86.109	360.57	0.89	942.3	5.8	238.2	0.8	3011.0	12.7	4.979	0.024	0.571	0.657	0.042
RO745-8_AA7250'+17cm	Angus	2209.97	87.187	261.48	0.64	901.9	4.9	259.9	0.9	2001.8	8.4	3.446	0.017	0.577	0.536	0.029
RO745-9_AA7263'-4cm	Angus	2213.72	87.548	242.38	0.59	759.5	4.3	209.5	0.7	2301.8	9.7	3.936	0.019	0.582	0.577	0.033
RO745-10_AA7267'+13.5cm	Angus	2215.12	87.682	223.65	0.55	610.0	3.7	157.9	0.6	2817.8	12.0	4.688	0.023	0.586	0.569	0.040
RO750-10_AA7277'-14cm	Angus	2217.89	87.949	191.17	0.47	524.0	3.2	135.6	0.5	2804.4	12.1	4.690	0.023	0.589	0.577	0.041

Table A2.2.: Carbon chemistry and geochemical data summary of the SK1-S core in the Songliao Basin of northeast China (see text for discussion).

Well	Lithostratigraphic Unit	Depth (m)	Age (Ma)	%CaCO3	%TOC	Avg. d13C	Stdev. d13C (dups)	C/N (atm. Ratio)
SK1-S	Yaojia Formation	1153.77		5.5	0.51	-27.30		3.96
SK1-S	Yaojia Formation	1204.23		19.3	0.30	-28.76		3.88
SK1-S	Yaojia Formation	1210		1.8	0.29	-27.10		2.64
SK1-S	Yaojia Formation	1230		2.7	0.15	-27.07		1.45
SK1-S	Yaojia Formation	1240		2.5	0.24	-27.49		2.34
SK1-S	Yaojia Formation	1260		8.9	0.37	-27.01	0.04	5.55
SK1-S	Yaojia Formation	1270		6.2	0.76	-28.56	0.06	8.55
SK1-S	Yaojia Formation	1275.00		0.4	4.21	-31.06	0.01	-
SK1-S	Yaojia Formation	1285.10		0.4	0.32	-23.53		9.44
SK1-S	Qingshankou Fm. Members 2&3	1295.00		18.6	0.03	-		-
SK1-S	Qingshankou Fm. Members 2&3	1300		14.5	0.14	-26.60		1.48
SK1-S	Qingshankou Fm. Members 2&3	1310.00	86.72	7.4	0.40	-27.23		7.45
SK1-S	Qingshankou Fm. Members 2&3	1320.00	86.82	7.9	0.77	-29.45	0.02	12.31
SK1-S	Qingshankou Fm. Members 2&3	1330.00	86.93	9.1	0.43	-28.20		6.84
SK1-S	Qingshankou Fm. Members 2&3	1340	87.04	11.6	0.69	-29.62		6.38
SK1-S	Qingshankou Fm. Members 2&3	1350	87.15	16.5	0.61	-29.84	0.04	6.93
SK1-S	Qingshankou Fm. Members 2&3	1360	87.25	19.4	0.57	-28.99		9.23
SK1-S	Qingshankou Fm. Members 2&3	1370	87.36	8.5	0.61	-28.43		6.60
SK1-S	Qingshankou Fm. Members 2&3	1380	87.47	8.7	0.45	-28.37	0.03	5.30
SK1-S	Qingshankou Fm. Members 2&3	1390	87.57	5.7	0.18	-27.28		1.48
SK1-S	Qingshankou Fm. Members 2&3	1400	87.68	7.4	0.45	-26.05		4.40
SK1-S	Qingshankou Fm. Members 2&3	1410	87.79	5.8	0.20	-25.40		1.63
SK1-S	Qingshankou Fm. Members 2&3	1420	87.89	8.4	0.44	-26.72		5.07
SK1-S	Qingshankou Fm. Members 2&3	1430	88.00	5.4	0.14	-25.83		0.88
SK1-S	Qingshankou Fm. Members 2&3	1440	88.11	5.8	0.75	-28.28	0.01	5.92
SK1-S	Qingshankou Fm. Members 2&3	1450	88.22	12.2	0.52	-27.93		4.37
SK1-S	Qingshankou Fm. Members 2&3	1460	88.32	5.7	0.47	-30.77	0.05	2.91
SK1-S	Qingshankou Fm. Members 2&3	1469.88	88.43	7.3	0.76	-30.54		8.28
SK1-S	Qingshankou Fm. Members 2&3	1480	88.54	6.4	1.02	-29.63		8.11
SK1-S	Qingshankou Fm. Members 2&3	1490	88.64	11.6	0.92	-30.42		7.37
SK1-S	Qingshankou Fm. Members 2&3	1500	88.75	6.2	1.92	-28.15		14.21
SK1-S	Qingshankou Fm. Members 2&3	1510.00	88.86	8.9	0.81	-28.74	0.09	8.25
SK1-S	Qingshankou Fm. Members 2&3	1520.00	88.96	9.7	0.78	-28.56		7.00
SK1-S	Qingshankou Fm. Members 2&3	1530.00	89.07	9.1	0.61	-28.83		6.05
SK1-S	Qingshankou Fm. Members 2&3	1540.00	89.18	10.3	0.49	-28.20		4.62
SK1-S	Qingshankou Fm. Members 2&3	1550.00	89.29	15.0	0.54	-28.62		4.62
SK1-S	Qingshankou Fm. Members 2&3	1560.00	89.39	21.2	0.55	-28.81		5.08
SK1-S	Qingshankou Fm. Members 2&3	1570.00	89.50	5.2	0.84	-29.27	0.06	6.80
SK1-S	Qingshankou Fm. Members 2&3	1580.00	89.61	11.1	0.86	-28.32		5.45
SK1-S	Qingshankou Fm. Members 2&3	1590.00	89.71	5.2	1.50	-30.32		11.67
SK1-S	Qingshankou Fm. Members 2&3	1600.00	89.82	10.9	4.43	-25.65		24.40
SK1-S	Qingshankou Fm. Members 2&3	1609.93	89.93	22.4	0.53	-28.70		4.90
SK1-S	Qingshankou Fm. Members 2&3	1620.00	90.03	4.5	1.01	-30.38		5.28
SK1-S	Qingshankou Fm. Members 2&3	1630.00	90.14	3.0	2.04	-28.29		10.21
SK1-S	Qingshankou Fm. Members 2&3	1640.00	90.25	2.5	1.68	-28.67		8.84
SK1-S	Qingshankou Fm. Members 2&3	1649.50	90.35	4.6	1.24	-32.25		6.03
SK1-S	Qingshankou Fm. Members 2&3	1660.00	90.46	5.0	9.16	-27.21		16.89
SK1-S	Qingshankou Fm. Members 2&3	1670.00	90.57	6.0	2.10	-28.74		9.97
SK1-S	Qingshankou Fm. Members 2&3	1680.00	90.68	8.8	1.58	-30.43		9.56
SK1-S	Qingshankou Fm. Members 2&3	1690.00	90.78	6.5	2.69	-29.95		11.62
SK1-S	Qingshankou Fm. Members 2&3	1700.00	90.89	3.2	2.09	-29.84		7.67

Well	**Lithostratigraphic Unit**	**Depth (m)**	**Age (Ma)**	**%CaCO3**	**%TOC**	**Avg. d13C**	**Stdev. d13C (dups)**	**C/N (atm. Ratio)**
SK1-S	Qingshankou Fm. Member 1	1709.88	91.00	2.2	2.56	-28.50		8.76
SK1-S	Qingshankou Fm. Member 1	1720.00	91.11	2.5	2.70	-30.04		8.85
SK1-S	Qingshankou Fm. Member 1	1730.00	91.21	10.5	2.25	-31.32		8.51
SK1-S	Qingshankou Fm. Member 1	1740.00	91.32	1.1	4.90	-32.40	0.19	16.79
SK1-S	Qingshankou Fm. Member 1	1750.54	91.43	1.0	3.47	-31.53		12.42
SK1-S	Qingshankou Fm. Member 1	1760.00	91.53	0.1	4.83	-31.70		17.61
SK1-S	Qingshankou Fm. Member 1	1770.00	91.64	2.1	8.11	-29.94	0.13	25.62
SK1-S	Qingshankou Fm. Member 1	1780.00	91.75	3.2	2.31	-29.45		13.26
SK1-S	Quantou Formation	1805.00		1.0	0.13	-28.20		0.78
SK1-S	Quantou Formation	1810.00		0.2	0.11	-25.91		0.85
SK1-S	Quantou Formation	1815.00		0.5	0.13	-27.18		1.11
SK1-S	Quantou Formation	1845.00		3.2	0.10	-25.91		0.97
SK1-S	Quantou Formation	1865.00		0.5	0.18	-27.13		2.10
SK1-S	Quantou Formation	1895.39		0.2	0.11	-25.12		1.93
SK1-S	Quantou Formation	1903.10		0.1	0.12	-24.70		2.21

Data Summary

TOC Units	median	average	stdev
Yaojia/Quantou	0.16	0.46	1.0
Qingshankou	0.82	1.64	1.9
Qingshankou Member 1	2.70	3.69	
Qingshankou Members 2-3	0.76	1.20	

$\delta^{13}C_{org}$ duplicates	
count (n)	**12**
average (‰)	**0.05**

Carbonate	median	maximum
Qingshankou	6.88	22.41

C/N	median	average
Qingshankou Member 1	12.84	13.98
Qingshankou Members 2-3	7.19	8.11

$\delta^{13}C_{org}$	median	average	min	stdev
Yaojia/ Quantou	-27.10	-26.98		
Qingshankou	-28.78	-29.00		
Qingshankou Member 1	-30.04	-30.53	-32.40	
Qingshankou Members 2-3	-28.68	-28.67		1.49

Table A2.3.: Updated $\delta^{13}C$ chemostratigraphy from the Niobrara Formation of the Angus core (Denver Basin, Colorado), including new bulk carbonate $\delta^{13}C$ data ($\delta^{13}C_{carb}$). Lithostratigraphy, age model, and bulk organic carbon $\delta^{13}C$ ($\delta^{13}C_{org}$) from Joo & Sageman (2014). See Ch. 3 text for discussion.

Formation	Member	Sub-Member	Depth (m)	Age (Ma)	$\delta^{13}C_{org-avg}$	$\delta^{13}C_{carb}$	$\Delta^{13}C$
Niobrara	Smoky Hill	Middle Shale	2194.72	86.526	-26.23	2.00	28.23
Niobrara	Smoky Hill	Middle Shale	2195.12	86.553	-26.39	1.82	28.21
Niobrara	Smoky Hill	Middle Shale	2195.62	86.587	-26.12	1.96	28.08
Niobrara	Smoky Hill	Middle Shale	2196.11	86.621	-26.34	1.90	28.24
Niobrara	Smoky Hill	Middle Shale	2196.60	86.654	-25.23	1.95	27.18
Niobrara	Smoky Hill	Lower Limestone	2197.11	86.689	-26.07	1.85	27.92
Niobrara	Smoky Hill	Lower Limestone	2197.57	86.72	-25.92	1.89	27.81
Niobrara	Smoky Hill	Lower Limestone	2198.21	86.763	-26.38	1.91	28.29
Niobrara	Smoky Hill	Lower Limestone	2198.96	86.814	-26.1	1.87	27.97
Niobrara	Smoky Hill	Lower Limestone	2199.71	86.865	-25.7	1.83	27.53
Niobrara	Smoky Hill	Lower Limestone	2200.32	86.906	-26.22	1.91	28.13
Niobrara	Smoky Hill	Lower Limestone	2201.07	86.958	-25.98	1.14	27.12
Niobrara	Smoky Hill	Lower Limestone	2201.75	87.004	-25.67	2.12	27.79
Niobrara	Smoky Hill	Lower Limestone	2202.25	87.038	-25.59	1.75	27.34
Niobrara	Smoky Hill	Lower Limestone	2202.83	87.077	-25.77	1.84	27.61
Niobrara	Smoky Hill	Lower Limestone	2203.33	87.111	-25.79	1.88	27.67
Niobrara	Smoky Hill	Lower Limestone	2203.83	87.145	-25.63	1.96	27.59
Niobrara	Smoky Hill	Lower Limestone	2204.33	87.179	-25.75	2.07	27.82
Niobrara	Smoky Hill	Lower Limestone	2204.84	87.214	-25.66	1.72	27.38
Niobrara	Smoky Hill	Lower Limestone	2205.34	87.248	-25.59	2.11	27.70
Niobrara	Smoky Hill	Lower Limestone	2205.84	87.282	-25.88	1.91	27.79
Niobrara	Smoky Hill	Lower Limestone	2207.05	87.364	-25.65	1.84	27.49
Niobrara	Smoky Hill	Lower Limestone	2207.55	87.398	-25.8	1.83	27.63
Niobrara	Smoky Hill	Lower Limestone	2208.05	87.432	-25.77	1.94	27.71
Niobrara	Smoky Hill	Lower Limestone	2208.55	87.466	-25.68	1.86	27.54
Niobrara	Smoky Hill	Lower Shale	2209.05	87.5	-25.79	2.12	27.91
Niobrara	Smoky Hill	Lower Shale	2209.55	87.534	-25.48	1.65	27.13
Niobrara	Smoky Hill	Lower Shale	2210.05	87.568	-25.92	1.84	27.76
Niobrara	Smoky Hill	Lower Shale	2210.55	87.602	-25.81	2.00	27.81
Niobrara	Smoky Hill	Lower Shale	2211.09	87.639	-25.86	1.46	27.32
Niobrara	Smoky Hill	Lower Shale	2211.57	87.671	-25.95	1.92	27.87
Niobrara	Smoky Hill	Lower Shale	2212.07	87.705	-25.66	1.55	27.21
Niobrara	Smoky Hill	Lower Shale	2212.57	87.739	-25.78	1.92	27.70
Niobrara	Smoky Hill	Lower Shale	2213.12	87.777	-26.36	1.77	28.13
Niobrara	Smoky Hill	Lower Shale	2213.62	87.811	-26.31	1.70	28.01
Niobrara	Smoky Hill	Lower Shale	2214.12	87.845	-26.49	1.62	28.11
Niobrara	Smoky Hill	Lower Shale	2214.64	87.88	-26.36	1.59	27.95
Niobrara	Smoky Hill	Lower Shale	2215.14	87.914	-26.45	1.86	28.31
Niobrara	Smoky Hill	Lower Shale	2215.64	87.948	-26.54	1.79	28.33
Niobrara	Smoky Hill	Lower Shale	2216.09	87.979	-26.38	1.59	27.97
Niobrara	Smoky Hill	Lower Shale	2216.61	88.014	-26.36	1.84	28.20
Niobrara	Smoky Hill	Lower Shale	2217.09	88.047	-26.32	1.90	28.22

Formation	**Member**	**Sub-Member**	**Depth (m)**	**Age (Ma)**	**$\delta^{13}C_{org\text{-}avg}$**	**$\delta^{13}C_{carb}$**	**$\Delta^{13}C$**
Niobrara	Smoky Hill	Lower Shale	2217.59	88.08	-26.25	2.02	28.27
Niobrara	Smoky Hill	Lower Shale	2218.09	88.114	-26.31	1.83	28.14
Niobrara	Smoky Hill	Lower Shale	2218.59	88.244	-26.3	1.88	28.18
Niobrara	Smoky Hill	Lower Shale	2219.09	88.284	-26.2	1.76	27.96
Niobrara	Smoky Hill	Lower Shale	2219.49	88.316	-25.87	1.93	27.80
Niobrara	Smoky Hill	Lower Shale	2219.99	88.356	-26.25	2.16	28.41
Niobrara	Smoky Hill	Lower Shale	2220.49	88.396	-26.13	1.87	28.00
Niobrara	Smoky Hill	Lower Shale	2220.99	88.436	-26.42	2.14	28.56
Niobrara	Smoky Hill	Lower Shale & Limestone	2221.49	88.478	-26.11	1.89	28.00
Niobrara	Smoky Hill	Lower Shale & Limestone	2222.00	88.522	-25.61	1.90	27.51
Niobrara	Smoky Hill	Lower Shale & Limestone	2222.55	88.568	-25.28	1.91	27.19
Niobrara	Smoky Hill	Lower Shale & Limestone	2223.05	88.611	-26.31	1.84	28.15
Niobrara	Smoky Hill	Lower Shale & Limestone	2223.55	88.653	-26.26	1.85	28.11
Niobrara	Smoky Hill	Lower Shale & Limestone	2224.05	88.695	-26.05	2.03	28.08
Niobrara	Smoky Hill	Lower Shale & Limestone	2224.55	88.737	-25.94	2.00	27.94
Niobrara	Smoky Hill	Lower Shale & Limestone	2225.05	88.779	-26.15	1.72	27.87
Niobrara	Smoky Hill	Lower Shale & Limestone	2225.55	88.822	-26.29	1.87	28.16
Niobrara	Smoky Hill	Lower Shale & Limestone	2226.05	88.864	-26.79	1.55	28.34
Niobrara	Smoky Hill	Lower Shale & Limestone	2226.55	88.906	-26.21	1.73	27.94
Niobrara	Smoky Hill	Lower Shale & Limestone	2227.05	88.948	-26.52	1.82	28.34
Niobrara	Smoky Hill	Lower Shale & Limestone	2227.55	88.99	-26.29	1.70	27.99
Niobrara	Smoky Hill	Lower Shale & Limestone	2228.05	89.033	-26.22	1.78	28.00
Niobrara	Smoky Hill	Lower Shale & Limestone	2228.55	89.074	-26.55	1.49	28.04
Niobrara	Smoky Hill	Lower Shale & Limestone	2229.10	89.121	-25.65	1.83	27.48
Niobrara	Smoky Hill	Lower Shale & Limestone	2229.60	89.163	-26.07	1.80	27.87
Niobrara	Smoky Hill	Lower Shale & Limestone	2230.10	89.205	-26.26	1.57	27.83
Niobrara	Smoky Hill	Lower Shale & Limestone	2230.60	89.247	-26.32	1.71	28.03
Niobrara	Smoky Hill	Lower Shale & Limestone	2231.10	89.29	-26.34	1.87	28.21
Niobrara	Smoky Hill	Lower Shale & Limestone	2231.60	89.332	-26.21	1.41	27.62
Niobrara	Fort Hays Limestone		2232.10	89.374	-27.09	1.41	28.50
Niobrara	Fort Hays Limestone		2232.60	89.416	-27.19	0.76	27.95
Niobrara	Fort Hays Limestone		2233.10	89.459	-26.09	1.49	27.58
Niobrara	Fort Hays Limestone		2233.60	89.501	-26.48	1.41	27.89
Niobrara	Fort Hays Limestone		2234.10	89.543	-26.78	0.94	27.72
Niobrara	Fort Hays Limestone		2234.77	89.6	-26.58	1.24	27.82
Niobrara	Fort Hays Limestone		2235.49	89.66	-26.53	1.32	27.85
Niobrara	Fort Hays Limestone		2236.07	89.709	-26.41	1.52	27.93
Niobrara	Fort Hays Limestone		2236.60	89.756	-26	1.10	27.10

Appendix 3: Supplemental Material for Chapter 4 and Jones et al. (in press)

Astronomical Pacing of Relative sea Level during Oceanic Anoxic Event 2 from the Expanded SH#1 Core, Utah

Contents

Figure A3.1.: Geophysical logs of the SH#1 borehole.

Figure A3.2.: MTM analysis of $\delta^{13}C_{carb}$ timeseries.

Table A3.1.: Geochemical data from the SH#1 core.

Table A3.2.: Floating astronomical age model (ATS) for SH#1 core.

Table A3.3.: SH#1 and SH#2 coring recovery rates and core-box depths.

Figure A3.1.: Downhole geophysical logs of the SH#1 borehole. From left to right: Caliper diameter, 3D caliper diameter, natural gamma ray (counts per second), shallow and deep resistivity (ohm-m), spontaneous potential and conductivity, Delta T (transit time), and sonic amplitude.

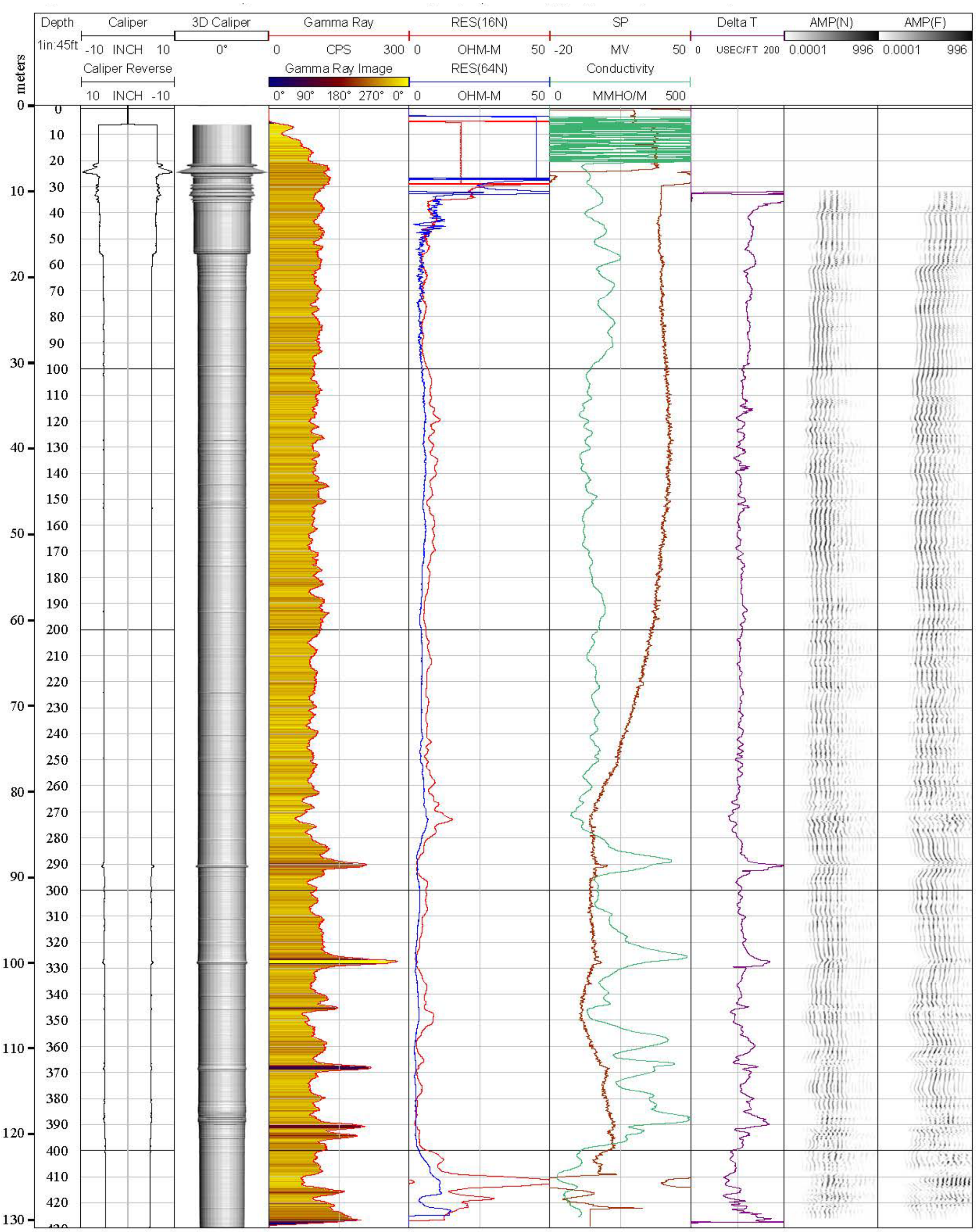

Figure A3.2.: Multi-taper method (MTM) spectral analysis (Thomson, 1982) results of astronomically tuned $\delta^{13}C_{carb}$ time series from SH#1 core, using the short eccentricity tracing timescale from EHA (see Chapter 4 Methods and Results). Significant frequencies in time series (numbered 1-7) identified for spectral peaks with red noise confidence levels (middle) and MTM F-test statistics (bottom) above 90% (see Meyers, 2012 for detailed discussion) and/or F-test statistics above 99%. Figure produced using "astrochron" R package (Meyers, 2014).

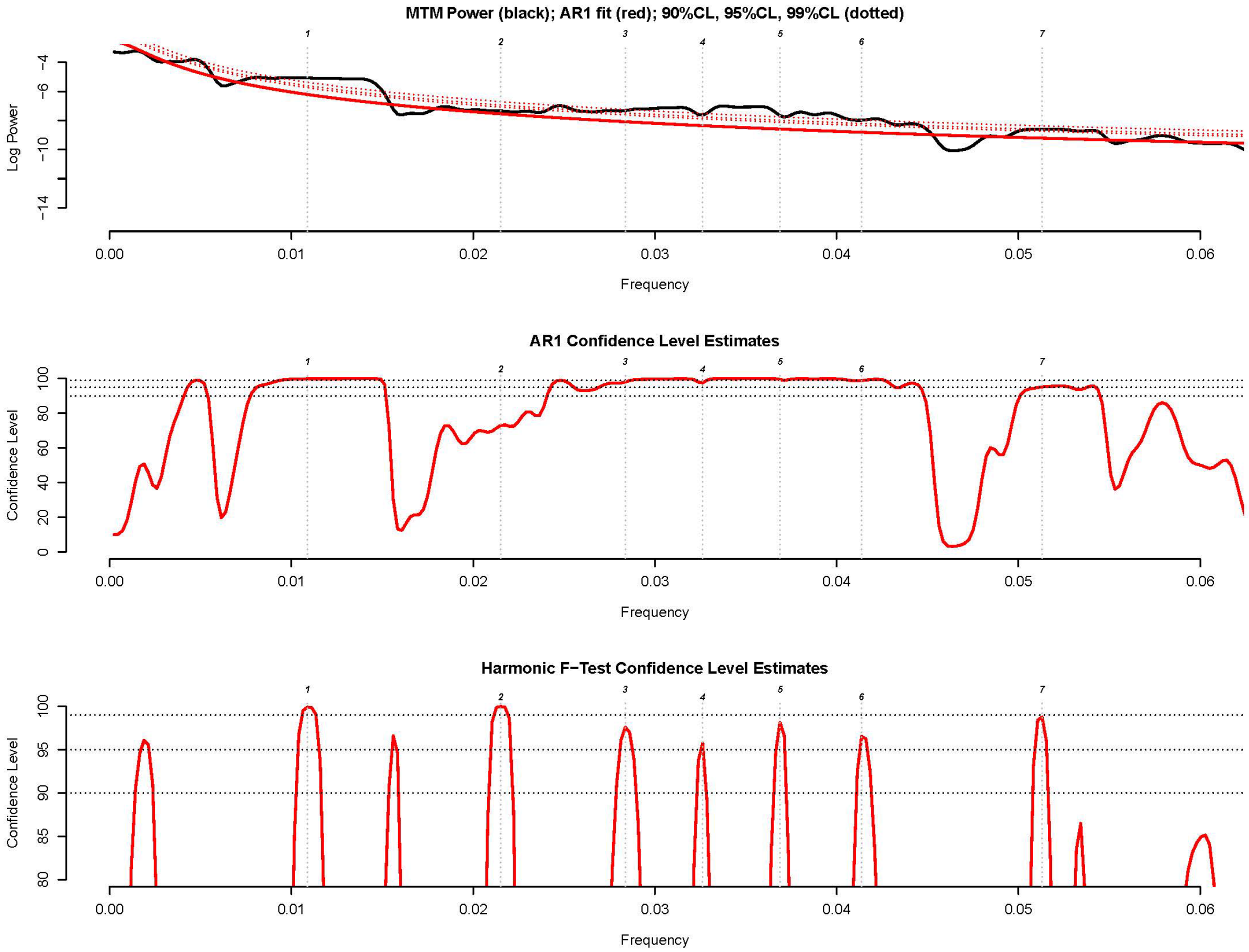

Table A3.1. (next page): Chemostratigraphic data from the Cenomanian-Turonian Boundary interval of the Tropic Shale from the SH#1 core. Bulk organic carbon isotope ratios ($\delta^{13}C_{org}$), bulk carbonate carbon isotope ratios ($\delta^{13}C_{carb}$), bulk carbonate oxygen isotope ratios ($\delta^{18}O_{carb}$), weight percent carbonate content (%Carb), weight percent total organic carbon (%TOC), and the difference between $\delta^{13}C_{carb}$ and $\delta^{13}C_{org}$ are reported. Standard deviations (σ) of replicate measurements of SH#1 samples and the Union Springs reference material from Northwestern University are noted at the bottom of the table. Correlation matrix of geochemical parameters (r-values) at base of table. See Chapter 4 text for discussion.

Depth (m)	Average $\delta^{13}C_{org}$ (‰ VPDB)	stdev $\delta^{13}C_{org}$	%Carb	%TOC	Average $\delta^{13}C_{carb}$ (‰ VPDB)	$\delta^{13}C_{carb}$ stdev	d18O-avg	d18O stdev	$\Delta^{13}C$
124.97	-25.57		7.80	1.04	-0.23		-7.37		25.34
124.76	-26.01		13.67	0.84	0.01		-6.98		26.03
124.56	-25.29		16.08	0.87	0.07		-7.32		25.35
124.37	-25.54		17.20	1.02	-0.12		-7.82		25.42
124.17	-25.41		10.08	1.05	0.09		-5.98		25.50
124.00	-25.15		11.43	1.13	-0.09	0.02	-8.01	1.52	25.06
123.79	-25.16		13.89	1.27	0.14		-7.63		25.30
123.60	-25.11	0.02	16.50	1.58	-0.21		-8.16		24.91
123.39	-25.24		15.57	1.52	-0.24		-7.44		25.00
123.20	-25.34	0.15	23.03	0.50	-1.65		-12.76		23.69
122.99	-25.12		14.96	1.28	-0.47		-8.57		24.65
122.80	-25.19		17.25	1.21	-0.19		-7.72		24.99
122.59	-25.18		13.97	2.42	-0.27		-9.82		24.92
122.40	-25.30		14.35	1.66	-0.06	0.01	-7.94	0.44	25.24
122.19	-25.66		3.52	0.68	1.16	0.18	-7.37	0.69	26.82
122.00	-24.88		5.02	0.72	2.07		-6.67		26.95
121.80	-25.45		3.34	0.79	1.65		-8.06		27.10
121.60	-25.57		2.98	0.78	1.41		-8.76		26.97
121.40	-25.45	0.12	5.09	0.74	1.33	0.23	-6.86	0.56	26.78
121.20	-25.56		7.59	0.98	1.78		-8.52		27.34
121.01	-24.78	0.27	23.63	1.37	-2.65		-11.84		22.14
120.80	-24.07		16.17	0.97	0.83		-9.68		24.89
120.60	-23.79		24.51	0.33	1.69		-9.99		25.48
120.40	-23.54		18.17	0.36	1.89	0.00	-8.89	0.02	25.43
120.20	-23.50	0.26	6.86	0.53	3.11		-8.11		26.61
120.00	-23.25		5.47	0.60	3.15		-8.96		26.41
119.80	-24.56	0.04	4.29	0.29	-0.46		-10.26		24.10
119.61	-24.98		4.92	0.46	1.41	0.02	-9.31	0.03	26.39
119.41			0.76	0.08					
119.21	-24.51	0.12	2.73	0.21	-1.19		-9.50		23.32
118.99	-24.95	0.13	5.34	0.37	1.76		-8.94		26.71
118.81	-24.76	0.05	5.83	0.50	2.26		-9.59		27.02
118.55	-24.45		3.97	0.29	1.91		-10.08		26.36
118.35	-23.71	0.00	7.35	0.43	3.63		-8.22		27.35
118.19	-24.12		12.19	0.59	2.47		-8.93		26.59
118.01	-24.93	0.07	14.76	0.54	1.70		-8.69		26.63
117.80	-24.23		16.31	0.60	2.43	0.10	-8.22	0.23	26.66
117.60	-24.17		20.11	0.41	2.94		-7.37		27.11
117.39	-23.42		14.07	0.86	2.98		-8.51		26.40
117.20	-23.75		10.75	0.91	2.65		-8.86		26.41
116.99	-23.35		10.13	0.90	2.62		-8.09		25.97
116.80	-23.73		13.55	0.94	2.80		-10.38		26.54
116.59	-23.23		23.56	0.76	2.10		-10.62		25.33
115.88	-23.01		14.76	0.53	3.25		-8.86		26.26
115.70	-22.84		19.23	0.96	3.45		-9.15		26.29
115.47	-22.65		21.48	0.83	3.62		-8.23		26.27
115.28	-23.22	0.08	20.23	0.48	2.69		-8.18		25.91

Depth (m)	Average $\delta^{13}C_{org}$ (‰ VPDB)	stdev $\delta^{13}C_{org}$	%Carb	%TOC	Average $\delta^{13}C_{carb}$ (‰ VPDB)	$\delta^{13}C_{carb}$ stdev	d18O-avg	d18O stdev	$\Delta^{13}C$
115.07	-23.37		22.21	0.71	3.36		-8.89		26.74
114.89	-22.96		23.42	0.90	3.17		-7.09		26.12
114.68	-22.88		26.85	0.97	2.56		-8.03		25.44
114.48	-23.10		32.17	0.97	2.37		-8.37		25.48
114.29	-22.98		36.05	2.12	2.89		-7.79		25.87
114.08	-23.20		19.76	1.73	3.36		-8.16		26.56
113.89	-23.36		25.57	1.14	3.04		-8.21		26.40
113.71	-23.61		24.05	1.18	3.23		-7.34		26.84
113.51	-23.31		23.34	1.51	3.24		-7.42		26.55
113.32	-23.66	0.15	14.87	1.03	3.35		-7.42		27.01
113.11	-24.25		11.37	1.43	3.86	0.03	-7.07	0.28	28.11
112.89	-23.60		13.53	2.88	3.78		-7.12		27.38
112.77	-23.48		23.35	1.65	3.29		-6.99		26.77
112.55	-23.72		24.76	1.71	3.15		-7.74		26.87
112.12			1.03	0.04					
111.87	-23.44		23.62	1.43	2.60		-8.37		26.04
111.69	-23.08		23.34	1.26	2.57		-9.00		25.65
111.46	-22.77		23.22	1.27	2.80		-9.56		25.57
111.25	-23.08		15.86	1.20	3.50		-8.12		26.58
111.06	-22.82		24.29	1.46	3.36		-8.14		26.18
110.87	-22.97		19.28	1.76	3.77		-7.47		26.74
110.65	-23.16		16.67	1.78	3.91		-7.12		27.07
110.45	-22.95	0.09	13.70	1.75	3.94		-7.21		26.89
110.25	-23.35		17.13	1.53	3.94		-7.21		27.30
110.05	-22.79		15.41	2.08	4.13		-7.20		26.93
109.86	-23.09		18.72	1.73	4.30		-7.73		27.39
109.66	-23.09		21.54	0.99	4.08		-7.46		27.17
109.46	-23.40		23.32	1.00	4.29		-6.77		27.68
109.26	-23.38		24.35	1.47	4.12		-6.40		27.51
109.07	-23.34		21.86	1.66	4.16		-7.26		27.50
108.87	-23.35		30.86	1.40	3.94		-7.36		27.29
108.67	-23.30		39.25	1.30	3.74		-7.95		27.05
108.45	-23.44		48.08	1.17	3.42		-8.19		26.86
108.25	-23.38		32.47	0.87	3.98		-7.90		27.36
108.05	-23.46		30.92	0.94	4.03		-7.42		27.49
107.85	-23.53		40.90	1.00	3.75		-7.19		27.28
107.65	-22.96		40.29	1.07	3.93	0.00	-7.22	0.13	26.89
107.44	-23.02		30.63	1.24	4.11		-7.36		27.13
107.26	-22.86		41.26	1.08	3.78		-7.82		26.63
107.06	-23.16	0.05	54.41	0.96	3.67		-7.38		26.83
106.86	-23.01		51.97	0.97	3.75		-7.44		26.77
106.66	-23.23		45.59	0.95	3.86		-7.56		27.10
106.46	-23.44		53.68	0.82	3.44		-7.54		26.88
106.27	-23.51		51.98	1.04	3.59		-7.49		27.10
106.08	-23.32		51.93	0.85	3.41		-7.69		26.73
105.68	-23.65		53.19	1.05	3.14		-7.77		26.79
105.88	-23.74		61.15	0.84	2.77		-7.65		26.52

Depth (m)	Average $\delta^{13}C_{org}$ (‰ VPDB)	stdev $\delta^{13}C_{org}$	%Carb	%TOC	Average $\delta^{13}C_{carb}$ (‰ VPDB)	$\delta^{13}C_{carb}$ stdev	d18O-avg	d18O stdev	$\Delta^{13}C$
105.49	-23.79		39.29	0.97	3.64		-7.90		27.43
105.12	-24.22		13.68	0.37	3.51		-7.60		27.73
104.91	-24.25		37.80	0.82	3.19		-7.93		27.43
104.71	-24.08		38.16	0.93	3.26		-8.32		27.34
104.51	-24.32		35.23	0.92	3.56		-8.00		27.88
104.31	-24.46		33.66	0.77	3.08		-8.08		27.55
104.12	-24.55	0.04	34.89	0.85	2.81		-8.02		27.35
103.93	-24.76		26.88	0.78	2.85		-8.19		27.61
103.73	-25.02		33.63	0.79	2.72	0.02	-8.20	0.03	27.74
103.52	-24.96		38.59	0.77	2.33		-8.51		27.30
102.75	-24.81	0.12	55.00	0.73	2.06		-8.07		26.87
102.55	-24.57		37.77	0.90	2.68		-7.89		27.25
102.35	-24.83		37.91	0.92	2.77		-7.89		27.60
102.15	-24.23		30.85	1.03	2.94		-7.84		27.18
101.96	-24.14		29.76	0.98	2.93		-7.78		27.08
101.77	-24.26		27.49	1.05	3.06		-7.65		27.32
101.56	-24.44		29.28	1.10	2.77		-8.33		27.21
101.36	-24.62		28.04	1.09	2.84		-8.10		27.46
101.16	-24.68		26.05	1.24	2.84		-8.36		27.52
100.95	-24.88	0.07	27.75	1.37	2.70		-8.01		27.59
100.73	-24.79		26.76	1.26	2.65		-7.75		27.44
100.54	-24.85		24.40	1.20	2.62		-7.70		27.47
100.31	-24.88		21.49	1.06	2.61		-7.73		27.50
100.11	-24.84		22.18	1.08	2.61		-7.46		27.45
99.96			1.16	-0.04					
99.73	-25.29		17.77	0.46	2.30		-8.10		27.58
99.57	-25.19		22.93	0.68	2.49		-8.48		27.68
99.37	-25.29		25.73	0.80	2.52		-8.09		27.81
99.17	-25.05		26.20	0.96	2.46		-8.20		27.51
98.97	-24.94		24.67	1.03	2.54		-8.06		27.47
98.77	-24.89		26.13	1.49	2.58		-8.40		27.46
98.60	-24.89		22.67	1.69	2.55		-7.96		27.44
98.39	-24.82		26.12	1.46	2.78		-8.02		27.61
98.20	-24.86		31.30	1.27	2.56		-8.06		27.42
98.00	-24.84		32.05	1.07	2.80		-8.04		27.64
97.80	-24.90		24.92	1.04	2.78		-8.16		27.67
97.60	-24.96		27.31	1.09	2.55		-8.79		27.51
97.31	-25.13		23.22	0.97	2.65		-8.23		27.78
97.10	-25.01		23.00	1.19	2.74		-8.04		27.75
96.91	-24.82		21.01	1.03	2.59		-7.96		27.41
96.72	-24.99		21.90	1.18	2.59		-8.30		27.58
96.51	-24.95		25.99	1.10	2.53		-8.07		27.48
96.30	-24.79		30.09	1.18	2.43	0.01	-8.23	0.17	27.21
96.11	-24.86		29.09	1.18	2.31		-8.42		27.16
95.91	-24.94		28.21	1.23	2.36		-8.24		27.30
95.70	-24.80		26.39	1.19	2.38		-7.93		27.18
95.51	-24.83		29.15	1.17	2.46		-8.11		27.30

Depth (m)	Average $\delta^{13}C_{org}$ (‰ VPDB)	stdev $\delta^{13}C_{org}$	%Carb	%TOC	Average $\delta^{13}C_{carb}$ (‰ VPDB)	$\delta^{13}C_{carb}$ stdev	d18O-avg	d18O stdev	$\Delta^{13}C$
95.30	-24.84		26.85	1.32	2.57		-7.99		27.41
95.12	-24.68		28.60	1.20	2.55		-7.87		27.23
94.93	-25.02		26.16	1.18	2.67		-7.96		27.69
94.71	-24.91		23.98	1.54	2.75		-7.87		27.66
94.51	-24.80	0.25	32.56	1.14	2.59		-8.07		27.39
	Avg. 1σ uncert.	0.11				0.06		0.37	

Union Springs internal reference material (n=15):	**Average $\delta^{13}C_{org}$ (‰ VPDB)**	**1σ $\delta^{13}C_{org}$ uncertainty**
	-30.32	0.08

r-values	**δ13Corg (‰ VPDB)**	**%Carb**	**%TOC**	**d13Ccarb**	**d18Ocarb**	**Δ13C**
δ13Corg (‰ VPDB)	1	-	-	-	-	-
%Carb	0.28	1	-	-	-	-
%TOC	0.16	0.09	1	-	-	-
d13Ccarb	0.65	0.40	0.16	1	-	-
d18Ocarb	0.12	0.18	0.31	0.46	1	-
Δ13C	-0.01	0.29	0.07	0.75	0.50	1

Table A3.2.: A floating astronomical time scale (ATS) for the lower Tropic Shale in the SH#1 core spanning Oceanic Anoxic Event 2 (OAE2) derived from spectral analysis of the $\delta^{13}C_{carb}$ chemostratigraphy. The upper interval of the ATS was constructed from sedimentation rates resulting from tracing the short eccentricity cycle after evolutive harmonic analysis (Meyers et al., 2001). The lowermost Tropic Shale ATS was constructed from a bandpass of the short eccentricity cycle.

Depth (m)	Floating time (kyr)
97.01	799.9
98.01	775.9
99.01	750.7
100.01	727.2
101.01	703.9
102.01	677.7
103.01	649.0
104.01	621.3
105.01	588.7
106.01	553.2
107.01	516.7
108.01	480.9
109.01	441.2
110.01	419.4
111.01	394.3
112.01	366.6
113.01	333.8
114.01	297.3
115.01	256.5
116.01	209.1
117.01	162.1
118.01	128.3
119.01	93.3
120.01	56.0
121.01	18.7
121.51	0.0

Table A3.3.: Core drilling summary and core box depth list for SH#1 and SH#2 cores.

Lat./Long. = N37°90’32.93”/W111°31’57.03”

Core: Smoky Hollow #1, dates cored by USGS (7/9/14-7/11/14)

Total Depth: 430.29 m, core recovery: 96%

Core: Smoky Hollow #2, dates cored by USGS (7/11/14-7/13/14)

Total Depth: 420.79 m, core recovery: 93%

Core	Box #	Interval Drilled - Top (m)	Interval Drilled - Base (m)
SH-1	27	310.00	319.58
SH-1	28	319.83	329.29
SH-1	29	329.29	340.04
SH-1	30	340.04	350.04
SH-1	31	350.04	359.79
SH-1	32	359.79	370.21
SH-1	33	370.21	379.71
SH-1	34	379.71	391.04
SH-1	35	391.04	400.63
SH-1	36	400.63	410.33
SH-1	37	410.33	420.00
SH-1	38	420.08	429.50
SH-1	39	429.50	430.29
Core	**Box #**	**Interval Drilled - Top (m)**	**Interval Drilled - Base (m)**
SH-2	1	310.75	320.17
SH-2	2	320.17	331.17
SH-2	3	331.17	340.75
SH-2	4	340.83	350.67
SH-2	5	350.67	361.17
SH-2	6	361.17	371.08
SH-2	7	371.08	380.21
SH-2	8	380.21	389.92
SH-2	9	389.92	401.13
SH-2	10	401.13	410.13
SH-2	11	410.13	419.08
SH-2	12	419.08	420.79

Appendix 4: Supplemental Material for Chapter 5

Regional Chronostratigraphic Synthesis of the Cenomanian-Turonian OAE2 Interval, Western Interior Basin: Astrochronology, Radioisotope Dating, and New Os and C Chemostratigraphy

Contents

A4.1: Depth adjustment for Angus core.

Table A4.1: Depth corrections for Angus core to adjust marked depths on core surface to true depths. Note the conventions that adding centimeters is equivalent to increasing core depth. Additionally, these corrections were implemented after studying the CTB interval of the Angus core only. Other discrepancies in the core markings could exist in deeper and shallower intervals, however, the corrections of the CTB interval permits accurate comparison of XRF scanning (astrochronologic time scale) and geochemical datasets.

Marked depth intervals	**Depth Corrections**
< 7475’	No corrections
>= 7475’ and < 7571’	Add 19.92 cm to marked depth
> 7571’	Add 15.15 cm to marked depth

A4.1 Minor Angus core depth scale correction

In previous studies, depth horizons of samples collected for geochemical analysis from the Angus core were recorded as a centimeter offset (+/-) from footage markers (e.g., “7474’-10 cm”, where + indicated shallower and - deeper depths than the footage marker) and then converted to meters depth (Joo and Sageman, 2014). However, several of the original footage markers on the core were not spaced at 12 inches or were mismarked during original splitting of core, such that some depths in Joo and Sageman (2014) are offset by a maximum of 19.92 cm. Although this offset is relatively minor, it is important to correct for our high-resolution study of the onset of OAE2 and to align previous continuous XRF core scanning data, the foundation of the Angus core astronomical time scale (Ma et al., 2014), with discrete geochemical samples. Sampling for this study and Ibarra et al. (in prep.) utilize the corrections of Table A4.1, and denote +x cm for samples *deeper,* and -x cm for samples *shallower,* than the footage marker on the core.